Development and characterization of high temperature and -pressure alkaline electrolysis cells (HTP-AECs)

Adolphsen, Jens Quitzau

Publication date:
2018

Document Version
Publisher's PDF, also known as Version of record

Technical University
of Denmark

Development and characterization of high temperature and -pressure alkaline electrolysis cells (HTP-AECs)

Jens Q Adolphsen

Ph.D. thesis

Department of Energy Conversion and Storage
August 2018

Tat Tvam Asi

Thou Art That or *That art Thou*

A Hindu aphorism from Chandogya Upanishad 6.8.7.

A book by Joseph Campbell.

Preface

This thesis is submitted as part of the PhD degree at the Technical University of Denmark (DTU). The thesis work has been carried out from August 1, 2015 to August 31, 2018. The majority of it has taken place within the Department of Energy Conversion and Storage (DTU Energy) as part of the section for Ceramic Engineering and Science at the DTU Risø campus in Roskilde, Denmark. The PhD has been supervised by principal supervisor Bhaskar R. Sudireddy and co-supervisors Christodoulos Chatzichristodoulou and Vanesa Gil. Bhaskar and Christos are senior researchers at DTU Energy, and Vanesa is a senior researcher at the Aragon Hydrogen Foundation, Huesca, Spain. A five month external stay with Professor Lennart Bergström as host was conducted from March 1, 2017 to July 31, 2017. It took place at the Department of Materials and Environmental Chemistry, Stockholm University, Sweden.
The PhD project has been internally funded by the section for Ceramic Engineering and Science under DTU Energy.

Jens Q Adolphsen
August 2018

Abstract

During the last three decades the Intergovernmental Panel on Climate Change (IPCC) has published several reports. Each new report has made it increasingly clear that climate change needs to be handled now - sooner rather than later. There is strong evidence that climate change is caused predominantly by human activities, grounded in the unprecedented increase in greenhouse gas concentrations, including carbon dioxide, since the beginning of the industrial era. The fact that the worlds energy supply has been relying mainly on fossil fuels during the entire industrial era and until now elucidates the need to implement sustainable energy technologies that carry a significantly smaller carbon footprint compared to fossil fuel based technologies. A major challenge in the shift from a fossil based energy system to sustainable energy system, based on renewable energy, is the storage of large amounts of electricity and the conversion of electricity to other useful forms of energy. We know that hydrogen can serve as an energy carrier between various forms of energy.

Currently, electrolysis is the most mature approach to produce hydrogen from renewable sources which means the electricity has to come from renewable sources. Hydrogen can be stored as chemical energy for long periods of time and production is feasible on the kW-GW scale. In addition, the hydrogen can be used as a precursor to make synthetic fuels, e.g., for parts of the transport sector that is hard to electrify. As mentioned hydrogen can be produced using electrolysis which is the electrochemical splitting of water into its constituents, oxygen and hydrogen gas, using electricity as the driving force. Alkaline electrolysis is the most proven electrolysis technology and the most utilized technology on a commercial level. There is, however, room for improvement of the technology, in terms of improving the efficiency and increasing the hydrogen production rate per unit area of electrolysis cell.

The work in this thesis is focused on improving the alkaline electrolysis technology utilizing a cell concept that allows for operation at high temperatures (150-250 °C) and high pressure (20-40 bar), as this can significantly improve the cell efficiency and hydrogen production rate per unit area of cells. Ultimately this can lead to lower production prices of electrolyzed hydrogen. These electrolysis cells are termed high temperature and pressure alkaline electrolysis cells (HTP-AECs).

The main objective in this project has been to develop, process and test porous oxygen electrodes. The starting point of the work carried out has been to identify electrocatalyst materials that are suitable to catalyse the evolution of oxygen; having in mind that the

materials have to be stable during operation at HTP conditions. Ceramic oxides (mixed metal oxides) have been investigated as candidates and among these some La, Ni and Fe based oxides with the perovskite (or related) structure have been tested. The overpotential of the materials towards the oxygen evolution reaction (OER) in 1 M KOH is in the range 0.38-0.45 V at 10 mA cm^{-2}. The most active electrocatalysts were a multiphase-$LaNiO_3$ and a $La_2Ni_{0.9}Fe_{0.1}O_4$. None of the candidates were chemically stable after exposure to concentrated KOH at 220 °C for one week; the main secondary phases identified were $La_2O_3/La(OH)_3$ and NiO. The perovskite $LaNi_{0.6}Fe_{0.4}O_3$ (LNF) is stable at 100 °C and appear to be the most stable among the candidates. It is also sufficiently active towards the OER, thus it has been used for the further work.

The processing of porous LNF electrodes was done by screen printing optimized inks stabilized with polyvinylpyrrolidone (PVP) as dispersant and graphite and poly(methyl methacrylate) (PMMA) as pore formers. Larger pores were generated after burn-out of Graphite and PMMA with different sizes and shapes and thus used to generate different microstructures. A partial sintering of the electrode layers left finer inter-particle pores. The resulting structures have 58-72 % porosity and the d10 % d90 pore sizes are 0.19-0.28 μm and 1.5-3.5 μm respectively. Electrodes were tested, at conditions relevant for conventional alkaline electrolysis cells, in 8 M KOH at 65 °C. The electrodes were tested as flooded electrodes, used in conventional alkaline electrolysis cells and gas diffusion electrodes, used in HTP-AECs, and showed similar performance in both cases. The overpotential of the most suitable cell was 0.42 V and 0.46 V at 0.2 A cm^{-2} in the flooded and gas diffusion mode respectively. The electrodes are sufficiently stable at these conditions. A screening of different electrode microstructures at room temperature in 1 M KOH showed that the sintering temperature was the most important parameter. A lower sintering temperature, resulted in more porous bodies, large inter-particle pore sizes and better electrode performance. The electrodes sintered at lower temperatures turned out to be too mechanically too weak.

Aqueous LNF suspensions containing rice starch as a pore former were also investigated as a possible way to fabricate porous electrodes with similar microstructures as mentioned above. The main advantage being that water based suspensions are more environmentally friendly than the organic solvents usually used in ceramic processing. Starch consolidation casting was used to process thin electrode layers but crack formation and delamination from the substrate could not be avoided after deposition and sintering. Quantification of the particle size and zeta-potential in the suspensions along with the sedimentation- and rheological behaviour, revealed that LNF is stabilized well electrostatically in aqueous suspensions at their intrinsic pH or sterically using the polymer PVP.

In relation to the HTP-AEC technology, the LNF electrodes developed in this work, though chemically unstable at HTP conditions, are relevant to test at HTP-AEC conditions. The reason being that valuable information, about performance of the microstructures and about the long-term chemical and mechanical stability, can be retrieved. This is valuable information for comparison with previous work and it can serve as a guide for future development work.

Resume

"Intergovernmental Panel on Climate Change" (IPCC) har de sidste tre årtier publiceret fem rapporter, der gør det mere og mere klart, at klimaforandringerne skal håndteres nu - hellere før end siden. Der er stærke beviser for, at klimaforandringerne, hovedsageligt er menneskeskabte. Beviserne er funderet i den hidtil usete stigning i koncentrationen af drivhusgasser, herunder især kuldioxid, i atmosfæren siden begyndelsen påden industrielle revolution. Det faktum at verdens energiforsyning har været langt overvejende baseret påfossile brændstoffer under hele den industrielle æra og frem til nu, understreger nødvendigheden af at implementere bæredygtige energiteknologier, som bærer et betydeligt mindre karbon fodaftryk sammenlignet med fossilt baserede teknologier. En af hovedudfordringerne i skiftet fra et fossilt funderet- til et til et bæredygtigt energisystem, funderet påvedvarende energikilder, er lagringen af store mængder el og konverteringen af el til andre nyttige energiformer. Vi ved, at brint kan agere som energibærer mellem forskellige energiformer.

Som det er nu, er elektrolyse den mest modne tilgang til at producere brint fra vedvarende energikilder, dvs. hvor elektriciteten i det her tilfælde kommer fra vedvarende energikilder. Brint kan lagres som kemisk bundet energi i lang tid og produktionen er gennemførlig påkW-GW skala. Derudover, kan brint bruges som en forløber til at lave syntetiske brændstoffer, for eksempel til de dele af transportsektoren, som er vanskellig at elektrificere. Det blev nævnt, at bring kan produceres vha. elektrolyse, hvilket er en elektrokemisk spaltning af vand til dens bestanddele, bring og ilt, hvor en elektrisk strøm udfører arbejdet. Alkalisk elektrolyse er den mest gennemprøede teknologi og den mest brugte pået kommercielt plan. Der er imidlertid stadig plads til forbedring af teknologien, mht. at forbedre effektiviteten og højne brint produktionsraten per areal enhed af elektrolysecelle.

Arbejdet i denne afhandling har været målrettet en forbedring af den alkaliske elektrolyseteknologi. Mere specifikt har det omhandlet et elektrolysecelle koncept, som tillader drift ved høje temperaturer (150-250 °C) og høje tryk (20-40 bar) (HTT), da det kan være med til at forbedre elektrolysecelle effektiviteten og brint produktionsraten per areal enhed af elektrolysecelle. Ultimativt kan det betyder lavere produktionsomkostninger til brint produceret vha. elektrolyse. Den før beskrevne elektrolysecelleteknologi kalder vi høj temperatur og tryk alkaliske elektrolyseceller (HTT-AEC).

Hovedmålsætningen i dette projekt har været at udvikle, processere og teste porøse oxygen elektroder. Udgangspunktet for arbejdet har været at identificere elektrokatalysator-

materialer, som kan katalysere iltudviklingsreaktionen med omtanke for, at materialerne skal være stabile under HTT forhold. Keramiske oxider (blandede metal oxider) er blevet identificeret som en relevant materialegruppe og iblandt dem er nogle La, Ni og Fe baserede oxider med perovskit-strukturen blevet testet. Materialernes overpotential ift. iltudviklingsreaktionen i 1 M KOH ligger i intervallet 0.38-0.45 V ved 10 mA cm^{-2}. De mest aktive elektrokatalysatorer var en multifaset $LaNiO_3$ og en $La_2Ni_{0.9}Fe_{0.1}O_4$. Ingen af kandidaterne er kemisk stabile efter eksponering i koncentreret KOH ved 220 °C; hoved sekundærfaserne som blev identificeret var $La_2O_3/La(OH)_3$ og NiO. Perovskiten $LaNi_{0.6}Fe_{0.4}O_3$ (LNF) er stabil ved 100 °C og ser ud til at være det mest stabile materiale iblandt kandidaterne. LNF er ogsåtilstrækkeligt aktivt mod iltudviklingsreaktionen, og derfor er det blevet brugt i det videre arbejde.

Processeringen af porøse LNF elektroder er blevet gjort ved at silketrykke optimerede suspensioner stabiliseret med dispergeringsmidlet polyvinylpyrrolidon (PVP) og tilsat poredannerne akryl og grafit. Større porer er blevet dannet efter afbrænding af grafit og akryl med forskellig størrelse, hvilket har givet sig udslag i forskellige mikrostrukturer. En partiel sintring af elektrodelagene efterlod mindre inter-partikel porer. De sintrede elektroder har 58-72 % porøsitet og d10 & d90 pore størrelser påhhv. 0.19-0.28 μm og 1.5-3.5 μm. Elektroderne er blevet testet under forhold relevant for konventionelle alkaliske elektrolyseceller i 8 M KOH ved 65 °C. De er blevet testet som hhv. oversvømmede elektroder brugt i konventionelle alkaliske elektrolyseceller, og som gas diffusionselektroder brugt i HTT-AEC. Overpotentialet for de mest egnede celler var 0.42 V og 0.46 V ved 0.2 mA cm^{-2} som hhv. oversvømmede- og gas diffusionselektroder. Elektroderne var stabile ved de her forhold. En screening af forskellige elektrodemikrostrukturer ved rumtemperatur i 1 M KOH viste, at sintringstemperaturen var den vigtigste parameter. En lavere sintringstemperatur resulterede i mere porøse strukturer med større inter-partikel pore størrelser og bedre elektrodeydeevne. Elektroderne sintret ved lavere temperaturer var imidlertid ogsåfor svage mekanisk.

Vandige LNF suspensioner, med risstivelse som poredanner, er også blevet undersøgt som en mulig vej til at fremstille porøse elektroder med lignende mikrostrukturer, som nævnt i forrige sektion. Den væsentligste fordel ved at bruge vandbaserede suspensioner er, at de er mere miljøvenlige end organisk solvent baserede suspensioner. De vandbaserede LNF suspensioner med risstivelse blev brugt til at processere tynd lag, men revnedannelse og delaminering fra substratet kunne ikke undgås i tørrings- og sintringsfasen. Kvantificering af partikelstørrelser og zeta-potentialet i suspensionerne samt deres sedimentations- og reologiopførsel viste at LNF stabiliseres effektivt elektrostatisk i vandige suspensioner ved deres intrinsiske pH eller sterisk vha. polymeren PVP.

I relation til HTT-AEC teknologien er det relevant at teste de udviklede LNF elektroder under realistiske driftsbetingeler ogsåselvom de er kemisk ustabile ved høje temperaturer. Årsagen er, at det kan give værdifuld information om mikrostrukturernes ydeevne og om deres langsigtede kemiske og mekaniske stabilitet. Denne information kan blive brugt til at sammenligne med tidligere arbejde, og det kan tjene som vejviser for fremtidigt udviklingsarbejde.

Acknowledgements

During the last three years I have learned a lot. At times it has been inspiring, at other times it has been puzzling and at yet other times it has been challenging. I have also been confused and unsure what is important to focus on when working as a Ph.D. student. Am I supposed to do something really novel or should I just make sure to get the task done? Do I have to do this on my own or can I seek assistance? Nonetheless, I feel that I have been able to rise to the occasion when needed and conducted a successful project.

The Ph.d. work has confirmed me in the view that no one really creates something truly on their own. We always find inspiration outside of ourselves and seek help from others. This has certainly also been the case during my Ph.D studies. I have received a lot of very qualified supervision, help in the lab and help with lab work. Moreover, I have had many fruitful discussions with people.

I would like to start thanking my section leader *Severine Ramousse*. You offered me the opportunity to become a Ph.D. student in the section and allowed me to decide, quite freely, what I wanted to work with. Thumbs up.

My main supervisor *Bhaskar R. Sudireddy*. Bhaskar, you have been inspiring to have as a supervisor, given me a lot of advice and also been concerned with how I relate to and identify with the what I am doing. I am very grateful for this. My co-supervisor *Christodoulos Chatzichristodoulou*, you have been indispensable to have in the project with all your knowledge about HTP-AEC and electrochemistry. You articulated during the first year the need to do what is expedient. At first, I did not get it but it has caught on, and I am grateful for this advice. I would also like to thank my last co-supervisor *Vanesa Gil*. You stepped up when I needed it and took the role as main supervisor. Thank you for that.

I have received a lot of help and advice in the labs. On the first floor, in the process lab, I would like to show my gratitude to *Søeren P. V. Foghmoes., Mads G. Sørensen , Karen Brodersen, Lene Knudsen, Kjeld B. Andersen, Jette Iversen, Henrik Paulsen, Søren Christensen, Marianne Nielsen, Jeanette Krambach* and *Agnes Kjøller* . You have always been eager to help and willing to share your knowledge and experience. *Karsten Agersted* and *Karsten Gynther*, I also owe you a thank you for the help in thermo-lab. Downstairs, in the chemistry lab and furnace room, *Ebtisam Abdellahi, Annelise Mikkelsen, John Johnson* and *June R. Flittner*, you have been very helpful so thank you for that. In the main electrochemistry lab, I was certainly exposed to something new.

I am happy that *Henrik Henriksen, Jens F. S. Borchsenius, Jens Østergaard, Bent F. Hansen* and *Martin Nielsen* were around and willing to help. Lastly, I would like to thank *Karl T. S. Thydé*n and *Janet J. Bentzen* for all your help and advice with the SEMs - that has been great.

Henrik L. Frandsen and *Peter S. Jørgensen*, you were very helpful with the modelling work. We got it started and going. Unfortunately, I had to let go of it to take care of other parts of the project. I would also like to thank *Marie L. Traulsen* and *Søren B. Simonsen* for helping out with the Raman spectroscopy and TEM imaging. *Connie M. Westergaard*, you have been very helpful when I got lost in DTUs administrative systems.

I have enjoyed the "low temperature" quarterly electrolysis meetings for Ph.D. students. Thank you for arranging them *Katrine Elsøe*, and thank you for participating *Mikkel R. Kraglund, Filippo Fenini* and *Florian Gellrich*.

In the end, I would like to thank my office mate *Søren P. V. Foghmoes*. We have enjoyed quite a few lunches together, I have had lots of general and project specific chemistry questions that you have been happy to discuss and you have also introduced me, properly, to whiskey and port wine. It has been a good time. Thank you.

Contents

List of Figures

List of Tables

Chapter 1

Introduction

1.1 Energy and the conversion of energy

We all use it every day and rely heavily upon it in our lives. We are talking about energy. Energy in itself is somehow abstract, a chameleon with a myriad of applications. Energy in various forms is what fuels the lives we live and yet it seems that it is only when it is absent we start to notice the importance it has in our lives.

There is plenty of energy available on earth so this is not the issue. Rather, the conversion of it to useful forms is where the main challenge lies. Fossil fuels are convenient because they can be used relatively easily in combustion processes with the release of energy to do useful work. The world has been on that path for several centuries and built an infrastructure around it. It has, however, also led to an unprecedented, for at least 800,000 years, rapid increase of greenhouse gasses in the atmosphere which is "extremely likely" to be correlated to global warming [1]. Global warming is impacting physical (e.g. glacial and droughts), biological (e.g. terrestrial and marine ecosystems) and human managed systems (e.g. food production). The scientific world, increasingly backed up by the public, has reached consensus that greenhouse gas emissions need to be drastically reduced in order to slow down their rising concentrations in the atmosphere which is the main driver behind global warming. Multiple pathways to mitigate the release of the most abundant greenhouse gas, CO_2, to the atmosphere can be envisioned. To limit the global warming to 2 ℃ relative to pre-industrial levels requires substantial emission reductions over the next decades and near zero emissions of CO_2 and other long-lived greenhouse gasses by the end of the century. This implies that fossil fuels to a large extent will have to be replaced, better sooner than later, by renewable sources.

A shift from a fossil based to a renewable based energy system is no easy shift. The figures are clear though: It is viable, the amount of renewable energy sources taken into account. The worlds consumption of primary energy was 18 TW in 2016 [2] and projected to grow $\approx 28\,\%$ by 2040 [3]. In comparison $\approx$ 90,000 TW of energy from the sun strikes the earths surface [4]. Most of this energy cannot be utilized but it should be clear that it is less than a per mille that is ultimately needed to power the planet [5]. In addition there are other renewable energy sources such as biomass, wind, wave and geothermal energy

and although they are available in much more limited quantity they are also potential sources that can be particularly attractive in certain geographical locations. When it comes to production, electricity based on renewable resources seems to have reached a breakthrough in terms of commercialising and implementing technologies such as wind turbines and photovoltaics, and a resulting shift towards electrification of the energy system is happening [6, 7].

Electricity is indeed a very useful type of energy as it can be transmitted over long distances with limited losses, it can be used to power all sorts of devices and to charge batteries which are used extensively in all sorts of portable devices. Renewable based electricity is, however, not suitable for all energy services; for instance long distance road transport, shipping, aviation, iron, steel & cement production and highly flexible electricity generation cannot easily be decarbonised [8, 9] but they account for approx. 27% of the global CO_2 emissions. Thus significant challenges still remain. It is evident that the transportation sector has begun to move towards battery powered cars and it works well for light transport and it is also being demonstrated for trucks, typically in combination with fuel cells though [10, 11]. It can, however, not be denied that the gravimetric and volumetric energy density of e.g. Li-ion batteries is inferior to liquid hydrocarbon fuels This is illustrated in figure 1.1. Seen in that light, it makes sense to continually pursue the production of liquid fuels such as ammonia, methanol or higher hydrocarbon. In fact liquid fuels with net zero emissions is possible if the CO_2 is captured directly from the atmosphere [12, 13]. Hydrogen is also a key player in this context as it is a necessary component for the production of all liquid fuels. Another large, difficult to eliminate, source of emissions are related to the highly flexible electricity production. Again H_2 or other hydrogen based products could be an important link as they can be used in e.g. gas turbines and be a part in a electricity-gas-electricity cycle where electricity is stored temporarily as H_2, thus enabling load balancing in an energy system with large fluctuations in electricity production [14]. Due to the relatively high energy losses in this electricity-to-electricity cycle, it would probably require favourable market conditions where electricity can be bought when there is an excess, at a low price, and sold at a significantly higher price again when there is a deficit in the system. Finally, H_2 as a fuel used in fuel cell based vehicles, possibly in combination with battery technology, is also likely to play some role in the transport sector. An infrastructure is being developed in places like Europe, California and Japan and several large vehicle manufacturers still believe fuel cell based vehicles have a future [15].

1.2 Hydrogen production technologies

Currently >95 % of all H_2 is produced from fossil fuels [17] using processes such as steam methane reforming, cracking of oil products in refineries and coal gasification. The remainder is produced by water electrolysis which, given the electricity mix is based on renewable sources, will be so as well, and hence close to a net zero source of CO_2 emission. Most of the H_2 produced by electrolysis is used in industry spanning from fertilizer production, over production of various chemicals, glass production and to the electronics

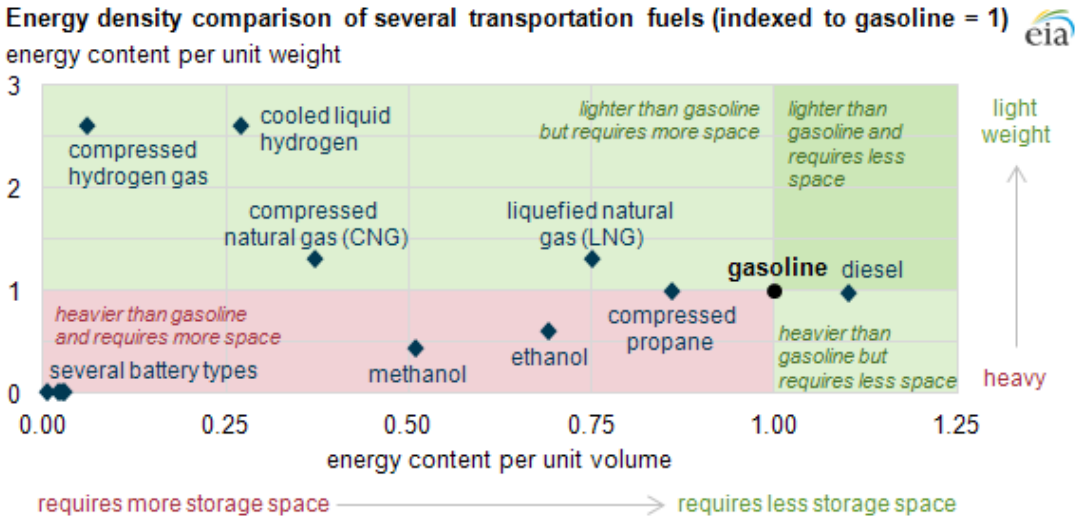

Figure 1.1: The energy content per unit weight vs the energy content per unit volume for fuels relevant in the transport sector. It is evident that it is hard to rival gasoline which is both ligher and requires less space than, e.g. batteries. Though hydrogen is lighter than gasoline it requires more space and pressurized containers. Methanol and methanol are evidently closer to gasoline. From [16]

industry [14]. The idea of water electrolysis seems very attractive: you take water and split it into its constituents to produce O_2 and H_2 using electricity as the driving force. The main barrier towards using the electrolysis of water to produce H_2 is the cost which is ≈ 4 times higher than the cost of producing H_2 from steam reforming [9]. This is a purely economic cost, however, not taking externalities into account; the economic cost excluding the social impacts, such as human health, a technology also is responsible for but not economically reliable upon [18]. This is of course another discussion but nonetheless an important point to make. The cost of electrolytic H_2 production is highly dependent on the electricity prices and for electricity prices around 5 US cents per kWh, the cost of electricity is more than half the total cost of the H_2 production [19]. Since commercial electrolysis plants only exhibit modest efficiencies there is a significant potential for driving down the costs by improving the electrolyzer efficiency. Increasing the production rate per cell area is another area which can drive down the H_2 production costs [20].

Electrolysis of water is a technology which has been known for around 200 years and in fact the technology has been employed for industrial purposes for more than 100 years. It has, however, not been able to compete with conventional steam reforming except in places where it has been combined with cheap hydroelectricity. Since the oil crisis in the 1970's new found interest has been paid to electrolysis, and in particular during the last couple of decades research has been intensified since the prospects of integrating renewable energy has termed it relevant again. Before describing the different electrolysis technologies it seems appropriate to define it first: electrolysis is the process whereby a non-spontaneous chemical reaction is forced by means of a direct current. To specify, it involves an electrochemical reaction where oxidation of one compound takes place at one electrode and reduction of another compound takes place at the other electrode, an

electrolyte is required as a medium for transmitting ions between the two electrodes and close the electrical circuit. Electrolysis has historically been used to separate elements, e.g. separate aluminium from alumina in the Hall–Héroult process. In the case of water electrolysis it is simply H_2 and O_2 which are separated from each other. The different water electrolysis cells differ, and are named, in terms of the electrolyte employed but the overall reaction is always the same:

$$H_2O \longrightarrow H_2 + \frac{1}{2}O_2 \tag{1.1}$$

Alkaline electrolysis cells

Alkaline electrolysis is the oldest electrolysis technology, employed on a commercial scale for more than a 100 years, and still the most widely used technology commercially [14]. It employs a concentrated KOH (or NaOH) electrolyte and hydroxide ions take the role as charge carriers in the electrolyte. A traditional cell setup is illustrated in figure 1.2The electrodes in alkaline electrolysis cells (AECs) are typically made of perforated steel, Ni or Ni-covered Fe sheets with a high surface area. Durability is sometimes enhanced by doping the metal sheets with e.g. Co or Mo or by applying a more corrosion resistant coating. The electrodes can also be additionally activated by increasing the surface area using micro-porous raney-Ni or a with oxide/sulfide electrocatalysts based on nickel, cobalt or noble metals [21]. A membrane, which is permeable to hydroxide ions but separate the H_2 and O_2 evolved at the two electrodes is necessary. In the old design there is few mm between the membrane and the electrodes which give rise to relatively large ohmic losses through the electrolyte. A newer design has therefore also been developed, called "zero-gap" because the electrodes are fixed directly to the membrane, thus eliminating the gap and improving performance but also requiring more accurate fabrication methods. The operating conditions employed are 50-80 ℃ at ambient pressure or pressurized up to 60 bar. The current density employed is typically 0.2-0.45 $\mathrm{A\,cm^{-2}}$ at a cell voltage of 1.8-2.4 V [20]. The lifetime is well proven and range from $55 - 120$kh [22]. The main AEC manufacturers constitute a group of around 20-25 companies that produce systems with a H_2 production capacity ranging from 0.4-1400 $\mathrm{Nm^3\,h^{-1}}$– [20, 22, 23] per stack which in terms of nominal power is a few kW - 6 MW. The H_2 purity is typically 99.8-99.9 %.

Proton exchange membrane electrolysis cells

Proton exchange membrane electrolysis cells (PEMECs) date back to the 1960's. The electrolyte is a solid membrane with a thickness of several hundred µm. It is a cross-linked, polymeric and gas tight structure containing sulfonic acid groups ($-SO_3H$) which give rise to the proton conductivity and its electrolytic properties when wetted with water. The electrocatalysts employed are noble metals such as platinum or iridium and in fact non-noble metals are generally not stable in the acidic environment. Catalysts are typically supported on carbon on the hydrogen side and titanium felt on the oxygen side. The cell concept is illustrated in figure 1.3a Compared to the AECs PEMECs employ a significantly higher and broader range of current density ranging from 0.5-2.50 $\mathrm{A\,cm^{-2}}$ [20].

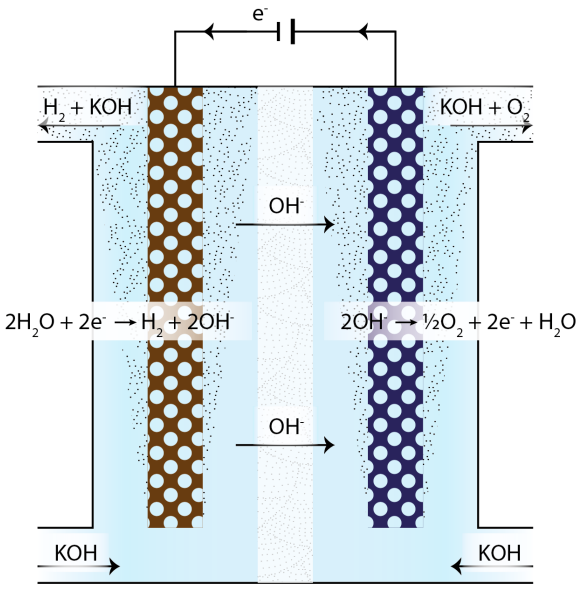

Figure 1.2: A traditional AEC with the electrodes immersed in the alkaline electrolyte. Water is reduced, H_2 evolved and OH^- generated at the hydrogen electrode . At the oxygen electrode OH^- ions are oxidized, O_2 evolved and regenerated. An external current is used to close the electrochemical circuit and drive the respecive electrode reactions. From [24]

The cell voltage is 1.7-2.1 V resulting in comparable efficiencies to the AECs. The operating temperature and pressure is typically 50-70 ℃ and 10-85 bar respectively. PEM electrolysis systems are suitable for more dynamic operation than alkaline electrolysis systems as they can be employed at lower partial loads and are faster to start up. They have reached also reached comparable life times ($60 - 100$kh). [22]. They are available commercially through several manufacturers and their H_2 production capacity per stack is 0.3-400 $Nm^3\,h^{-1}$– [20,22,23] which is a few kW-2 MW. The H_2 purity is typically 99.99 %.

Solid oxide electrolysis cells

Solid oxide electrolysis cells (SOECs) are operated at high temperatures (750-900 ℃)so water is supplied as steam. The electrolyte is a solid oxide material, typically 8 mol% yttria stabilized zirconia (YSZ) which becomes sufficiently oxygen ion conducting at the operating temperatures [25]. The oxygen ions are conducted through the crystal lattice so the electrolyte can and should be make as dense as possible. The oxygen electrode is composed of a ceramic oxide, which is either electronically conducting or mixed electronic and ionic conducting. Examples of the former and latter are the strontium doped perovskites lanthanum manganite (LSM) and lanthanum cobaltite (LSC) respectively. The hydrogen (fuel) electrode is typically a composite of Ni and 3 mol% YSZ. The cell concept is illustrated in figure 1.3b The cells are typically operated below 1 A cm^{-2} and 1.5 V to avoid too fast degradation, though operation up to several A cm^{-2} is possible. The electric efficiency is therefore also higher than in PEMECs and AECs. The main reason why electrolysis is attractive at these high temperatures is first of all that reaction kinet-

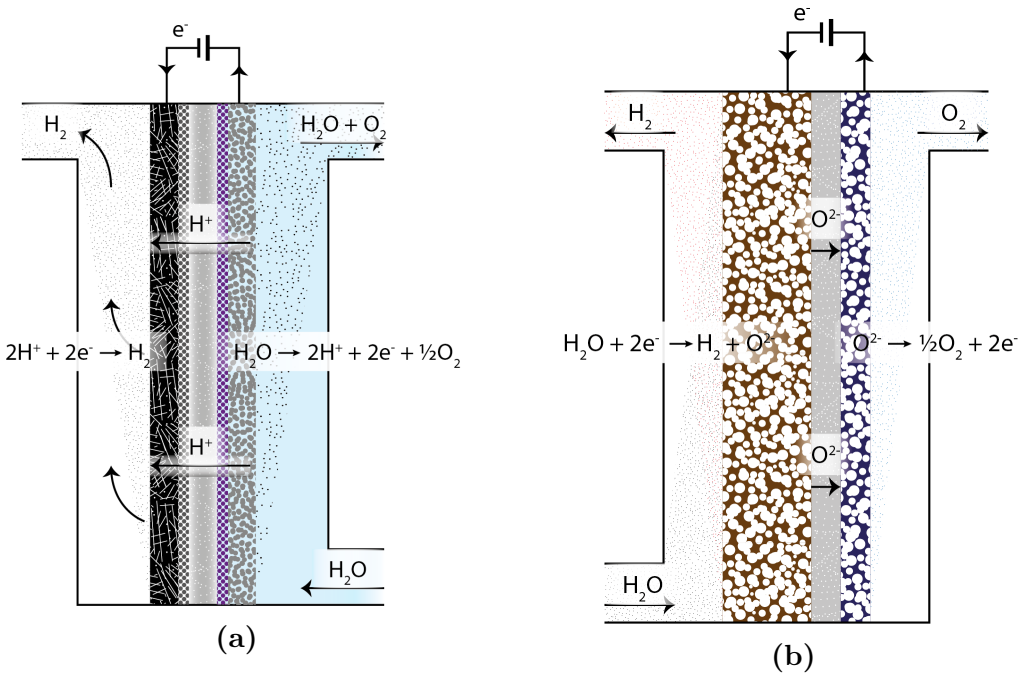

Figure 1.3: **(a)** A PEM electrolysis cell employing a proton conducting membrane. Water is fed from the side where it is reduced and O_2 evolved. The hydrogen side is left dry. **(b)** A SOEC employing a dense ceramic O_2^- conducting electrolyte and porous ceramic electrodes. Steam is fed on the hydrogen side and reduced to O_2^- while H_2 is evolved. On the oxygen side the O_2^- are oxidized to O_2. From [24].

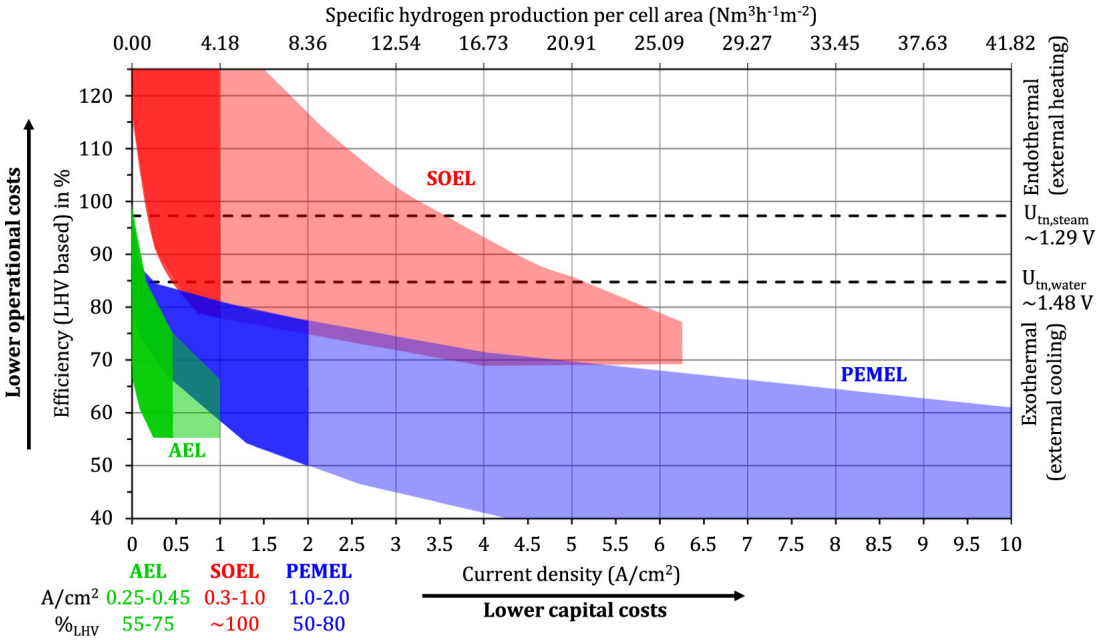

Figure 1.4: A comparisson of the alkaline, PEM and solid oxide electrolysis technologies in terms of current density, efficiency and H_2 production rate per cell area. From [22]

ics increase with temperature and the electric energy required to split water molecules is $\approx 20\,\%$ lower at 1000 ℃ compared to at 100 ℃. Moreover, co-electrolysis of water and CO_2 is also possible to produce synthesis gas - a mixture of H_2 and CO gas. The high temperatures posses a particular challenge when it comes to identifying suitable materials - not only for the cell components but for other stack components, such as sealings and interconnects, as well and this limits the life times compared to the other technologies. The SOECs are also less dynamic as they require longer start-up times than the alkaline and PEM electrolysis systems. A few commercial companies exist that produce SOECs systems [22]. A comparison of the current density, efficiency and specific H_2 production rate per cell area of various elctrolysis technologies is shown in figure 1.4.

Emerging H_2 production technologies

Other H_2 production technologies exist which rely on potentially renewable sources. These have been nicely summarized in ref. [26]. Biomass based technologies include gasification, dark fermentation, photo-fermentative processes, photolysis and microbial electrolysis. Biomass gasification is the partial oxidation of biomass into H_2, CH_4, CO, CO_2 and N_2. Dark fermentation uses anaerobic bacteria or algae to ferment biogradable biomass/biomass waste. Photo-fermentative processes uses light harvesting pigments to cellect solar energy and convert water into protons, electrons and O_2 in the membrane reaction sites of biomass. A nitrogenese catalyst is used to react the protons and electrons with nitrogen and (adenosine triphosphate) ATP to make ammonia, H_2 and adenosine diphosphate (ADP). Photolysis is combining the photosynthesis process with algae and bacteria that can use the excess solar energy to produce H_2 while a minimum of energy is used to produce carbohydrates and maintain life. Microbial electrolysis is a

bio-electrochemical cell which is aided by microbes in conversion of biogradable material into H_2 under anaerobic conditions.

Other methods for splitting water also exist that utilize other energy sources than electricity to drive the water splitting reaction. These are thermochemical water splitting- and photoelectrolysis devices. The former is based on the thermal decomposition of water at approx. 2500 ℃ and hence requires a heat source and materials that are stable at these temperatures; various chemical reagents have shown though to be able to lower the temperature significantly. Photoelectrolysis utilizes the sun's energy directly to split water. These are semiconducting devices where the electrons/holes generated are used to directly split the water molecules. These alternative H_2 production technologies posses various strengths and weaknesses. The common denominator for them all is that their maturity is lower than most water electrolysis systems and hence not competitive.

1.3 Project objectives

The project's scope has been to develop the high temperature (150-250 ℃) and pressure (20-40 bar) alkaline electrolysis cell (HTP-AEC) technology. Raising the operating temperature and pressure has several advantages including an approx. 10-fold increase in the power density, which results in a reduced stack volume and consequently cell materials volume. Moreover, the HTP-AEC can operate at thermo-neutral voltage with 100 % electrical efficiency whereas conventional AECs operate at an electrical efficiency below 85 % at about half the H_2 production rate. The power density and efficiency are important parameters when it comes to the prospects of making commercially attractive electrolysis systems. The focus of the project has been to identify and develop oxygen electrode materials. The use of cheap raw materials for the various cell components and the absence of expensive catalysts has formed part of the material selection criteria together with a focus on scalable low cost manufacturing methods. This to render the developed HTP-AECs economically feasible for large scale production. The project objective can be split into three parts:

Part 1: *Identification of oxygen electrode/electrocatalyst materials and determination of selected materials' oxygen evolution reaction (OER) activity.* Limited literature is available on the performance and stability of relevant oxygen electrode materials at high temperature and pressure HTP conditions. The determination of the intrinsic electrochemical activity of different promising electrode materials at standard conditions is therefore an important starting point. Recent literature had revealed that mixed metal (oxy)hydroxides, perovskites, and layered oxides are promising candidates for the OER in conventional AECs. Here focus will be placed on determining the stability at high temperature conditions and the intrinsic OER activity of selected candidates, primarily from the perovskite family.

Part 2: *Processing of oxygen electrodes with varying microstructures.* A key aspect for the development of high performance electrodes relies on understanding the relationship between the microstructure and the performance. Processing of the identified electrode

material(s), using standard methods such as tape casting, screen printing, etc., while controlling the resultant microstructure is another task. Various material and processing parameters such as particle size, rheology and additives will be explored in order to vary the microstructures in a controlled manner. The resultant porous electrode structures will be characterized for various microstructural characteristics and correlated with the electrochemical performance if possible. Identifying possible relations between processing parameters, microstructure and electrochemical performance of the resulting structures will be a priority as it will play a critical role in the rational design of optimized electrodes. Simple modelling of the microstructure-performance relationship will possibly be carried out on the basis of the porous electrode theory as a means of guiding the processing efforts and in order to facilitate the interpretation of electrode performance data.

Part 3 *Testing oxygen electrodes at operating conditions.* In addition to elucidating the processing-microstructure-property correlations, processing parameters will be optimized for up-scaling the fabrication of optimized HTP-AEC electrodes and cells. The demonstration of the integration of optimized oxygen electrodes at a cell area of $3\,cm^2$ in a test setup that allow measurements in the range 60-80°C is the last task.

1.3.1 Outline of the thesis

The thesis covers most of the work carried out during the last approx. 3 years of PhD work. It is divided into the following chapters.

Chapter 1 - Introduction

The introduction sets the context for the experimental work carried out for the thesis. It also introduces H_2 as an energy carrier and outlines how H_2 is produced today and what non-fossil based alternative technologies that exist.

Chapter 2 - Background

In the background the thermodynamics of electrochemical water splitting is outlined together with the more practical aspects of the electrochemistry required. A review of tested ceramic oxide materials for the oxygen electrode is also included. Lastly some general theory of ceramic processing and sintering is introduced.

Chapter 3 - Experimental methods

The main experimental methods used are introduced in this chapter. Moreover, the experimental details are described.

Chapter 4 - Results and Discussion

Results from the work carried out is presented. The results are included in article form. Three articles have been prepared, one has been published and the one is submitted for peer review and one will be submitted after this thesis is handed in. The outline of each is given below. In addition to the articles, some additional discussion sections have been included as additional subsections after the article manuscripts. Modelling work of the oxygen evolution reaction was initiated in COMSOLMultiphysics on porous three dimensional electrode structures that have similar microstructures as the tested electrodes. The model was successfully implemented on smaller structures, representing cubes of approx. $0.35\,\mu m \times 0.35\,\mu m$. On larger and more realistic microstructures issues with the COMSOLsolvers were encountered and not solved.

1. Articles published/submitted for publication
   (a) The first publication deals with the electrochemical activity of various La, Ni and Fe based perovskites towards the oxygen evolution reaction and their stability under HTP conditions in centrated alkaline media.
   (b) This second article's focus, is the characterization of aqueous $LaNi_{0.6}Fe_{0.4}O_3$ suspensions and examines the possibility of processing porous electrodes with rice starch as pore former. It has been submitted to the Journal of the European Ceramic Society. An additional subsection, which contains some additional discussion points, has been included after the article.
   (c) The third article is concerned with the processing and testing of porous $LaNi_{0.6}Fe_{0.4}O_3$ oxygen electrodes. A quantitative microstructural characterization of the electrodes has been performed and a qualitative assessment of the pre- and post-tested electrodes together with quantification of the electrodes performances' under various conditions. It will be submitted to the International Journal of Hydrogen. Two additional subsections with discussion, have been included after the article.

2. An overall discussion of the work carried out during the PhD is included, focusing on the overall aim of the project and the challenges encountered along the way.

Chapter 5 - Conclusion and Outlook

The overall lines are drawn up and the main findings are summarized. Finally an outlook, proposing the next steps, is presented.

Chapter 2

Background

In this chapter the most important background information is presented which has been adapted to the scope and content of the work presented in this thesis. We will start out treating some of the basic thermodynamics behind water splitting and follow it up by some of the electrochemical aspects of electrolysis. Next, we will treat the alkaline electrolysis technology and emphasize the HTP-AEC technology. After this follows some background information on the OER and some general aspects of the literature available in this area. Following this a literature study of ceramic oxide OER candidate materials is be presented. To conclude the chapter, aspects of the ceramic processing methods involved in the processing of ceramic suspension is presented.

2.1 Thermodynamics of water splitting

The decomposition of water into hydrogen and oxygen is an endothermic process[1]. A driving force, such as heat or electricity, is required to do the work of splitting the water molecules. In the electrolysis of water this driving force is electricity. The thermodynamic basis for the energy required to split water is the change in enthalpy of the reaction products minus the reactants:

$$\Delta H_r = H_{f,H_2} + \frac{1}{2} H_{f,O_2} - H_{f,H_2O} \tag{2.1}$$

where the $H_{f,x}$ denote enthalpy of formation of H_2, O_2 and H_2O respectively. The enthalpies of formation are pressure and temperature dependent implying the enthalpy of reaction also must be so. For isothermal or isobaric processes the Gibbs free energy states the amount of reversible work that can be extracted from a thermodynamic process. In this context, this is the minimum work which has to be put into driving the reaction. The remaining energy is thermal energy supplied as heat. The Gibbs free energy for the reaction (ΔG_r) can now be related to the enthalpy of reaction through the following relation:

$$\Delta G_r = \Delta H_r - T\Delta S_r = \Delta H_r - \Delta Q_r \tag{2.2}$$

[1]No references are provided in this section as it is considered very general. Suggested references are [20, 23]

where T is the absolute temperate, ΔS_r is the change of entropy for the reaction and Q_r is the thermal energy. The relation between enthalpy of the reaction and Gibbs free energy of the reaction is hence important because it tells us how much energy has to be supplied as work and heat respectively, at a given temperature and pressure, in order to drive the water splitting reaction. In particular the temperature dependence is important from the thermodynamic point of view. The enthalpy of reaction increases only slightly with temperature whereas the Gibbs free energy of reaction decreases significantly, implying the heat required increases as well. This is illustrated in Figure 2.1 In short work can be substituted for heat when increasing the temperature of the electrolysis process. As already pointed out the process of splitting water is not a spontaneous process; we need to apply work so $\Delta G_r > 0$. In addition it is an endothermic reaction so $\Delta H_r > 0$. If we now assume that we can run the electrolysis reaction without any energy losses we are running the cell at the reversible cell voltage V_{rev}, which is related to ΔG_r:

$$V_{rev} = \frac{\Delta G_r}{zF} \tag{2.3}$$

where z is the number of electrons transferred per molecule of produced hydrogen and F is Faraday's constant ($96485\,\mathrm{C\,mol^{-1}}$), representing the charge of one mole of electrons. The dependence of the reversible cell voltage on the temperature of the reaction and the activity of the reactants and products is:

$$V_{rev} = V^0_{rev} - \frac{RT}{zF}\ln Q_r = V^0_{rev} - \frac{RT}{zF}\ln\frac{[H_2O]}{[H_2][O_2]^{1/2}} \tag{2.4}$$

where V^0_{rev} is the reversible cell voltage at standard state ($298.15\,\mathrm{K} = 25\,^\circ\mathrm{C}$ and 101,325 Pa $= 1\,\mathrm{atm}$,) and the second term is the factor correcting for deviations from standard conditions. Here R is the gas constant ($8.314\,\mathrm{J\,K^{-1}\,mol^{-1}}$), which represent the average energy of the particles in a mol of gas per temperature increment, Q_r is the reaction quotient relating the activity of the reactants and products which is approximated to one in dilute electrolytes and the partial pressures of gasses. In concentrated electrolytes (e.g. 35 wt% KOH) used for industrial electrolyzers the activity of water cannot simply be assumed equal to one and empirical or calculated values have to be used for more accurate results.

The thernoneutral voltage, V_{tn}, is the voltage at which no heat has to be added and no heat is supplied from the surroundings hence isothermal operation. Above this voltage the process becomes exothermic while it is endothermic below this temperature. This means it is defined from the enthalpy of the reaction:

$$V_{tn} = \frac{\Delta H_r}{nF} \tag{2.5}$$

The thermoneutral voltage is 1.481 V at 25 °C. Under non-ideal conditions heat tend to be dissipated from the system which increases the voltage where no heat has to be supplied to the system. From an industrial point of view the voltage where no heat has to be supplied to the system is an important parameter.

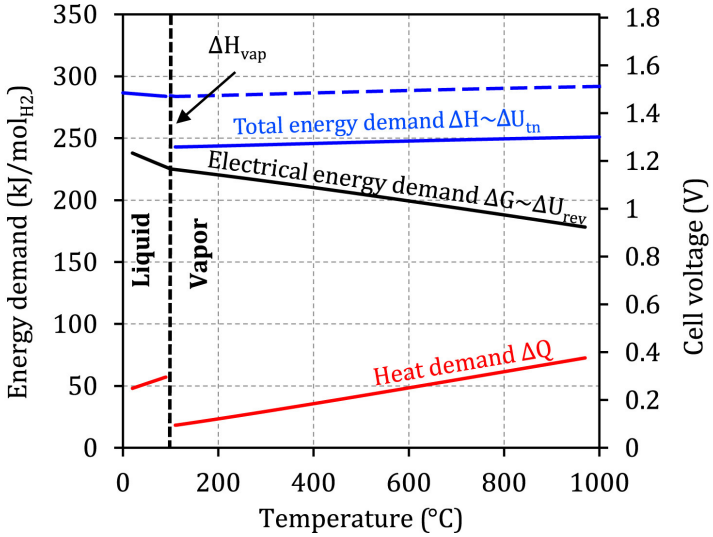

Figure 2.1: A schematic of the thermodynamic properties, enthalpy of reaction (ΔH_r), Gibbs free energy of the reaction (ΔG_r) and entropy change of the reaction associated with a heat demand (ΔQ_r), governing the water splitting reaction. The blue line represents water's enthalphy of formation and dashed blue line represent water's enthalphy of formation including the latent heat of vaporization associated with the phase change from liquid water to steam. From [22]

2.2 Electrochemistry of water electrolysis

The general thermodynamics provide a theoretical framework for water electrolysis under ideal and equilibrium conditions[2]. In any real operation of an electrolysis cell an overvoltage (η) has to be applied to drive the electrolysis reaction. The overvoltage is simply defined as the voltage difference between the applied voltage and the reversible cell voltage:

$$\eta = V_{cell} - V_{rev} \tag{2.6}$$

The overvoltage is hence excess work put in to drive the reaction, which eventually is dissipated as heat and hence representative of all irreversible reactions occurring in the cell. It increases with increasing current density and is commonly divided into different categories.

The two most general types of losses are electrokinetic losses at the electrodes and ohmic losses. The electrokinetic losses are mainly concerned with the activation of the oxygen- and hydrogen evolution reactions (OER and HER) occurring at the two electrodes. A way of explaining this is that each electrode reaction require a number of steps for charge transfer to take place between the electrolyte species and the electrode. An energy barrier has to be overcome for each step for the charge transfer reactions to take place. The resulting energy barrier is therefore highly dependent on the materials used at the two electrodes as they help to catalyse the reactions. In addition the charge transfer reaction is generally larger in the OER compared to the HER, because it requires a transfer of

[2]No references are provided in this section as it is considered very general. Suggested references are [20–23]

four electrons compared to just two electrons in the HER. Kinetic losses can also show up at high current densities if the kinetics at one electrode become the limiting factor in the overall electrolysis reaction. The ohmic losses are called so because they obey Ohm's law and scale linearly with the current density. They are related to charge transport in the electrolyte phase and in the solid phases and interfaces including electrodes current collectors and interconnects. The ohmic losses increases with temperature and if the charge transport pathway is increased.

Gas bubble formation on the electrode surface is also common source of losses. They decrease the interfacial area between the electrode and electrolyte leading to an increase in the effective current density. Moreover, bubbles stuck in a porous electrode can hinder efficient transport of electrolyte species. Lastly, mass transfer is a last source of losses, which show up if charge carriers are depleted at the electrode surfaces due to diffusion limitations of reaction species.

The Butler-Volmer equation is commonly used to describe the relation between the current density and overvoltage in an electrochemical cell. In particular it describes how the current density responds exponentially when the cell is forced, by means of an overvoltage, away from the equilibruim situation where no net current is running in the cell. This is in other words related to the kinetics of activating an electrode reaction and assuming no other limitations to be present. The equation states:

$$i = i_0\big(\exp\frac{\alpha_a z F}{RT}\eta - \exp\frac{-\alpha_c z F}{RT}\eta\big) \tag{2.7}$$

where i is the current density, i_0 is the exchange current density that describes the current density of the forward anodic and cathodic reaction with no overpotential applied, α_a is the anodic charge transfer coefficient and α_c is the cathodic charge transfer coefficient. The charge transfer coefficients are dimensionless symmetry factors which sum is equal to unity. When the reaction is driven in the positive direction, far enough away from equilibrium, the anodic reaction begins to dominate, which allows for the simplified tafel equation to describe the behaviour of the electrochemical cell:

$$i = i_0 \exp\frac{\alpha_a z F}{RT}\eta \Leftrightarrow \ln\frac{i}{i_0} = \frac{\alpha_a z F}{RT}\eta \Leftrightarrow \tag{2.8}$$

$$\eta = \frac{RT}{\alpha_a z F}\ln\frac{i}{i_0} = \frac{2.3RT}{\alpha_a z F}(\log i - \log i_0) = b\log i - a \tag{2.9}$$

$$\tag{2.10}$$

$$b = \frac{2.3RT}{\alpha_a z F}, \qquad a = -\frac{2.3RT}{\alpha_a z F}\log i_0 \tag{2.11}$$

where b is denoted the tafel slope which represents the increase in overpotential per decade of current density, typically in $\mathrm{mV\,dec^{-1}}$and a is a constant used to determine the exchange current density. The tafel slope is a frequently used figure of merit to determine intrinsic electrocatalytic activity of electrocatalyst. Like all models, the tafel equation should be used thoughtfully. In particular for complex electrochemical reactions, such as the OER which involves the transfer of 4 electrons per molecule of oxygen the tafel equation is not

per se valid. An implicit assumption is that there is one rate limiting step in the reaction. The rate limiting step can, however, change with current density which changes the tafel slope or other non-intrinsic factors.

2.3 Alkaline Electrolysis

An alkaline electrolysis cell (AEC) for water splitting is an electrochemical device consisting of three main components: an anode (referred to from now as oxygen electrode), a cathode (referred to from now as fuel electrode) and an alkaline electrolyte. When an overpotential is applied to the cell the OER takes place at the oxygen electrode and simultaneously the hydrogen evolution reaction HER takes place at the fuel electrode. These are electrochemical reactions which are sustained as long as a current is supplied from an external power supply and water is available. The OER and HER constitute a set of reduction-oxidation (redox) reactions which together gives the water splitting reaction:

$$\text{OER}: \qquad 2\,OH^- \longrightarrow H_2O + \frac{1}{2}\,O_2 + 2\,e^- \tag{2.12}$$

$$\text{HER}: \qquad 2\,H_2O + 2\,e^- \longrightarrow 2\,OH^- + H_2 \tag{2.13}$$

$$\text{Total}: \qquad H_2O \longrightarrow H_2 + \frac{1}{2}\,O_2 \tag{2.14}$$

It is seen from eq. 2.12 and 2.13 that the OH^--ions consumed at the OER are produced at the HER in the same quantity and vice versa for the electrons so these constitute the charge carries in the electrolyte and electrode respectively. It was already stated that the reversible voltage required to split water at RT is 1.23 V and this implies that the potential difference between the initiation of OER and HER must be equal to 1.23 V as well. The potential of the OER and HER with respect to the standard hydrogen electrode is $E^o_{OER} = 0.401\,\text{V}$ and $E^o_{HER} = -0.8277\,\text{V}$ respectively.

The main components of an AEC are besides the two electrodes and an electrolyte, a gas tight but ion-permeable diaphragm to separate produced gasses and a direct current (DC) power supply. This is schematically shown in 1.2. One cell is not enough so several cells are connected, which can be done in a uni- or bi-polar (parallel or serial) configuration. The former is constituted of individual modules so it is a more simple and robust system but also requires more space. The unipolar configuration is essentially a stack of cells and also known as the "zero-gap" design where the gap between the electrode and the diaphragm is eliminated. The current through each cell is the same as the total current in the system which reduces ohmic losses, the system requires a higher precision in design and manufacturing to avoid electrolyte and gas leakage. Several additional components are needed for industrial operation of AECs and often include a gas handling system to remove water vapour and other impurities, a feed-water conditioning system, a cooling water system, a nitrogen purge system for use during start-up and shot-down, a monitor and control system and power electronics systems [27]. As stated in section 1.2 industrial operation is commonly carried out at 50-80 ℃ under atmospheric pressure or in pressurized operation up to 15 bar. The current density employed is typically 0.2-0.45 A cm^{-2}

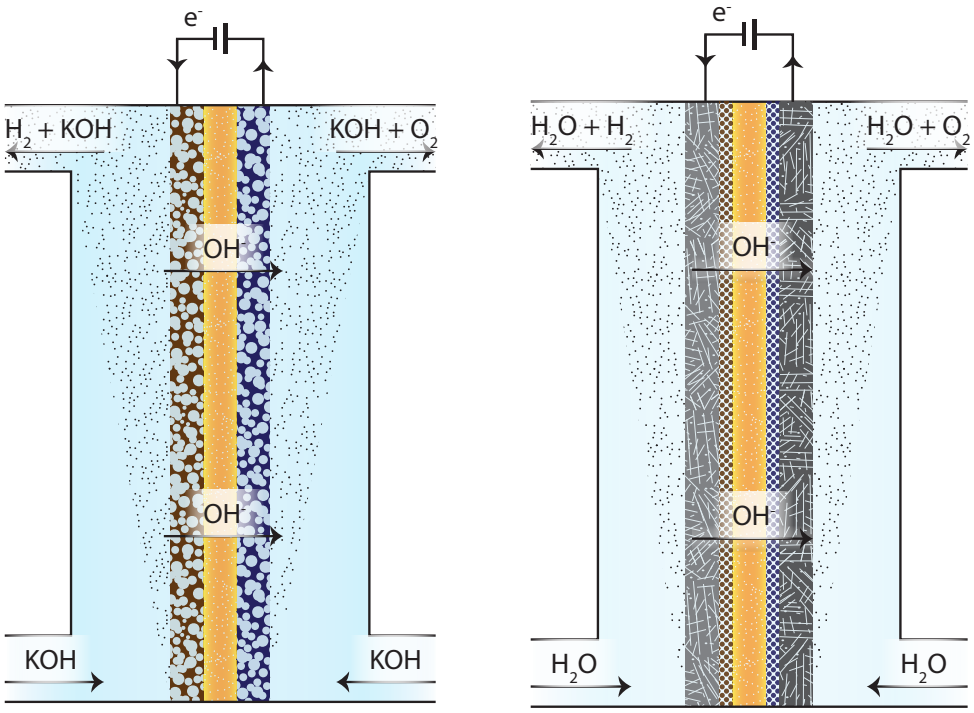

(a) **(b)**

Figure 2.2: a)The zero-gap type alkaline electrolysis cell concept where porous electrodes are attached directly to the OH^- conducting polymeric membrane b) A schematic of an anion exchange alkaline electrolysis cell only fed with water. A ionic pathway from the membrane to the electrodes is required, so the electrodes consist of mixed ionomer and catalyst layer with an integrated porous transport layer. From [24]

and the cell voltage 1.8-2.4 V. Improvements to the conventional AECs are necessary to decrease hydrogen production costs. A zero-gap configuration where the electrodes are attached directly to a polymeric membrane, which is OH^- conducting, is one of the areas that can improve performance of the cells by e.g. decreasing ohmic losses. Polymeric anion exchange membrane cells are the newest low temperature alkaline electrolysis concept, similar to the concept of the PEM electrolysis cells, but the membrane is alkaline and conducts hydroxide ions instead of protons, using only water as the feed. These two concepts provide a way forward that can bring the performance of alkaline electrolysis cells closer to the PEM electrolysis cells [28, 29]. The zero-gap type cells and anion exchange membrane cells are illustrated in figure 2.2a and 2.2b. Another option is to double or triple the operating temperature, use a porous ceramic membrane as separator and a zero-gap configuration to improve performance.

2.3.1 High Temperature and Pressure Alkaline Electrolysis Cells

High temperature and pressure alkaline electrolysis cells, operating above 150 ℃ have been investigated in several research projects during the last 50 years or so [30–34]. The basic idea is that an increase in temperature will allow for improved performance of the cells. An adequate pressure has to be applied though to avoid too fast evaporation of water from the electrolyte. The research has shown substantial improvements in terms of electrode kinetics and thereby cell performance compared to conventional AEC. Challenges have also been encoutered and is mainly related to the stability of the electrode materials and the diaphragm at the elevated temperatures. Ceramic oxide electrode materials have been proposed as both active and stable electrode and diaphragm materials. For the diaphragm fluorinated diaphragms, such as perfluoroalkoxy alkanes (PFA), polytetrafluoroethylene (PTFE) or polyphenylene sulfide (PPS) are stable up to at least 200 ℃ in concentrated KOH [35] but they are hydrophobic and easily become clogged with gas bubbles. In contrast inorganic ceramic type materials are generally hydrophilic. The ceramic type materials that can withstand the corrosive environment, in a concentrated KOH solution, and hence identified as the best candidates are nickel-, zirconium- and titanium based oxides. [35, 36].

A high temperature and pressure alkaline electrolysis cell (HTP-AEC) has been developed at DTU Enegy [37]. The cell design is inspired by some of the previous work mentioned above and carry the prospects of dramatically improving several of the drawbacks associated with conventional alkaline electrolysis cells [38–42]. HTP-AECs are operated at 150-250 ℃ and 20-40 bars. The high temperature has a highly activating effect on the electrokinetics of the electode reactions hence allowing for approx. 10-fold improvements in terms of current density. The electrical efficiency, based on higher heating value (HHV), is likewise significantly improved. The pressurized operation is necessary to avoid too fast evaporation of water from the electrolyte but it also implies that the hydrogen and oxygen gas is produced under pressure which saves approx. 5 % of the energy demand for subsequent pressurization of the gas to several hundred bars. HTP-AECs are thought out from the cell concept of solid oxide cells. The electrolyte is in the liquid from but it is immobilized in a ceramic membrane. The 3YSZ membrane is sandwiched in between the two electrodes which are deposited on either site of the membrane; the cell concept is schematically shown in Figure 2.3. The cell is sintered with each electrode to finalize the electrode microstructure and create strong interfaces. Since all three layers are porous the electrolyte can be infiltrated into the electrode layers and make most of the electrode surface area utilizable for the electrode reactions. The membrane has to be porous and penetrable to contain the electrolyte and allow ionic transport between the electrodes, it has to be mechanically strong as it also serves as a support for the entire cell, it has to be electronically insulating and it has to be corrosion resistant. A material that lives up to these criteria is 3 mol% yttria stabilized zirconia (3YSZ).

The performance status of the HTP-AECs concept is uplifting. Using 1 cm^2 cells, consisting of a tape casted 3YSZ membranes sandwiched between Ni foams which was impregnated with polytetrafluoroethylene (PTFE) and Ag wires at the oxygen electrode and coated with Inconcel 625 at the hydrogen electrode, a record current density of 3.75 Acm^{-2}

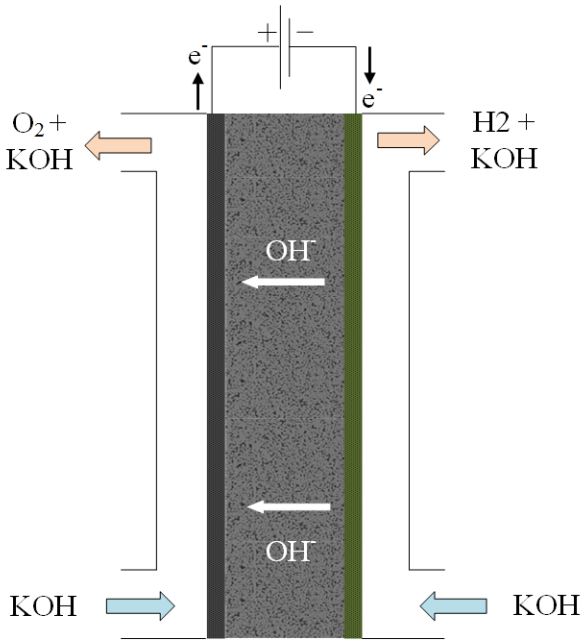

Figure 2.3: A schematic of the HTP-AEC concept. The electrodes are porous and could be ceramic or metal foams. The electrodes are not necessarily thinner than the porous membrane. The membrane is the support so it is typically around 200-300 µm. It also has to be porous to allow transport of electrolyte species through it. Pore sizes are less than 100 nm.

has been achieved at 1.75 V under 200 ℃ and 20 bar pressure. This means the electrical efficiency based on the HHV is 85 %. In comparisson conventional AECs are operated at much lower current densities (0.2-0.45 A cm^{-2}) at efficiencies in the range 50-80 % [20]. These measurements were obtained using cyclic voltammetry (CV) scans and subsequent steady state chronopotentiometry measurements confirmed the performance, of the CVs, up to 1.0 A cm^{-2}. A similar cell with the exception that the Ni foam was replaced with a NiFeCrAl alloy foam at the oxygen electrode (still impregnated with PTFE and Ag wires) was tested for 400 h at 200 ℃ and 20 bar and exhibited a constant performance of 1.5 ±0.1 V at 0.5 A cm^{-2}. The serial resistance, R_s, of this cell is 3-4 larger than the previous cell the and polarization resistance, R_p, approx. 3 times larger which gives an approx. 0.2 V higher cell voltage than the previously described cell. A likely explanation for this large deviation is a larger contacting resistance. and hence not directly related to the electrolysis cell.

There are, of course, also challenges associated with the HTP-AEC concept. The main challenge is identifying corrosion resistant materials that can withstand the harsh operating environment. It has been established that conventional metals such as Ni or stainless steel are not able to withstand the conditions but corrode away whereas Inconel 625 and the NiFeCrAl alloy has improved matters substantially. There is not much literature on the stability of materials during HTP conditions in a strongly alkaline environment so explorative investigation is required to investigate possible electrode materials. In fact it is not enough that they are sufficiently chemically stable, they also need to be electrochem-

ically stable for around 5 years lifetime and thereby maintain adequate electrocatalytic activity. Safety is also a factor to consider. A HTP-AEC is a potent combination of high temperature and pressure with the presence of both hydrogen and oxygen in a highly corrosive environment. This is, however, an engineering challenge just like the development of stable materials for the electrodes.

Overall it is clear that HTP-AECs possess some clear advantages if they can be developed to a more mature state with larger cell sizes that exhibit long term stability. In particular the power density can be dramatically improved. A previous study calculated the power density of a mature HTP-AEC stack, based on the performance obtained so far, to be $2.28\,\mathrm{W\,cm^{-2}}$ at $4.2\,\mathrm{kWh\,Nm^{-3}}$ H_2 and compared this to a commercial stack compromising 150 NEL A 485 elctrolysers which posses a power density of $0.13\,\mathrm{W\,cm^{-2}}$ [42]. This demonstrates the prospects for decreased investment costs while also decreasing the hydrogen production costs due to the ability to run the system at a higher efficiency.

2.3.2 The Oxygen Evolution Reaction

The OER is the more troublesome of the two electrode reactions. It posses the larger potential for improvement, both in terms of the overpotential it invokes on the cell performance and electrochemical stability, compared to the HER. It is therefore this reaction we will be concerned with in the following. The OER is more complicated than the HER because it involves the transfer of 4 electrons per oxygen molecule compared to only to electrons per hydrogen molecule. This implies that there are several possible reaction pathways with various intermediate steps where a rate determining step can be assigned to each reaction. The main reaction pathways proposed are summarized in [43, 44]. The overall reaction rate is constrained by the reaction step with the highest kinetic barrier. Several kinetic descriptors have been proposed in this context, generally for a specific class of materials, that correlate a microscopic parameter with the intrinsic electrocatalytic activity and will allow for direct comparisson of different materials. Examples are found in [45–47] and good review is found in [48]. An alternative scheme to the rate determining step approach is a potential determining step approach which looks at the reaction from a thermochemical point of view and bases its arguments on density functional theory (DFT) calculations [49], [50]. This potential determining step in a reaction pathway (differs from the ones described in [43]), is the maximum difference in the Gibbs free adsorption (chemisorption) energy of two subsequently adsorbed species and is a function of applied potential. In addition to looking at the potential determining step, the importance of scaling relations between the adsorption potentials of the different reaction steps are also stressed which implies that they are interdependent. This can be visualized in a volcano plot, see figure (Volcano Plot) with bonding strength (energy of adsorption) of one of the adsorped species on the first axes and overpotential on the second axes. The optimum electrocatalyst hence follows the Sabatier principle [51]: the bonding strength of the surface should be neither too strong nor too weak to allow for reaction of intermediate reactants while also allowing for desorption of the intermediate products. The potential determining step approach does not take kinetics into account but it is stressed that this approach should precede considerations regarding kinetics as it is more fundamental.

The electrocatalytic avtivity of OER electrocatalytsts is, however, only one side of the medal as any real world application also requires the electrotrocatalysts to be stable for years under realistic operating conditions. This is an area that has been neglected compared to discovering or developing the most active electrocatalysts under standard temperature and pressure conditions in dillute KOH (0.1 or 1.0 M KOH) [44]. The main reason for the limited litterature on electrocatalyst stability is related to the fact that long-term stability assesments, intuititvely require long term testing. The challenge therefore seems to develop methods that allow for short term testing of long term stability. This can either be accelerated testing protocols or methods that are sufficiently sensitive, e.g. various spectroscopy methods or highly sensitive methods to determine mass changes, to make early predictions about the stability of the materials. Recently, some interesting experimental protocols and methods have been proposed [52,53]. As the understanding of the degradation mechanisms evolve computational methods are certainly also becoming more important. Further, it is experimentally more complicated to test materials at realistic operating conditions because other, non-intrinsic factors become harder to suppress. It is important to stress though that the electrocatalytic activity usually not simply can be extrapolated to higher current densities [54]. Despite the previous statements it makes a lot of sense to make initial screenings under RT as this can filter the materials away that are definitely not stable and not electrocatalytically active.

2.4 Electrocatalysts for the oxygen evolution reaction

2.4.1 Electrocatalyst materials for the OER in alkaline media

The requirement of any material to be used as electrocatalyst is the ability to catalyse the reaction, thereby minimizing the overvoltage produced at the electrode, while being sufficiently stable in the environment of operation for the desired life time of the system. By sufficiently stable is meant that the electrocatalyst can undergo some structural and chemical changes at the surface as long as it does not compromise performance or lifetime of the cell. In fact, it has been pointed out, based on thermodynamic considerations, that all oxides exposed to OER conditions eventually will become unstable leading to structural changes or dissolution from the surface [55]. The lattice oxygen evolution reaction (LOER) which generally take place simultaneously with the OER is the reason for this instability. If the reaction kinetics of the OER and LOER are sufficiently decoupled the ceramic oxide will appear stable. The electrocatalyst, typically referred to as state-of-the-art at standard temperature and pressure are noble metal oxide catalysts RuO_2 and IrO_2 [56,57]. The main problems with IrO_2 and RuO_2 is that Ir and Ru are noble metals, which are scarce and expensive [58] and they do not provide substantial improvements compared to conventional oxygen electrodes. It has also been reported that they are not sufficiently stable [59,60]. The benchmark of oxygen electrode materials for AECs is Ni based electrodes, possibly with the addition of some electrocatalyst [20,27]. It posses a good stability under typical AEC conditions, it is abundant and inexpensive.

Even though Ni based electrodes have proven their worth as electrode/electrocatalyst

for OER in conventional alkaline electrolysers, the overvoltage at the oxygen electrode needs to be decreased further to make the technology more viable. Therefore research has continued in this area. Density functional theory calculations on Pt(111) and Au(111) surfaces have shown that metals have to be oxidized for the OER to proceed at the relatively low overpotentials observed experimentally. The trend in OER activity has been investigated experimentally on metal oxides surfaces and found the following activity trend Ru > Ir ≈ Pt ≈ Rh ≈ Pd ≈ Ni ≈ Os ≫ Co ≫ Fe > Mn [61] which agrees with later computational activity trends: Ni > Co > Fe > Mn [61,62]. Research has identified various ceramic oxides crystal structures. Most of the early work has investigated various spinels and perovskites materials as possible candidates for the OER. In these studies the electrocatalytic activity has generally not been well separated from other electrode properties such as electrical resistivity and active electrode surface area. It is thus mainly the performance of electrode materials that have been investigated and not solely the electrocatalytic activity. The test conditions have usually also been close to the operating conditions in the range 70-110 ℃ and the electrolyte concentration is in the range of 5-10 M. In particular during the last two decades the focus has been on determining the intrinsic electrocatalytic activity of various materials at standardized conditions. This has the advantage of making a comparison easier, it is also problematic, as pointed out in section 2.3.2, since the stability of the electrocatalyst is typically not well investigated.

The literature study has made it clear that determining intrinsic electrocatalytic activity for a given material is not feasible. The intrinsic electrocatalytic activity varies with synthesis conditions, probably due to differences in morphology, surface area and presence, or formation during operation, of secondary phases, which are difficult to detect with conventional experimental methods. The presence of impurities can also influence the electrocatalytic behaviour substantially. More advanced spectroscopy methods are, however, becoming more frequently implemented which is helping elucidate the influence of some of the above mentioned factors.

It is generally found that Ni and Co based materials, possibly in combination with Fe have shown to be the most active electrocatalysts. In table 2.1 the (intrinsic) catalytic activity of some of the most promising and tested materials to date are compared. To make the comparison as valid as possible only results obtained under similar conditions have been compared. The figures of merit are the current density produced at a constant overvoltage of 300 mV and the overvoltage resulting from a current density 10 mA cm^{-2}, mainly because these are commonly employed and in contrast to the e.g. the tafel slope well defined on the IV-curve. The results are either normalzied based on the geometric or actual surface area. The actual surface area represents a more intrinsic activity but there is no golden standard yet that provide comparable results for different classes of materials. Generally speaking, *in-situ* and *ex-situ* approaches are employed for determining the actual surface area. The former estimates the true physical surface area and the latter the active electrochemical surface area(ECSA). The most common method is probably an *in-situ* method where the double layer capacitance of the electrode surface is determined and normalised with respect to the double layer capacitance of an ideal flat oxide surface, thus obtaining a roughness factor (R_f) [45,60,63,64] which can be used to estimate the ECSA. A general normalization factor is typically used which is not correct but it is pointed out

in [60] that reported values are in the range 0.022-0.13 mFA cm^{-2} so the accuracy of this method is a factor ≈ 3 if a value in the middle of the inverval is employed. The double layer capacitance can either be determined using cyclic voltammetry or electrochemical impedance spectroscopy. The former is performed around the flat band potential and the latter with a specific polarization of or current density applied to the electrode which are different circumstances and therefore different results are also obtained.

Two other ex situ methods have also been employed based on either electron microscopy imaging using a spherical approximation of the catalyst shape [47, 65, 66] or based on the BET specific surface area of the oxide particles [67–69] and are therefore an estimation of the actual electrocatalyst surface. Shao Horn and co-workers have found these methods to be mutually consistent and estimate the accuracy of the former method to be within a factor of approx. 3. From the standpoint of gaining a more fundamental understanding of the intrinsic electrocatalytic activity of various materials it makes sense to normalize with respect to the ECSA or actual surface area. From a more practical and applied standpoint it is, however, more questionable. The main argument being that the morphology and microstructure of one material not necessarily can be reproduced when synthesizing another material and some crystal surfaces may be preferential over others. In line with this argument it can be argued that a normalization of the current with respect to the mass of the catalyst is the most appropiate [66, 70].

An alternative also commonly used figure of merit for the intrinsic electrolcatalytic activity is the turnover frequency (TOF) which is essentially the number of oxygen molecules produced per active site per second [56, 71]. This method determines the total number of available electrocatalyst sites from the surface area and the number of available active sites (e.g. Co atoms) per surface area of the electrocatalyst. Assuming a 100 % Faradaic efficiency the number of oxygen molecules produced can be determined from the current. The TOF is now:

$$TOF = \frac{\text{number of oxygen molecules produced per second}}{\text{total number of active sites}} \tag{2.15}$$

This method assumes that we know what sites are active so it is best applied when comparing similar materials or it can be used as an estimate of the lower bound of the surface activity by assuming all sites are active.

In the following a review of the most important classes of ceramic oxides, employed as OER electrocatalysts, is performed trying to summarise some of the knowledge which is being accumulated about electrocatalytic activity and stability. It is hence not the intention to elucidate and deconstruct every detail of information available about the intrinsic electrocatalytic activity mechanisms as these are not understood. The literature is also somehow chaotic since so many parameters can be varied and have shown to influence electrocatalyst performance. The material classes investigated are spinel type materials, perovskites and related structures such as double perovskites and lastly metal (oxy)hydroxides. As comparison, the commonly referred to state-of-the-art IrO_2 electrocatalyst will be used. Since Ir is a scarse noble metal this is not considered a viable option [58]. It should be noted that during the last three years non-oxide based materials

have become a new group of materials studied for the OER. These include Ni-, Co- and Fe-based phospates, sulfides, selenides and nitrides. A recent publication reviews these non-oxide based (and oxide based) electrocatalysts [72].

2.4.2 Spinel type materials

The spinel structure has the composition AB_2O_4 with A and B typically being divalent and trivalent transition metal ions respectively. The oxygen ions can be regarded as arranged in a cubic close packed structure and the A and B ions occupy some of the octahedral and tetrahedral sites. In the normal spinel structure, visualised in figure 2.4a, the A ion occupy an octahedral site in the unit cell and the B ions occupy half the tetrahedral sites. Inverse spinel structures, e.g. $NiFe_2O_4$ also exist where the Ni^{2+} ion and one of the Fe^{3+} ions occupy octahedral sites and the other other Co^{3+} occupy a tetrahedral site. Intermediates also exist and for simplicity they will all be referred to as spinels in the following.

The type structure has been tested widely at realistic operating conditions during the 1970's and 1980's. Tseung et al. [73] identified the spinel $NiCo_2O_4$ as an active and stable (for several hundred hours) electrocatalyst in combination with Ni electrodes. Later publications confirmed this though the improvements compared to, e.g., Raney Ni is not unambigious [32, 59, 74]. The isolated electrocalytic effect of the $NiCo_2O_4$ electrocatalyst is, however, not elucidated. Similar studies were conducted on Co_3O_4 electrocatalysts and also identified this material as a very active electrocatalyst. More recent work has supplied some more information about the intrinsic electrocatalytic activity of particularly $NiCo_2O_4$ and Co_3O_4. It is clear that both materials perform well but it should be noted that in table 2.1 current density is generally normalised with respect to the geometric surface area as the this the common practice for these materials. A roughness factor or the Brunauer–Emmett–Teller (BET) specific surface area (SSA) has been supplied in most cases.

The most common methods employed for the synthesis of these materials are the co-precipitation method and thermal decomposition method. It was found by ,e.g., Monteverde Videla et al. that intrinsic electrocatalytic activity depends on the synthesis method and subsequent calcination temperature [75]. They compared a co-precipitation method followed by calcination at various temperatures, a solution combustion method and a method employing impregnation of silica hard templates followed by thermal decomposition. The overpotential at $10\,\mathrm{mA\,cm}_{ox}^{-2}$ was found to vary from 440-530 mV. The intrinsic electrolytic activity for a specific material is provided by Esswein et al. which found that a factor 10 increase in BET SSA of Co_3O_4 nanoparticles, synthesized using the same method, resulted in a 50 mV decrease of the overpotential at a current density of $10\,\mathrm{mA\,cm}_{geo}^{-2}$ [71]. One parameter that seems to be relatively consistent throughout the literature is the tafel slope at low overvoltage which consistently is reported in the range 50-70 $\mathrm{mV\,dec}^{-1}$ for both Co_3O_4 and $NiCo_2O_4$.

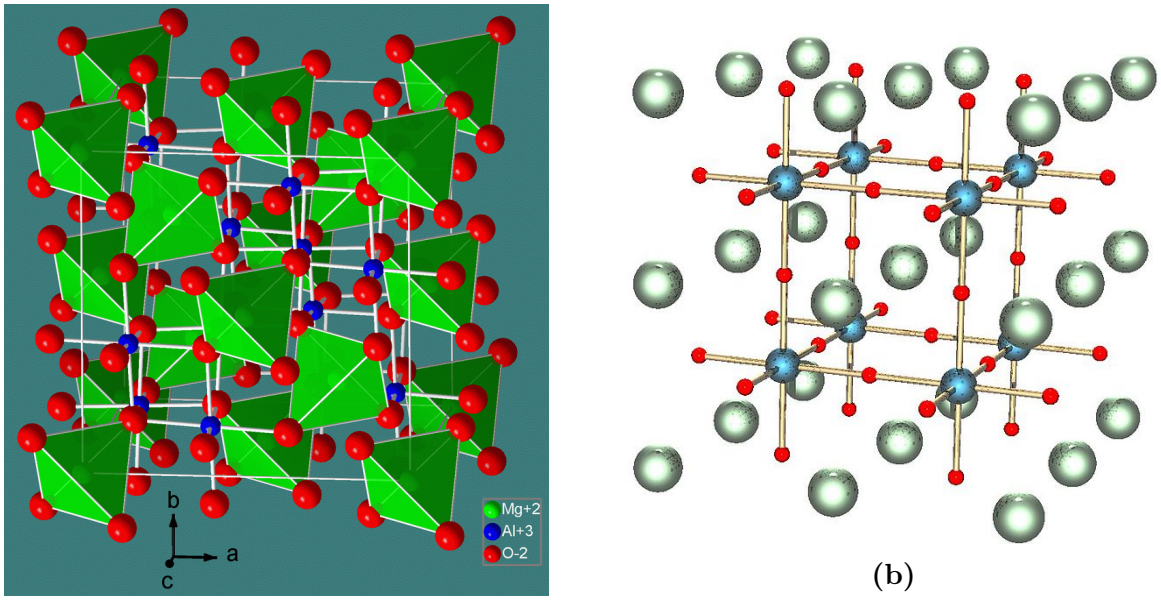

(a) **(b)**

Figure 2.4: (a) The spinel structure visualized, in this case as a $MgAl_2O_4$ spinel. From [76].**(b)** The perovskite structure visualized. The blue spheres are A-site, the green the B-site and red are oxygen. From [77].

2.4.3 Perovskite structures

The ideal perovskite structure (ABO_3) is cubic and shown in figure 2.4b. It is composed of a alkaline earth or rare earth element (A) which can be regarded as sitting at the corners of a cube, a smaller transition metal (B) is bodycentered in the cube and oxygen atoms are sitting in face centered positions of the cube. The stability and degree of distortion from the cubic perovskite structure of a given set of A and B site cations can be predicted from the Goldschmidt tolerance factor which is a dimensionless number calculated from the ionic radii of the cations and anion [78]. For the cubic structure this is very close to unity and represent a case where all ions "touch" each other. In practice most perovskites exhibit distortions from the ideal cubic structure and are found in tetragonal, orthohombic or hexagonal/rhombohedral crystal systems. Both the A and B sites are frequently substituted with elements in different oxidation states to tune the electrocatalyst behaviour. This also leads to various compensation mechanisms, e.g. oxygen deficiency, which will not be explicitly stated in the following chemical formulas.

The perovskites have been investigated as electrocatalyst, at least, since the 1980's. Matsumoto et. al. [79] investigated the family $La_{1-x}Sr_xFe_{1-y}Co_yO_3$ and found $La_{0.2}Sr_{0.8}Fe_{0.2}Co_{0.8}O_3$ to be most active. Bockris et al. [45] investigated various La based perovskites with Mn, Co, Ni and Fe as the B-site and identified $LaNiO_3$ and $La_{0.6}Sr_{0.4}CoO_3$ as the most active electrocatalysts. Both of these electrocatalysts have subsequently been surpassed in terms intrinsic electrocatalytic activity. $Ba_{0.5}Sr_{0.5}Co_{0.8}Fe_{0.2}O_3$ and later $Pr_{0.5}Ba_{0.5}CoO_3$ were identified as a highly active electrocatalysts by the same group [47, 67]. The same group later showed that the activity increases over time and this was ascribed to the

surface amorphization in the case of $Ba_{0.5}Sr_{0.5}Co_{0.8}Fe_{0.2}O_3$ [65]. It was later shown that the carbon black(from now referred to as C) used as conductivity enhancing agent in the catalyst ink, enhances the electrocatalytic activity of $Ba_{0.5}Sr_{0.5}Co_{0.8}Fe_{0.2}O_3$ compared to a catalyst ink with no C [80]. The activity of both materials was, however, seen to change upon potential cycling [70]. This also raises the question whether this enhancing effect of C on the electrocatalytic activity is common effect for perovskites or not?

The common method to test electrocatalytic activity of perovskites is certainly by making an ink that contain electrocatalyst and C and it is also known that C eventually will oxidise during the OER so it is not feasible to use it in actual OER electrodes. In a later study an end of service life test was introduced which continually cycled the potential between 1 V and 2.1 V vs reversible hydrogen electrode (RHE) on 100 nm thick perovskite thin films at 80 ℃ in 1 M KOH [52]. In both cases the long term degradation mechanism was identified as A-site leaching from the surface which is kinetically limited at room temperature. The study, however, showed that whereas the electrocatalytic activity of $Ba_{0.5}Sr_{0.5}Co_{0.8}Fe_{0.2}O_3$ plummets during the first hour of testing the electrocatalytic activity of $Pr_{0.2}Ba_{0.8}CoO_3$ remained stable for 11 h before plummeting. The important point to stress here is that though the surface of both materials changes over time at a similar rate, the electrocatalytic activity of $Pr_{0.2}Ba_{0.8}CoO_3$ is not compromised in the short term. The resulting change in defect chemistry and structure is pointed out by the authors as critical in the context of how the electrocatalytic activity is affected, also highlighting the importance of defect chemistry engineering.

To sum up this seems to suggest that electrocatalytically active perovskites identified so far are also inherently chemically unstable. This instability is activated with temperature and also dependent on the applied voltage; it can, however, be partially decoupled from the electrocatalytic activity by tuning the structure and in particular the defect chemical structure.

2.4.4 Simple metal oxides and metal (oxy)hydroxides

Metal (oxy)hydroxides are a class of very active electrocatalysts. They have exceeded the activity or at least shown comparable activity to state-of-the-art IrO_2 and RuO_2 electrocatalysts [56, 81, 82] and they show at least comparable intrinsic activity to the best performing perovskites to date, e.g. $Ba_{0.5}Sr_{0.5}Co_{0.8}Fe_{0.2}O_3$. The metal (oxy)hydroxides are layered structures with edge sharing octahedrally coordinated metal cations forming a layer. For the best understood structure, Ni (oxy)hydroxide, four different phases are known to exist: α-$Ni(OH)_2$, β-$Ni(OH)_2$, β-NiOOH and γ-NiOOH. They are illustrated in bode diagram in figure 2.5. The α-$Ni(OH)_2$ and γ-NiOOH phases allow intercalated water molecules in the between layers in contrast to the β-$Ni(OH)_2$ and $\beta - NiOOH$ phases which layers are not hydrated. An example of the redox between β-$Ni(OH)_2$ and β-NiOOH is: $Ni(OH)_2 + OH^- \leftrightarrow NiOOH + H_2O + e^-$. The oxidation state of Ni is in practice observed to vary between +2 in α-$Ni(OH)_2$ and $\beta Ni(OH)_2$, to +3 in βNiOOH and up to +3.5-3.7 in γ-NiOOH. The later allowing Ni to overcharge due to the incorperation of anions, typically CO_3^{2-}, as charge compensating. This phase is also known as layered

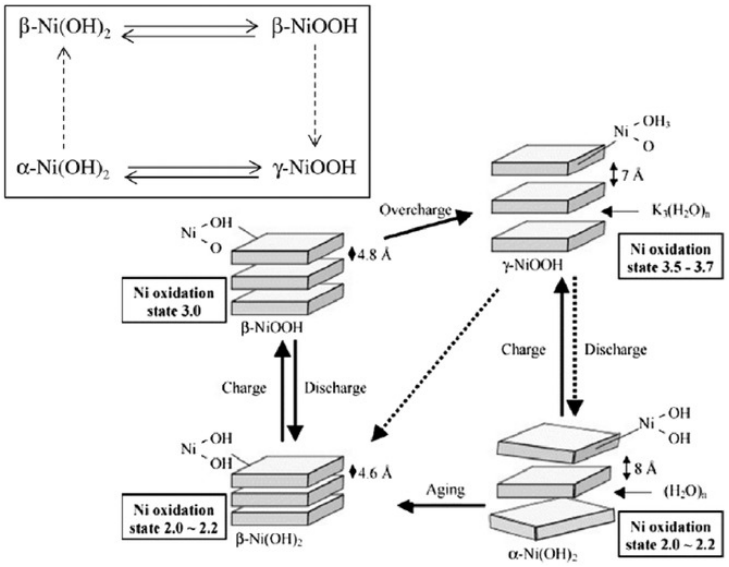

Figure 2.5: A bode diagram illustrating the two phases of Ni hydroxides and Ni oxyhydroxides respectively and under what conditions one phase transforn another phase. Only the α-Ni(OH)$_2$ phase and γ-NiOOH are hydrated. From [83].

double hydroxides and their layers can be exfoliatied which allow for thin sheets down to one atomic layer thickness to be separated.

The most active metal oxyhydroxides studied to date are the NiFe (oxy)hydroxides [83, 84]. Fe is an impurity always found together with Ni, which has made it difficult to separate the electrocatalytic activity of purely Ni-based from NiFe-based (oxy)hydroxides [85]. It turns out that Fe plays a key role in the electrocatalysis even at very low Fe concentrations (0.01 wt%) [86] which is convenient now that the elements are so hard to separate. Fe is known to have both an enhancing effect on the electrocatalytic activity and the electronic conductivity; the latter is poor for metal (oxy)hydroxides, and probably one of the reasons why the electrocatlytic activity seems to be dependent on substrate material and electrocatalyst layer thickness [87]. Further, the ageing of Ni hydroxides in concentrated alkaline solutions has shown to increase the crystallinity of the material and incorperate Fe impurities from the electrolyte into the structure simultaneously, leading to enhanced electrocatalytic activity. The optimum amount of Fe in the structure is not clear but it seems to lie in the interval 10-50 %. The electrocatalytic activity seem to be consistently high in most of the literature reported. The overpotential at 10 mA cm^{-2} has been reported in the interval 210-360 mV and tafel slopes in the interval 30-70 mV/dec [83]. Several publications have tried to incorperate a third metal into the NiFe oxides and shown that this can have an enhancing effect on the electrocalytic activity. For example, it was shown that the incorperation of Al can improve the electrocatalytic activity of NiFe, CoFe and CoNi oxides even though Al in itself is not electocatalytically active [88]). Another study found Mn to have en enhancing effect on the electrocatalytic activity of NiFe (oxy)hydroxides [89]. A recent study testing intrinsic electrocatalytic active of NiFe hydroxides at industrially relevant conditions found that they, not surprisingly, are very active at these conditions; reaching 2.0 A cm^{-2} an overvoltage of approx. 350 mV (in 30

wt%, KOH at 60 °C). In terms of stability of these electrocatalysts there is, to my knowledge, no evidence under conditions relevant for alkaline water electrolysis. At standard conditions, such as $10\,\mathrm{mA\,cm^{-2}}$ 1 M KOH at RT, they have shown to exhibit good electrocatalytic activity.

Material	Reference (year)	Catalyst loading ($mg\,cm^{-2}$)	substrate	Conditions	Surface normalization	η (mV) at J=10 $mA\,cm^{-2}$	J ($mA\,cm^{-2}$) at η=300 mV
$NiCo_2O_4$	[90] (2004)	n/a	Ni	1.0 M KOH, 25 ℃	$A_{geo}, R_f = 1800$	≈ 350	≈ 2.5
$NiFe_2O_4$	[68] (2014)	2.5	GC	0.1 M NaOH, 25 ℃, IR cor.	$A_{BET}, SSA_{BET} = 1.8\,m^2\,g^{-1}$	> 520	< 0.001
$NiCo_2O_4$	[91] (2017)	0.2	GC	1.0 M KOH, 25 ℃, IR cor.	$A_{geo}, SSA_{BET} \approx 100\,m^2\,g^{-1}$	≈ 350	<1
$Ni_{0.6}Co_{2.4}O_4$	[91] (2017)	0.2	GC	1.0 M KOH, 25 ℃, IR cor.	$A_{geo}, SSA_{BET} \approx 100\,m^2\,g^{-1}$	330	<1
$NiCo_2O_4$	[64] (2018)	0.24	GC	1.0 M KOH, 25 ℃, IR cor.	$A_{geo}, SSA_{ECSA} = 19.1$	340	≈ 2
$NiFeAlO_4$	[68] (2014)	2.5	GC	0.1 M NaOH, 25 ℃, IR cor.	$A_{BET}, SSA_{BET} = 9.3\,m^2\,g^{-1}$	> 400	< 0.01
Co_3O_4	[92] (2007)	3.4	Ni	1.0 M KOH, 25 ℃ IR cor.	$A_{ECSA}, R_f = 3255$	>400	0.12
Co_3O_4	[93] (2015)	0.1	FTO	1.0 M KOH, 25 ℃ IR cor.	$A_{ECSA}, R_f = 6.2$	377	≈ 0.5
Co_3O_4	[75] (2017)	0.055	CG	0.1 M KOH, 25 ℃ IR cor.	$A_{ECSA}, R_f = 50$	440	≈ 0.1
Co_3O_4	[75] (2017)	0.055	GC	0.1 M KOH, 25 ℃ IR cor.	$A_{ECSA}, R_f = 19$	520	≈ 0.01
Co_3O_4	[91] (2017)	0.2	GC	1.0 M KOH, 25 ℃, IR cor.	$A_{geo}, SSA_{BET} \approx 100\,m^2\,g^{-1}$	≈ 370	<1
La doped Co_3O_4	[92] (2017)	2.8	Ni	1.0 M KOH, 25 ℃ IR cor	$A_{ECSA}, R_f = 3580$	>400	0.08
$LaNiO_3$	[45] (1984)	n/a (pressed powder)	None	0.1 M KOH, 25 ℃ IR cor.	$A_{ECSA}, R_f = 5600$	>420	0.013
$LaNiO_3$	[94] (2011)	0.25	GC	0.1 M KOH, 25 ℃ IR cor.	$A_{cat}, SSA_{cat} \approx 3.5\,m^2\,g^{-1}$	>490	0.02-0.03
$LaNiO_3$	[95] (2016)	0.32	GC	0.1 M KOH, 25 ℃ IR cor.	$A_{BET}, SSA_{BET} = 3.0\,m^2\,g^{-1}$	>650	< 0.02
$La_{0.6}Sr_{0.4}CoO_3$	[45] (1984)	n/a (pressed powder)	none	0.1 M KOH, 25 ℃ IR cor.	$A_{ECSA}, R_f = 1500$	>492	0.01
$La_{0.6}Sr_{0.4}CoO_3$	[96] (2016)	0.21	GC	0.1 M KOH, 25 ℃ IR cor.	A_{geo}	469	n/a
$La_{0.4}Sr_{0.6}CoO_3$	[65] (2014)	0.25	GC	0.1 M KOH, 25 ℃, IR cor.	$A_{cat}, SSA_{cat} \approx 1.2\,m^2\,g^{-1}$	420-430	≈ 0.2
$La_{0.8}Sr_{0.2}Co_{0.2}Fe_{0.8}O_3$	[97] (2016)	0.212	GC	0.1 M KOH, 25 ℃ IR cor.	A_{geo}	414	≈ 0.4
$La_{0.58}Sr_{0.4}Co_{0.8}Fe_{0.2}O_3$	[96] (2016)	0.21	GC	0.1 M KOH, 25 ℃ IR cor.	A_{geo}	423	n/a
$Ba_{0.5}Sr_{0.5}Co_{0.8}Fe_{0.2}O_3$	[65] (2012))	0.25	GC	0.1 M KOH, 25 ℃, IR cor.	$A_{cat}, SSA_{cat} \approx 0.2\,m^2\,g^{-1}$	360	≈ 2-3
$Ba_{0.5}Sr_{0.5}Co_{0.8}Fe_{0.2}O_4$	[80] (2014)	GC	0.46	0.1 M KOH, 25 ℃, IR cor.	$A_{geo}, SSA_{BET} = 10\,m^2\,g^{-1}$	> 540	≈ 0.01-0.02
$Ba_{0.5}Sr_{0.5}Co_{0.8}Fe_{0.2}O_3$	[69] (2015)	0.32	GC	0.1 M KOH, 25 ℃, IR cor.	$A_{BET}, SSA_{BET} = 0.43\,m^2\,g^{-1}$	> 520	≈ 0.1
$Pr_{0.5}Ba_{0.5}CoO_3$	[67] (2013)	0.25	GC	0.1 M KOH, 25 ℃, IR cor.	$A_{BET}, SSA_{BET} = 0.35\,m^2\,g^{-1}$	≈ 380	≈ 0.8-1
$SrCo_{0.9}Ti_{0.1}O_3$	[69] (2015)	0.32	GC	0.1 M KOH, , 25 ℃, IR cor.	$A_{BET}, SSA_{BET} = 0.91\,m^2\,g^{-1}$	> 550	≈ 0.08
$Ni_{0.9}Fe_{0.1}OOH$	[56] (2012)	1.17×10^{-3}	Au/Ti or ITO	1.0 M KOH, 25 ℃ IR cor.	A_{geo}, thin film ≈ 2 nm	≈330-340	1.2-1.3
$Ni_{0.6}Fe_{0.4}OOH$	[63] (2013)	≈ 0.02-0.04	Au	1.0 M KOH, 25 ℃	$A_{ECSA}, R_f = 2-6$	280	20
$Ni_{0.75}Fe_{0.25}OOH$	[98] (2014)	0.07	GC	1.0 M KOH, 25 ℃, IR cor.	A_{geo}	347	2.1
$Ni_{0.9}Fe_{0.1}Ox$	[68] (2014)	2.5	GC	0.1 M NaOH, 25 ℃, IR cor.	$A_{BET}, SSA_{BET} = 4.5\,m^2\,g^{-1}$	> 530	< 0.001
$Ni_{0.75}Co_{0.25}OOH$	[56] (2012)	1.04×10^{-3}	Au/Ti or ITO	1.0 M KOH, 25 ℃, IR cor.	$A_{geo,}$, thin film ≈ 2 nm	≈360	0.4-0.5
$Ni_{0.67}Co_{0.33}OOH$	[98] (2014)	0.07	GC	1.0 M KOH, 25 ℃, IR cor.	A_{geo}	385	0.46
IrO_2	[66] (2012)	0.05	GC	0.1 M KOH, 25 ℃, IR cor.	$A_{cat}, SSA_{cat} \approx 71\,m^2\,g^{-1}$	> 470	≈ 0.012-0.02
IrO_2	[56] (2012)	4.12×10^{-3}	Au/Ti or ITO	1.0 M KOH, 25 ℃, IR cor.	$A_{geo,}$, thin films with thickness ≈ 2 nm	≈540°	0.06-0.07
IrO_2	[98] (2014)	0.21	GC	1.0 M KOH, 25 ℃, IR cor.	A_{geo}	338	1.49
IrO_2	[64] (2018)	0.24	Li	1.0 M KOH, 25 ℃, IR cor.	$A_{geo}, SSA_{ECSA} \approx 29.0$	290-300	≈ 10

Table 2.1: Selected results from the literature comparing the (intrinsic) electrocatalytic activity of spinels, perovskites and metaloxides/-(oxy)hydroxides. Substrates are either Ni, Au, Ti, glassy carbon (GC), fluorine or iridium doped tin oxide (FTO or ITO). The figures of merit chosen are the overpotential at a constant current density of $10\,mA\,cm^{-2}$ and the current density produced at a constant overvoltage of 300 mV. The current density is generally normalised with respect to the BET specific surface are (A_{BET}), the estimated catalyst surface area (A_{cat}), the electrochemical surface area (A_{ECSA}) or the electrode geometric surface area (A_{geo}). values which are termed < or > are extrapolated with the tafel slope and ≈ values are read from a graph.

2.5 Processing of ceramic suspensions

2.5.1 Processes for fabrication of thin ceramic oxide layers

The methods best suited for the fabrication of ceramic oxide layers has been assessed with several aspects in mind. First of all the ceramic oxide layer will serve an electrode, a high surface area and accessibility of the surface area are therefore key requirements. Methods for fabrication of porous electrodes is therefore a starting point. The optimal thickness is not known a priori but the method employed should allow for varying the thickness and a thickness on the order of 20-50 µm is the order of magnitude we are aiming at. Since we are trying to develop the technology HTP-AEC and we would like to be able to use methods that are easily scalable and allow for a high throughout at a minimum cost per cell. The best suited methods for this purpose are traditional ceramic forming methods. The best suited methods are tape casting, screen printing, dip coating and spin coating. From this it was deduced that tape casting would be tricky as electrode thicknesses on the order og 20-50 µm would be difficult to process without co-coasting and thereby also co-sinter which complicates matters. Dip coating would require masking of the back side of the sample and spin coating produces too thin layers so multiple layers would have to be processed. Screen printing has the advantage that thin layers can be applied on green or sintered substrates. You need relatively small amounts of ink per print and the thickness of the print can be varied by choosing a particular mesh.

2.6 Processing of ceramic oxide suspensions and sintering of green bodies

The processing of thin layers of ceramic oxides using screen printing require a well dispersed suspension. Metal oxide powders are generally composed of agglomerates [99], many of which can be broken up during the processing of the ink. The traditional method used to break up loose agglomerates in ceramic oxides is horizontal ball milling where ceramic oxide powder is dispersed in a solvent often using a dispersant. The ceramic oxide suspension is put in a container with a hard milling media and kept rolling [100]. Collisional and frictional forces will now do the work of breaking up agglomerates. In figure 2.6 the motion of the milling media in a horizontal ball mill is shown at different rotational speeds.

The size and the shape of the milling media are factors to consider. The optimal size is a trade-off where on the one hand a smaller size will provide more contact points between the milling media and the ceramic oxide particles and, on the other hand, a sufficient amount of energy is required to break up the agglomerates. To break up agglomerates require sufficient energy and impact between ceramic oxide particles or between different ceramic oxide particles. The impact is large due to shearing forces or due to gravitation forces. Smaller sized milling media provide more possibilities for impact but also less energy during impact. Regarding the shape of the milling media, spherical and cylindrical media are common shapes. The spherical balls will provide a smaller contact area and are seen to produce a wider particle size distribution and is less effective in reducing the

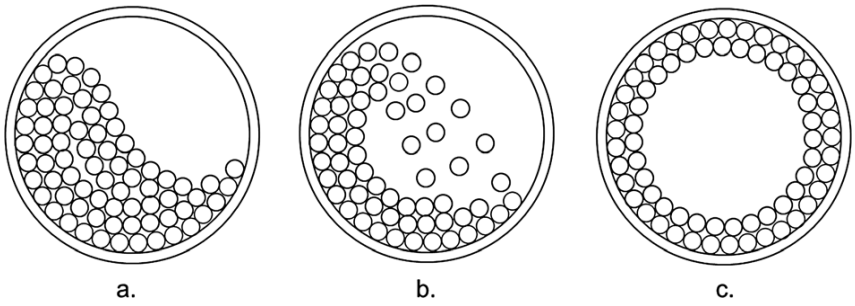

Figure 2.6: The motion of the milling media in a horizontal ball mill is shown for different rotational speeds. The situation in b. is optimal in terms of milling efficiency due to the optimal use of gravity. From [102]

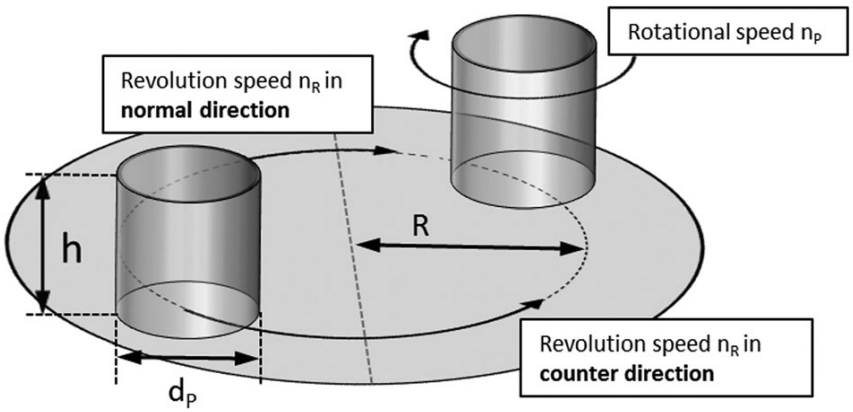

Figure 2.7: (a) (b) The milling chamber of a planetary ball mill is rotating around two axes and thereby greatly increasing the mechanical energy inside the chamber. From [102]

particle size compared to cylindrical balls [101]. Other issues to consider are not to overfill the milling chamber as this will lower the milling efficiency, and the ratio between milling media and powder/slurry will also affect milling efficiency. A higher ratio will generally increase milling efficiency.

In terms of the operation there are two parameters to consider. These are the milling time and the rotational speed during milling. A longer milling time tend to decrease the particle size in the suspension. The relationship between time and particle size is, however, not linear as smaller particles become increasing difficult to break up. A reverse process of agglomeration of particles becomes increasingly important when the particles decrease in size and inter-particle surface forces become more important due to an increase in surface area. A dispersant (see section 2.7) is standard additive that hinders re-agglomeration of particles. The other parameter, the rotational speed, is also important as the milling media will gain more kinetic energy when the rotational speed is increased. The rotational speed should not exceed the critical speed where the centrifugal force exceeds the force of gravity, as the milling media will not be able to transfer its energy. This corresponds to situation "c." in figure 2.6 [102].

The main issue with traditional ball milling is that it requires long milling times com-

pared to alternative high energy milling equipment such as planetary ball mills. Planetary ball mills have shown to decrease the milling time drastically as the energy density of the medium in these mills is 100-1000 times higher than in traditional ball mills [103]. The reason for this very high energy density of a planetary ball mill it that is has two axes of rotation. The chamber spins around itself and moreover the chamber is connected to a shaft, which is rotated around the shaft anchoring point as shown in figure 2.7 [102]. Since the energy density in such mills are much higher than in traditional ball mills one risk that small pieces of milling media will come off and end up as impurities in the ink. It is therefore important to consider because most impurities are unwanted during the sintering process and for the functionality of the sintered layer. Therefore a milling media with high hardness and fracture toughness compared to the media being milled should be used. Moreover, the rotational speed should be kept at a minimum and the milling time adjusted. Spherical milling media should also be used. The preparation of screen printing inks require a rather viscous ink and the last part of the ink preparation where the viscosity enhancing binder is added (2.7.4) provide difficulties when using conventional ball milling. In this case the binder should be added dissolved in the solvent. By making use of a planetary ball mill with largel sized milling media ($\approx 30\,\mathrm{mm}$) the binder can be dissolved directly in the suspension, which is advantageous as a high solid loading of ceramic powder is preferred in the final ink.

2.7 Dispersion of ceramic oxide powder

A liquid system with ceramic particles dispersed in a solvent along with a dispersing additive (dispersant from now on) is a common way of stabilising ceramic particles, which is used for most traditional ceramic processing methods. Forming a stable suspension, where agglomeration or settling of the particles is negligible within the time frame of the deposition method is important for the subsequent processing steps of deposition and sintering.

In most cases a dispersant needs to be added to the suspension, that can prevent the particles from agglomerating, to obtain a stable colloidal dispersion. A very general way of examining this problem is to look at a situation with two particles approaching each other. The total potential energy of this interaction is the sum of the attractive (U_a) and repulsive energy (U_r).

$$U_\mathrm{t} = U_\mathrm{a} + U_\mathrm{r} = U_\mathrm{vdW} + U_\mathrm{el} \tag{2.16}$$

where U_vdW is the attractive term due to Van der Walls forces acting between the surfaces of particles, U_el is the electrostatic repulsive term arising due to charges residing on the particle surface.

The question is now how to create sufficiently repulsive forces between the particles in a suspension and prevent agglomeration. Two main mechanisms used to produce a stable dispersion exist. These are steric and electrostatic stabilisation [99]. A combination of these is also possible and this is called electrosteric stabilisation. The electrostatic and steric effect is illustrated schematically in figure 2.8 [104].

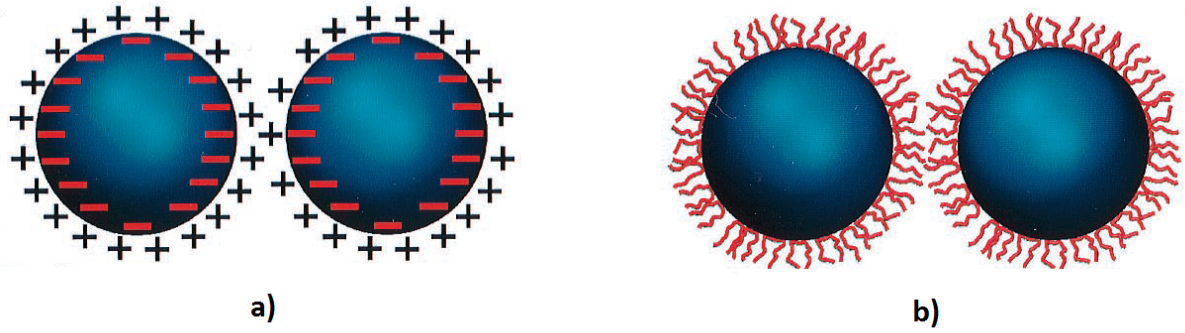

Figure 2.8: The two main methods of stabilisation af suspension by electrostatic forces **(a)** or by steric stabilisation using polymers **(b)**. From [104]

2.7.1 Electrostatic stabilisation

Electrostatic stabilisation relies on electrostatic forces arising from charged particle surfaces in the suspension. This surface charge can be altered by several means and for ceramic oxides the means are preferential absorption of ions from the solution onto the particle surface or dissociation of amphoteric hydroxyl groups present on the oxide surfaces [99, 104]. A common way to change the electrostatic repulsion of oxide particles is therefore to add an electrolyte such as an acid or a base to the solution. If an acid is added the surface becomes more positively charged and if a base is added the surface becomes more negatively charged. This essentially means that at low pH the surface of the particles will be positively charged and at high pH the surface will be negatively charged. The pH where the net surface charge is zero is termed the point of zero charge (PZC). The strength of the stabilisation depends on the induced surface potential of the particles, the dielectric properties of the solvent and the ionic strength of the solution.

The electrostatic potential can be measured indirectly by means of electro-kinetic or electro-accoustic methods and is known as the ζ-potential. The pH where the potential is zero is called the isoelectric point (IEP). To produce a well-stabilised suspension the pH should therefore be adjusted away from the IEP as this will lead to a numerically high ζ-potential. Assessing the electrostatic stabilisation on the microscopic level has shown that for a charged particle surface adsorption of an equal neutralising countercharge is not the outcome. Instead, due to thermal induced motion of the ions in the solution, an electrical double layer is formed around the charged particles, constituting a compact and a diffuse layer.

The electrical double layer of an isolated particle essentially constitutes a compact layer of counterions interacting directly with the surface of the particles, the stern layer, which is a few molecular diameters thick and further away from the particle's surface a diffuse layer, first described by Gouy and Chapman, containing counter ions as well as polar liquid molecules. This is illustrated in figure 2.9 [105]. The diffuse layer is less compact because as the distance from the surface is increased the electric potential decreases, which means that the thermal energy,becomes increasingly important leading to motion

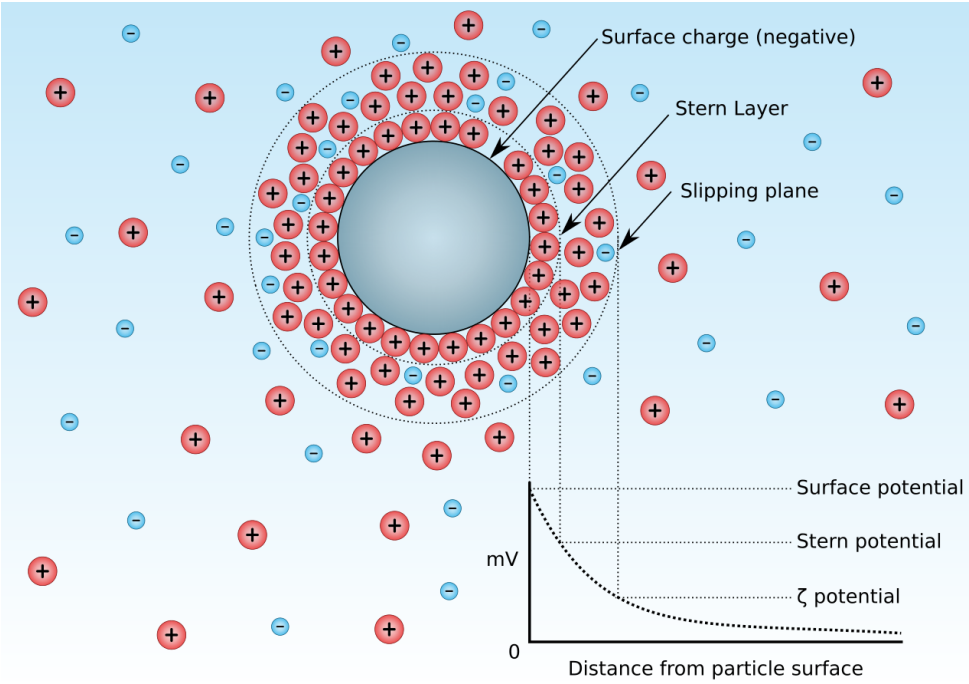

Figure 2.9: Stabilisation by means of electrostatic forces is caused by the formation of an electrical DL around a charged particle. The DL is formed to counteract the surface charge. This results in a repulsion between the suspended particles. The ζ-potential is used to measure how strong this repulsion is and thereby how good the stabilisation is. From [105]

of the particles in this layer. The resulting charge distribution, which occurs close to a uniformely charged surface and results in a potential difference is capacitive in nature. In fact it can be approximated to that of a parallel plate capacitor in the limit of small surface potentials relative to the thermal energy (up to approx. 50 mV at room temperature). The capacitance (C) of a parallel plate capacitor (the electrical double layer) is inversely proportional to its thickness and $C = \frac{Q}{V}$ the electrical potential is proportional to the double layer thickness.

$$\kappa^{-1} = \frac{\epsilon_r \epsilon_0 N_A k_B T}{F^2 \Sigma c z_i^2}^{1/2} \tag{2.17}$$

2.7.2 Steric stabilisation

The other main mechanism used to form a stable suspension is by steric stabilisation, which relies on mechanical blocking of the particles from each other. This is done by the addition of organic molecules, usually polymeric, to the solution. After addition of particles to the solution with dissolved polymers the particle surfaces are gradually covered by means of chemical or physical adsorption. Ball milling enhances the mixing effect. For the steric stabilisation to be effective the adsorption of the polymers should be sufficiently strong to prevent desorption upon collisions between particles during ball milling. The steric repulsive energy depends on the adsorbed layer thickness (δ), the adsorbed layer

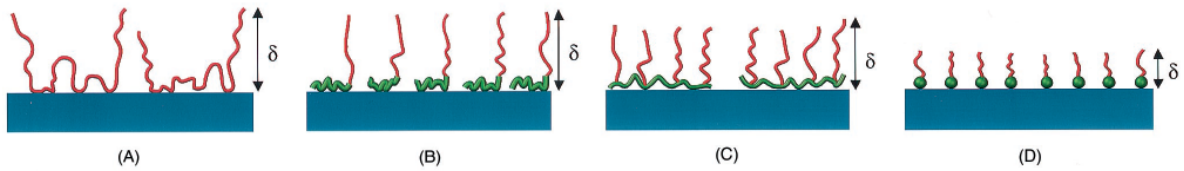

Figure 2.10: Examples of common polymer/molecule types used to form steric stabilisation. (A) homo polymers, (B) diblock polymers, (C) comb-like polymers and (D) functional short chain surfactants. From [104].

density, the solvent quality and the separation distance between interacting particles.

A dense layer is also important to prevent entanglement of polymers residing on different particles as this can lead to bridging flocculation, where the particles form loose agglomerates due to the interactions of steric polymers residing on their surfaces. Examples of different polymer structures are homo polymers, diblock polymers, comb-like polymers and functional short chain surfactants with an anchoring head group and an extended tail. These are illustrated in figure 2.10 [104].

In order to obtain an optimal dispersion it is important that the steric dispersant is added in correct quantities. If too small amounts are added there will be empty sites on the particles where polymers from neighbouring particles can adsorb. This can lead to bridging flocculation, as explained above. On the contrary, a too large amount of dispersant can also be problematic as the the excess polymers can promote interaction between particles and lead to depletion flocculation, which is caused by an osmotic pressure difference when a polymer is excluded from a small gab between two particles. The net effect of too high amounts of dispersant can, however, also promote stabilisation if there is no interaction between the dispersant polymers [104].

2.7.3 Electrosteric stabilisation

Electrosteric stabilisation is a combination of the electrostatic and steric stabilising effects. It is commonly obtained by using polyelectrolyte polymers that carry at least one ionic group which (partically) dissociate in aqueous solutions. The polymers can have either cationic or anionic groups. The best electrosteric effect is obtained if the particle surface and the ionised group carry opposite charges. The non-ionic part of the polyelectrolyte is the anchoring group and the ionic group is directed away from the particle surface due to the electrostatic effect. The electrosteric effect can be increased by changing either the pH and/or the ionic strength of the solvent. Different types of polymers can be used electrosterically including homopolymers, diblock polymers and comb-like polymers (cf. Figure 2.10).

2.7.4 Solvents and other additives

The solvent, which is used to disperse the ceramic particles, is important for several reasons. First of all, it should provide sufficient wetting of the particles for them to flow easily and secondly it should dissolve dispersants and other additives and provide the means for creating a uniform solution. There are generally two types of solvents, which are water and organic solvents. The organic solvents can further be classified into non-polar (or weakly polar) and polar liquids. Important physical characteristics of solvents are the dielectric constant, functional groups, surface tension, viscosity and latent heat of evaporation or the vapour pressure. Water has a very high dielectric constant, which is at least twice that of most polar liquids. Water likewise has a very high surface tension and it is non-toxic, which is the most important reason for using water. On the contrary most organic solvents are toxic to some degree and they have low flash points. Organic solvents are important for several reasons though. They offer a wide spectrum of polarity and the surface tension is, as mentioned above, lower. In addition, they have varying vapour pressure, which means that their evaporation rate spans a wide interval from very low to very high. A low evaporation rate is desirable for a processing method such as screen printing where the solvent fraction is already low and evaporation therefore can have a profound influence on the flow behaviour. The solvent, used in a system, is often composed of several solvents as this allows to tune the solvent system to the required properties.

Other additives include a wide variety and in the following only the relevant ones for screen printing will be presented briefly. A binder is generally an additive, which provides strength to the green body. Binders are typically long chain polymers, which means that they also can be used to change the rheological characteristics of the ink. Plasticizers alter the plasticity of the green body allowing it to be handled without causing fractures. This is especially relevant if the green body is not deposited on a rigid surface. The combination of solvents and additives is not trivial to match and often trial and error is the best option. The number of additives should therefore be kept at a minimum and likewise the amount as all solvent and other additives eventually have to be removed during the sintering.

2.7.5 Sintering

When stable suspension has been made this is followed by forming or creating the desired geometry of the ceramic oxide. The next step is drying of the body to evaporate remaining solvent. This can be done in a ventilated place at room temperature or in a oven if the solvent has a low vapour pressure. After the drying stage the body is referred to as a green body. The green body is still just a body of relatively loosely bound particles.

In order to form a consolidated ceramic oxide body the green body has to be fired. The overall aim of firing ceramic oxides is the sintering process whereby the individual particles are mobilized and joined together which macroscopically resemble a monolithic type structure [101]. Before the actual sintering process can take place all the non-ceramic oxide parts have to be removed from the structure in a pre-sintering step. This includes

all the organic additives used in the processing such as dispersants, plasticizers, binders and other additives used e.g. pore formers. The pre-sintering step is essentially heating the green body using a slow heating rate and possibly holding the temperature constant at critical temperatures where large amounts of additives are removed. The result of a poorly controlled pre-sintering step is typically deformation of the green body formation of crack and possible delamination from a substrate. This is directly related to the burnout of the organics. When heated, the organics gradually start to decompose and/or evaporate which means products have to be able to escape the green body to avoid large internally build up pressures. For green bodies containing relatively high amount of organics, e.g. tape casted layers, the mass diffusion of the organics can also be rate-limiting, requiring extended holding times - in particular for thicker structures. Following the pre-sintering step the temperature is usually increased at a higher rate towards the sintering temperature.

The sintering process proceeds in several stages and depends first of all on the material to be sintered and secondly on other factors such as the particle sizes and their distribution. For a material with a homogeneous particle size distribution, the initial stage of sintering involves surface smoothing of the particles, formation of grain boundaries, necking between particles and a decrease of the porosity. During the intermediate stage, open pores intersecting grain boundaries shrink, porosity decreases significantly and grain growth is initiated. In the final stage grain growth proceeds which can lead to widely varying grain size, pores shrink to a minimum size or disappear completely depending on their relative position and size and closed pores form. The driving force behind sintering is the minimization in the total (Gibbs) free energy of the system. But in order for this reduction to occur the particles have to be mobilized which require a certain energy, in most cases supplied by heat. The initial sintering stage is dominated by the reduction of the surface free energy which essentially is the reduction of the free surface. Later the reduction of the free energy associated with grain boundaries and the volume become more important as grain growth and volume shrinkage is being observed. The sintering process can be controlled by controlling temperature and time. It can also be stopped pre-maturely to avoid too much densification and hence leave the sintered structure intentionally porous. After the sintering process has finished the material is cooled. This often done under similar conditions as the heating to avoid thermal shocks. For some ceramics an annealing step is also included to release built up stresses or allow for a reorganization in the structure (e.g. a phase transformation) to occur prior to cooling.

Chapter 3

Experimental methods

In this chapter the experimental techniques used during the thesis work will be introduced together with the materials and procedures used for the experimental work. A brief, mainly conceptual, description of the working principles behind the experimental techniques is included when appropriate. For a more comprehensive description of the theory of the experimental techniques the reader is referred to some of the many book, articles etc. available on these subjects. Several of these are refereed to in the following.

3.1 Characterization of the ceramic oxide powders

3.1.1 Ceramic oxide powders

The ceramic oxide powders used were purchased from two different suppliers. The powders for the evaluation of intrinsic electrochemical activity towards the OER and for chemical stability measuremetns were 99.9 % purity and synthesized by Praxair Surface Technologies (Praxair Technology, USA) using the combustion spray pyrolysis method. The compositions included four perovskites and one Ruddlesden-Popper phase: $LaNiO_3$ (LN), $La_{0.97}NiO_3$ (L97N), $LaNi_{0.6}Fe_{0.4}O_3$ (LNF), $La_{0.97}Ni_{0.6}Fe_{0.4}O_3$ (L97NF) and $La_2Ni_{0.9}Fe_{0.1}O_4$ (L2NF). The calcination temperature of the LNF powder was 700 ℃ and for the others the calcination temperature is higher but not known. The LNF powder used for the successive processing of porous electrodes was also 99.9 % purity and synthesized using the solid state reaction method by Kceracell Co. (Republic of Korea). It was synthesized at 830 ℃ followed by calcination at 1150 ℃.

3.1.2 Polycrystalline X-ray diffraction measurements

Polycrystalline X-ray diffraction (XRD) measurements are a standard method used to identify the crystalline phases in a solid material and used for more advanced analysis such as accurate determination of lattice parameters, determination of crystallite size and internal elastic strains [106]. Identification of the crystalline phases in a material is possible because of the light matter interaction between the X-rays and the atoms in a material. In fact, X-rays are used because their wave length is comparable to the interatomic distance in solid materials and thereby provide high enough resolution.. During an

XRD measurement an incident X-ray beam is scanned across the surface of the material while varying the angle with respect to material surface. A part of the incident beam is elastically scattered by the periodic planes in a crystalline material and this scattered signal can be detected. Bragg's law provides the most intuitive understanding of the principle of XRD. If the relation between the incident X-ray wavelength (λ), distance between the successive lattice planes (d) and angle between the incoming x-ray and the lattice plane (θ) meets the criteria set by Bragg's law, constructive interference of the diffracted beams from multiple planes will enhance the signal. Bragg's law states the following relation [106]:

$$n\lambda = 2d\sin\theta \tag{3.1}$$

where n is any integer. If Bragg's law is not met, destructive interference will occur and no enhancement of the diffracted signal occurs. The peaks, positioned along the 2Θ axis, in a crystalline material's XRD pattern informs about the spacing between adjacent planes (d) in the crystal and the relative intensity among the peaks inform about the scattering power of the atoms in the crystal lattice. There is hence no concrete information about the phase(s), which is why a database with known phases are used to determine the possible phase(s) present in a material. In polycrystalline materials, e.g. powder, it is convenient that there are sufficiently many differently oriented crystal planes in the sample which will satisfy Bragg's law. It is usually an implicit assumption that the crystallites are randomly oriented though this is not always valid.

The XRD measurements carried out in this project have been used to make a phase analysis of the materials. Powder samples were prepared by pressing the powder bed flat and horizontal. Solid polycrystalline samples were attached to the sample with a plastic solid and levelled. Measurements were done on powder samples or on polycrystaline surfaces using Bruker Advance D8 (Bruker, USA) operated with a Cu Kα source (8.04 keV). They were performed at RT with 2θ=20-80 ° and a step size of 0.008 °. Samples were rotated during measurements. The software DIFFRAC.EVA ver.4.0 (Bruker, USA) was used to substract the background signal from the measurements and to identify phases. The obtained XRD patterns are matched with PDF-2 2003 (sets 1-53 + 65 + 70-89) database. All th XRD patterns used are listed in Table 3.1. The pattern no. used for LN and L97N was PDF 33-0711 and for LNF and L97NF was PDF 88-0637. Both LN and LNF XRD patterns are in the rhombohedral perovskite structure. The L2NF pattern was not listed in the database so here the matching was based on the XRD pattern produced in [107]. This is the orthohombic structure.

3.1.3 Specific surface area measurements

The specific surface area of a given ceramic powder is the surface area per unit mass of powder. In all reactions involving (electro)catalytic reactions the surface area should be maximised because this will provide more available sites for the catalysis. It is, however, crucial that the surface area is accessible for the reactions. The specific surface area is also an important parameter when using traditional slurry based processing methods. It is used to determine the amount of dispersant to be added.

Chemical structure	Database no.	Unit cell	Space group	no.
$LaNiO_3$	PDF 33-0711	Rhombohedral	$R\bar{3}m$	166
$LaNi_{0.6}Fe_{0.4}O_3$	PDF-88-0637	Rhombohedral	$R\bar{3}c$	167
$La_2Ni_{0.9}Fe_{0.1}O_4$	-	Orthohombic	Fmmm	69
La_2NiO_4	PDF-50-0243	Orthohombic	Pban	50
$La_3Ni_2O_7$	PDF 50-0244	Orthohombic	-	-
$La_4Ni_3O_{10}$	PDF 86-1668	Orthohombic	-	-
$La(OH)_3$	PDF 36-1481	Hexagonal	P63/m	176
NiO	PDF-44-1159	Rhombohedral	$R\bar{3}m$	166
$Ni(OH)_2$	PDF 73-1520	Hexagonal	$P\bar{3}m1$	164
Fe_2O_3	PDF 39-0238	Cubic	Ia-$\bar{3}$	206

Table 3.1: Overview of the indexed phases and relevant information about these.

A common method used to measure the specific surface area is gas adsorption on the surface. The basic idea is to determine the relationship between the amount of gas adsorbed in a sample and the applied pressure in the chamber. The physical adsorption of inert gas molecules on a surface is dependent on the applied pressure. The theory, commonly employed, is developed by Brunauer, Emmett and Teller and referred to as the BET theory [108]. The theory takes multi-layer absorption into account and results in the following equation:

$$\frac{1}{V((P_0/P)-1)} = \frac{1}{V_{\mathrm{m}}\chi} + \frac{\chi-1}{V_{\mathrm{m}}\chi}\frac{P}{P_0} = \beta + \alpha\frac{P}{P_0} \tag{3.2}$$

where V is the absorbed volume of gas, P is the applied pressure, P_0 is the saturation vapour pressure, V_m is the amount of gas absorbed in a monolayer and χ is a constant depending on the surface interaction energy. For many inorganic materials the absorption isotherms obtained correspond to the type II and IV standardized isotherms and are fitted well to the BET-equation in the relative pressure inverval, $\approx 0.05 < P/P_0 < 0.3$ [109]. Applying the relationship in 3.2 to appropriate experimental measurements and plotting the left-hand-side as a function of P/P_0 should therefore yield a straight line. The intercept (β) and slope (α) is used to determine the monolayer coverage:

$$V_{\mathrm{m}} = \frac{1}{\beta+\alpha} \tag{3.3}$$

The volume of monolayer coverage of a specific gas makes it possible to calculate the specific surface area per unit mass (S_{BET}):

$$S_{\mathrm{BET}} = \frac{N_{\mathrm{A}}A_{\mathrm{cs}}V_{\mathrm{m}}}{V_0 m} \tag{3.4}$$

where N_{A} is Avogadro's number, A_{cs} is the cross-sectional area of the adsorbate gas molecules ($0.162\,\mathrm{nm}^2$ for N_2), V_0 is the volume of 1 mole of adsorbate gas at standard temperature and pressure and m is the sample mass.

In this work, BET measurements of the SSA were carried out with a Autosorb 1-MP (Quantachrome Instruments, USA). The samples were degassed for 3 h prior to measurements at 300 ℃. The BET measurements took place at 77.3 K in N_2 in the relative pressure interval $0.05 < P/P_0 < 0.31$. The correlation linear coefficient for the straight line fit was > 0.9995 for all samples.

3.1.4 Density measurements

Density measurements of solids are classed into three types: the true density, the apparent density and the theoretical density. The true density is the density of material in itself. The apparent density is the density of the material including pores and the theoretical density is the density of specific material determined from, e.g., its crystal structure. The density of the ceramic powders can be measured accurately with gas pyncnometry, a method based on Boyle-Mariotte's law of volume pressure relationships [110]. A simple gas pyncnometer consists of two chambers, a sample and a reference chamber. The sealed sample chamber is first pressurized with an inert gas that can easily enter all pores (read small molecule size) to a target pressure with the sample residing in the chamber. Next, the gas is allowed to expand into the reference chamber and the pressure drop ratio between the two chambers is recorded. This pressure drop ratio can be compared to a known standard and the resulting volume of the sample can be determined. The density is now straighforward to measure as the mass of the sample divided with its volume. The true volume of the powder was measured with a AccuPyc 1330 gas pyncnometer (Micromeritics, USA) using He gas. The mass of the sample was measured with a scale with 4 significant digits (e.g. 9.5649 g). The powders were not degassed prior to the measurements.

3.1.5 Thermal analysis

Thermal analysis includes a range of methods used to investigate the physical and chemical response of a material to heating under predefined conditions such as heating rate, atmosphere and flow rate of gases. The results that come out of a thermal analysis is dependent on several factors. The design of the instrument, e.g., placement of heating zones and thermocouples can influence the results. The sample's ability to attain equilibrium with the surroundings is also important and influenced by factors such as the heating rate, the atmosphere and the gas flow. An increase in heating rate, e.g., means the sample has less time to reach equilibrium during the measurements. In the following, the techniques dilatometry and thermal gravimetric analysis (TGA) will be briefly described

Dilatometry measurements

Dilatometry can be used to determine various properties and mechanisms of materials. For ceramic materials dilatromety is commonly used to determine the thermal expansion coefficient, investigate the sintering process/kinetics and determine various physical characteristics. A common type of dilatometer is the push-rod dilatometer where a push-rod is maintained in contact with the sample [111]. A linear variable differential transducer (LVDT) is often used to monitor the linear displacement of the push rod as a function

of temperature. Materials expand with increasing temperature and for packed ceramic powders this expansion is eventually superseded by densification or shrinkage due to the sintering process which is activated at a certain temperature and eventually, at a higher temperature, reaches a maximum densification rate. Since the pushrod is also heated and therefore is subject to thermal expansion, a base line is required to subtract the expansion/shrinkage caused by the push-rod.

The sintering behaviour of the LaNi(Fe) based powders from Praxair technologies was investigated using a DIL 402 C push rod dilatometer (Netzsch, Germany).Cylindrical pellets were fabricated by uniaxially pressing the powders to loose pellets followed by isostatic pressing at 28 MPa for 30 s. A binder solution of polyvinylpyrrolidone (PVP) in ethanol was mixed with the powder if required to hold the powder together. The pellets were heated in air from RT-400 with a heating rate of $1\,\mathrm{K\,min^{-1}}$ followed by a 2 h dwell time to remove any PVP binder. Next, they were heated to 1400 ℃ with a $5\,\mathrm{K\,min^{-1}}$ heating rate and a dwell time of 5 h before cooling with $5\,\mathrm{K\,min^{-1}}$ to RT. The measurements were mainly used to compare the sintering behaviour and estimate the required sintering behaviour of the materials.

Thermoal Gravimetric Analysis

TGA is used to measure the weight loss or gain of a material as a function of temperature or time using a thermobalance. A modern TGA instrument can detect mass changes in the sub- μg range and can hence be used to determine properties associated with only minor weight losses such as decomposition and oxidation behaviour [112]. For ceramic materials where TGA temperatures typically exceed 1000 ℃ the most commonly used crucible materials are aluminia-based though Pt/Rh can also be used. At higher temperatures, especially alumina crucibles might react with the sample which needs to be considered beforehand. During a TGA performed on a ceramic material an initial weight loss is typically experienced due to the loss of water vapour. At higher temperatures the material might start to decompose. If the atmosphere is cycled between reducing and oxidizing it is also possible to detect changes in e.g. oxygen stoichimetry for some materials due to the formation or elimination of oxygen vacancies.

In this work the TGA measurements were performed on LN and L97N powders to asses their thermal stability in air and O_2 respectively which was relevant for the subsequent sintering of the pellets used for electrochemistry. The measurements were performed using a STA 409 C/CD (Netzsch, Germany) which allows for simultaneous TGA-differential thermal analysis(DTA) measurements. The DTA signal was not helpful though and has therefore not be described. Around 50 mg of sample was heated in an alumina crucible in air and O_2 to 1100 and 1250 ℃ respectively. The heating rate was $10\,\mathrm{℃\,min^{-1}}$ from room temperature(RT) to 700 and 850 ℃ respectively followed by 5 $\mathrm{℃\,min^{-1}}$ from 750 to 1100 ℃ and 850 to 1250 ℃ respectively. The flow rate of the gas was $50\,\mathrm{ml\,min^{-1}}$ during the experiment. TGA measurements were also performed on rice starch to asses its decomposition behaviour. It was heated from RT to 500 ℃ with $1\,\mathrm{℃\,min^{-1}}$ heating rate and $30\,\mathrm{ml\,min^{-1}}$ air flow.

Figure 3.1: The PTFE line autoclave used for the chemical stability of the ceramic oxide powders and porously sintered pellets

3.1.6 Particle size and morphology

The particle size and morphology was investigated with scanning electron microscopy (SEM) (see section 3.5.1 for a description of SEM). A very small amount of powder was sprinkled on a SEM stub covered with carbon tape. All excess powder not sticking to the surface of the tape was remove with a pressurized N_2 gun. Micrographs were recorded with a Merlin field emission scanning electron microscope (FE-SEM) (Zeiss, Germany) which is equipped with a Schottky field emitter gun. The particles were investigated with the InLens detector using an acceleration voltage of 10 kV.

3.1.7 Chemical stability of ceramic powders at high temperatures in concentrated KOH

The chemical stability of the materials was assessed by exposing the as-received powders to 30/31/45 wt% KOH inside a PTFE lined autoclave which is seen in figure 3.1. The PTFE liner was cleaned in nitric and hydrochloric acid between measurements. The autoclave was left at room temperature or heated in a furnace at 100/220 ℃ for a week. No external pressure was applied to the autoclave, so the internal build-up pressure at 220 ℃ was approx. 15 bar, corresponding to the vapour pressure of the KOH solution. Afterwards the KOH solution was extracted and the residual powder was rinsed in milipore water until a neutral pH of the water was reached. The rinsed powder was dried in a furnace, heating with 1 ℃ h^{-1} to 500 ℃ and back to room temperature prior to phase analysis by XRD (cf. subsection 3.1.2). Similar chemical stability measurements, as just described, were conducted with powder pressed into pellets and sintered at 1100 ℃ for 1 h.

3.2 Characterization of LNF suspensions

Among the different La,Ni,Fe-based materials investigated for the OER, LNF was chosen for the fabrication of electrodes. The LNF suspensions were characterized in terms of particle size and rheological behaviour as a means to quality check and document the processing work of LNF inks used for screen printing. Aqueous LNF suspensions were also characterized more rigorously using dynamic light scattering to determine particle sizes, electrophoresis to determine the ζ-potential, multiple light scattering to determine the sedimentation behaviour and rheology to determine the rheological behaviour. All with the aim of gaining a better fundamental understanding of LNF stabilized in aqueous suspensions.

3.2.1 Particle size distribution measurements

Particle size measurements of a suspension is a way to check the particle sizes of powders or suspensions. It can be used to check to which degree the particles in a suspension are being de-agglomerated and dispersed effectively by the dispersant. It is also a common quality check used during the processing of inks. A common way of determining the PSD is using light scattering techniques. There are three regimes, in terms of the general theory usually employed depending on the particle size (x) relative to the wave length of the light(λ) [99].

1.	$x << \lambda$	Rayleigh scattering theory
2.	$x \approx \lambda$	Mie scattering
3.	$x >> \lambda$	Fraunhofer diffraction theory

The particle sizes of the ceramic oxide particles in the inks used in this project are on the order of 0.1 µm to several µm so it is the Mie theory which is typically employed. Mie scattering provides mathematical solutions to Maxwell's equations, is valid for homogeneous spheres and takes all light-matter interactions into account. It is therefore also applicable to larger particles but some simplifying assmptions can be made for larger particles making Fraunhofer diffraction theory more appropiate. When using Mie theory the real and imaginary index of refraction of the particles must be known along with the refractive index of the solvent in which the measurement is carried out. The particles size measurements were carried out with two pieces of equipment: one, a Beckmann Coulter LS13 320 (Beckman Coulter, USA) laser diffraction particle size analyser which utilizes mainly the Fraunhofer and Mie theory and two, a Zetasizer Nano ZS (Malvern Panalytical, UK) dynamic light scattering particle size analyser. The laser diffraction particle size analysis has monochromatic laser source (λ=780 nm) and a series of detectors are used to detect, mainly the forward scattered light. The signal provides a volume based particle size distribution. Beckmann Coulter has adopted a polarization intensity differential scattering (PIDS ™) method as an extension to the Mie theory which basically intensifies the signal of sub-μm particles and they claim to be able to measure particle sizes down to 17 nm. In our case this is not relevant but in it does justify measuring particle sizes on the order of 100 nm.

The dynamic light scattering method is, as implied by the name, a dynamic method which measures the backscattered light from nanoparticles, which are subject to Brownian motion [113]. Brownian motion is the random movement of particle in a liquid due to the collision with fast moving molecules from the liquid. The size and speed of nanoparticles subjected to Brownian motion is related through the Stokes-Einstein relations. In dynamic light scattering a correlation function describes the evolution of the backscattered intensity with time as function of particle size, and this gives rise to an intensity based particle size distribution which can be converted to a volume based particle size distribution. The Zetasizer is not well suited for the measurement of particle sizes of several microns due to the technology employed - especially for ceramic oxides which have a high density (LNF density $\approx 7\,\mathrm{g\,cm^{-3}}$) and sediment fast, it can be problematic.

The refractive indices of LNF is not known so some rough guidelines for blackish powders have been used. The refractive indices were also varied to check the sensitivity of these in relation to the measured particle sizes. The sensitivity was small and did not influence the results significantly. All particle size measurements of LNF inks for screen printing are performed with the laser diffraction particle size analyser. The measurements, for organic solvent based inks, are performed in ethanol (EtOH) which is miscible with the glycol ether used as solvent. The measurements are performed in water for the water based inks. The procedure is as follows: a 3 mL plastic container is filled with approx 2 mL solvent. Next, 1-6 drops of ink is added depending on the concentration. This mixture is shaken during the initialization of the standard operation procedure which the equipment performs prior to the measurement. When the equipment is ready a 3 mL disposable pipette is used to suck up all the ink and release it into the chamber a couple of times before adding it drop-wise to the chamber for analysis. The loading used was 45-55 % on the PIDS scale. Through experience we have found that the preparation steps are important for the measured particle size distribution. The particle size measurements of aqueous LNF suspensions were performed with the zeta sizer and later checked for reproducibility with the Beckman Coulter. The measurements were performed in water using disposable polystyrene cuvettes. Samples were prepared by adding LNF suspension drop-wise to a glass bottle with ≈ 250 ml millipore water until suspension turned turbid ($\approx 10^{-4}\,vol.\%$). The suspension was shaken, ultrasonicted and the appropiate amount of sample added to the cuvette. Samples were in some cases left to stand for approx. 5-10 min to allow larger agglomerates to sediment. Three sets of measurements were performed for each sample and the average used.

3.2.2 Zeta potential measurements

The zeta potential is, as explained in section 2.7.1, a measure of the potential at the slipping plane in the electrical double layer surrounding particles in electrolytes. One way to determine the zeta potential is by means of electrokinetic methods, specifically the electrophoretic mobility of charged particles is related to the zeta potential. The electrophoretic mobility can be determined by applying an electric field across the electrolyte which will cause the charged particles to move towards the oppositely charged electrode. Viscous forces will oppose this movement and when the net force acting on the particle

is zero, it moves at constant speed and the electrophoretic mobility can be determined. Laser dopler velocimetry is one way of determining the electrophoretic mobility of the moving particles. The Henry equation relates the zeta potential to the electrophoretic mobility of a particle [114].

The zeta potential measurements were carried out on aqueous LNF suspensions. Samples were collected from the supernatant of suspensions which have been pH adjusted and ball milled before centrifugation. A folded capillary cell was used as sample container. Three sets of measurements were performed for each sample and the average used.

3.2.3 Rheology

Rheology is the science of deformation and flow of matter. Rheological experiments can be used to identify the flow behaviour of liquids as well as the deformation behaviour of solids. When dealing with slurries for ceramic processing, they often possess a combination of the ideal viscous behaviour of a liquid and the ideal elastic behaviour of a solid which is termed viscoelastic behaviour.

The shear viscosity (from now on referred to as viscosity) is usually the main parameter of interest when dealing with ceramic slurries. It represents the fluid's resistance to flow. In order to define viscosity two terms need to be defined first, which are the shear stress and the shear rate. The two-plates model provides an illustrative exemplification of this in figure 3.2 [115]. An upper plate with shear area A is set in motion by a shear force F. The lower plate remains stationary. In between the two plates is the sample, which is affected by the relative motion of the plates. Now assuming the plates are sufficiently large to neglect what happens at the edges, zero slip conditions at the two plates and laminar flow conditions, the velocity of the sample at the bottom plate will be zero and at the top plate the velocity of the sample is equal to the moving plate's velocity (v). The shear stress (τ) and shear rate ($\dot{\gamma}$) are now defined as:

$$\tau = \frac{F}{A} \tag{3.5}$$

$$\dot{\gamma} = \frac{\delta v}{\delta y} = \frac{v}{h} \tag{3.6}$$

Under shear stress the viscosity (η) is related to the shear rate through the relation:

$$\tau = \eta \dot{\gamma} \tag{3.7}$$

Since the shear stress has the unit of Pa and the shear rate is in s^{-1} the viscosity is given as Pa s with an order of magnitude for ceramic slurries being approx. 0.01-10 Pa s. If η is independent of shear rate, the flow is said to be Newtonian. Most liquids are Newtonian but colloidal suspensions are generally not Newtonian. A typical ceramic ink exhibit shear-thinning behaviour. Shear-thinning means that a sample exhibit decreasing viscosity with increasing shear rate. Since viscosity is now a function of the shear rate the term apparent viscosity is used to emphasize this dependence. This is illustrated in

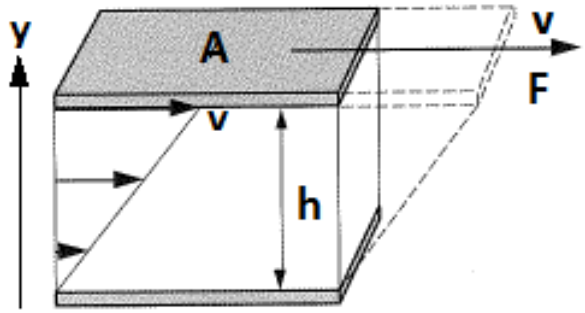

Figure 3.2: A schematic of the two-plates-model used to define the shear stress and the shear rate. The bottom plate remains stationary while the upper plate moves towards the right, which creates a shear stress in the sample between the plates. From [115]

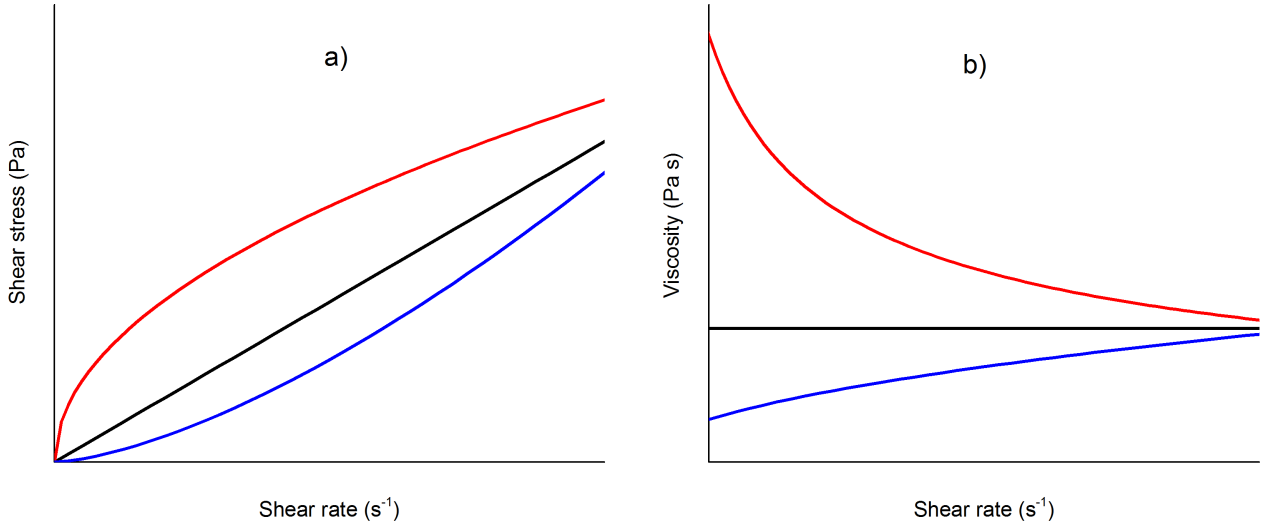

Figure 3.3: **(a)** Examples of flow curves of newtonian flow behaviour (black), shear-thinning flow behaviour (red) and shear-thickening flow behaviour (blue). In **(b)** the same colors represent the viscosity functions.

fig. 3.3. Thixotropic behaviour is the decrease in viscosity over time under a constant shear rate. When the shearing is stopped it takes a finite amount of time for the slurry to return to the equilibrium state.

Rheometry

Rheometry is the measuring technology that can be used to determine rheological properties of a sample. Rotational tests can be used to determine the flow behaviour of liquid solutions and dispersions. A rotational test is performed by rotating either the top part or the bottom part of the measurement system (MS) while keeping the other part at rest (see figure 3.4 for examples of MSs). The test mode can be either controlled shear rate (CSR) or controlled shear stress (CSS). In CSR the rotational speed is controlled and the

torque is determined by the instrument; in CSS it is vice versa. From the measured raw data the shear rate and shear stress can be determined according to eq. 3.5 and eq. 3.6 and the viscosity calculated.

Three typical MSs are the concentric cup and cylinder (CC) MS, the cone-and-plate (CP) MS and the Parallel plate (PP) MS. The MS's are shown in fig 3.4 [116]. The CC MS is ideally suited for low viscosity samples as it has a higher sensitivity compared to the CP and PP MS but turbulence can occur at high shear rates. It also requires a relatively large amount of sample. The PP MS has the advantage over the CP MS that the gab distance between the two plates can be adjusted and thereby the max particle size, which should be approx. 10-times smaller than the gab distance, is not limited which is crucial when dealing with ceramic slurries [115]. The CP MS is scientifically more appropriate than the PP MS because the shear rate is independent of the distance from the rotation axis, which provides a more homogeneous flow and analytical solutions to the rheological properties.

Oscillating rheology tests are another type of test, where either the top or the bottom part of the MS is rotated back and forth. Oscillatory tests can be used to identify the loss modulus (G'') and the storage modulus (G'), which represent the energy lost or dissipated due to viscous flow and the energy stored due the elastic behaviour. Initially, an amplitude sweep test is performed to identify the linear viscoelastic (LVE) range, where G' and G'' are constant. This ensures the validity of Hooks law for the G', and that of a Newtonian fluid for the G'', which are basic assumptions in the test. Based on the LVE range a value of the shear stress within this range is identified and used for the subsequent frequency sweep oscillation (FSO) test. A FSO test is performed at constant shear stress and varying frequency and determines the G' and G'' as a function of frequency. The ratio of $\frac{G''}{G'}$ is called the damping factor and if $\frac{G''}{G'} < 1$ the response is mainly elastic and for $\frac{G''}{G'} > 1$ the response is mainly viscous.

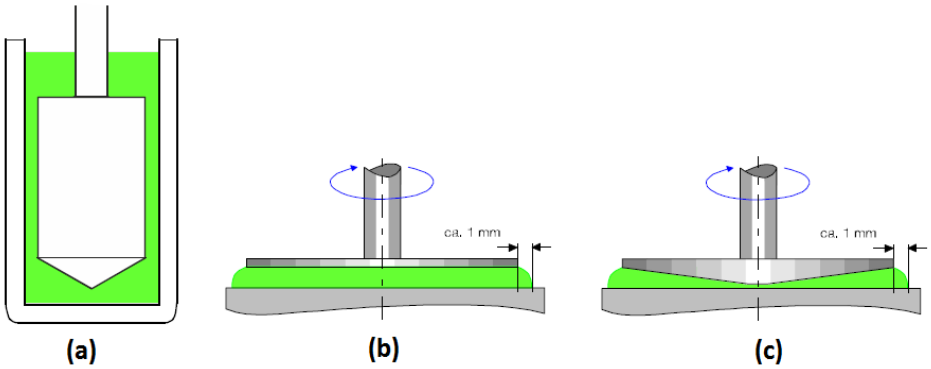

Figure 3.4: Some of the standard MS used for rheological measurements. The green part represents the sample. **(a)** is CC MS, **(b)** is the PP MS, **(c)** is CP MS and. From [116]

The rheological measurements included in this project were performed with rheometers from Anton Paar (Austria). The work, in section 4.3, performed for the characterization

on aqueous LNF suspensions was carried out with an Anton Paar MCR 301 rheometer using a CC MS system at 25 ℃. A calibration of the instrument was performed before each set of measurements. Three main steps were carried out for each sample: an amplitude sweep, a frequency sweep and flow curves. A 2 min. rotational pre-shear conditioning step (shear rate: $10\,s^{-1}$) was performed before each step. A pre-strain step was performed before the amplitude sweep and consisted of an initial 2 min. pre-strain (amplitude: 0.1 %, angular frequency: 10 rad s^{-1}) followed by the amplitude sweep (amplitude: $10^{-3} - 10$ %, angular frequency: 10 rad/s) to determine the linear viscoelastic (LVE) range. Next, another pre-strain was performed before performing the frequency sweep (angular frequency range: 0.1-500 rad/s). Flow curves were measured after the oscillatory measurements at shear rates from 0.1-100 s^{-1} immediately followed by 100-0.1 s^{-1}. The characterization of the inks for screen printing, see section 4.4, was carried out on an Anton Paar MCR 303 rheometer. The flow behaviour of the inks was measured with Ø 25 mm polished steel PP MS with a gap distance of 0.5 mm. Rotational measurements were performed in CSR mode with a set temperature of 21 ℃. The programme consists of some initial conditioning steps with three 120 s interval at 0.1, 0 and 0.1 s^{-1} respectively, followed by a 120 s interval at 1.0 s^{-1}, a 10 s interval at 100 s^{-1} and lastly a 544 s recovery interval at 1.0 s^{-1} to investigate their thixotropic behaviour.

3.2.4 Sedimentation measurements

Sedimentation in a solution can be monitored by means of light scattering techniques which analyses the backscattered or transmitted light from/through the sample along the sample height. The backscattered (BS) intensity depends on the photon transport mean free path which can be interpreted as the penetration depth of photons into the solution [117]. The higher the penetration depth of the photons, the lower the BS intensity will be. In a system containing particles where sedimentation is observed the backscattering rate will decrease over time, starting from the top of the sample due to an increase in transmission or decrease in absorption in this area. Likewise the BS intensity in the bottom will increase due to formation of a sediment layer. Sedimentation behaviour can in this way be detected. Similarly, phenomena such as flocculation and creaming can be detected. Flocculation means that larger agglomerates are formed and hence the average particle size increases. This influences the photon mean free path and hence the BS intensity which will shift uniformly along the height of sample because it is a phenomenon occurring everywhere.

Sedimentation studies were performed in a Turbiscan lab (Formulaction, France) using the Turbiscan software version 2.2.0.82. The Turbiscan monitors the sedimentation behaviour using light scattering technology. A pulsed 880 nm light signal is generated and two detectors, one for backscattered light positioned at 45 ° with respect to the laser and one for transmitted light positioned at 180 °, are used to detect the light intensity for every 40 µm along the glass vial height. The backscattered detector allows the sedimentation behaviour of opaque samples to be measured which implies that more concentrated suspensions can used compared to manual sedimentation measurements. Samples were loaded to approx. 40 mm height in Ø 27 mm glass vials. Data was recorded at 25 °C

every 1 hour for the first 24 h to get an estimation of the sedimentation speed and after this, measurements were recorded every 1-7 days.

3.3 Processing and preparation of samples

3.3.1 Preparation of polished electrodes for electrochemical measurements

The samples used for the electrochemical activity measurements were pressed and sintered bars of as-received powder. Bars were pressed using the same procedure as in 3.1.5 subsequently, they were sintered at 1400 ℃ for 24 h in air to achieve geometric densities $> 91\,\%$ and densities based on the Archimedes method $> 96\,\%$. The sintering profile is shown in table 3.2. The bars used for electrochemical testing were further cut, grinded and polished (Struers Tegrapol-32, Denmark) in successive steps to similar dimensions (17-18 mm x 5-6 mm x 0.9-1.5 mm). The final polishing was carried out with a 1 µm diamond dispersion (Nap B1 Diapro, Struers, Denmark) using a MD-Nap polishing pad (Struers, Denmark). An example of the polished bars used for testing can be seen in figure 3.5. The phase analysis of the sintered and polished samples was carried out using XRD. The root-mean-square roughness of the polished pellets was measured with a Cyberscan Vantage Profilometer (Cyber Technologies, Germany). The root mean square roughness is given as:

$$R_{RMS} = \sqrt{\frac{1}{n}\Sigma_i^n y_i^2}$$

where y_i is the vertical deviation of a point on the surface from the mean surface height and n is the number of points included in the calculation. The scanned area was min. $10\,\mathrm{mm}^2$ with a 10 µm step size, corresponding to min. 100,000 points. Any systematic sloping of the pellet surface was compensated for in the ScanCT 7.5 software accompanying the equipment.

From (℃)	To (℃)	Heating rate ($℃\,h^{-1}$)	holding time (h)
RT	400	60	0
400	1400	30	24
1400	1000	15	0
1000	RT	30	0

Table 3.2: The sintering profile used to sinter dense bars of the investigated materials.

3.3.2 Processing of LNF Suspensions

LNF is a ceramic oxide that can be synthesized into a powder. In order to form a solid, the powder has to be processed first. The processing describes here is wet processing where the powder is dispersed in a solvent using a dispersant. Depending on the deposition method, various additives can be added such as polymeric binders and plastisizers to

Figure 3.5: An example of polished L97NF bars used for electrochemical testing

mention a few. In this section the processing of two types of suspensions is described: the processing of aqueous LNF suspensions for dispersant study and non-aqueous inks with various additives for screen printing.

Processing of aqueous LNF suspension with rice starch as pore former

Aqueous LNF (Kceracell Co, Republic of Korea) slurries were processed with various dispersants to characterize the behaviour and sinter porous microstructures. LNF with a specific surface area of 12.6 m2/g was used. Initially, the dispersants were dissolved in Millipore water (resistivity 18.2 MΩ cm at 25 ℃) prior to adding the LNF powder. Three dispersants were used: polyvinylpyrrolidone k15 (PVP, Fluka Chemie, Germany) with molecular weight 10,000 g mol^{-1}, poly(acrylic acid) (PAA Polysciences Europe GmbH, Germany), 50 % solution in water with molecular weight 5,000 g mol^{-1} and poly(methacrylic acid) ammonium salt (PMAA, Polysciences Europe GmbH, Germany), 30 % solution in water with molecular weight 15,000 g mol^{-1}. Rice starch (Sigma Aldrich, Sweden) was added (vol.% with respect to LNF) when the LNF powder was well dispersed.

LNF suspensions for sedimentation analysis, particle size measurements and zeta potential measurements were 5 vol.% of solid loading. Ball milling was performed at 25-50 RPM for a minimum of 72 hours using 10 mm spherical 3 mol.% yttria stabilised zirconia (3YSZ) beads in a beads to LNF powder ratio of 16:1. The pH of the suspensions was measured with a Seven ExcellenceTM (Mettler Toledo, Switzerland) pH meter while continuously stirring the suspensions. The pH was adjusted with 1 M NaOH.

The suspensions used for the rheological characterization, deposition and sintering contained 19/10 vol.% LNF. Ball milling was carried out with a 5:1 ratio 10 mm cylindrical

3YSZ beads to LNF powder for a minimum of 24 hours before the addition of rice starch. The suspensions with added rice starch were ball milled for another 24 hours. An overview of all aqueous LNF suspension prepared can be found in table 3.3.

The suspensions were applied with a brush on sintered 8 mol % YSZ substrates. The green layers were dried in a closed water bath for 30 min at 80°C before sintering at 1100 °C for 1 hour with a 60 °C/h heating and cooling rate. An example of some sintered samples can be seen in figure 3.6.

Figure 3.6: Sintered LNF electrodes on 3YSZ substrates

Solid loading LNF (vol %)	Dispersant	Dispersant loading ($mg\,cm^{-2}$)	Amount of rice starch (vol %)
5	None	n/a	None
5	PVP	0.25, 0.79, 2.5 and 8.0	None
5	PAA	0.25, 0.5, 0.75 and 1.0	None
5	PMAA	0.25, 0.5, 0.75 and 1.0	None
19	None	n/a	0, 25
19	PVP	5.0	0, 25, 35, 50
10	PMAA	0.5	0, 25, 50

Table 3.3: Overview of the composition of aqueous LNF suspensions prepared

Preparation of screen printing inks

Ceramic powder processing in a non-aqueous solvent-borne system was used as means to process inks for screen printing. For the LNF suspensions, polyvinyl pyrolidone (PVP) k15 (Applichem, Germany) was first dissolved in the solvent (an alkyl poly oxy propylene ether) in a polyethylene bottle. The loading of PVP was $5.0\,mg\,m^{-2}$ relative to the LNF powder's specific surface area. Next, the LNF powder was added to the solution in 55 vol.% with respect to solvent. Spherical 3YSZ beads with Ø 15 mm were added in 4.2:1 ratio beads:LNF. The suspension was then ball milled in a 500 mL container in planetary mill (PM 400, Retsch, Germany) at 150 rounds per min. (RPM) for 30 min.,

after which the particle size distribution remained stable. An additional amount of solvent was added before adding 25 vol.% of the first pore former with respect to LNF powder. This was mixed for 15 min. at 15 RPM in the PM before adding 25 vol.% of the second pore former and mixing for another 15 min. The pore formers used were two grades of graphite: GK V-UF 1 and GK AF spezial (Graphit Kropfmühl, Germany) and two grades of Poly(methyl methacrylate) (PMMA): MX-180 and MX-500 (Esprix technologies, USA). The grinding media was then removed before adding PVP k90 (Sigma Aldrich, Denmark) to the solution. The PVP k90 was added in portions of 0.5 vol.% with respect to total volume. The suspension was now ball milled for 2 h at 150 RPM to fully dissolve the PVP k90. The finished suspensions contained 0.9-1.7 vol.% PVP k90. When the right viscosity was obtained a Grindsted® Soft-n-Safe plasticizer (Danisco - Dupont Group, Denmark) was added in a volume ratio 1-1.5:1 relative to the PVP k90 binder. Additional solvent was added if the suspension was too viscous and followed by 1-2 h ball milling at 150 RPM.

Quality checks of the inks were carried out during the processing. Besides visual inspections, these involved measurements of the particle size distribution before the pore formers were added, before the PVP 90 was added and on the finished screen printing inks. In addition a rheological characterization of the viscosity of the finished ink was carried out to determine any thixotropic behaviour. The procedure consisted of an conditioning phase followed by 2 min. at shear rate $1.0\,\mathrm{s}^{-1}$, 10 s at shear rate $100\,\mathrm{s}^{-1}$ and 9 min at shear rate $1.0\,\mathrm{s}^{-1}$ again.

Three different suspensions with combinations of pore formers were prepared. The first ink (LNF P3) contained GK V-UF 1 graphite ($d50 = 2.8\,\mu\mathrm{m}$, $d90 < 12\,\mu\mathrm{m}$) and MX-180 PMMA ($d50 = 1.8\,\mu\mathrm{m}$). The second ink (LNF P4) contained AF spezial graphite ($d50 = 6 - 8.5\,\mu\mathrm{m}$, $d90 < 25\,\mu\mathrm{m}$) and MX-500 PMMA ($d50 = 5.0\,\mu\mathrm{m}$) The third ink (LNF P5) contained GK V-UF 1 and GK AF spezial graphite.

Step #	Description	Amount / time	Comments
1	Add PVP k15 dissolved in the solvent	18.1 g	3.1 g PVP k15 + 15.0 g solvent
2	Add LNF powder	60 g	
3	Add milling beads (Ø 15 mm)	250 g (25 pcs)	
4	Mix in PM at 150 RPM	30 min.	
5	Measure particle size distribution (PSD)		
6	Add additional solvent	5.0 g	
7	Add pore former #1 (graphite)	4.85 g	
8	Mix in PM mill at 150 RPM	15 min.	
9	Add pore former #2 (PMMA)	2.55 g	
10	Mix in PM mill at 150 RPM	15 min.	
11	Measure PSD	d50; d90	Compare the PSD distribution to other
12	Remove Ø 15 mm beads	-	
11	Add Ø25 mm beads	3 pcs.	
12	Add PVP k90 binder in successive steps of 0.25 g	0.5 g	1-3 additions depending on pore formers etc.
13	Mix in PM mill after each addition of PVP k90	1 h	
14	(Add final amount of solvent if necessary)		1-2 g at a time
15	Mix in PM	30 min.	
16	Measure PSD of final ink	d50 = , d90 =	
		η = 130-220 Pa s at 0.1 s^{-1}	
17	Perform rheological characterization	η = 20-45 Pa s at 1.0 s^{-1}	Typical values
		η =3-5 Pa s at 100 s^{-1}	

Table 3.4: The procedure used for preparing screen printing inks.

From (℃)	To (℃)	Heating rate (℃ h^{-1})	holding time (h)
RT	600	15	4
600	1100-1125	102	1
1100-1125	600	102	0
600	RT	120	0

Table 3.5: The sintering protocol used for both the 3YSZ substrates and the LNF electrode layer.

3.3.3 Screen printing and sintering of LNF electrodes onto ytria stabilized zirconia substrates

Yttria stabilized zirconia substrates

The LNF inks described in the previous section were deposited onto porous sintered 3 mol.% ytrria stabilized zirconia (3YSZ) substrates. The 3YSZ substrates were made by tape casting sheets of 3YSZ with 1 mol.% nano-sized alumina (for a description of the processing of the 3YSZ substrates see the experimental part of section 4.4). The 3YSZ substrates were stamped out to circular pieces with a diameter of 32 mm, put through a lamination machine at 90 ℃ to flatten them and sintered at 1100 ℃ for 1 h. The detailed sintering program is shown in table 3.5. The sintered substrates had a diameter of ≈27.5 mm.

Screen printing of LNF inks

Screen printing is the process whereby an ink is squeezed through a woven mesh by means of a squeegee which is illustrated in figure 3.7. The squeegee is driven across the mesh with a fixed downward force. The mesh is elastic so the area where the squeegee is pressing will come in contact with the substrate. As the squeegee moves across the mesh, the area behind the squeegee will snap off leaving the ink behind. The mesh is covered with cured photoemulsion in areas where no print is desired which allows for complex geometries to be printed with sub mm resolution.

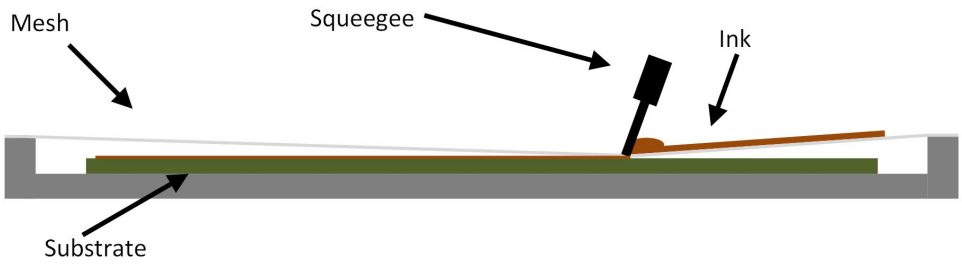

Figure 3.7: The principle of screen principle illustrating how thin layers can be printed onto flat substrates

The deposition of the LNF inks onto the sintered 3YSZ substrates was performed with a DEK 248 (DEK Printing Machines Ltd, England) screen printer. For the screen printing a polyester mesh with 92 mesh counts per inch and a mesh opening of 174 µm (Lasertech A/S, Denmark) was used. The tension was 25 N and the open area of the mesh ≈50 %. Rubber squeegees were used for the printing and each printed electrode consisted of a forward and a backward movement of the squeegee across the open area in the mesh. The printing speed was $5\,\mathrm{m\,s^{-1}}$ and the printing pressure 100 N. The contact height was set manually and the snap off distance adjusted to ≈0.8 mm with respect to the contact height. The printed layers were dried in a furnace at 90 ℃ for about 30 min. Sintering was performed at 1100-1125 ℃ for 1 h. The sintering protocol is listed in table 3.5.

3.4 Electrochemical measurements

The electrochemical measurements were carried out to asses the intrinsic electrochemical activity of flat and polished La,Ni and Fe based perovskites and to asses the electrochemical performance of porous LNF electrodes towards the oxygen evolution reaction. Hence only half-cells were tested.

The potentiostat and software

The electrochemical measurements were conducted in polytetrafluoroethylene (PTFE) set-ups using a Gamry Reference 3000 potentiostat (Gamry Instruments, USA). The Reference 3000 potentiostat allows for relatively high voltages and current (± 32 V at ± 1.5 A). In addition the frequency range for electrochemical impedance spectroscopy is 10 μHz -1 MHz. Gamry Framework software was used to set-up the programme for the electrochemical measurements and to conduct them. EIS data was fitted using the Gamry Echem Analyst software.

The reference electrode

A three electrode set-up was used in all cases with a Hydroflex® (Gaskatel, Germany) reversible hydrogen electrode (RHE). The Hydroflex, schematically shown in figure 3.8, has a replaceable H_2 cartridge inserted in the top of the electrode so it has an outflow of H_2 through a Pt/Pd electrode opening in the electrode sensing area. The electrode is in direct contact with the electrolyte and its potentials with respect to the standard hydrogen electrode (SHE) is therefore pH dependent. The pH dependent potential (E_0) with respect to the SHE can be expressed as:

$$E_0 = 0.000 - 0.059 \times \mathrm{pH\,V} \tag{3.8}$$

Since the electrode materials tested are exposed to the same pH conditions as the RHE, the overpotential (η) is equal to the measured potential (E_m) minus the standard oxygen evolution potential ($E^{\circ}_{O_2}$):

$$\eta = E_m - E^{\circ}_{O_2} = E_m - 1.229V \tag{3.9}$$

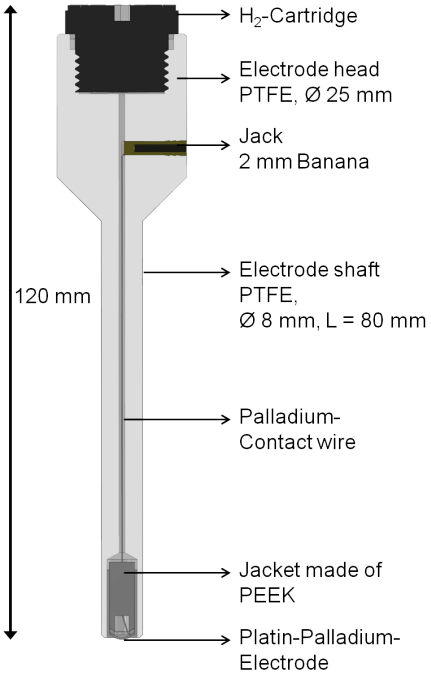

Figure 3.8: The Hydroflex® RHE used for all electrochemical measurements. From [118]

The parts of the Hydroflex which are in contact with the electrolyte are made of PTFE, Polyether ether ketone (PEEK) and Pt/Pd. Moreover, there are no issues with contamination of heavy metals such as Hg and no inner electrolyte. It can be used in concentrated alkaline solutions up to a temperature of 210 ℃.

The KOH electrolyte

The electrolyte was prepared from KOH pellets (> 85 %, ACS reagent) and Milipore water (18 MΩ · cm). The electrochemical characterisation performed in ca 1 M KOH solution. It is denoted ca because KOH is quite hygroscopic so there is an uncertainty about the actual amount of KOH in the pellets. The measured pH of an apparent 1 M KOH was 14.0. Besides KOH the pellets also contain ≤2.0 % K_2CO_3, ≤0.053 % cation and heavy metal traces, ≤0.013 % anion traces and ≤0.021 % other impurities. The concentrated electrolytes were prepared as wt.% due to the simpler calculation of the amount of KOH and water to be combined.

The Zirfon separator

In order to separate the compartment with the working electrode from the compartment with the counter electrode a 0.5 mm Zirfon Perl (Agfa, Belgium) separator was used. Zirfon consists of zirconia powder and a polysulfone matrix. It is stable in concentrated KOH up to 110 ℃.

3.4.1 Electrochemical Impedance Spectroscopy

Electrochemcial impedance spectroscopy (EIS) is a method employed to gain more knowledge about the processes influencing the electrochemical system under investigation. Compared to conventional electrochemical methods which are measured with a DC signal, EIS utilizes an alternating current (AC) signal. The fact that we are dealing with an AC signal also means that electrical phenomena that, e.g., are capacitative or inductive in nature can be revealed which is not the case for DC signals that only reveal resistive behaviour. Impedance is the general term used for all these AC electrical phenomena which are frequency (ω) dependent and somehow resist the flow of electrical current. A general assumption during impedance spectroscopy is that the applied AC signal response is small and hence can be treated as linear. This means that the region of an IV-curve where the EIS measurement is performed is in any practical sense linear. Now, since impedance (Z) is defined as the ratio between the excitation signal (E(ω, t) and the current response (I(ω,t)), this means that the current response is going to be a superposition of the exitation voltage [119]

$$Z(\omega) = \frac{E(\omega, t)}{I(\omega, t, \phi)} \tag{3.10}$$

where (ϕ) is the phase shift. Impedance is properly defined in complex notation and in this way it can be stated as:

$$Z(\omega) = \frac{E_0 \exp(j\omega t)}{I_0 \exp(j\omega t - j\phi)} = \frac{E_0}{I_0} \exp(j\phi) = Z_0 \exp(j\phi) = Z_0(\cos\phi + j \sin\phi) \tag{3.11}$$

This implies that impedance is a two dimensional quantity. It can be mapped in a complex plane plot containing a real part on the first axis and an imaginary part on of the second axis. The processes that can be uncovered using EIS are frequency dependent and an impedance measurement is therefore conducted within a range of frequencies, typically over 6 decades. Since several processes can be occuring at overlapping frequencies it is not trivial to uncover the different physical and chemical processes which might be limiting a system. The most common ways to visualize impedance data is in the Nyquist and Bode plots. In the Nyquist plot the first axis denotes the real part of the impedance and the second axis denotes the negative of the imaginary part of the impedance response. This representation does not show the frequency of the individual data points but the frequency always decrease in the direction of the first axis. It is possible to identify common properties such as the serial resistance (R_s) and the polarization resistance (R_p) in the Nyquist representation. The R_s is commonly referred to as the intersection between the impedance graph and the first axis in the high frequency part of the graph. The R_p is the R_s subtracted from the total resistance which is identified at the intersection between the impedance graph, in the low frequency part of the plot, and the first axis. The Bode plot depicts the absolute impedance and/or the phase shift vs the frequency and is therefore a good way to indicate the frequency at which different processes occur.

A common way to treat EIS data is to fit the graph to a model. A model is a combination of circuit elements connected in either series or parallel. Common elements include, resistors (R), capacitors (C), inductors (L) and constant phase elements (CPEs). The

CPE is essentially a circuit element exhibiting non-ideal behaviour and the actual physical interpretation is not straight forward.

The measurement protocol

The electrochemical protocol is described in table 3.6. The cyclic voltammetry (CV) measurements were performed for 5 cycles with a 2 mV step size and 50 $mV\,s^{-1}$ scan speed. The chronopotentiostatic (CP) measurements were performed at 0.5, 1, 2, 5, 10, 25, 50 $mAcm^{-2}$ (with respect to geometric surface area). After each CP measurement followed an amperostatic EIS measurement to determine the ohmic contribution (R_s). This was performed in the range 0.1Hz - 1.0 MHz with a AC amplitude of approx. $^1/_{100}$ of the DC signal and 11 points/decade. Similar settings were used for the potentiostatic EIS. All CP measurements are corrected for the serial resistance ($i \cdot R_s$) contribution.
The protocol was altered a bit for the electrochemcical performance measurements described in section 3.4.3 to avoid errors during measurements. In particular the potentiostatic EIS at open cirucit potential (OCP) was omitted and the high frequency limit of the amperostatic EIS measurements was decreased to 0.05 MHz to remove inductive behaviour. Amperostatic EIS measurements were also performed at 100 and 200 $mAcm^{-2}$

Step	**Intrinsic OER activity**	**Electrode OER performance**
OCP	15 min	5 min
Potentiostatic EIS at OCP	Yes	-
Cyclic voltammetry	1.0-1.8 V vs. RHE	1.0-2.0 V vs. RHE
CP + amperostatic EIS	30 min per CP at 0.5, 1, 2, 5, 10, 25, 50 $mAcm^{-2}$	20 min per CP at 0.5,1, 2, 5 10, 25, 50, 100, 200 $mAcm^{-2}$
Cyclic voltammetry	1.0-1.8 V vs. RHE	1.0-2.0 V vs. RHE
Potentiostatic EIS at OCP	Yes	-
Open circuit potential	15 min	5 min

Table 3.6: Electrochemical testing protocol for the intrinsic OER activity measurements and LNF OER performance measurements.

3.4.2 Intrinsic electrochemical activity measurements

All measurements took place in a PTFE holder (see figure 3.9). The electrochemical characterisation was performed in ca 1 M KOH. The polished bars were used as working electrode with an Au current collector pressed against its backside. A Pt mesh with a Pt wire attached to it was used as the counter electrode and a RHE as the reference electrode. A Zirfon separator was used to separate the working electrode from the reference and counter electrode. The three electrode set-up was placed in a somewhat closed container with a N_2 flow into the container. The current densities were normalised according to the exposed geometrical surface area of the bar being tested.

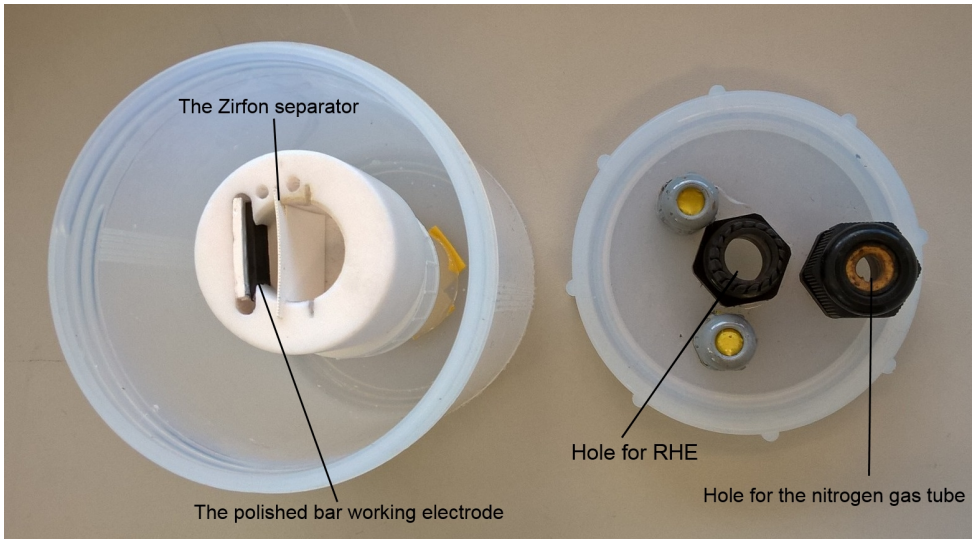

Figure 3.9: The set-up used for the intrinsic OER activity measurements with a bar and zirfon separator. The sample (blackish) is pressed against the opening with thick zirfon membrane. The Au current collector is not shown and neither is the counter electrode. The measurements took place in the container shown. The reference electrode was inserted through the middle hole and the tube with nitrogen gas through the other hole.

3.4.3 Electrochemical performance of porous LNF electrodes

The electrochemical performance of porous LNF electrodes was investigated at RT and 65 ℃ in 1 M and 35 wt.% KOH respectively. The measurements were carried out using an all PTFE FlexCell (Gaskatel, Germany) set-up which can be seen in figure 3.10a. The sealings were silicone and the O-rings were ethylene propylene diene M-class rubber (EPDM rubber). The working electrode was Ø 20 mm and positioned symmetrically across from the counter electrode (Ø 20 mm spiral Ni wire), such that the field lines between working and counter electrode were horizontal and parallel. A Haber-Luggin capillary was used to established electrolytic contact between the RHE and working electrode. A Zirfon separator was used to separate the working electrode from the counter electrode. The sample was tested in either an infiltrated configuration with the electrode facing away from the electrolyte compartment or in the flooded electrode configuration with the electrode facing the electrolyte. A Ni plate with a hole was pressed against the working electrode and used as current collector. This is illustrated in figure 3.10b. PTFE scews were used to tighten the whole Flexcell set-up around the working electrode and thereby also to ensure proper electrical contact to the current collector.

3.5 Characterization of microstructures

The microstructures were characterized using various methods. For the electrodes SEM imaging was used to quantify porosity and pore size distribution. A similar quantification of the 3YSZ backbones was conducted using Hg-intrusion porosimetry. Even though Hg-intrusion porosimetry gave an impression of the electrode microstructure, it was not used quantitatively due to the much higher fraction of 3YSZ substrate compared to LNF

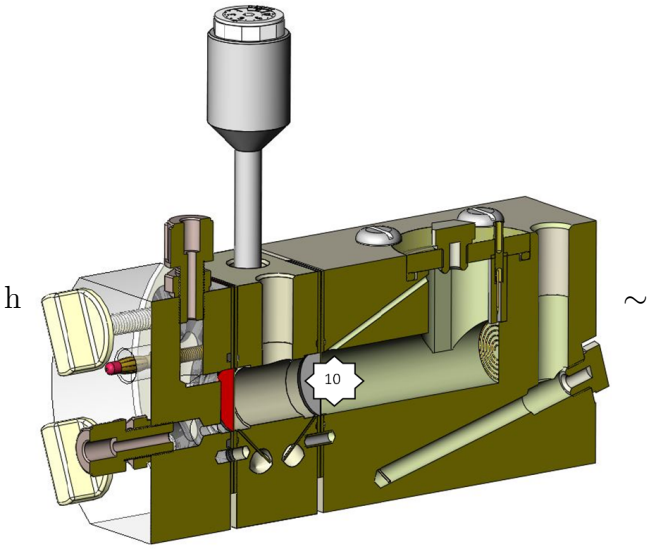

(a)

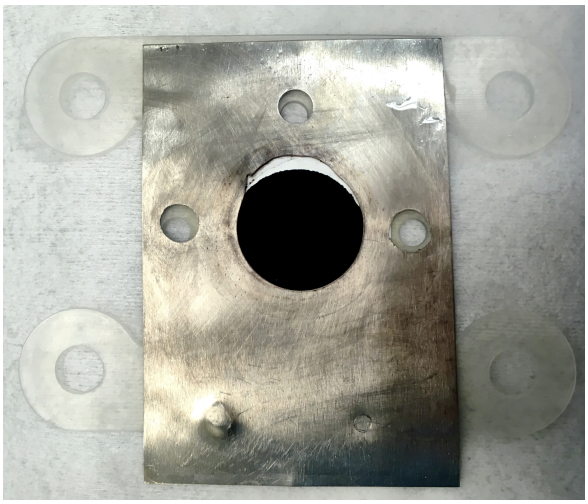

(b)

Figure 3.10: **a)** The Flexcell set-up used for the electrochemcial characterization of porous LNF electrodes. **b)** The assembly of the current collector and electrode with the silicone sealings. The upper part was kept free of electrode in order not to disturb the RHE signal. From [120]

electrode fraction.

3.5.1 Scanning electron microscopy

Scanning electron microscopy (SEM) is a microscopy technique that allows for significantly higher resolution compared to conventional light microscopy due to the much smaller wavelength of electrons compared to visible light [121]. Instead of light a focused beam of electron is scanned across the sample surface in a raster pattern. The electrons are accelerated to high voltages (≈1-30 kV) which means they will penetrate into the material under investigation and interact with the atoms in sample. The interaction volume between incoming electrons and the sample is shaped as a tear drop and will vary in size depending on the acceleration voltage. In the interaction volume various signals are produced which can be detected and provide information about tomography of the surface and the sample composition. Since the position of the electron beam is controlled with nm precision it is possible to convert the signals electronically into accurate data, which can be visualized as an image.

The most common signal that is detected are secondary electrons, which are electrons produced due to inelastic scattering between the incoming electrons and mainly k-shell electrons from the atoms in the material under investigation. These are numerous but have a relatively small energy and are therefore emitted from the top layer of the sample. Secondary electrons mainly provide information about the sample topography. The other main type of electrons detected are backscattered electrons which, as the name implies, are incoming electrons being scattered back out of the sample again due to the elastic interaction with the atoms in the sample. These are more directional and possess a higher energy, thus they are emitted from a larger volume of the interaction volume. Since heavy atoms scatter more forcefully than light atoms, the backscattered electrons from heavy elements appear brighter than the corresponding electrons from light elements. Backscattered electrons are therefore useful for providing visual information about the chemical composition of the sample and to distinguish different grain orientations.

The last important signal is characteristic X-rays that typically are produced when an incoming electron scatters inelastically with an inner shell electron of an atom. An electron from a higher energy outer shell can now jump to the inner shell; its loss in energy gives rise to a characteristic X-ray which is specific to the type of atom. The characteristic X-rays provide quantitative information about the atomic elements in the sample and their position. The X-rays are detected with an energy dispersive X-ray spectroscopy (EDX) detector. EDX is not a very accurate method for small features which means volumes smaller than the interaction volume. The interaction depth of the EDX signal is typically $> 1\,\mu$m at 15 kV. In materials with many elements several characteristic X-ray signals will often be overlapping and have to be deconvoluted for quantification. The accuracy of the elemental quantification of adequate sized feature/area is typically within a few percent.

The electrons scattered from the sample are detected using various detectors optimized for the specific type of electrons but essentially only detecting intensity of electrons; a high intensity gives rise to bright areas and a low intensity to darker areas. The Everhart-Thornley secondary electron (SE2) detector is used to detect mainly secondary electrons. It is positioned out to the side from the electron beam and a large positive bias is applied to attract the low energy electrons from the sample surface. The backscattering electron detector is typically positioned in the pole piece relatively high above the sample so it mainly detects the energetic backscattered electrons. A last type of detector is the InLens detector which also mainly detects secondary electrons. It is positioned close to the beam and is very surface sensitive and most efficient at low acceleration voltages (<5 kV) and low working distance (<5 mm) in contrast to the SE2 detector.

Charging is a common problem in SEM and is caused by a built up of electronic charge in the sample which produce very bright areas in the resulting image. A coating such as C or Au is therefore commonly applied to the sample surface to avoid this phenomenon.

3.5.2 Quantification of electrode microstructure pre- and post electrochemical testing

Microstructural characterization was performed on sample surfaces and polished cross sections embedded in epoxy and coated with carbon. All micrographs were recorded with a Merlin SEM (cf. section 3.1). Images for quantification of porosity and pore size distribution were recorded at 3 keV, 20 pA probe current, 2.8-3.0 mm working distance at constant brightness and contrast using the Everhart Thornley secondary electron detector (SE2). For each microstructure 20 micrographs have been analysed. The micrographs had a pixel size of 13.7 nm and the dimensions were 28 µm x 21 µm. Based on pixel intensity all micrographs were segmented into a LNF and pore phase using the in-house built Matlab application ThreshAlyzer [122]. The threshold value for the segmentation was carried out individually on each image and based on a relative position between the two peaks in the greyscale intensity spectra. An additional post-processing filter was used to remove very small isolated areas of one phase residing in the other phase. Pore sizes were estimated as the largest circle, which can be fitted into a given pore. Another stereology method, the line intercept method, was used to quantify porosity of the samples. This method was carried out with the semi-automatic ManSeg software which suggests possible intercepts to the user along a straight line on the micrograph [123]. The actual segmentation of a line into segments is, however, performed manually. A total of 3600 segments were sampled on 84 horizontal and vertical lines.

3.5.3 Characterization of electrode microstructure pre- and post electrochemical testing

Microstructures were visualized with a Merlin SEM (cf. section 3.1) before and after testing to identify degradation of the microstructures. Two types of surfaces were visualized: the top electrode surface and epoxy embedded polished cross sections coated with carbon. Micrographs were recorded at 3-5 kV with a working distance of 3-6 mm using either

the SE2 or InLens detector. Energy dispersive X-ray analysis (EDS) was also performed with a Quantax XFlash (Bruker, USA) at a working distance of ≈8.3 mm using 10-15 kV acceleration voltage. The EDS was used to compare the ratio of La:Ni:Fe:O before and after electrochemical testing and to detect impurities in the electrodes.

3.5.4 Hg intrusion porosimetry measurements

Hg intrusion porosimetry is a method used to determine open porosity and pore sizes of solid porous bodies. The basic principle is that the sample is loaded into a sealed chamber which is evacuated and heated to remove water vapour and gases from the pore space. The Hg is now led into the sealed chamber and a pressure is gradually applied to force the Hg into the pores of the porous body. The pore size (d_p) and the applied pressure (P) can be related through Washburn's equation [124]:

$$d_p = \frac{-4\gamma \cos\theta}{P} \tag{3.12}$$

where γ represents the interfacial surface tension of Hg and θ is the contact angle between Hg and the solid phase. The Washburn equation assumes the pores are cylindrical and for other geometry pores the pre-factor in the nominator of eq. 3.12 can be changed. The advantage of using Hg is that it is highly non-wetting and it will therefore not intrude pores before it is forced by the applied pressure. During intrusion the pore throats control the applied pressure and thereby the calculated pore sizes.

The Hg intrusion porosimetry measurements were carried out with Poremaster GT (Quantachrome Instruments, USA) on porously sintered 3YSZ substrates and on LNF electrodes sintered together with the 3YSZ substrates. The contact angle of Hg was assumed to be 140 ° and the surface tension 0.48 N m^{-1}. The intrusion pressure was 0.06-412 MPa. For the determination of the pore size distribution the ratio between the sample with intruded Hg and the apparent sample density at a given applied pressure was used. The pore size distribution is visualized as $\frac{\mathrm{d}V/V_0}{\mathrm{d}\log d_p}$ vs. d_p where V/V_0 represent the ratio of intruded volume over apparent sample volume. Only the data in pressure range approx. 1.5-412 MPa was considered which correspond to a maximum pore size of approx. 10 µm.

Chapter 4

Results and Discussion

In this chapter the outcome of the experimental work is presented in article form. The three articles included, cover most of the experimental work carried out. The first article deals with OER activity measurements of the identified materials and assessment of their stability, including their their chemical stability at HTP conditions. The second article presents the first iteration of the processing of porous LNF electrodes with hierarchical pore size distributions. Various dispersants are tested and suspension stability is assessed in aqueous suspensions. In the third article porous LNF electrodes with different microstructures are processed in organic-based suspensions. These are screen printed and tested as oxygen electrodes at conditions relevant for conventional alkaline electrolysis cells. Additional discussion sections have been included after the first and third article (sections 4.2 , 4.4.1 and 4.4.2). To finalize the chapter an overall discussion of the PhD work, in the relation to the overall project objectives, is conducted.

4.1 Oxygen Evolution Activity and Chemical Stability of Ni and Fe based Perovskites in Alkaline Media

Journal of The Electrochemical Society, **165** (10) F827-F835 (2018)
0013-4651/2018/165(10)/F827/9/$37.00 © The Electrochemical Society

Oxygen Evolution Activity and Chemical Stability of Ni and Fe Based Perovskites in Alkaline Media

Jens Q Adolphsen,[1,z] Bhaskar R. Sudireddy,[1] Vanesa Gil,[2,3] and Christodoulos Chatzichristodoulou[1]

[1]*Department of Energy Conversion and Storage, Technical University of Denmark, 4000 Roskilde, Denmark*
[2]*Aragon Hydrogen Foundation, 22197 Huesca, Spain*
[3]*Fundación Agencia Aragonesa para la Investigación y Desarrollo (ARAID), Zaragoza, Spain*

The electrochemical activity of $LaNiO_3$, $La_{0.97}NiO_3$, $LaNi_{0.6}Fe_{0.4}O_3$, $La_{0.97}Ni_{0.6}Fe_{0.4}O_3$ and $La_2Ni_{0.9}Fe_{0.1}O_4$, toward the oxygen evolution reaction (OER) was measured in 1M KOH at room temperature. All materials showed comparable OER activity with Tafel slopes in the range 56–98 mV/dec. The overvoltage at 10 $mA \cdot cm^{-2}$, measured on a well-defined geometric surface area, was in the range 0.38–0.45 V. The best performing materials among the ones investigated were $LaNiO_3$ (multiphase) and $La_2Ni_{0.9}Fe_{0.1}O_4$. The chemical stability of the stoichiometric materials was also assessed in 31wt% and 45 wt% KOH respectively at 100°C and 220°C. All materials were partially decomposed after 1 week of exposure at 220°C. After 1 week of exposure at 100°C $LaNiO_3$ had formed secondary phases whereas $LaNi_{0.6}Fe_{0.4}O_3$ and $La_2Ni_{0.9}Fe_{0.1}O_4$ showed only traces of secondary phase. The main secondary phases were in all cases $La(OH)_3$, NiO, $Ni(OH)_2$ and Fe_2O_3. These observations indicate that the investigated oxygen electrode materials are not suitable for operation in alkaline electrolysis cells above 100°C.
 [DOI: 10.1149/2.0911810jes]

Manuscript submitted April 13, 2018; revised manuscript received June 7, 2018. Published July 21, 2018.

The electrolysis of water in alkaline electrolysis cells (AECs) has been used commercially for around 100 years but it has remained a niche technology for hydrogen production, far surpassed by steam reforming due to lower production prices.[1] With the increased focus on renewable energy though, alkaline electrolysis is experiencing a renewed interest. At its current level of technological maturity alkaline electrolysis suffers from a low power density (~0.3–0.9 $W \cdot cm^{-2}$) and only a moderate efficiency (60–80% based on higher heating value) compared to proton exchange membrane electrolysis cells (PEMECs) and solid oxide electrolysis cells (SOECs).[2] The main advantages of AECs are their long lifetime and the fact that none of the electrodes require the use noble metals.

Improving the power density and the cell efficiency is therefore needed for the technology to become more competitive relative to other hydrogen production technologies. It is possible to increase the power density and efficiency without the use of noble metals. Raising the operating temperature is an effective way to enhance performance. Typically, AECs are operated at approximately 80°C. Recent results, using a new cell design, allowing the temperature to be increased up to at least 250°C upon pressurized operation, show a sharp increase in power density (by a factor of 10) and improved cell efficiency[3–5] compared to conventional AECs. However, increasing the operating temperature poses a challenge for the chemical stability of the electrode materials. Conventionally used oxygen electrode materials, such as nickel, are not an option because of their break-away oxidation at the operating conditions. Hence, the chemical stability of the oxygen electrode poses a significant challenge. Certain classes of (complex) oxides hold the potential to offer much better stability compared to the conventional metals used, as they are already oxidized, while also being able to provide adequate electrocatalytic activity.

The main challenge is therefore to identify suitable materials, which besides having good electrocatalytic activity toward the oxygen evolution reaction (OER) also exhibit adequate chemical stability at high temperature and pressure (HTP) conditions. Perovskite oxides, with the structural formula ABO_3, are of interest as OER electrocatalysts and many of them are also electronically conductive, allowing them to be used as both electrocatalyst and current collector. The A-site contains a large cation, e.g. La, Sr or Ba, compared to the B-site, which is typically a transition metal, e.g., Ti, Mn or Ni. Several perovskites and related structures containing Ni and Co as the transition metal have been shown to possess good electrocatalytic activity toward the OER.[6–9] It is, however, still questionable whether they can provide adequate performance over time at operating conditions. The double perovskite $Pr_xBa_{1-x}CoO_3$ (PBCO)[8–11] has been suggested as both an active and stable electrocatalyst at standard conditions with comparable electrocatalytic activity to the state-of-the-art materials IrO_2 and RuO_2.[12–14] A study, utilizing cyclic voltammetry to determine stability of PCBO at 80°C in 1 M KOH, showed that the performance of a 100 nm layer drops after less than 12 hours. This was correlated to surface leaching of Pr and Ba and hence a change in surface composition and structure. The above exemplifies that the stability of electrocatalysts at standard conditions provide insufficient information about their stability at operating conditions. Therefore, electrocatalyst characterization requires improved protocols for assessing the performance over time under realistic operating conditions.

Having a mix of Ni and Fe in the structure has been shown to improve the electrochemical activity toward the OER of Ni/Fe-metal oxyhydroxides[15,16] and perovskites.[17] In the following study, we show the results of the electrochemical activity of various La-Ni-Fe-oxides toward the OER. Four perovskite type materials were tested with the following nominal compositions: $LaNiO_3$ (LN), $La_{0.97}NiO_3$ (L97N), $LaNi_{0.6}Fe_{0.4}O_3$ (LNF) and $La_{0.97}Ni_{0.6}Fe_{0.4}O_3$ (L97NF) and one Ruddlesden-Popper phase: $La_2Ni_{0.9}Fe_{0.1}O_4$ (LNF-RP). In addition, the chemical stability of these materials, under high temperature conditions in concentrated KOH, was investigated.

Experimental

Characterization of powders.—All the powders are 99.9% purity and synthesized with the combustion spray pyrolysis method by Praxair Surface Technologies (Praxair Technology, USA). The phase analysis of the powders was carried out using X-ray diffraction (XRD, Bruker Advance D8, operated with a Cu Kα source). The powder's specific surface areas (SSAs) were determined by the Brunauer-Emmett-Teller (BET) method (Autosorb 1-MP, Quantachrome Instruments, USA) using N_2 gas. The powders were degassed for 3 h at 300°C prior to the measurements. The density of the powder was determined using gas pycnometry (AccuPyc 1330, Micromeritics, USA). Cylindrical pellets were fabricated by uniaxially pressing the powders to pellets followed by isostatic pressing at 280 MPa for 30 s. These pellets were used for sintering dilatometry (DIL 402C, Netzsch, Germany) measurements in the temperature range room temperature (RT)-1400°C in air with a heating rate of 5°C /min and holding time at 1400°C of 5 h. In addition, the thermal stability during sintering of the $LaNiO_3$ powder was determined by thermogravimetric analysis-differential thermal analysis (TGA-DTA, STA 409 C, Netzsch, Germany). The samples were heated in air/O_2 to 1100/1250°C with heating rates 10°C /min from RT-700°C/850°C followed by 5°C/min from 750–1100°C/850-1250°C. The flow rate of the air/O_2 was 50 ml/min.

[z]E-mail: jenqui@dtu.dk

Preparation of samples for electrochemical measurements.— The samples used for the electrochemical activity measurements were pressed and sintered bars of as-received powder. Bars were pressed using the same procedure as described above and subsequently, they were sintered at 1400°C for 24 h in air to achieve geometric densities > 92% and densities based on the Archimedes method > 96%. The bars used for electrochemical testing were further cut, grinded and polished (StruersTegrapol-32, Denmark) in successive steps to similar dimensions (17–18 mm × 5–6 mm × 0.9–1.5 mm). The final polishing was carried out with a 1 μm diamond dispersion (Nap B1 Diapro, Struers, Denmark) using a MD-Nap polishing pad (Struers, Denmark). The phase analysis of the sintered and polished samples was carried out using XRD. The root-mean-square roughness of the polished pellets was measured with a Cyberscan Vantage Profilometer (Cyber Technologies, Germany).

The root mean square roughness is given as:

$$R_{RMS} = \sqrt{\frac{1}{n}\sum_{i}^{n} y_i^2}$$

where y_i, is the vertical deviation of a point on the surface from the mean surface height and n is the number of points included in the calculation. The scanned area was min. 10 mm^2 with a 10 μm step size, corresponding to minimum of 100,000 points. Any systematic sloping of the pellet surface was compensated for in the ScanCT 7.5 software accompanying the equipment.

Electrochemical measurements.—The electrochemical activity measurements were performed using a three electrode setup. All measurements took place in a polytetrafluoroethylene (PTFE) holder, which was positioned in a closed, not airtight, container with N_2 flowing into it. The electrochemical characterization employed a ca. 1 M KOH solution (ACS reagent., >85% KOH basis, Fluka) prepared with Milipore water (18 MΩ·cm). KOH is hygroscopic. Besides the ACS reagent contains ≤ 2.0% K_2CO_3, ≤0.053% cation and heavy metal traces, ≤0.013% anion traces and ≤0.021% other impurities. The measured pH of the ca. 1 M solution was 14.0. A Gamry Reference 3000 potentiostat (Gamry Instruments, USA) was used. The polished bar was the working electrode with an Au current collector pressed against its back side. A Pt mesh with a Pt wire attached to it was used as the counter electrode and a relative hydrogen electrode (Hydroflex, Gaskatel, Germany) as the reference electrode. A Zirfon separator was used to separate the working electrode from the reference and counter electrode. The current densities were normalized according to the exposed geometrical surface area of the bar being tested. The electrochemical data collected consists of chronopotentiostatic (CP) measurements performed at 0.5, 1, 2, 5, 10, 25 and 50 $mA \cdot cm^{-2}$ with 30 min duration at each current density. Each CP measurement was followed by an amperostatic electrochemical impedance spectroscopy (EIS) measurement to determine the ohmic contribution (R_s). All results presented have been corrected for the serial resistance ($i \cdot R_s$) contribution. The amperostatic EIS measurements were used to determine the electrochemically active surface area (ECSA) from the ratio of the double layer capacitance of the tested surface relative to an ideal smooth oxide surface.

The surface of the polished bars before and after the electrochemical measurements was investigated with a field emission scanning electron microscope (FE-SEM) from Zeiss (Merlin Zeiss, Germany) equipped with a Schottky field emitter gun.

Chemical stability measurements.—The chemical stability of the materials was assessed by exposing the as-received (in case of LNF, a pre-calcined version is also included for the reasons explained in Results and discussion section) powders to 45 wt% KOH inside a polytetrafluoroethylene (PTFE) lined autoclave. No electrical potential was applied during these tests. The autoclave was heated in a furnace at 220°C for a week. No external pressure was applied to the autoclave, so the internal buildup pressure was approx. 15 bar, corresponding to the vapor pressure of the KOH solution at 220°C. Afterwards the KOH solution was extracted and the residual powder was rinsed in milipore water until a neutral pH of the water was reached. The rinsed powder was dried by heating with 1°C/min to 500°C and back to room temperature prior to phase analysis by XRD. Chemical stability analysis was also conducted after exposing the powders in 31 wt% KOH at 100°C and in 30 wt% KOH at RT for a week. Similar chemical stability measurements, as mentioned, above were conducted with powder pressed into pellets and sintered at 1100°C for 1 h.

Results and Discussion

Phase analysis.—The XRD patterns of LN, L97, LNF, L97NF and LNF-RP powders are shown and indexed in Figure 1. LN and L97N are indexed with PDF 33-0711, LNF and L97NF are indexed with PDF-88-0637 and LNF-RP is indexed with the XRD spectrum from Ref. 18 together with PDF 86-1668. The powders are phase pure according to XRD, except the L97N powder, which contains traces of NiO (PDF-44-1159), illustrated in Figure 1, and the LNF powder which contains traces of $Ni(OH)_3$ (PDF 36-1481). The LNF powder is phase pure after calcination at 800°C and hence the calcined LNF powder's XRD pattern is referred to in Figure 1. For these reasons pre-calcined LNF powder is also included in the chemical stability studies.

The XRD patterns of the densely sintered and polished LN, L97N pellets diverge a lot from the as-received powders because the perovskite phase is partially decomposed during sintering. During the partial decomposition, a loss of O_2 occurs while Ruddlesden Popper phases ($La_{n+1}Ni_nO_{3n+1}$, n = 1, 2 and 3) are formed in successive steps along with NiO.[19–21] The TG curves shown in Figure 2, exhibit the onset for partial decomposition at 1000°C in air and 1070°C in O_2 which is in agreement with previous work.[21,22] The weight loss is caused by O_2 escaping the material. The initial decline of the TG curves up to approx. 300°C can be ascribed to water evaporation and the continued decline of the TG curves between 300°C and the decomposition onset temperature is ascribed to O_2 being expelled from the LN structure due to the reduction of Ni^{3+} to Ni^{2+}. Overall the LN powder is seen to drop weight faster when heated in air compared to in O_2; suggesting that the thermal stability of the perovskite phase is lower when heated in air compared to in O_2-.

The sintered and polished LNF bars contain no secondary phases whereas the L97NF bars contain traces of NiO and the LNF-RP bars contain traces of unidentified phase(s). The electrochemically tested bars show no deviation in their XRD patterns from those of the sintered and polished bars.

Powder size and sintering characteristics.—The as-received powders differ in terms of particle size and SSA, as shown in Figure 3. The as-received LNF powder exhibit significantly larger SSA (25.1 $m^2 \cdot g^{-1}$) than the other powders. After calcination at 800°C the SSA is reduced to 8.0 $m^2 \cdot g^{-1}$ and hence comparable to the order powders. The LNF powder has the smallest particle sizes followed by LN, L97N and L97NF, which have similar sizes. The LNF-RP particle size is significantly larger than the other powders.

The sintering profiles in Figure 4 of the powders in pressed pellet form show similar sintering characteristics though the LN and L97N exhibit two stages of sintering. Initially, the sintering of LN and L97N starts around 1000°C, followed by a plateau and finally a maximum sintering rate in the interval 1300–1350°C. The plateau is assumed to be associated with the decomposition of the perovskite phase (cf. Figure 2). The LNF and L97NF reach the maximum sintering rate around 1200°C. The decrease in the elongation rate of LNF from around 200°C is associated with the combustion of remains from the synthesis process. This is supported by the XRD patterns (not shown), which showed traces of $La(OH)_3$. Additionally, density measurements show that there is an increase in powder density from 6.1 to 6.9 $g \cdot cm^{-3}$ before vs after calcination. This is pointing toward the fact that the synthesis process was stopped prematurely, resulting also in a larger SSA. The theoretical density of the rhombohedral LNF

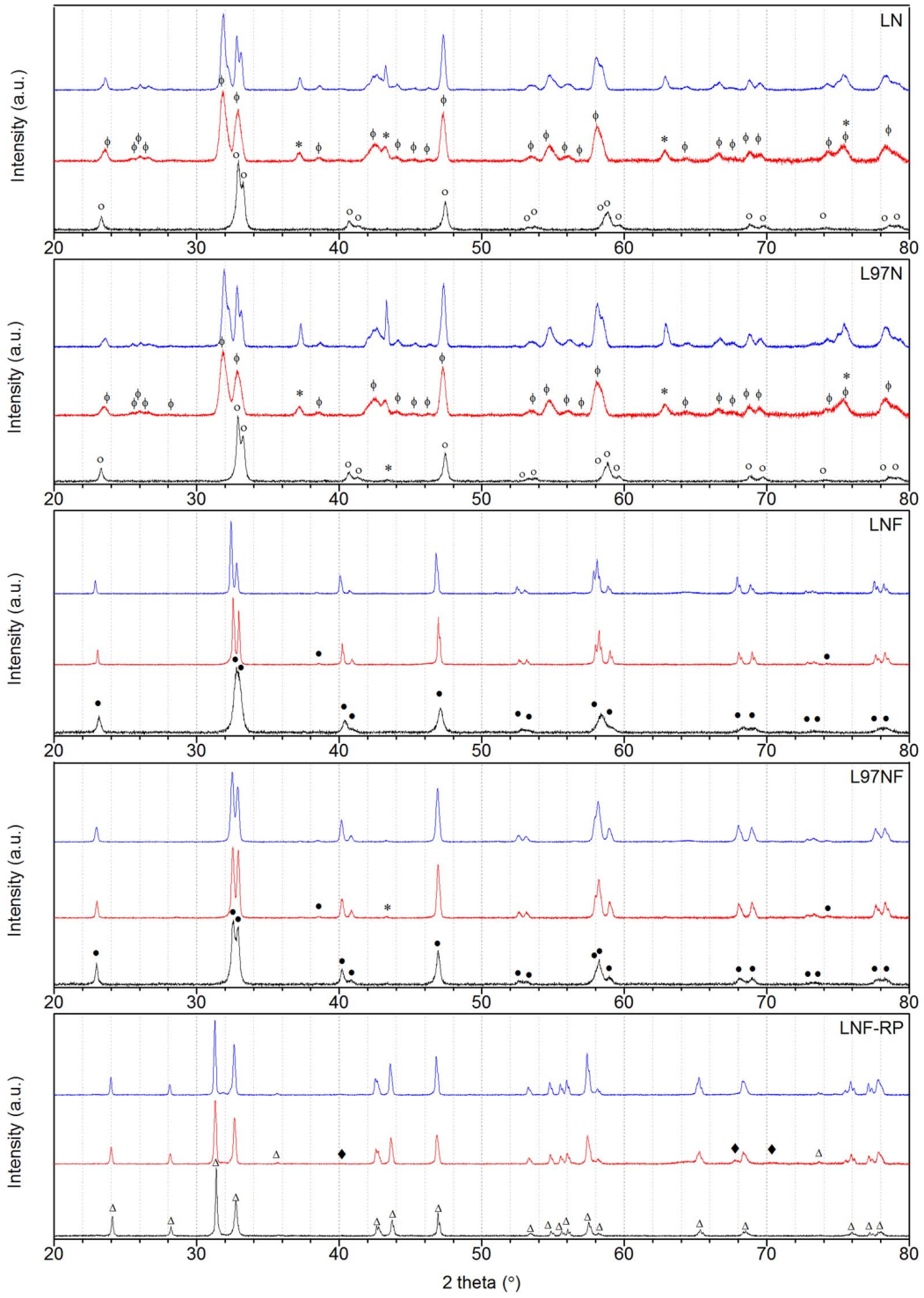

Figure 1. The XRD patterns of the as-received/calcined powder (black), the densely sintered and polished bars (red) and the electrochemically tested bars (blue). The symbols represent the following phases: ○LN, ● LNF, Δ LNF-RP, Φ $Lan_{+1}Ni_nO_{3n+1}$, n = 1, 2 or 3, * NiO and ♦ unidentified. Only additional peaks are indicated above in the red and blue spectra.

perovskite phase is 7.0 $g \cdot cm^{-3}$; hence close to that of the calcined powder. The LNF-RP is the last to sinter and has possibly not reached its maximum sintering rate at 1400°C. This is not surprising, when taking the relatively large particle sizes into account.

Electrochemical activity toward the OER.—The electrochemical measurements were carried out in a 1 M KOH solution made form ACS reagent KOH and milipore water. The fact that it is only >85% KOH, due to KOH's hydroscopic nature, is not considered problematic as the pH of the 1 M was measured to 14.0. The amount of impurities in this KOH is important as e.g. Fe impurities as low as <1 ppm have been shown to have a catalytic effect on the OER of Nickel oxyhydroxides.[23] In our KOH the level of Ni and Fe impurities is <10 ppm and hence it could influence the electrocatalytic activity of non-Fe containing materials. A commonly used grade of KOH, for determination of intrinsic electrocatalytic activity toward the OER, is 99.99% trace metals basis.[7,9] This grade contains <150 ppm trace metal ions (excluding Na) compared to 100 ppm in ACS reagent. It

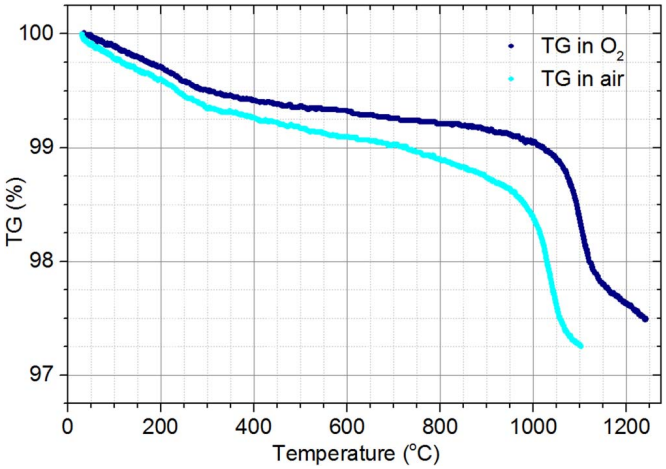

Figure 2. The TG curves of LN heated in air and O_2. The main onset on the TG curves was determined to be 1000°C and 1070°C in air and O_2 respectively.

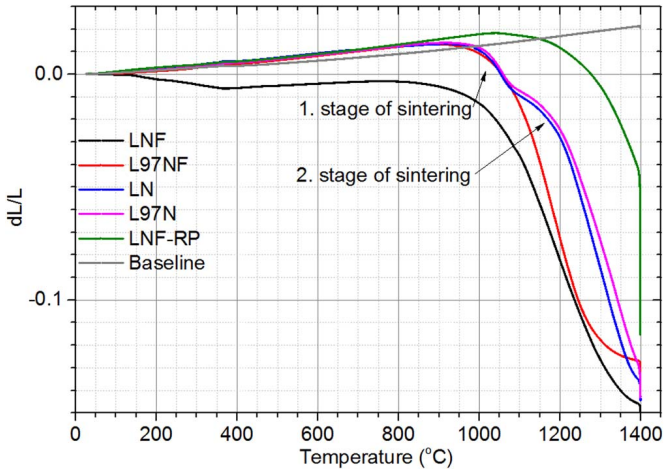

Figure 4. Sintering dilatometry curves of the pressed powders from RT to 1400°C in air.

is hence clear that the effect of impurities, such as Fe, on the OER cannot be excluded unless the highest purity grade of KOH (e.g. Fluka Analytical TraceSelect) is used and for all industrial applications this is not realistic.

The electrochemical characterization was carried out in two sequences, labelled test 1 and test 2 using the same sample for each test. Test 2 was carried out in a new KOH solution sometime after test 1. After the completion of test 2 the materials have been polarized toward the OER for a total time of 10 hours. In Figure 5a, the series of CP measurements for LNF test 2 are shown and the corresponding galvanostatic EIS measurements are presented in Figure 5b. The CP measurements at different current densities quickly reach equilibrium and remain stable, in most cases, for the 30 min duration of the measurement. The CP measurements are stable up to a current density of 5–10 mA · cm^{-2} above which significant fluctuations, attributed to bubble formation on the sample surface, appear. When a bubble grows on the sample surface, less surface area is available for the OER and the overpotential increases. When the bubble detaches from the surface, the overpotential decreases abruptly. For this reason, the CP measurements at 25 and 50 mA · cm^{-2} are not included in the data analysis. All the tested samples showed comparable serial resistance in the range of 2–4 Ω · cm^2.

A comparison of the OER activity of the tested materials is attempted in the Tafel plots shown in Figure 6. LN and LNF-RP exhibit the lowest overpotentials at 10 mA · cm^{-2} and the lowest Tafel slopes. The Tafel slope is obtained from the fitting of the data to the Tafel equation given by:

$$\eta = b \ln\left(\frac{i}{i_0}\right)$$

where η is the overpotential, b is the Tafel slope, i is the current density and i_0 is the exchange current density. The fitting parameters i_0 and b are listed in Table I together with the coefficient of determination (R^2) for each fit. It should be noted that the exchange current density, i_0, has no clear physical meaning in the OER as it is a multi-electron transfer process involving several reaction steps.[24] The Tafel slope in Table I is determined in the interval 0.5–5 mA · cm^{-2}. In addition all overpotentials in Table I and Figure 6 were average values of the first 5 min of the CP measurement to limit the influence of bubble formation on the overpotential.

The Tafel plots of test 1 and test 2, shown in Figure 6, suggest that the electrochemical performance increases over time. A loss of gloss on the sample surface was easily visible with the naked eye when comparing the area of the sample that was exposed to the OER conditions versus the area that was not exposed. The improved activity is attributed to an increase in the exposed surface area due to increased surface roughness. SEM micrographs of the surfaces of the bars before and after testing clearly support this observation as shown in Figure 7. In the figure the LN (a), b) and c)), LNF (d), e) and f)) and LNF-RP (g), h) and i)) surfaces are shown before and after OER testing. Trenches are formed on the surface after electrochemical testing, which is particularly visible on the LN and LNF-RP surfaces (Figures 7b, 7c, 7h and 7i). The surface of the exposed LNF (Figures 7e and 7f) is less affected though some smaller trenches are also visible here. Reference surfaces exposed to 1 M KOH for approx. 15 h but not polarized toward the OER are found in Figure S1. They show that the LN and LNF surfaces are similar to the polished non-exposed surfaces. There are some small crater like features, visible in the high magnification LNF-RP surface. This is likely a result of chemical etching. The trenches formed in the surface of the electrochemically exposed samples are more pronounced, and it is therefore conjectured

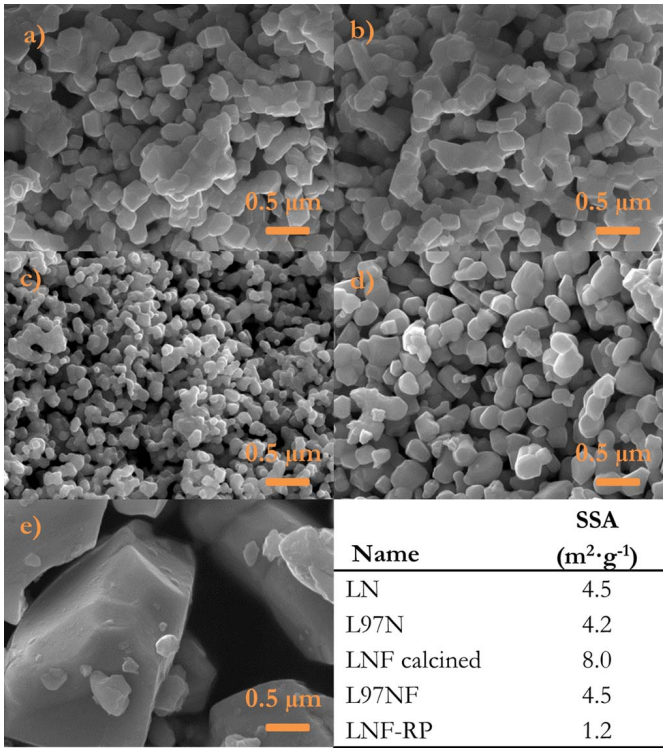

Name	SSA ($m^2 \cdot g^{-1}$)
LN	4.5
L97N	4.2
LNF calcined	8.0
L97NF	4.5
LNF-RP	1.2

Figure 3. SEM micrographs of the powders as received from the supplier (the LNF has been calcined and is not as received) and their respective SSA. The order is as follows: a) LN, b) L97N, c) LNF, d) L97NF, e) LNF-RP.

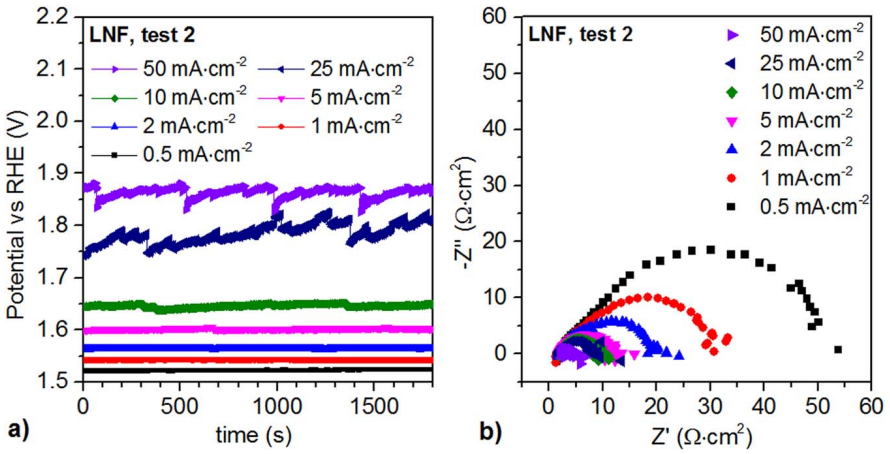

Figure 5. a) A set of CP measurements at different current densities for LNF and b) the corresponding amperostatic EIS measurements. The CP measurements above 10 mA · cm^{-2} are fluctuating due to bubble formation.

Table I. Tafel fit parameters for the first (test 1) and second (test 2) set of CP measurements. *LN and L97N decomposed during sintering to a multiphase material containing LN, NiO and La_2NiO_4.

Material	b(mV/dec)	i_0 (mA · cm^{-2})	R^2	η (V)@ 10 mA · cm^{-2}
Test 1				
$LaNi_{0.6}Fe_{0.4}O_3$	98	7×10^{-4}	1.00	0.44
$La_{0.97}Ni_{0.6}Fe_{0.4}O_3$	83	1×10^{-4}	0.97	0.45
$LaNiO_3$*	68	5×10^{-5}	0.99	0.38
$La_{0.97}NiO_3$*	78	4×10^{-5}	0.96	0.44
$La_2Ni_{0.9}Fe_{0.1}O_4$	66	2×10^{-5}	0.98	0.40
Test 2				
$LaNi_{0.6}Fe_{0.4}O_3$	81	1×10^{-4}	1.00	0.42
$La_{0.97}Ni_{0.6}Fe_{0.4}O_3$	68	2×10^{-5}	0.96	0.42
$LaNiO_3$*	56	2×10^{-6}	0.99	0.38
$La_{0.97}NiO_3$*	80	6×10^{-5}	1.00	0.43
$La_2Ni_{0.9}Fe_{0.1}O_4$	57	3×10^{-5}	0.97	0.39

that these are a result of the OER. In Table II the tested bar's root mean square roughness is listed before test 1 and after test 2. In all cases it is seen to increase but there is no clear quantitative correlation between the increase in surface roughness and the improvement in electrocatalytic activity. The mass change of the bars after vs before electrochemical testing has been recorded. For all materials there appear to be a mass loss but it is insignificant due to the uncertainty on the scale, which means the mass loss, if any, is $\leq$ 0.2 mg ($\leq$ 0.4 ‰).

To get more insight into the activation of the electrode surfaces the ECSA has been determined as the ratio of the electrode surface

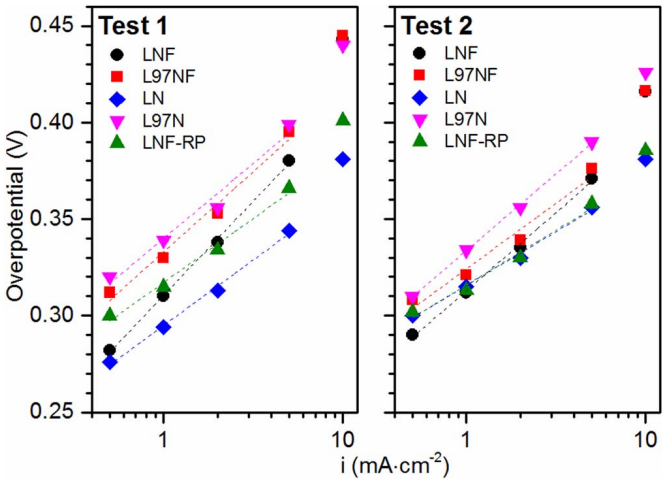

Figure 6. Tafel plots for the two sets of measurements (test 1 and test 2) of the different compositions. The dotted lines correspond to the linear fitting of the data using the Tafel equation.

double layer capacitance (C_{dl}) to that of an ideal oxide surface. The latter reference used is 60 μF/cm^2.[25] The C_{dl} is determined from chronopotentiostatic EIS fits to a resistor in series with a parallel connection of a constant phase element (CPE) and a resistor (R_s[CPE-R_p]). The double layer capacitance of the electrode surface is extracted from Ref. 26:

$$C_{dl} = Y^{1/\alpha}\left(\frac{1}{R_s} + \frac{1}{R_p}\right)^{1-1/\alpha}$$

Where Y and α are the parameters describing the non-ideal capacitive behavior of the CPE. The change in ECSA at 0.5, 10 and 50 mA · cm^{-2} is compared in Table III. Firstly, it is seen that the ECSA is close to 1 (real surface area) and comparable for the different samples. Secondly, it is seen that LN and L97N exhibit a 3–4 fold increase in the ECSA from test 1 to test 2, which is substantially lower for the LNF, L97NF and LNF-RP. A clear correlation to the electrochemical activity measurements is not present. This is clear when comparing e.g. LN/L97N to LNF. The former exhibit a larger increase in ECSA compared to LNF, but LNF shows a larger improvement in electrocatalytic

Table II. The root mean square roughness of the polished bars' surface before electrochemical testing (pre) and after two electrochemical test cycles (post).

Sample	R_{RMS} (pre) [μm]	R_{RMS} (post) [μm]	Increase (%)
LN	0.41	0.79	93
L97N	0.43	0.92	114
LNF	0.37	0.68	84
L97NF	0.37	0.49	32
LNF-RP	0.20	0.64	220

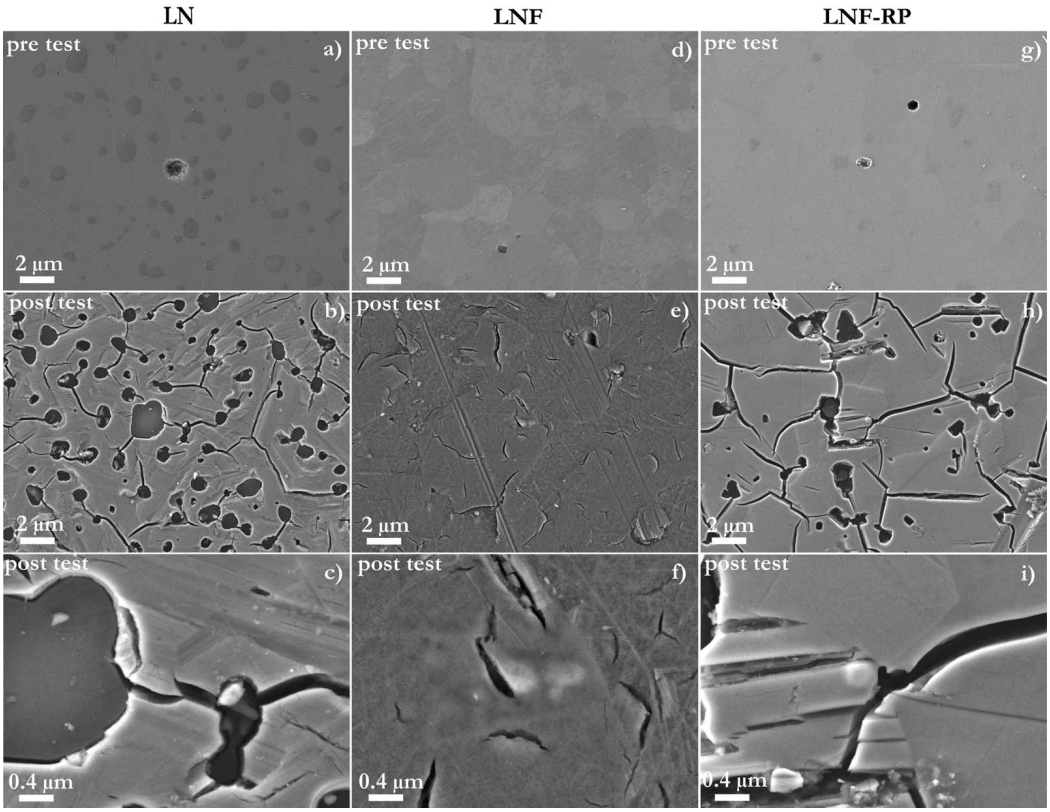

Figure 7. The surface of polished LN, LNF and LNF-RP bars before (pre test) and after (post test) the two sequences of electrochemical measurements. The darker spots in a), b) and c) is NiO formed during sintering.

activity. The last trend observable is a decrease in the absolute ECSA when increasing the current density. This suggests that gas bubbles are partially blocking the electrode surface and influencing the results already at 10 mA · cm^{-2}.

The oxygen evolution activity of the investigated materials is compared to some of the state-of-the art materials such as IrO_x, $Ni_{0.9}Fe_{0.1}O_x$ and $PrBaCo_2O_{5+x.}$ in Table IV. The comparison is based on the Tafel slope and the overpotential at 10 mA · cm^{-2}. Since the surface is seen to change over time, results from the first set of measurements (test1) are chosen as more representative of the intrinsic activity of the materials. The activity of LN varies substantially when looking into the literature; the Tafel slopes reported vary from 43–122 mV,[6,28–31] in 0.1/1.0 M KOH. The variation is likely a result of several factors. Firstly, that different (ratio of) components are used in the electrocatalyst layer e.g. different types of carbon, nafion and PTFE used to collect current and support the catalyst particles. Secondly, that the synthesis method influences the intrinsic OER activity.[27] This is related to changes in the actual crystal structure and phase composition. In Ref. 28 it was for example shown that the change of crystal structure from rhombohedral to cubic LN perovskite has an enhancing effect on the OER activity. Lastly, surface roughening and instability of the surface perovskite phase is likely a third factor influencing the results. In Ref. 30 the intrinsic OER activity of LN and $La_{n+1}Ni_nO_{3n+1}$ (n = 1, 2 and 3) was investigated and the lowest Tafel slope was found for LN (122 mV/dec), followed by $La_4Ni_3O_{10.26}$ (142 mV/dec) $La_2NiO_{4.27}$ (180 mV/dec) and $La_3Ni_2O_{7.15}$ (250 mV/dec). Finally, the OER activity of NiO has generally been reported for the related $Ni(OH)_2$ and NiO(OH) species as these can be formed as a surface layer in alkaline conditions[32] and known to be the electrocatalytically active phases. Tafel slopes reported are generally low, on the order of 30–40 mV/dec[33–35] though higher values have also been reported (70/100 mV/dec)[15,36] when no Fe impurities are present. The other materials, investigated in this article have, to our knowledge, not been investigated toward the OER in alkaline media previously.

Chemical stability of the materials at high temperatures in concentrated KOH.—The XRD patterns of LN, LNF, and LNF-RP powders after 1 week of ageing under conditions similar to actual HTP-AECs operating conditions (45 wt% KOH at 220°C but no electrochemistry involded) are shown in Figure 8. The results show that all

Table III. The electrochemical active surface area (ECSA) of the tested bars at different current densities.

	ECSA test 1	ECSA test 2	Change (%)	ECSA test 1	ECSA test 2	Change (%)	ECSA test 1	ECSA test 2	Change (%)
Sample	0.5 mA · cm^{-2}			10 mA · cm^{-2}			50 mA · cm^{-2}		
LN	2.5	12.3	390%	1.3	5.7	334%	0.8	N/A	-
L97N	2.7	12.2	351%	1.4	3.8	167%	1.3	0.9	−34%
LNF	4.7	5.4	14%	1.9	2.5	33%	0.8	1.0	24%
L97NF	3.0	7.3	142%	1.8	3.6	102%	0.7	0.8	10%
LNF-RP	2.0	4.5	123%	0.7	0.7	0%	0.5	0.4	−9%

Table IV. Figures of merit for various perovskites and metal oxides from the literature. IrO_x and $NiFeO_x$ are state-of-the-art OER catalysts. $PrBaCo_2O_{5+x}$ is one of the best performing perovskites (double perovskite), which also shows stable performance at standard conditions.

Material	b(mV/dec)	η (V) @10 mA · cm^{-2}	Conditions
IrO_x[33]	49	n/a	1 M KOH, RT, geometric surface area
IrO_x[36]	n/a	0.32	1 M KOH, RT, geometric surface area
$Ni_{0.9}Fe_{0.1}O_x$[33]	30	n/a	1 M KOH, RT, geometric surface area
$Ni_{0.69}Fe_{0.31}O_x$[34]	30	0.28	1 M KOH, RT, geometric surface area
$PrBaCo_2O_{5+x}$[8]	∼70	∼0.38	0.1 M KOH, RT, oxide surface area
$PrBaCo_2O_{5+x}$[37]	∼95	n/a	0.1 M KOH, RT, mass based normalization

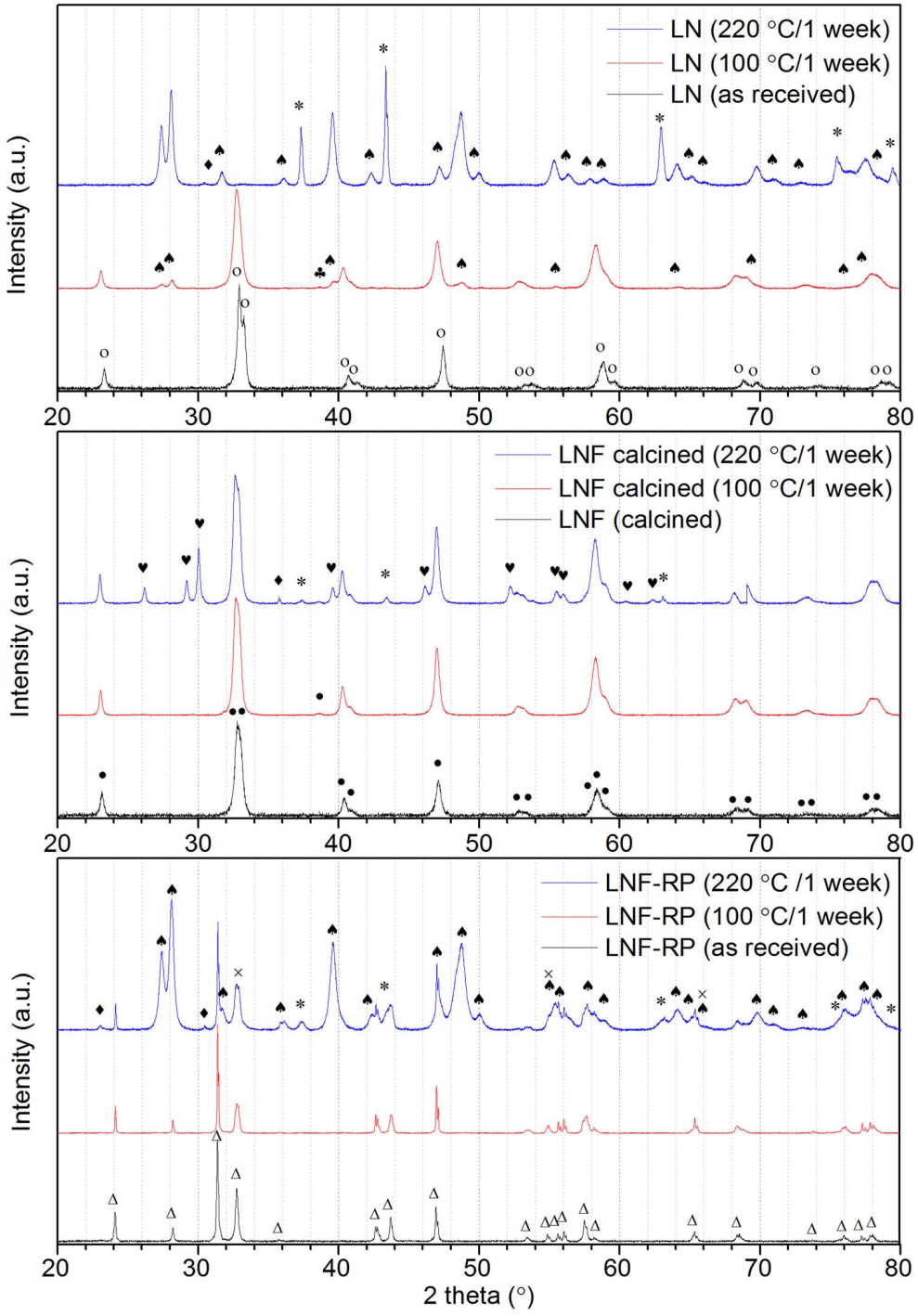

Figure 8. The XRD pattern of the LN, LNF and LNF-RP powder and the same powder after 1 weeks exposure to 31 wt% KOH at 100°C and 45 wt% KOH at 220°C, respectively. The symbols represent the following phases: ○LN, ● LNF, Δ LNF-RP, ♥ La_2O_3, ♠ $La(OH)_3$, * NiO, ♣ $Ni(OH)_2$, × Fe_2O_3 and ♦ unknown. Only additional peaks are indicated in the red and blue spectrum.

materials have decomposed. The peaks corresponding to the decomposition products are indexed to $La(OH)_3$ (PDF 36-1481)and NiO (PDF-44-1159) in the case of LN and $La(OH)_3$, NiO and Fe_2O_3 (PDF 39-0238) in the case of LNF and LNF-RP. A few minor peaks in the XRD patterns remained unidentified. The perovskite phase is almost completely decomposed to $La(OH)_3$ and NiO in the LN powder. In the LNF-RP powder the $La(OH)_3$ peaks dominate while the perovskite phase is still the main phase in the LNF powder. The XRD patterns of the powders after exposure to less harsh conditions (31 wt% KOH at 100°C) are also found in Figure 8. The LN perovskite phase shows some decomposition but significantly less than after the 220°C test. The LNF and LNF-RP powder exhibit very limited degradation after the 100°C test. At higher magnification it appears that small traces of LaO(OH) (PDF 19-0656), $La(OH)_3$ and NiO are present. A longer stability test is necessary though to reach a clear conclusion on whether the apparently improved stability at 100°C vs 220°C is associated with slow kinetics for the decomposition process or improved thermodynamic stability of the perovskite phases explored. The chemical stability test of the powders exposed to concentrated KOH for a week at RT, show signs of secondary phases in the LN XRD spectrum and no signs in the LNF and LNF-RP XRD spectra (see Figure S2).

Apart from the LNF and L97NF, the other porously sintered pellets exposed to the 220°C chemical stability test had crumbled into powder. All the porous pellets exposed to the 100°C test remained intact. The XRD patterns of the LNF and LNF-RP pellets exposed to the 100°C test showed a similar pattern as the powders exposed to the same conditions. The LN pellets were already partially decomposed during sintering to NiO and Ruddlesden-Popper phases. Clear signs of $La(OH)_3$ were present in the XRD of the tested pellets, thus indicating that the sintered mixed phase material is not chemically stable. It cannot be concluded whether the new phases formed are only the $LaNiO_3$ decomposing further or also a result of the Ruddlesden-Popper phases, formed during sintering, decomposing.

Conclusions

La, Ni (and Fe) based perovskites and a Ruddlesden-Popper compound were investigated as electrode materials for the OER in alkaline medium. The intrinsic electrochemical activity was determined at room temperature in 1 M KOH and found to be comparable for all materials, with the multiphase-LN (LN, $La_{n+1}Ni_nO_{3n+1}$, NiO) and the LNF-RP exhibiting the highest activity. The Tafel slopes were in the range 56–98 mV/dec. and the overpotential at 10 mA cm^{-2} in the range 0.38–0.45 V, which is similar to that of state-of-art, non-noble metal electrocatalysts. The roughness of the polished surface of all materials was increasing over time, accounting for the increase in electrochemical activity observed over time. The decrease in the ECSA, observed at higher current densities (50 mA·cm^{-2}), is probably due to the formation of gas bubbles on the electrode surface.

Chemical stability measurements of the powders exposed to 31 wt% and 45 wt% KOH respectively at 100°C and 220°C for 1 week showed that all the studied materials were chemically unstable at 220°C, decomposing to simple metal oxides and hydroxides. At 100°C the LNF and LNF-RP powders showed only traces of secondary phases, whereas the LN powder is clearly decomposing. These materials are therefore not appropriate for HTP-AECs but LNF and LNF-RP could potentially be used at temperatures below 100°C. Further stability investigations of even longer duration are required to assess this.

Acknowledgments

The authors thank Jette Iversen, Jeanette Krambech and Carsten G. Sørensen for their help with sample preparation and carrying out measurements. We are also grateful for the help Jens F. S. Borchsenius, Henrik Henriksen and Jens Østergaard provided in conjunction with the electrochemical characterization.

ORCID

Jens Q Adolphsen https://orcid.org/0000-0001-5062-0118

References

1. T. Smolinka, E. T. Ojong, and J. Garche, in *Electrochemical Energy Storage for Renewable Sources and Grid Balancing*, P. T. Moseley and J. Garche, Editors, p. 103, Elsevier (2014).
2. K. Zeng and D. Zhang, "Recent progress in alkaline water electrolysis for hydrogen production and applications," *Prog. Energy Combust. Sci.*, **36**(3), 307 (2010).
3. F. Allebrod, C. Chatzichristodoulou, and M. B. Mogensen, "Alkaline electrolysis cell at high temperature and pressure of 250°C and 42 bar," *J. Power Sources*, **229**, 22 (2013).
4. F. Allebrod, C. Chatzichristodoulou, and M. B. Mogensen, "Cobalt and molybdenum activated electrodes in foam based alkaline electrolysis cells at 150–250 C and 40 bar," *J. Power Sources*, **255**, 394 (2014).
5. C. Chatzichristodoulou, F. Allebrod, and M. B. Mogensen, "High Temperature Alkaline Electrolysis Cells with Metal Foam Based Gas Diffusion Electrodes," *J. Electrochem. Soc.*, **163**(11), 3036 (2016).
6. J. O. Bockris and T. Otagawa, "The Electrocatalysis of Oxygen Evolution on Perovskites," *J. Electrochem. Soc.*, **131**(2), 290 (1984).
7. J. Suntivich, K. J. May, H. A. Gasteiger, J. B. Goodenough, and Y. Shao-Horn, "A Perovskite Oxide Optimized for Oxygen Evolution Catalysis from Molecular Orbital Principles," *Science*, **334**, 1383 (2011).
8. A. Grimaud, K. J. May, C. E. Carlton, Y.-L. Lee, M. Risch, W. T. Hong, J. Zhou, and Y. Shao-Horn, "Double perovskites as a family of highly active catalysts for oxygen evolution in alkaline solution.", *Nat. Commun.*, **4**, 2439 (2013).
9. R. Mohamed, X. Cheng, E. Fabbri, P. Levecque, R. Kotz, O. Conrad, and T. J. Schmidt, "Electrocatalysis of Perovskites: The Influence of Carbon on the Oxygen Evolution Activity," *J. Electrochem. Soc.*, **162**(6), F579 (2015).
10. D. S. Bick, A. Kindsmüller, G. Staikov, F. Gunkel, D. Müller, T. Schneller, R. Waser, and I. Valov, "Stability and Degradation of Perovskite Electrocatalysts for Oxygen Evolution Reaction," *Electrochim. Acta*, **218**, 156 (2016).
11. D. Bick, T. B. Krebs, D. Kleimaier, A. F. Zurhelle, G. T. Staikov, R. Waser, and I. Valov, "Degradation Kinetics during Oxygen Electrocatalysis on Perovskite-based Surfaces in Alkaline Media," *Langmuir*, **34**, 1347 (2018).
12. S. Trasatti, "Electrocatalysis in the anodic evolution of oxygen and chlorine," *Electrochim. Acta*, **29**(11), 1503 (1984).
13. Y. Matsumoto and E. Sato, "Electrocatalytic properties of transition metal oxides for oxygen evolution reaction," *Mater. Chem. Phys.*, **14**(5), 397 (1986).
14. Y. Lee, J. Suntivich, K. J. May, E. E. Perry, and Y. Shao-Horn, "Synthesis and Activities of Rutile IrO_2 and RuO_2 Nanoparticles for Oxygen Evolution in Acid and Alkaline Solutions," *J. Phys. Chem. Lett.*, **3**, 399 (2012).
15. D. A. Corrigan, "The Catalysis of the Oxygen Evolution Reaction by Iron Impurities in Thin Film Nickel Oxide Electrodes," *J. Electrochem. Soc.*, **134**(2), 377 (1987).
16. M. D. Merrill and R. C. Dougherty, "Metal oxide catalysts for the evolution of O_2 from H_2O," *J. Phys. Chem. C*, **112**(10), 3655 (2008).
17. D. Zhang, Y. Song, Z. Du, L. Wang, Y. Li, and J. B. Goodenough, "Active $LaNi_{1-x}Fe_xO_3$ bifunctional catalysts for air cathodes in alkaline media," *J. Mater. Chem. A*, **3**(18), 9421 (2015).
18. E. V. Tsipis, E. N. Naumovich, M. V. Patrakeev, J. C. Waerenborgh, Y. V. Pivak, P. Gaczyński, and V. V. Kharton, "Oxygen non-stoichiometry and defect thermodynamics in $La_2Ni_{0.9}$ $Fe_{0.1}O_{4+d}$," *J. Phys. Chem. Solids*, **68**, 1443 (2007).
19. C. Brisi, M. Vallino, and F. Abbattista, "Composition and structure of two hitherto unidentified phases in the system La_2O_3-NiO-O," *J. Less-Common Met.*, **79**(2), 215 (1981).
20. J. Drennan, C. P. Tavares, and B. C. H. Steele, "An Electron Microscope Investigation of Phases in the System La-Ni-O," *Mater. Res. Bull.*, **17**, 621 (1982).
21. H. E. Höfer and W. F. Kock, "Crystal Chemistry and Thermal Behavior in the La(Cr, Ni)O_3 Perovskite System," *J. Electrochem. Soc.*, **140**(10), 2889 (1993).
22. M. Zinkevich, N. Solak, H. Nitsche, M. Ahrens, and F. Aldinger, "Stability and thermodynamic functions of lanthanum nickelates," *J. Alloys Compd.*, **438**, 92 (2007).
23. L. Trotochaud, S. L. Young, J. K. Ranney, and S. W. Boettcher, "Nickel-Iron oxyhydroxide oxygen-evolution electrocatalysts: The role of intentional and incidental iron incorporation" *J. Am. Chem. Soc.*, **136**(18), 6744 (2014).
24. W. T. Hong, M. Risch, K. A. Stoerzinger, A. Grimaud, Jin Suntivich, and Y. Shao-Horn, "Toward the rational design of non-precious transition metal oxides for oxygen electrocatalysis," *Energy Environ. Sci.*, **8**, 1404 (2015).
25. S. Levine and A. L. Smith, "Theory of the differential capacity of the oxide/aqueous electrolyte interface," *Discuss. Faraday Soc.*, **52**, 290 (1971).
26. G. J. Brug, A. L. G. Van Den Eeden, M. Sluyters-Rehbach, and J. H. Sluyters, "The Analysis of Electrode Impedances Complicated by the Presence of Constant Phase Element," *J. Electroanal. Chem.*, **176**, 275 (1984).
27. R. N. Singh, S. K. Tiwari, S. P. Singh, A. N. Jain, and N. K. Singh, "Electrocatalytic activity of high specific surface area perovskite-type $LaNiO_3$ via sol-gel route for electrolytic oxygen evolution in alkaline solution," *Int. J. Hydrogen Energy*, **22**(6), 557 (1997).
28. W. Zhou and J. Sunarso, "Enhancing Bi-functional electrocatalytic activity of perovskite by temperature shock: A case study of $LaNiO_{3-d}$," *J. Phys. Chem. Lett.*, **4**(17), 2982 (2013).
29. R. A. Silva, C. O. Soares, M. D. Carvalho, C. M. Rangel, and M. I. Da Silva Pereira, "Stability of $LaNiO_3$ gas diffusion oxygen electrodes," *J. Solid State Electrochem.*, **18**(3), 821 (2014).

30. J. Yu, J. Sunarso, Y. Zhu, X. Xu, R. Ran, W. Zhou, and Z. Shao, "Activity and Stability of Ruddlesden-Popper-Type $La_{n+1}NinO_{3n+1}$ (n = 1, 2, 3, and ∞) Electrocatalysts for Oxygen Reduction and Evolution Reactions in Alkaline Media," *Chem. Eur. J.*, **22**, 2719 (2016).
31. A. Ashok, A. Kumar, R. R. Bhosale, F. Almomani, S. S. Malik, S. Suslov, and F. Tarlochan, "Combustion synthesis of bifunctional $LaMO_3$ (M = Cr, Mn, Fe, Co, Ni) perovskites for oxygen reduction and oxygen evolution reaction in alkaline media," *J. Electroanal. Chem.*, **809**, 22 (2018).
32. Y. Miao, L. Ouyang, S. Zhou, L. Xu, Z. Yang, M. Xiao, and R. Ouyang, "Electrocatalysis and electroanalysis of nickel, its oxides, hydroxides and oxyhydroxides toward small molecules," *Biosens. Bioelectron.*, **53**,428 (2014).
33. L. Trotochaud, J. K. Ranney, K. N. Williams, and S. W. Boettcher, "Solution-Cast Metal Oxide Thin Film Electrocatalysts for Oxygen Evolution," *J. Am. Chem. Soc.*, **134**, 17253 (2012).
34. Y. Qiu, L. Xin, and W. Li, "Electrocatalytic oxygen evolution over supported small amorphous Ni-Fe nanoparticles in alkaline electrolyte," *Langmuir*, **30**(26), 7893 (2014).
35. M. S. Burke, S. Zou, L. J. Enman, J. E. Kellon, C. A. Gabor, E. Pledger, and S. W. Boettcher, "Revised Oxygen Evolution Reaction Activity Trends for First-Row Transition-Metal (Oxy)hydroxides in Alkaline Media," *J. Phys. Chem. Lett.*, **6**, 3737 (2015).
36. C. C. L. McCrory, S. Jung, J. C. Peters, and T. F. Jaramillo, "Benchmarking Heterogeneous Electrocatalysts for the Oxygen Evolution Reaction," *J. Am. Chem. Soc.*, **135**, 16977 (2013).
37. R. Mohamed, X. Cheng, E. Fabbri, P. Levecque, R. Kotz, O. Conrad, and T. J. Schmidt, "Electrocatalysis of Perovskites: The Influence of Carbon on the Oxygen Evolution Activity," *J. Electrochem. Soc.*, **162**(6), F579 (2015).

4.2 Comments on surface changes of the bars tested as OER electrotrocatalysts

The images showed in figure 7 in section 4.1 do not tell the whole story. On the tested LNF surface nano-sized needle-like pieces were observed on the surface, which can be seen in Figure 4.1. In some places a thin, hazy layer was observed above the needle-covered surface. Raman spectroscopy was used to investigate this top layer but it was not possible to draw any conclusions on the phases present. The samples had been quickly rinsed in ultrasonicated milipore water before investigating them in the SEM, and after a second thorough cleaning in ultrasonicated milipore water, the surface layer disappeared and the surface shown in figure 7 in section 4.1 appeared. This is taken as an indication that the surface microstructure is changing during the OER. The mass change of the pellets before vs after the activity measurements did not reveal any significant changes in the mass of the samples. It is suggested that the needle-like objects could be La_2O_3 as similar appearing structures discussed in section 4.5.5 were identified to be crystalline La_2O_3. These observations elucidate that the sample surfaces change upon ultrasonication in milipore water. The question that naturally arises is hence whether the surface of the LN and LNF-RP have undergone similar changes during their first rinsing. It seems likely, considering the surface changes observed.

The chemical stability measurements of LNF performed at 220 ℃ showed that $La(OH)_3$ is the main secondary phase formed which is in line with the suggestion that the needle-like objects are La_2O_3. It is, however, interesting to note that during the chemical stability measurements no signs of secondary phase formation was observed at room temperature and 100 ℃. In this context it should of course be pointed out that XRD was the only method used to asses the chemical stability of the powders, and this method is essentially only assessing the bulk phases and is not sensitive to changes in surface chemistry.

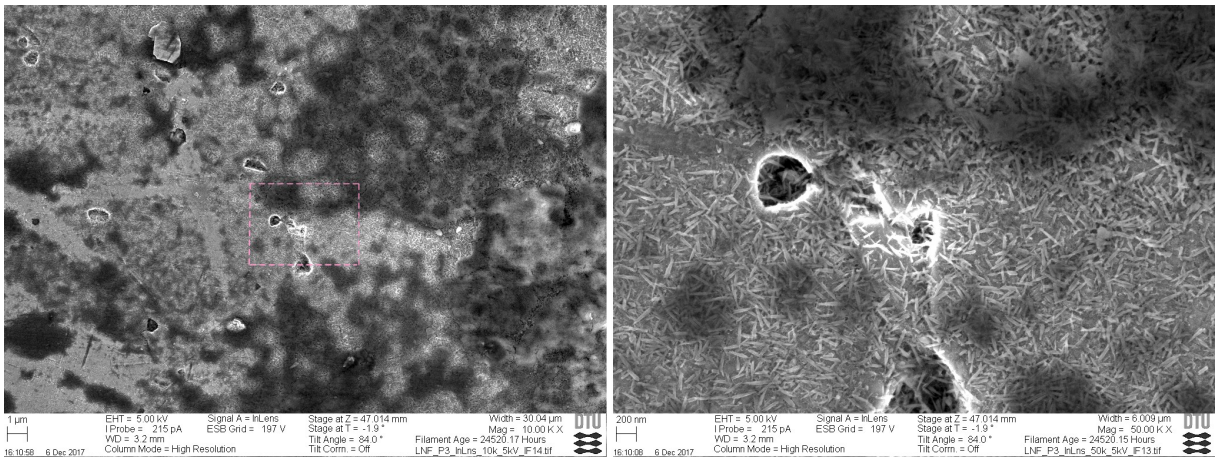

Figure 4.1: The polished LNF surface after the OER activity measurements. The sample had been cleaned shortly in ultrasonicated millipore water. The dashed pink rectangle represents the magnified area in the right micrograph.

4.3 Characterization and Processing of Aqueous $LaNi_{0.6}Fe_{0.4}O$ Suspensions into Porous Electrode Layers for Alkaline Water Electrolysis

Characterisation and Processing of Aqueous $LaNi_{0.6}Fe_{0.4}O_3$ Suspensions into Porous Electrode Layers for Alkaline Water Electrolysis

Jens Q. Adolphsen[1]*, Vanesa Gil[2], Bhaskar R. Sudireddy[1], Lennart Bergström[3]

[1]Department of Energy Conversion and Storage, Technical University of Denmark, DK-4000 Roskilde
[2] Aragon Hydrogen Foundation, Parque Tecnológico Walqa Ctra. N330-A Km 566, 22197 Huesca, Spain
Fundación Agencia Aragonesa para la Investigación y Desarrollo (ARAID), Zaragoza, Spain
[3] Department of Materials and Environmental Chemistry, Stockholm University, SE-10691 Stockholm
*Corresponding author (jenqui@dtu.dk)

Abstract

The colloidal properties and processing of aqueous $LaNi_{0.6}Fe_{0.4}O_3$ suspensions into electrode layers with hierarchical pore sizes has been investigated by light scattering, electron microscopy and rheology. We found that the colloidal stability of the oxide particles and the resulting microstructure of the electrode layers were similar when dispersing the particles at their intrinsic pH, or when adding polyvinylpyrrolidone. The addition of the ammonium salt of poly(methaacrylic acid) resulted in a poor colloidal stability and the concentrated suspensions became viscoelastic during processing. Addition of rice starch resulted in an increase of the porosity but the cast electrode layers cracked and delaminated.

Introduction

Energy conversion of electricity into storable chemicals and chemical precursors is one feasible piece in the puzzle of transforming the energy infrastructure, from relying on fossil fuels to being based on renewable energy sources [1–4]. The electrochemical conversion of water into hydrogen and oxygen, water electrolysis, is an example of an energy conversion technology where electricity is used as a driving force to split the water molecules into its constituents. This chemically storable energy can be converted back into electricity for the purpose of grid balancing in an energy system with a high penetration of renewables or used as precursors for synthetic fuel production. Several technologies exist for the electrolysis of water [5], of which the most predominant are alkaline electrolysis cells (AEC) [6,7], proton exchange membrane electrolysis cells (PEMEC) [8,9] and solid oxide electrolysis cells (SOEC) [10]. The AEC technology relies on an alkaline electrolyte to conduct hydroxide ions (OH^-) between the hydrogen and oxygen electrode. The main advantage of AEC over the other two technologies is that noble metal electrocatalysts are not necessary at the electrodes. Drawbacks are that the efficiency of the cells is only modest and current density is lower than in PEMECs and SOECs. An approach to try and combine the pros of the three main water electrolysis technologies is to take an alkaline electrolysis cell and increase the operating temperature from around 80°C to 150-200°C, thus enhancing the electrode kinetics leading to improved efficiency while still not relying on noble metal electrocatalysts [11,12].

However, at these higher temperatures traditional Ni-metal based electrodes, used on the oxygen side of the cell, are not chemically nor mechanically long term stable[13]. It is hypothesized that various metal oxides can replace the Ni-based electrodes and improve stability. Several metal oxides including metal(oxy)hydroxides and perovskites (and related) structures have shown promising electrochemical performance [14,15] but the performance and in particular the stability during realistic operating conditions is not well explored. Metal oxides are also of interest because stable oxide particles can be colloidally processed using conventional ceramic processing methods, e.g. dip coating or screen printing[16,17]. Indeed, the development of colloidal processing routes, to produce metal oxide films with a hierarchical porosity, could allow the electrolyte to be infiltrated into the electrode and allow for efficient gas diffusion of the gases that are produced at the electrode-electrolyte interphase.

Many approaches for tailoring hierarchically porous materials have been reported, but the methods are often limited for generating pores sizes in a certain size range [18–21], and there are only few methods that are suitable to generate a hierarchical pore size distribution [22]. The method selected in this work combines sacrificial templates (referred to as pore formers from here on) with colloidal processing and careful control of the densification process. The larger pores will thus be determined by the size of the sacrificial pore formers and the smaller pores will be determined mainly by the particle size of the dispersed powder and the degree of densification [23]. For the sacrificial pore formers, with sizes in the range 2-10 μm, several materials exist; these include polymeric pore formers such as poly(methyl methacrylate) (PMMA) or polystyrene (PS) microspheres, graphite and starches [24–26]. Starch is attractive from both an environmental and economic point of view, and is easily burned out during sintering. Among the different starches, rice starch is the best option due to its well defined size and spherical shape [27]. One of the main challenges when using sacrificial pore formers is to obtain a percolating porous network and hence eliminate closed porosity after the burnout of the pore formers. Depending on pore former size, shape and distribution in the green body there is a certain volume fraction range, above which closed porosity, is gradually abated [28]. It has been shown that starch consolidation casting (SCC) can solve this problem[28–30]. In SCC the green body undergoes a heating step at 60-80°C before sintering, where the starch swells due to an uptake of water and subsequently undergoes an irreversible crosslinking. The starch is therefore acting as a consolidator and binder in addition to serving as a sacrificial pore former.

In this work, we intend to process the perovskite, $LaNi_{0.6}Fe_{0..4}O_3$ (LNF), into electrode layers in aqueous suspensions using the SCC technique together with a partial sintering to achieve a percolating hierarchical porous network leading to high performance oxygen electrodes. The LNF thus served as both electrocatalyst and electronically conducting backbone material. The aim is to produce a hierarchical pore size distribution consisting of both fine pores < 0.1 μm and larger pores with a size around 2-10 μm. The pores should be interconnected, thus forming a complete percolating phase. The LNF layer will be deposited on a sintered porous support of yttria-stabilised zirconia, which function is to contain the liquid electrolyte while providing mechanical stability to the cell structure.

Materials and Methods

Materials for the ceramic suspensions

The ceramic powder used was $LaNi_{0.6}Fe_{0.4}O_3$ (Kceracell Co, Republic of Korea) with a specific surface area of 12.6 m^2/g. The dispersants were dissolved in Millipore water (resistivity 18.2 MΩ·cm at 25°C) prior to adding the LNF powder. Three dispersants were used: polyvinylpyrrolidone k15 (PVP, Fluka Chemie, Germany) with molecular weight 10,000 g/mol, poly(acrylic acid) (PAA Polysciences Europe GmbH, Germany), 50% solution in water with molecular weight 5,000 g/mol and poly(methacrylic acid) ammonium salt (PMAA, Polysciences Europe GmbH, Germany), 30% solution in water with molecular weight 15,000 g/mol. Rice starch (Sigma Aldrich, Sweden) was added when the LNF powder was well dispersed.

Processing of aqueous suspensions

LNF suspensions for sedimentation analysis, particle size measurements and zeta potential measurements were 5 vol% of solid loading. Ball milling was performed at 25-50 RPM for a minimum of 72 hours using 10 mm spherical 3 mol% yttria stabilised zirconia (3YSZ) beads in a beads to LNF powder ratio of 16:1. The pH of the suspensions was measured with a Seven Excellence™ (Mettler Toledo, Switzerland) pH meter while continuously stirring the suspensions. The pH was adjusted with 1 M NaOH.

The suspensions used for the rheological characterization and further processing contained 19 vol% LNF. Ball milling was carried out with a 5:1 ratio 10 mm cylindrical 3YSZ beads to LNF powder for a minimum of 24 hours before the addition of rice starch. The suspensions with added rice starch were ball milled for another 24 hours. The ready suspensions were applied with a brush on sintered 8 mol.% YSZ substrates. The green layers were dried in a closed water bath for 30 min at 80°C before sintering at 1100 °C for 1 hour with a 60 °C/h heating and cooling rate.

Characterization of rice starch and LNF suspensions

Aqueous suspensions with 5 vol% rice starch were used to measure the particle size of the rice starch in a laser diffraction analyser (Beckman Coulter LS 13 320, USA). In addition the rice starch suspension was drop casted on a Scanning Electron Microscopy (SEM) stub and after drying Au was sputtered on the surface before further analysis in the SEM. The quantification of particle sizes was based on the line-intercept method derived from the theory of stereology taking the average of horizontal and vertical line intercepts. Thermogravimetric analysis (Netzsch STA 409PC/PG, Germany) was carried out from room temperature to 500 °C, using a heating rate of 60 °C/h and an air flow of 50 ml/min, to check the decomposition behaviour.

Particle size measurements were performed with the dynamic light scattering method using a Zetasizer Nano ZS (Malvern Instruments Ltd., UK). Samples were turbid and hence very diluted (~10^{-4} vol%). Zeta potential measurements were also performed with the Zetasizer Nano ZS using laser dopler velocimetry to determine the electrophoretic mobility. Samples were collected from supernatants of suspensions with had been pH adjusted and ball milled before centrifugation.

Sedimentation studies were performed in a Turbiscan lab (Formulaction, France) using the Turbiscan software version 2.2.0.82. The Turbiscan monitors the sedimentation behaviour using light scattering technology. It is equipped with a detector for transmitted light and a detector for backscattered light. The latter allows the sedimentation behaviour of opaque samples to be measured, which implies that compared to manual sedimentation measurements the sedimentation behaviour of more concentrated suspension can be monitored. Samples were loaded to approx. 40 mm height in Ø 27 mm glass vials. Data was recorded at 25 °C every 1 hour for the first 24 h to get an estimation of the sedimentation speed and after this, measurements were recorded every 1-7 days. A more detailed description of the equipment and method can be found in [31].

The rheological characterisation was performed using an Anton Paar MCR 301 rheometer at 25 °C with a concentric cup and cylinder (CC) measuring system. A calibration of the instrument was performed before each set of measurements. Three main steps were carried out for each sample: an amplitude sweep, a frequency sweep and flow curves. A 2 min rotational pre-shear conditioning step (shear rate: 10 s^{-1}) was performed before each step. A pre-strain step was performed before the amplitude sweep and consisted of an initial 2 min pre-strain (amplitude: 0.1%, angular frequency: 10 rad/s) followed by the amplitude sweep (amplitude: 10^{-3}-10 %, angular frequency: 10 rad/s) to determine the linear viscoelastic (LVE) range. Next, another pre-strain was performed before performing the frequency sweep (angular frequency range: 0.1-500 rad/s). Flow curves were measured after the oscillatory measurements at shear rates from 0.1-100 s^{-1} immediately followed by 100-0.1 s^{-1}.

All microstructural characterization was carried out with a JSM-7000F (JEOL Ltd., Japan) field emission scanning electron microscope (FE-SEM) equipped with a schottky type field emission gun. The secondary electron detector was used at a gun voltage of 15 kV.

Results

Materials characteristics:

The micrograph in **Figure 1 a)** shows the rice starch particles. The median volume fraction (d_{50}) of the rice starch is 4.3 μm and the span ($[d_{90}-d_{10}]/d_{50}$) is 0.8 μm. For comparison, the d_{50} of rice starch dispersed in water measured with laser diffraction is 6.5 μm and the span is 1.0 μm. The particle size distribution is shown in **Figure 1 b)**. The thermogravimetric analysis in **Figure 2** shows that complete combustion of the rice starch occurs around 440 °C. Initially, there is a loss of 10%, which is related to adsorbed water, followed by a plateau from 100-240 °C. The rice starch is combusted in two stages: the main part (around 55%) in the interval 240-320 °C and the remaining part from 320-440 °C.

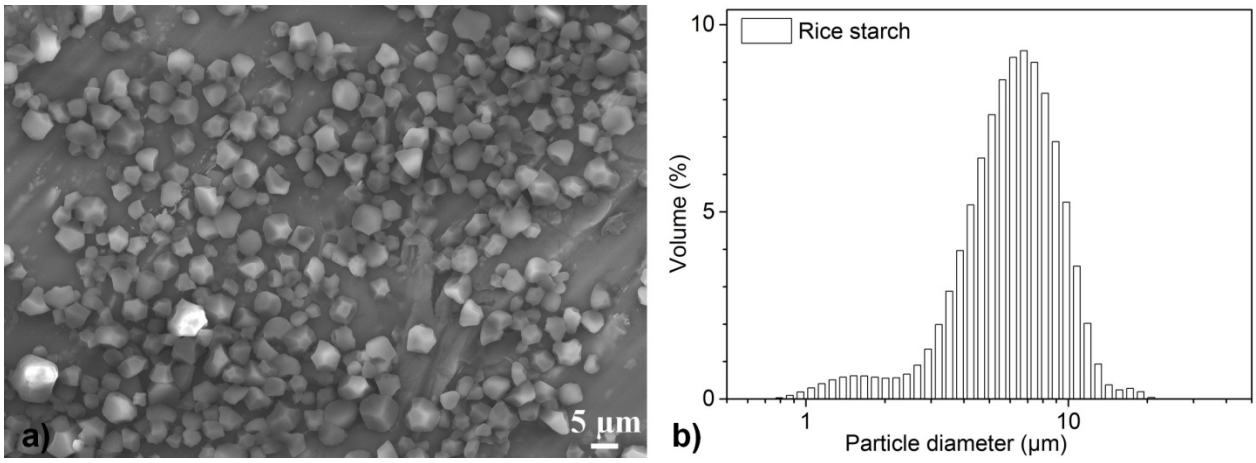

Figure 1 a) SEM micrograph of the rice starch particles. **b)** The laser diffraction particle size measurement of ball milled rice starch dispersed in water.

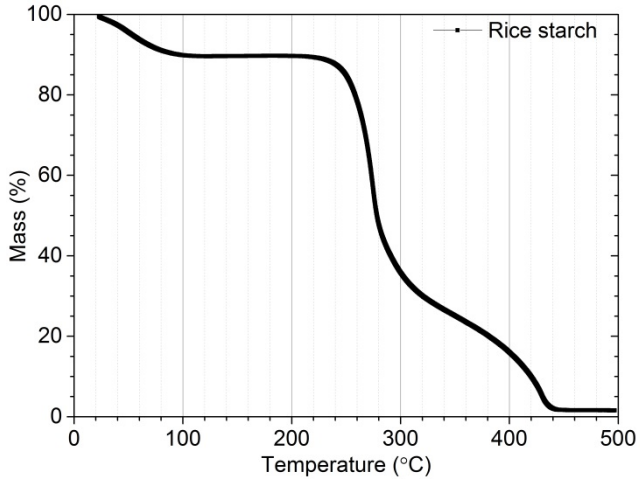

Figure 2 Thermogravimetric analysis of rice starch heated in air.

Particle size measurements for the suspensions

All suspensions referred to in the following are listed in **Table 1**. The LNF-5 and LNF-5-PVP suspensions have a d_{50} of 0.23 µm, which is shown in **Figure 3**. The LNF-5-PMAA suspension exhibit a more narrow distribution with a d_{50} of 0.82 µm. The LNF-5-PAA suspension exhibit a much wider particle size distribution stretching from less than 0.1 µm to several µm.

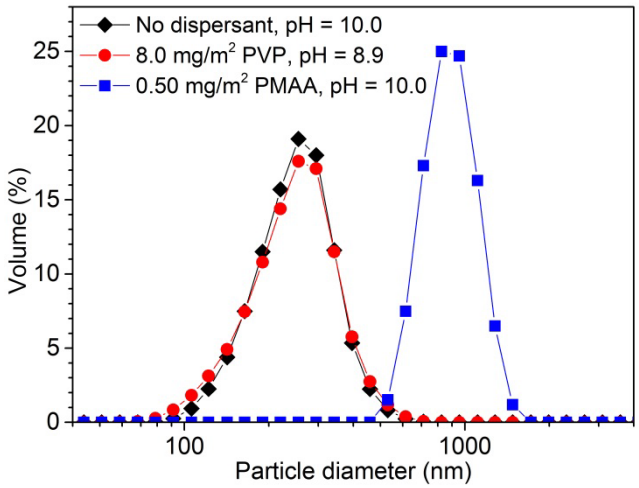

Figure 3 Particle size measurements of LNF without dispersant, PVP and PMAA

Table 1 List of suspensions referred to in the text.

Name	Description
LNF-5	LNF (5 vol%), no dispersant, pH = 10.0
LNF-5-PAA	LNF (5 vol%), 0.5 mg/ m^2 PAA dispersant, pH = 3
LNF-5-PVP	LNF (5 vol%), 8 mg/m^2 PVP dispersant, pH = 8.9
LNF-5-PMAA	LNF (5 vol%), 0.5 mg/m^2 PMAA dispersant, pH = 10.0
LNF-19	LNF (19 vol%), no dispersant
LNF-19-RS-25	LNF (19 vol%), no dispersant, 25 vol% rice starch
LNF-19-PVP	LNF (5 vol%), 5 mg/m^2 PVP dispersant
LNF-19-PVP-RS-X	LNF (5 vol%), 5 mg/m^2 PVP dispersant, 25, 35, 50 vol% rice starch
LNF-10-PMAA	LNF (5 vol%), 0.5 mg/m^2 PMAA dispersant
LNF-10-PMAA-RS-X	LNF (5 vol%), 0.5 mg/m^2 PMAA dispersant, 25, 50 vol% rice starch

.

Zeta potential measurements

The effect of the dispersant loading on the electrostatic stability of the LNF powder and pH of the solution is quantified with the zeta potential measurements; a high zeta potential indicating high electrostatic stability of the suspension. The zeta potential versus dispersant loading, shown in **Figure 4**, is decreasing for all the dispersants with decreasing amount of dispersant loading (expressed as mg dispersant per m^2 oxide powder). The zeta potential is similar for the PAA and PVP stabilised suspensions at comparable dispersant loadings. The zeta potential of the PMAA stabilised suspensions was 15-35 mV lower than the PAA stabilised suspensions with the same dispersant loading. The maximum zeta potential of the LNF-5-PAA stabilised suspensions at the intrinsic pH is 49.0 mV +/- 1.0 mV. The zeta potential of the LNF-5-PVP and LNF-5-PMAA stabilised suspensions prepared at the intrinsic pH is 47.4 mV +/- 1.1 mV and 32.2 mV +/- 2.3 mV, respectively. In comparison, the zeta potential of the LNF-5 dispersion is 47.8 mV +/- 0.5 mV. The measured zeta potentials vs pH are included in **Figure S1**.

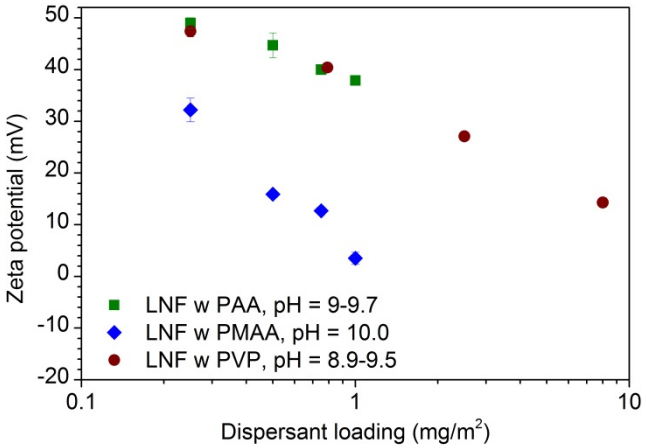

Figure 4 Zeta potential measurements vs dispersant loading.

Sedimentation analysis

The sedimentation analysis of the LNF suspensions, shown in **Figure 5**, without dispersant and stabilized with PVP, showed qualitatively similar behaviour. The backscattering intensity drops gradually, starting from the top of the glass vial and later the back scattering intensity begins to drop uniformly along the entire height of the glass vials. The drop in backscattering intensity along the height of the vial is faster in the case of the suspension with no dispersant. In contrast, the PMAA stabilised suspension shows very little change in the backscattering intensity over time.

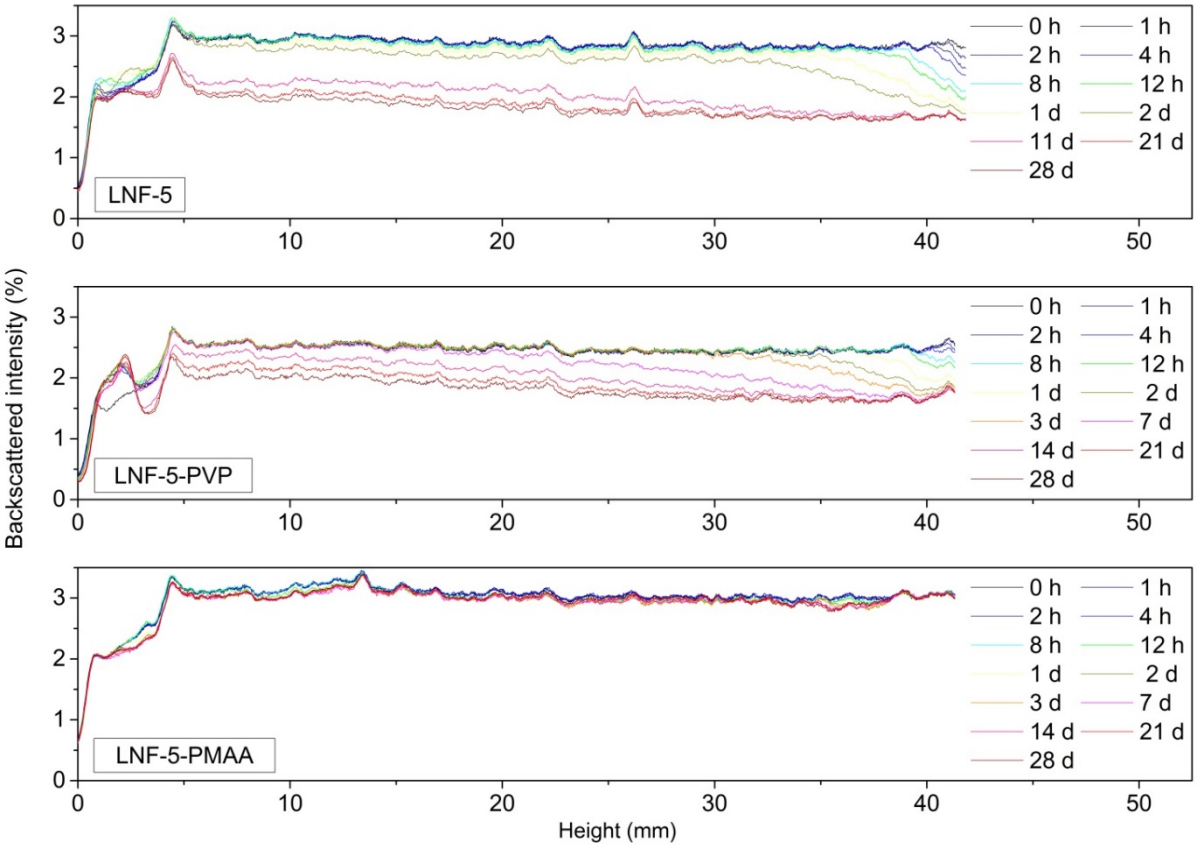

Figure 5 The sedimentation analysis of the 5 vol% LNF suspensions. The backscattered intensity is shown on the second axis and the height from the bottom of the vial on the first axis. Since the suspensions are black and relatively high solid loading the light transmission spectra are not able to depict any significant changes over time.

Rheological characterisation of LNF suspensions

Figure 6 shows that the LNF-19 suspension exhibit a viscosity of approx. 5 x 10^{-3} Pa·s and only little shear thinning. After the addition of rice starch, the dispersion becomes strongly shear thinning and the viscosity increases to 0.4-150 Pa·s depending on the shear rate. The LNF-19-PVP suspension is somewhat shear thinning and exhibits a higher viscosity (10-40 x 10^{-3} Pa·s) than the LNF-19 suspension. With the addition of starch, the viscosity increases to 0.24-6.7 Pa·s and the shear thinning behaviour becomes more pronounced. The LNF-19-PVP suspensions with varying amount of rice starch are very similar both in terms of viscosity and shear thinning behaviour. The LNF-19-PMAA stabilised suspension shows a higher degree of shear thinning, stretching over more than two decades of viscosity, 0.12-36 Pa·s, and the addition of rice starch has little effect on the flow behaviour compared to the LNF-19-PVP suspensions with rice starch.

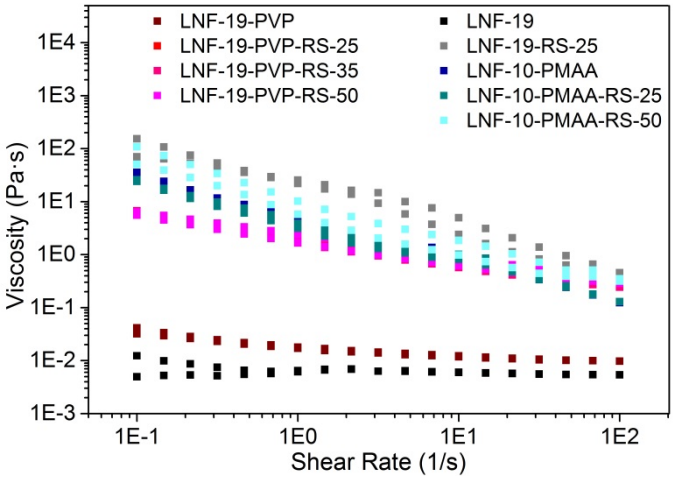

Figure 6 Flow curves of the LNF-19, LNF-10-PMAA and LNF-19-PVP suspensions. A shear thining behaviour is observed in all cases.

The amplitude sweeps, in **Figure 7 a)**, show that the LNF-19 and LNF-19-PVP suspensions display a liquid-like behaviour with negligible storage modulus but after addition of rice starch the dispersions become viscoelastic. The amplitude sweeps of the LNF-19-PVP-25/35/50 suspensions all look similar. The LNF-10-PMAA and LNF-10-PMAA-25/50 all exhibit viscoelastic behaviour as evidenced in **Figure 8 a)**. The LNF-PMAA-RS-50 suspension is seen to have a broader LVE range than the other two suspensions. In **Figure 7 b)** the frequency sweeps of the LNF-19-RS-25 and LNF-19-PVP-RS-25 are shown. The LNF-19-RS-25 suspension is seen to be viscoelastic over the entire angular frequency range, whereas the LNF-19-PVP-RS-25 suspension becomes essentially liquid-like above 50 rad/s in angular frequency. The LNF-10-PMAA suspensions are all viscoelastic over the entire angular frequency range (see **Figure 8 b)**)

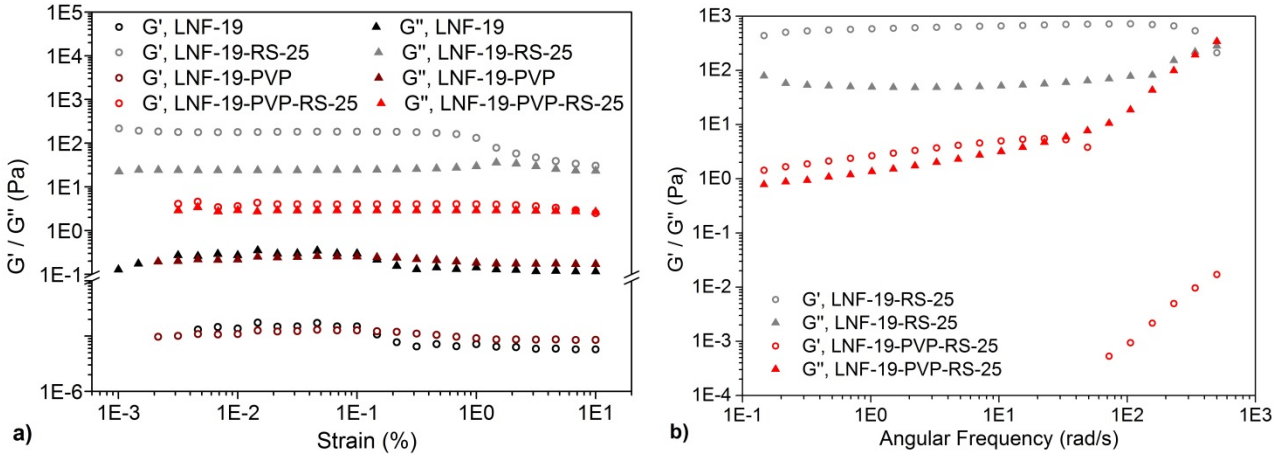

Figure 7 The amplitude sweeps **a)** and frequency sweeps **b)** performed, within the LVE range, on the LNF-19 and LNF-19-PVP suspensions.

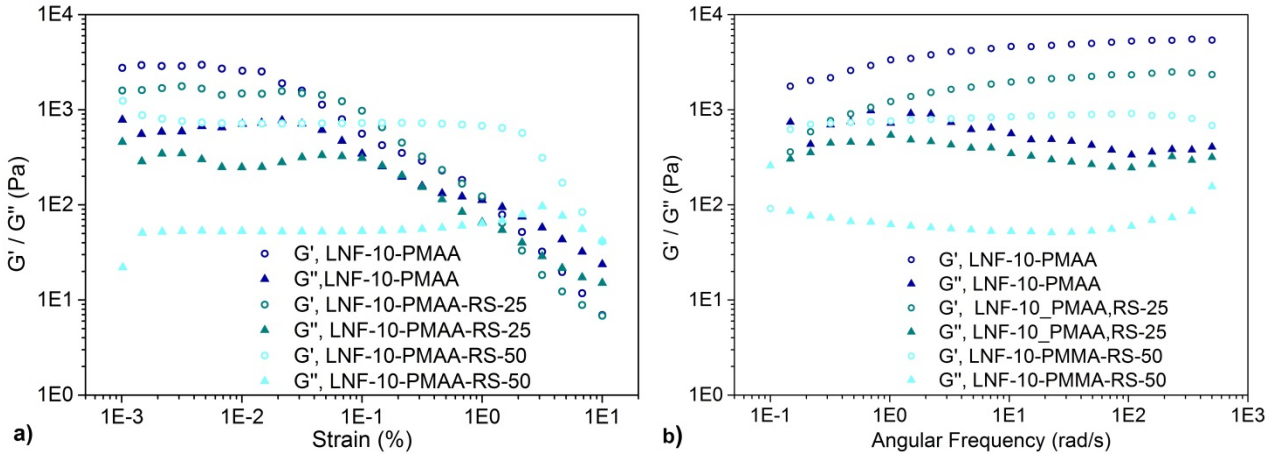

Figure 8 The amplitude sweeps **a)** and frequency sweeps **b)** performed, within the LVE range, on the LNF-10-PMAA suspensions.

Microstructures of porous LNF layers

Figure 9 shows that the microstructures of the sintered LNF layers containing rice starch display a bimodal pore size distribution. The burnout of the rice starch results in large pores that are several μm in size while the interparticle pores that remain after partial sintering, range in size between 50 to several hundred nm. The amount of large macro pores increase with the amount of added starch (**Figure 9**). With 50 vol% rice starch the amount of larger macro pores are seen to increase and hence more likely to form a continuous network. A comparison, of the top surfaces of the sintered layers, shown in **Figure 10**, shows a difference in microstructure depending on the stabilizing agent used. The microstructures of the partially sintered layer prepared from the LNF-19 and LNF-19-PVP suspensions (**Figure 10 a)** and **b)** respectively), look similar; exhibiting homogenous pore size distributions with similar particle sizes. In contrast, the microstructure of the partially sintered layer prepared from the LNF-19-PMAA suspension, shown in **Figure 10 c)**, exhibits a less homogenous surface, compared to **Figure 10 a)** and **b)**, with essentially larger pores and a wider pore size distribution.

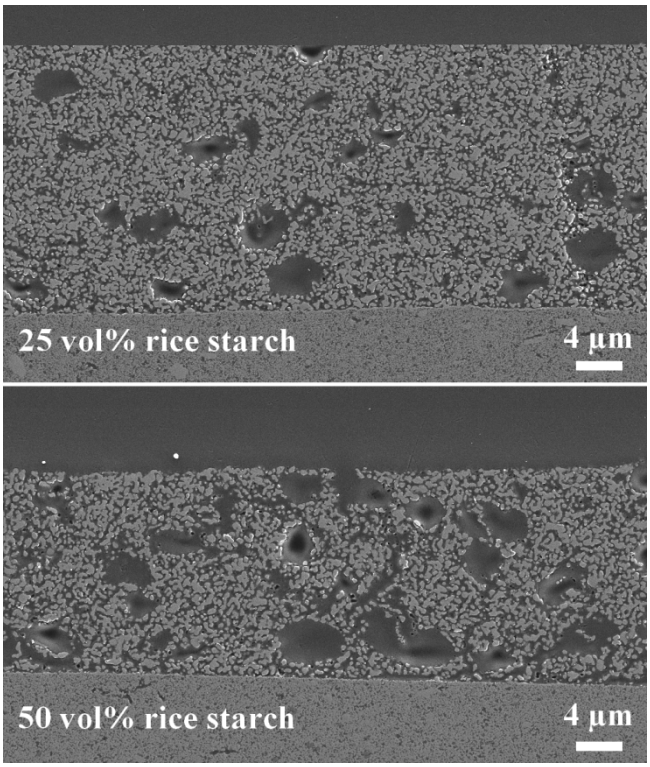

Figure 9 Cross sections of two sintered microstructures (LNF-19-PVP-25 and LNF-19-PVP-50). The larger pores on the micrographs are formed when the rice starch is combusted.

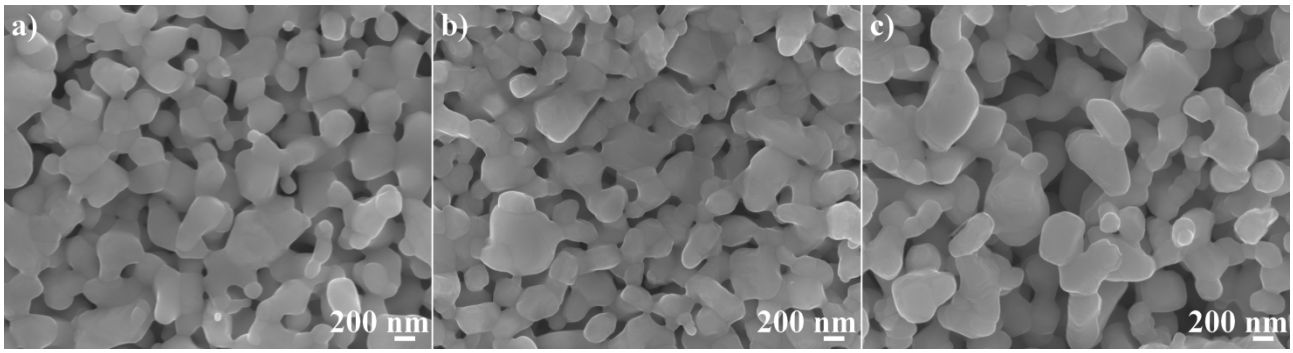

Figure 10 Micrographs showing the top surface of the sintered microstructures. The order is as follows: **a)** LNF-19, **b)** LNF-19-PVP and **c)** LNF-19-PMAA. The micrographs are from a smooth surface area with no large macro pores.

Discussion

Rice starch size distribution

The rice starch suspension analysed using laser diffraction (**Figure 1 b)**) shows a larger d_{50} and a larger span compared to the stereology analysed sample, which is likely a result of agglomerates being present in the first sample. The SEM analysis is hence more representative of the rice starch particle sizes whereas the laser diffraction analysis is representative of the actual sizes of rice starch when dispersed in water and therefore relevant from a processing point of view.

Characteristics of PVP and PMAA stabilised LNF suspensions

The PAA was discarded as dispersant after doing some initial sedimentation, particle size and zeta potential studies. Essentially, addition of PAA showed a similar behaviour at similar pH to that of PMAA, the main difference being that PAA is much more acidic when dissolved in water. The pH of dissolved PAA in water was around 3 which is problematic; LNF not being stable in acidic conditions. The PMAA contain ammonium counter ions, which create a buffered system with an initial pH around 9. It was therefore decided not to use PAA for further investigation.

The particle size distribution changes were insignificant when adding 2.5 or 8.0 mg/m^2 PVP dispersant, and likewise for the addition of 0.50, 0.75 and 1.0 mg/m^2 PMAA dispersant. This suggests that addition of PVP between 2.5 and 8 mg/m^2 and PMAA between 0.5 and 1.0 mg/m^2 should result in robust dispersions with well-defined colloidal properties. In all cases agglomerates on the order of 4-8 μm were observed if the measurement was performed before larger agglomerates had time to sediment. We have used of 5.0 mg/m^2 PVP for the preparation of concentrated suspensions and for PMAA, we used an 0.5 mg/m^2. The somewhat higher amount of PVP was based on past experience working with PVP [31,32], which showed that overloading PVP can be beneficial, as it tends not to impact the processing noteworthy, while providing higher suspension stability.

The LNF-5 contained well dispersed particles and displayed a high zeta potential. The stabilization is probably generated by the high electrostatic repulsion between the particles. The LNF-5-PVP suspension is also well stabilised but with a zeta potential around 20 mV lower than the suspension without dispersant, so here it is clearly the steric hindrance exhibited by the PVP polymers, which also contributes to the stabilization mechanism. In fact, the particle size distribution of the LNF-5-PVP suspension is almost identical to the LNF-5 suspension, which suggests that this is the primary particle size distribution.

The backscattering intensity graphs reveal that sedimentation is taking place. The decrease in the backscattering intensity, shown in **Figure 5,** starts from the top of the vial and progressing downwards over time shows that both the LNF-5-PVP and LNF-5 suspensions sediment slowly. In addition, there are also signs of agglomeration, which is observed as a downward shifting of the backscattering intensity along the whole middle part of the vial height. Two phenomena can cause this shift: the change of effective particle size and effective volume fraction, resulting from the particles agglomerating. Both affect the backscattering intensity leading to either an increase or a decrease depending on the physical characteristics (e.g. size, volume fraction and refractive indices) of the particles in the suspension. In this case it is reasonable to assume that the effective particle size is increasing and the effective volume fraction decreasing over time as a consequence of agglomeration and some sedimentation also taking place. Comparing the LNF-5 and LNF-5-PVP suspensions, it is seen that agglomeration starts occurring slowly during the first day in the LNF-5 suspension and this process is significantly delayed in the LNF-5-PVP suspension. Visible signs of agglomeration are seen after seven days in this case.

The LNF-5-PMAA suspension shows signs of agglomeration taking place initially (see **Figure 5)** but after approx. one day, little change in the backscattering intensity is observed. This is at first surprising since the particle size is in fact larger in the PMAA suspension. In fact, Stoke's sedimentation law [17]

predict the sedimentation time for 0.5 μm LNF particles, sedimenting a 40 mm distance, to be around 1.3 days. It becomes clear what is going on after physically looking at the glass vial with the PMAA suspension. There is a thin layer of solvent at the top but below this the suspension has become a solid paste that does not flow. It is hence clear that the little visible change in the backscattering intensity is not to be interpreted as a well dispersed system but rather as a flocculated system where PMAA is acting as a coagulant catalysing the flocculation process. It is also interesting to note that initially some lower vol% suspensions (1-2 vol%) were prepared and the sedimentation simply observed without the Turbiscan. In this case the PMAA stabilized suspensions showed complete sedimentation after 2 days, which is in accord with Stoke's law. This indicates that the solid loading in this case is too low to form a rigid flocculated system and instead fast sedimentation is observed due to the large particle sizes of the LNF particles.

Rheological properties

The viscosity is low and very liquid-like, and no signs of viscoelastic behaviour are observed for the LNF-19 and LNF-19-PVP suspensions (**Figure 6**). The higher viscosity of the LNF-19-PVP suspension compared to the LNF-19 suspension is likely caused by the fact that PVP is coating the particle surface leading to more drag between particles and that excess PVP is dissolved in the suspension also increasing the viscosity. We had to decrease the particle concentration to 10 vol% when PMAA was used as dispersant as the LNF suspension prepared at 19.0 vol% with PMAA as dispersant did not flow after ball milling. This supports the sedimentation results that using PMAA as dispersant over time leads to the formation of particle gels. The viscoelastic nature of the LNF-10-PMAA suspensions is also clearly observed form **Figure 8 a)** and **b)**. The addition of rice starch, in fact, has very little influence on the resulting rheological properties.

The LNF-19-RS-25 and LNF-19-PVP-RS-25/35/50 exhibit a pronounced change in the rheological behaviour compared to the LNF-19 and LNF-19-PVP suspensions that do not contain any rice starch. The transition from a liquid-like to strongly viscoelastic behaviour with the addition of rice starch is reflected in both the substantial increase of the viscosity and from the decrease of the damping factor from >20,000 to 0.6-0.8 for the LNF-19-PVP suspensions, and from >20,000 to 0.1-0.2 for the LNF-19 suspensions (see **Figure 7 a**). The fact that the G' of the LNF-19-PVP-RS-25/35/50 suspensions drop rapidly when reaching an angular velocity around 50 rad/s suggest that the rice starch is forming a weak network in this suspension. This network is broken up at higher angular velocities and the suspension displays an essentially liquid-like behaviour, evidenced by the damping factor >20,000. The LNF-19-RS-25 suspension shows indications of a similar rapid drop of the storage moduli at the maximum angular frequency but this cannot be confirmed as the maximum measured angular frequency was already very close to the rheometers maximum angular frequency. The LNF-10-PMAA suspensions (**Figure 8 a) and b)**) are less affected by the addition of rice starch. In

Microstructures of sintered LFN layers prepared from PVP and PMAA stabilised suspensions

The fine microstructures of the sintered LNF layers resulting from the LNF-19-RS-25, LNF-19-PVP-RS-25/35/50 and LNF-10-PMAA-RS-25/50 suspensions show, as already mentioned, some noticeable differences in terms of the microstructure. The well-stabilised suspensions (LNF-19-RS-25 and LNF-19-PVP-RS-25/35/50) display a more narrow size distribution of fine macro pores compared to the LNF-19-PMAA-RS-25/50 suspensions. This is likely a result of the denser packing of the particles in

the suspensions without dispersant / with PVP upon deposition compared to the PMAA suspensions. Essentially, this is supporting the statement that the particle network is dominating the PMAA suspensions, which is hindering optimal packing of the particles. The particles in the well-stabilised suspensions (LNF-19-RS-25 and LNF-19-PVP-RS-25/35/50) are much more mobile and therefore also more easily packable into a denser green layer. It is important to mention that the microstructures, which are compared in **Figure 10**, are top surfaces and it is conjectured that these are similar to actual bulk microstructure. The larger macro pores are seen to be well distributed in the cross sections in **Figure 9**. The actual SCC step does not seem to be complete though as the larger macro pores do not seem to be well connected. Also supporting this is the fact that crack formation and in some cases delamination was observed on all samples upon drying. A plausible explanation for the crack formation is that the water in the deposited layer evaporated before it could be heated and absorbed by the rice starch. The arguments are that the deposited sample layer is fairly thin (< 500 μm) and the process of depositing the thin layer, transferring the sample to a water bath and putting the water bath in the oven took a couple of minutes. The delamination is likely a result of the interfacial tension, between the water in the deposited layer and the substrate, being too high. Long chained (360,000 g/mol) PVP was added to improve adhesion between deposited layer and substrate and to limit the crack formation but it only showed marginally better results. More work is therefore required in order to form sintered layers, which do not form cracks nor delaminate. An approach could be to lower the surface tension of the suspension by adding a co-solvent or a surfactant.

Conclusion

Sintered electrode layers of LNF on 8YSZ substrates have been produced from aqueous suspensions containing either no dispersant, PVP or PMAA respectively. The microstructures exhibit pore sizes on two length scales with smaller macro pores (50-200 nm) close to the meso-pore range, left after the sintering, and larger macro pores on the order of 1-8 μm formed by the pore former rice starch. The smaller macro pores look qualitatively similar when using either no dispersant or PVP dispersant. In comparison the use of PMAA results in less densely packed microstructures and the smaller macro pores are also larger and more irregular in this case. The suspensions with PVP and without dispersant are well dispersed, exhibiting similar particle sizes and the suspension stability is adequate in both cases. Further, rheological characterization of suspensions stabilized with PVP show a relatively smaller increase in viscosity and less viscoelastic behaviour after the addition of rice starch compared to the suspensions without dispersant. The PMAA polymer is not dispersing the LNF well; the particle sizes in the suspensions are larger compared to the other two cases and the suspension stability much poorer. The rheological characterization indicates a much higher viscosity and more viscoelastic behaviour for these suspensions regardless of whether rice starch is added or not. We conclude that although colloidal processing could be used to control the pore size distribution in the cast layers, issues of crack formation and delamination remain to be solved.

Acknowledgements

We would like to thank Søren Christensen, Karen Brodersen and Jeanette Krambach from DTU for their help with the tape casting of the 8YSZ substrates. We are also grateful for the helpful on rheology measurements inputs provided by Hugo Voisin, from Stockholm University. Lastly, we would like to

thank the JECS Trust for funding part of the external stay of Jens Q Adolphsen at Stockholm University.

References

[1] M.B. Mogensen, E.S. Jensen, J. Sehested, K. Asberg-Petersen. Technologies for producing hydrogen, in: H. Larsen, R. Feidenhans, L.S. Petersen (Eds.). Risø Energy Report 3. Hydrogen and its Competitors, Forskningscenter Risø, 2004.

[2] J.D. Holladay, J. Hu, D.L. King, Y. Wang. An overview of hydrogen production technologies, Catal. Today. 139 (2009) 244–260.

[3] Fuel Cells and Hydrogen Joint Undertaking (FCH JU). Commercialisation of Energy Storage in Europe: Final report, 2015.

[4] B. V. Mathiesen, H. Lund, D. Connolly, H. Wenzel, P.A. Østergaard, B. Möller, S. Nielsen, I. Ridjan, P. Karnøe, K. Sperling, F.K. Hvelplund. Smart Energy Systems for coherent 100% renewable energy and transport solutions. Appl. Energy. 145 (2015) 139–154.

[5] T. Smolinka, E.T. Ojong, J. Garche. Hydrogen Production from Renewable Energies-Electrolyzer Technologies. in: Electrochemical Energy Storage for Renewable Sources and Grid Balancing., Elsevier, 2014.

[6] K. Zeng, D. Zhang. Recent progress in alkaline water electrolysis for hydrogen production and applications. Prog. Energy Combust. Sci. 36 (2010) 307–326.

[7] D. Pletcher, X. Li. Prospects for alkaline zero gap water electrolysers for hydrogen production. Int. J. Hydrogen Energy. 36 (2011) 15089–15104

[8] M. Carmo, D.L. Fritz, J. Mergel, D. Stolten. A comprehensive review on PEM water electrolysis. Int. J. Hydrogen Energy. 38 (2013) 4901–4934

[9] N.Z. D. Bessarabov, H. Wang, H. Li. PEM Electrolysis for Hydrogen Production: Principles and Applications. first edition, CRC Press, Boca Raton, 2015.

[10] D. Ebbesen, S.H. Jensen, A. Hauch, M.B. Mogensen. High Temperature Electrolysis in Alkaline Cells, Solid Proton Conducting Cells, and Solid Oxide Cells. Chem. Rev. 114 (2014) 10697–10734

[11] J.C. Ganley. High temperature and pressure alkaline electrolysis. Int. J. Hydrog. Energy. 34 (2009) 3604–3611.

[12] F. Allebrod, C. Chatzichristodoulou, M.B. Mogensen. Alkaline electrolysis cell at high temperature and pressure of 250 °C and 42 bar. J. Power Sources. 229 (2013) 22–31.

[13] C. Chatzichristodoulou, F. Allebrod, M.B. Mogensen. High Temperature Alkaline Electrolysis Cells with Metal Foam Based Gas Diffusion Electrodes. J. Electrochem. Soc. 163 (2016) 3036–3040.

[14] D.A. Corrigan. The Catalysis of the Oxygen Evolution Reaction by Iron Impurities in Thin Film Nickel Oxide Electrodes. J. Electrochem. Soc. 134 (1987) 377–384.

[15] A. Grimaud, K.J. May, C.E. Carlton, Y.-L. Lee, M. Risch, W.T. Hong, J. Zhou, Y. Shao-Horn. Double perovskites as a family of highly active catalysts for oxygen evolution in alkaline solution.. Nat. Commun. 4 (2013) 2439.

[16] J.A. Lewis. Colloidal Processing of Ceramics. J. Am. Ceram. Soc. 83 (2000) 2341–2359.

[17] T.A. Ring. Fundamentals of Ceramic Powder Processing and Synthesis. Academic Press Limited, San Diego, 1996.

[18] D. Dong, Y. Huang, X. Zhang, L. He, C.-Z. Li, H. Wang. Shape forming of ceramics with controllable microstructure by drying-free colloidal casting. J. Mater. Chem. 19 (2009) 7070-7074.

[19] P. Colombo, C. Vakifahmetoglu, S. Costacurta. Fabrication of ceramic components with hierarchical porosity. J. Mater. Sci. 45 (2010) 5425–5455.

[20] F. Akhtar, L. Andersson, S. Ogunwumi, N. Hedin, L. Bergström. Structuring adsorbents and catalysts by processing of porous powders. J. Eur. Ceram. Soc. 34 (2014) 1643–1666.

[21] S. Deville. Ice-templating, freeze casting: Beyond materials processing. J. Mater. Res. 28 (2013) 2202–2219.

[22] A.R. Studart, U.T. Gonzenbach, E. Tervoort, L.J. Gauckler. Processing routes to macroporous ceramics: A review. J. Am. Ceram. Soc. 89 (2006) 1771–1789.

[23] H. Shang, A. Mohanram, R.K. Bordia. Densification and Microstructural Evolution of Hierarchically Porous Ceramics during Sintering. J. Am. Ceram. Soc. 98 (2015) 3424–3430.

[24] J.J. Haslam, A.Q. Pham, B.W. Chung, J.F. DiCarlo, R.S. Glass. Effects of the use of pore formers on performance of an anode supported solid oxide fuel cell. J. Am. Ceram. Soc. 88 (2005) 513–518

[25] V. Gil, K.K.K. Hansen. High Performance Infiltrated Backbones for Cathode-Supported SOFC's. ECS Trans. 64 (2014) 41–51.

[26] B. Charlas, C. Grings Schmidt, H. Lund Frandsen, K. Bøhm Andersen, D. Boccaccini, K. Kammer Hansen, A. Roosen, A. Kaiser. Influence of pore former on porosity and mechanical properties of Ce0.9Gd0.1O1.95 electrolytes for flue gas purification. Ceram. Int. 42 (2015) 4546–4555

[27] E. Gregorová, W. Pabst, I. Bohačenko. Characterization of different starch types for their application in ceramic processing. J. Eur. Ceram. Soc. 26 (2006) 1301–1309.

[28] S.F. Corbin, P.S. Apté. Engineered Porosity via Tape Casting, Lamination and the Percolation of Pyrolyzable Particulates. J. Am. Ceram. Soc. 82 (1999) 1693–1701.

[29] J.M.F. Lyckfeldt, O.; Ferreira. Processing of Porous Ceramics by 'Starch Consolidation'. J. Eur. Ceram. Soc. 18 (1998) 131–140.

[30] W. Pabst, E. Gregorová, J. Havrda, E. Týnová, Gelatin Casting and Starch Consolidation of Alumina Ceramics. in: J.G. Heinrich, F. Aldinger (Eds.), Ceram. Mater. Componoents Engines, Wiley-VCH Verlag GmbH, 2001

[31] M. Della Negra, S.P.V. Foghmoes, T. Klemensø. Complementary analysis techniques applied on

optimizing suspensions of yttria stabilized zirconia. Ceram. Int. 42 (2016) 14443–14451.

[32] S. Lakhwani, M.N. Rahaman. Adsorption of polyvinylpyrrolidone (PVP) and its effect on the consolidation of suspensions of nanocrystalline CeO2particles. J. Mater. Sci. 34 (1999) 3909–3912.

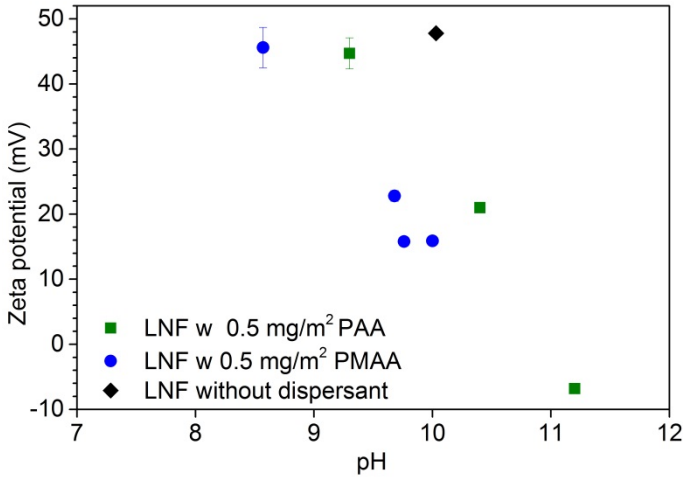

Figure S1 Zeta potential measurements vs pH of suspension.

4.4 Electrochemical Performance of Porous $LaNi_{0.6}Fe_{0.4}O_3$ Oxygen Electrodes for Alkaline Water Electrolysis

Electrochemical Performance of Porous $LaNi_{0.6}Fe_{0.4}O_3$ Oxygen Electrodes for Alkaline Water Electrolysis

Jens Q Adolphsen[1], Karen Brodersen[1], Peter Stanley Jørgensen[1], Christodoulos Chatzichristodoulou[1], Bhaskar R. Sudireddy[1]

[1]Department of Energy Conversion and Storage, Technical University of Denmark, 4000 Roskilde Denmark

Abstract

We present results on the oxygen evolution reaction performance of porous $LaNi_{0.6}Fe_{0.4}O_3$ (LNF) electrodes tested at 25 °C and 65 °C in 8 M KOH. The electrodes remain stable for 10 h of operation and exhibit an overvoltage of 0.43 V and 0.35 V respectively at 0.1 $A \cdot cm^{-2}$. The study concludes that the LNF electrode microstructures make insufficient use of the available surface area, which means the effective current density is significantly higher. This is attributed to oxygen bubble formation on the inner and outer surfaces of the electrode, and to a poor release of these gas bubbles. The LNF electrodes are processed using a conventional ceramic processing method, screen printing, with various graphite and PMMA pore formers, resulting in different microstructures. Image analysis of 2D SEM images shows that the electrodes exhibit porosities in the range of 58-72 % and the mean pore size in the range of 0.61-0.87 μm. A screening of the different microstructures' performance at RT in 1 M KOH shows that microstructural differences are either insignificant or overshadowed by other effects.

Introduction

Electrolysis of water is a sustainable method to produce hydrogen and oxygen without the direct use of fossil fuels. Currently 95 % of all industrially produced hydrogen is based on fossil fuels, produced by means of steam reforming of natural gas, cracking of hydrocarbons in refineries and coal gasification[1,2]. Electrolysis of water is therefore an attractive alternative seen from both an environmental and a global warming perspective[3] assuming the energy mix for electricity production is sufficiently based on renewable sources. The majority of hydrogen today is used to produce ammonia, for hydrocracking and for removing sulphur from fossil fuels. In the future it is likely that more and more hydrogen will be used as a precursor for production of synthetic fuels (e.g. methanol) and also a secondary energy carrier, which can store renewably produced electricity temporarily or be used in fuel cells.

Alkaline electrolysis is currently the most mature technology for non-fossil fuel based hydrogen production[2,4]. The electricity cost is around 50 % of the overall cost of large electrolyser plants (100-1000 kg H_2/day[5]. Increasing the efficiency of the electrolysis cells is an effective means to drive down the electricity cost spent per unit of hydrogen production. Commercial alkaline electrolysis cells possess electric efficiencies with respect to higher heating value (HHV) on the order of 50-80 %, which means

there is room for improvement. In addition running at higher current densities can decrease the required electrode area and thereby costs of materials.

High temperature and pressure alkaline electrolysis cells (HTP-AEC) are electrochemical devices with a novel architecture designed to be operated at high temperature (150-250 °C) and pressure (20-40 bar) [6,7]. The cell is composed of a porous membrane, which contains and immobilizes the electrolyte and two porous electrodes on either side of the porous membrane. The two electrodes are in direct contact with the membrane, hence allowing for transport of electrolyte species between the two electrodes. The HTP-AEC concept has shown very promising performance with a record current density of 3.75 $A \cdot cm^{-2}$ at 1.75 V at 200 °C and 20 bar for a cell with a Ni foam impregnated with polytetrafluoroethylene (PTFE) and Ag nano-wires on the oxygen evolution side and Inconel 625 coated Ni foam on the hydrogen evolution side. A 400 h stability test under similar conditions and with a similar cell, except the Ni foam on the oxygen side was first coated with the corrosion resistant alloy NiFeCrAl, showed stable performance generating 0.5 $A \cdot cm^{-2}$ at 1.5 V. This represents an electrical efficiency with respect to HHV of 98 %. Corrosion resistant electrode materials are critical for the success of the HTP-AECs as experience has proven that conventional metal based electrodes are not chemically and dimensionally stable under OER conditions and therefore ceramic oxide based electrodes are investigated as possible alternatives that can withstand HTP alkaline OER conditions. In particular, various Ni, Co and Fe-based spinel, perovskite and metal (oxy)hydroxides have been investigated as electrocatalysts for the oxygen evolution reaction in (OER) in alkaline media, but focusing on their activity only at standard conditions [8–13]. Few studies have also tested perovskite and spinels as electrocatalysts at more realistic alkaline electrolysis conditions (50-130 °C) and shown stable performance for several hundred hours though the chemical stability is more uncertain and hence also the active phases[14–17].

In the present paper we explore the effects of using different electrode microstructures on the performance of an oxygen electrode. The perovskite $LaNi_{0.6}Fe_{0.4}O_3$ (LNF) is used as conducting electrode backbone and electrocatalyst. The selection of LNF is based on a previous study that characterized La, Ni and Fe based perovskites in terms of their intrinsic electrochemical activity towards the oxygen evolution reaction (OER) and their chemical stability[18]. LNF was not termed suitable for operation at HTP conditions but found to catalyse the OER so here we present results for operation at conventional alkaline electrolysis conditions. The scope of the current study is to investigate the performance-microstructure relationship and stability of porous LNF electrodes. More specifically, LNF electrodes with different microstructures were tested at room temperate and ambient pressure conditions in 1 M KOH and at 25/65 °C in 8 M KOH. The LNF electrodes were deposited on a ca. 300 μm thick porous ceramic oxide membrane and were tested with the electrode facing an electrolyte bath (flooded mode) and with the electrode facing away from the electrolyte (gas diffusion mode). The latter is similar to HTP-AECs as the electrolyte will migrate through the porous space in the ceramic oxide membrane to reach the electrode.

Experimental

Materials – The electrode material, $LaNi_{0.6}Fe_{0.4}O_3$ (LNF) powder was of 99.9% purity and synthesized using solid state reaction by Kceracell (Kceracell Co, Republic of Korea), the membrane material, 3 mol% Y_2O_3 stabilised ZrO_2 (3YSZ) powder (TZ-3Y, Tosoh, Japan) was approx. 99.51% purity (exluding HfO_2) and the additive to membrane material, α-Al_2O_3 powder (Nanocrystalline α-Al_2O_3, Inframat Advanced Materials, USA) was 99.85 % purity. The powder's specific surface areas (SSAs) were determined by the BET method (Autosorb 1-MP, Quantachrome Instruments, USA) using N_2 gas. The powders were degassed for 3 h at 300 °C prior to the measurements. The phase analysis of the LNF powder was carried out using X-ray diffraction (XRD, Bruker Advance D8, operated with a Cu Kα source).

Preparation of 3YSZ backbones – Slurries were prepared by ball milling 63 wt.% of dried 3YSZ powder and 0.5 wt.% of Al_2O_3 powder for 72 h at 50 rpm in an azeotropic methyl ethyl ketone and ethanol solvent mixture (MEKET) using polyvinylpyrrolidone (PVP) k15 BioChemica (PanReac AppliChem GmbH, Germany) as dispersant. Alumina is primarily a sintering aid and will be etched away during operation in KOH. A binder solution, consisting of a polyvinyl butyral resin (Mowital B60H Kuraray, Japan) dissolved in MEKET with the subsequent addition of two plasticizers (Solusolv 2075, Eastman Chemical Company, USA) and Polytethylene glycol (PEG-400 for synthesis, Merck KGaA, Germany) and a (Additol VXL 1105, Allnex, Germany), was added and the slurry was ball milled for an additional 24 h at 25 rpm before filtering the slurry through a 21 μm filter followed by de-airing with a vacuum pump. The viscosity was around 3.6 Pa·s at 4 s^{-1} shear rate. Tape casting was performed with a 1.2 mm gap distance and a 20 $cm \cdot min^{-1}$ casting speed. After drying, the thickness of the tape was around 330 μm. Circular pieces of 32 mm diameter were cut from this tape and heated slowly to 600 °C, held there for 4 h and eventually heated with 102 °C/h to 1100 °C and sintered for 1 h followed by cooling to RT with the same rate.

Characterization of 3YSZmembranes – The open porosity and pore size distribution of 3YSZ membranes was measured using Hg-intrusion porosimetry (Poremaster© GT, Quantachrome Instruments, USA).

LNF ink preparation - Screen printing inks of LNF electrode material were prepared by first dissolving the PVP k15 dispersant in glycol ether solvent. Next, approx. 60 g LNF was added to the solvent dispersant mixture in a 500 mL jar together with 25, 15 mm in diameter, 3YSZ beads. The ink was ball milled for 30 min at 150 rpm in a planetary ball mill (Retsch PM 400, Retsch GmbH, Germany). Additional solvent was added together with graphite pore former (GK V-UF1 99.9%/GK AF Spezial , Graphit Kropfmühl GmbH, Germany). This was ball milled for 15-30 min before adding another pore former, either graphite (GK AF Spezial) or poly(methyl methacrylate) (PMMA, MX-180 / MX-500, Esprix Technologies, USA). After another 15-30 min., the milling beads were removed. PVP binder (PVP k90, Sigma Aldrich Denmark, Denmark) was added in successive steps to increase the viscosity of the ink. This was dissolved in the planetary ball mill with Ø25 mm 3YSZ beads for minimum of 1 h after each addition of PVP k90. Finally, the viscosity was adjusted by extra solvent if needed. The final solid loading of the inks was 16.4-21.7 vol.% LNF. The PVP loading with respect to LNF's surface area (10.7 $m^2 \cdot g^{-1}$) is 4.8 $mg \cdot m^{-2}$.

Ink characterization - The particle size distribution of LNF ink was measured before the addition of pore former, before the addition of binder and in the finished ink using a laser diffraction analyser (Beckman Coulter LS 13 320, Beckman Coulter Inc., USA). The flow behaviour of the inks was measured with a rheometer (MCR 302, Anton Paar, Austria) using a Ø 25 mm polished steel parallel plate geometry with a gap distance of 0.5 mm. Rotational measurements were performed in constant shear rate mode with a set temperature of 21 °C. The programme used consists of some initial conditioning steps with three 120 s interval at 0.1, 0 and 0.1 s^{-1} respectively, followed by a 120 s interval at 1.0 s^{-1}, a 10 s interval at 100 s^{-1} and lastly a 544 s recovery interval at 1.0 s^{-1} to investigate the thixotropic behaviour.

Printing of electrode layers - A DEK 248 (DEK Printing Machines Ltd, England) screen printer was used to deposit Ø20 mm electrode layers onto Ø27.5 mm porously sintered 3YSZ membranes. The screen used had a polyester mesh with 92 mesh per inch and a mesh opening of 174 μm. After deposition, the deposited layers were dried in a furnace at 90 °C for approximately 1 h followed by gradual heating to fully decompose all organics and pore formers before sintering at 1100-1125 °C for 1 h. The sintering profile was similar to the one described above under "Preparation of 3YSZ backbones".

Electrochemical testing – The porous electrodes were tested using chronopotentiometry towards the oxygen evolution reaction (OER) using a Flexcell PTFE rig (Gaskatel GmbH, Germany). A piece of Ni foil was used as current collector and silicone gaskets were used to seal around the electrode. A Ni spiral wire counter electrode was used together with a HydroFlex (Gaskatel GmbH, Germany) reversible hydrogen reference electrode. The electrochemical tests were performed at room temperature (RT) and employed ca. 1 M KOH solution (ACS reagent., >85% KOH basis, Fluka) prepared with Milipore water (18 MΩ cm) as electrolyte. KOH is hygroscopic so the water content can vary considerably. Besides water, the ACS reagent contains ≤ 2.0 % K_2CO_3, ≤0.053% cation and heavy metal traces, ≤0.013% anion traces and ≤0.021% other impurities. The measured pH of the ca. 1 M solution was 14.0. A Gamry Reference 3000 potentiostat (Gamry Instruments, USA) was used. Measurements were also carried out in 35 wt.% KOH (~8 M - referred to as 8 M in the following) at 25 and 65 °C. A Gamry Reference 3000 potentiostat (Gamry Instruments, USA) was used to record the electrochemical test data. Galvanostatic electrochemical impedance spectroscopy (EIS) measurements, from 0.1 to min. 5 kHz, were carried out after each chronopotentiometry measurement to determine the serial resistance which is corrected for in all results. The EIS was also used to determine the electrochemical surface area (ECSA).

Microstructural Characterization of electrodes– Microstructural characterization was performed on sample surfaces and polished cross sections that are imbedded in epoxy and coated with carbon. All micrographs were recorded with a field emission scanning electron microscope (FE-SEM) from Zeiss (Merlin Zeiss, Germany) equipped with a Schottky field emitter gun. Images for quantification of the microstructures were recorded at 3 keV, 201 pA probe current, 2.8-3.0 mm working distance at constant brightness and contrast using the SE2 detector. For each electrode microstructure 20 micrographs were analysed. The micrographs had a pixel size of 13.7 nm and the dimensions were 28 μm x 21 μm. Based on pixel intensity all micrographs were segmented into LNF phase and pore phase using an in-house built MATLAB application (ThreshAlyzer ver. 1.0.1). The threshold value for the segmentation was carried out individually on each image and based on a relative position between the

two peaks in the greyscale intensity spectra. An additional post-processing filter, a morphological closing operation on the segmented data was used to remove very small isolated areas of one phase residing in the other phase. Pore sizes were estimated as the largest circle, which can be fitted into a given pore. Another stereology method, the line intercept method, was used to quantify porosity of the samples. This method was carried out with the semi-automatic ManSeg software which suggests possible intercepts to the user along a straight line on the micrograph[19]. The actual segmentation of a line into segments is, however, performed manually. A total of 3600 segments were sampled on 84 horizontal and vertical lines. The random error per phase and systematic error was estimated as:
Random error per phase = $\sum_i^n (pixel\ size\ \cdot 0.5/segment\ length)$
Systematic error = $(3 \cdot pixel\ size \cdot 0.5)/Mean\ linear\ intercept$
The main advantage of the line intercept method over the threshold analyser method is that the user decides on each intercept between two phases which will avoid some biases arising from automated methods; e.g. quantifying some electrode positioned below the polished surface as electrode area.

For the chemical analysis, energy dispersive X-ray analysis (EDX) was performed with a Quantax XFlash EDX detector (Bruker USA).

Results

LNF inks

In order to generate electrode microstructures with different amount of porosity, various combinations of pore formers were added to the LNF screen printing inks. In **Table 1** the labelled inks are listed with pore former type, size and amount (relative to LNF). The particle size distribution of ink LNF-P3 is shown in **Figure 1.** The distribution is predominantly bimodal in nature. The particle size distribution of LNF-P4 and LNF-P5 is similar to LNF-P3. The particle size distribution of LNF-P3-2 and LNF-P3-3 exhibit a broader second peak extending to 6 μm. The rheological characterization of the inks showed similar flow characteristics. The viscosity of the most viscous ink, LNF-P4, is 3.8 Pa·s at 100 s^{-1} and 41 Pa·s at 1 s^{-1}. Likewise the viscosity of the least viscous ink, LNF-P3-3, is 2.0 at 100 s^{-1} and 28 Pa·s at 1 s^{-1}.

Table 1 The labelling of the LNF inks and the specification of pore former type, size and amount added. The pore former amount is relative to the amount of LNF.

Ink name	Pore former 1 (size)	Pore former 2 (size)	Amount of Pore former 1 (vol. %)	Amount of Pore former 2 (vol. %)
LNF-P3	Graphite V-UV1 (d50 =2.8 μm)	PMMA MX-180 (d50 = 1.9 μm)	25	25
LNF P3-2	Graphite V-UV1 (d50 =2.8 μm)	PMMA MX-180 (d50 = 1.9 μm)	32.5	32.5
LNF-P3-3	Graphite V-UV1 (d50 =2.8 μm)	PMMA MX-180 (d50 = 1.9 μm)	40	40
LNF-P4	Graphite AF spezial (d50 = 6-8.5 μm)	PMMA MX-500 (d50 = 5.0 μm)	25	25
LNF-P5	Graphite V-UV1 (d50 =2.8 μm)	Graphite AF spezial (d50 = 6-8.5 μm)	25	25

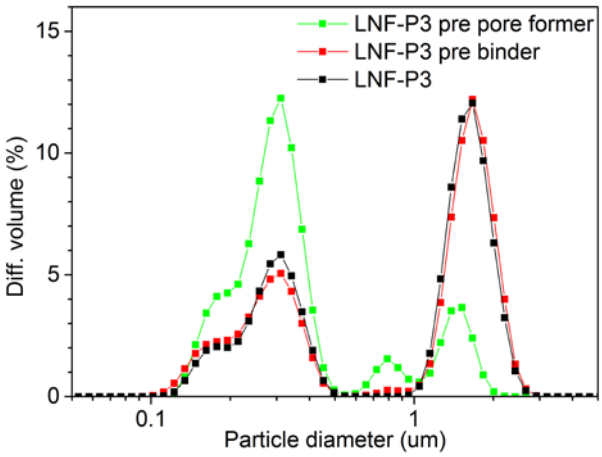

Figure 1 The particle size distribution of LNF-P3 ink before adding pore formers, before adding binder and in the finished ink.

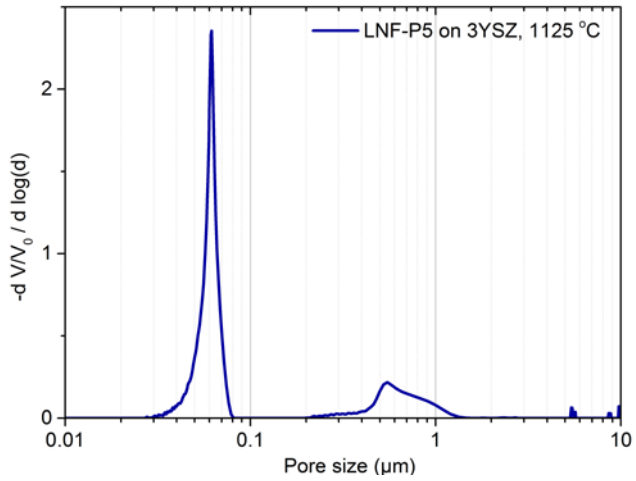

Figure 2 Pore size distribution of LNF-P5 on the 3YSZ membrane sintered at 1125 °C.

The microstructure of sintered 3YSZ membranes and LNF electrodes

The sintered 3YSZ membranes are approx. 270 µm thick. The porosity of membranes sintered at 1100 °C, 1115 °C and 1125 °C is 40 %, 32 % and 28 % respectively. The pore size distribution of LNF-P5_1125 (see **Table 2)** on 3YSZ membrane is shown in **Figure 2**. The main peak, associated with the 3YSZ membrane, is approx. at 60 nm and increased to approx. 70 nm for samples sintered at 1100 °C. The second peak, from 0.2-1.2 µm, is associated with the electrode layer on top of the membrane. Porosimetry measurements with no electrode layer confirm this (See **Figure S1**).

The electrodes from different inks were sintered at two different temperatures, 1100 °C and 1125 °C for 1 h in air. The investigated electrodes are labelled as show in **Table 2**, the number after the underscore being the sintering temperature. The average electrode layer thickness differs among the different microstructures; LNF-P3_1125 and LNF P4_1125 being the thinnest electrodes and LNF-P3-2_1100 and LNF-P3-3_1100 being the thickest as shown in **Table 2**. The sintered LNF layers on 3YSZ membranes show good adhesion with no signs of delamination. LNF-P5_1125 °C showed an enhanced

densification in the interface between the 3YSZ membrane and the LNF electrode which is indicated by the dashed pink lines in **Figure 3**. Similar behaviour is observed for all other electrodes. After sintering at 1100 °C similar densification behaviour, with a slightly thinner densified layer, was observed.

Table 2 The main parameters characterizing the porous phase of electrodes sintered at either 1100 °C or 1125 °C. Results are obtained with the image segmentation method (ThresAlyzer).

Electrode name	Electrode thickness (μm)	Porosity (%)	d10 (μm)	d50 (μm)	d90 (μm)
LNF-P3_1125	24 ± 2.0	60 ± 2.4	0.19 ± 0.009	0.61 ± 0.021	1.6 ± 0.03
LNF-P4_1125	25 ± 2.0	58 ± 3.4	0.19 ± 0.008	0.72 ± 0.019	3.5 ± 0.05
LNF-P5_1125	32 ± 3.5	62 ± 1.9	0.22 ± 0.005	0.66 ± 0.014	1.6 ± 0.03
LNF-P3_1100	27 ± 4.4	65 ± 1.0	0.22 ± 0.004	0.61 ± 0.011	1.5 ± 0.03
LNF-P3-2_1100	38 ± 8.2	69 ± 1.3	0.24 ± 0.004	0.72 ± 0.013	1.5 ± 0.03
LNF-P3-3_1100	37 ± 7.1	72 ± 1.0	0.28 ± 0.003	0.87 ± 0.012	1.7 ± 0.03

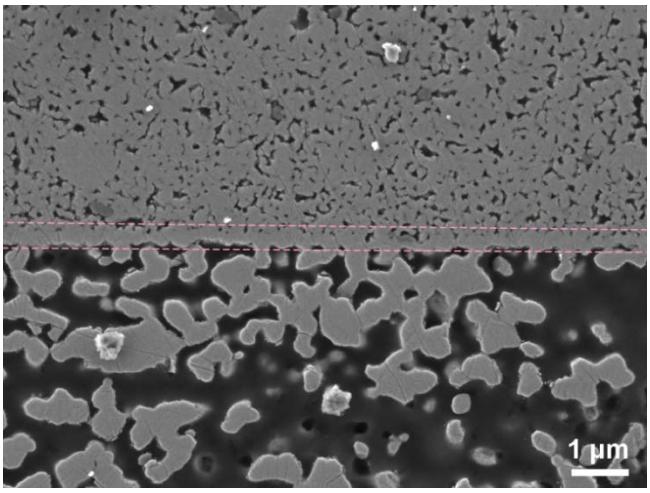

Figure 3 A polished cross section of the interface between the 3YSZ membrane (top) and the porous LNF-P5 electrode (bottom) sintered at 1125 °C. A higher densification is observed in the interface, between the dashed pink lines, than elsewhere.

The microstructures that came out of the inks prepared (cf. **Table 1**), LNF-P3_1125, LNF-P4_1125 and LNF-P5_1125, are compared in **Figure 4.** The effect of using different pore formers is reflected in the microstructures: The LNF-P3_1125 has larger round and elongated pores, 1-3 μm in size, which are well interconnected; the LNF-P4_1125 has larger round and elongated pores on the order of 2-15 μm which are less interconnected and the LNF-P5_1125 has few large elongated pores that are up to 15 μm in length and also many smaller interconnecting pores which are 1-3 μm in size. All microstructures also have inter-grain porosity with pore sizes approx. 0.1-0.3 μm. The micrographs in **Figure 4** are also

examples of microstructures that have been used to quantify the porosity and pore size distribution of the different electrodes. The porosity, d10, d50 and d90 of the pore size distribution are also listed in **Table 2**. It is observed that the porosity for microstructures with the same amount of pore former and the same sintering temperature (LNF-P3_1125, LNF-P4_1125 and LNF-P5_1125) is similar. When the sintering temperature is lowered from 1125 °C to 1100 °C the porosity increases by 5 % for LNF-P3. Likewise the porosity is seen to increase from 65 % to 69 % to 72 % when increasing the amount of pore formers from 50 vol.% to 65 vol.% to 80 vol.%. The pore size distributions of LNF-P3_1125 and LNF-P5_1125 are relatively similar whereas LNF-P4_1125 has a significantly larger d90. For the LNF-P3_1100, LNF-P3-2_1100 and LNF-P3-3_1100, it is observed that the d10, d50 and d90 all increase with increasing amount of pore former.

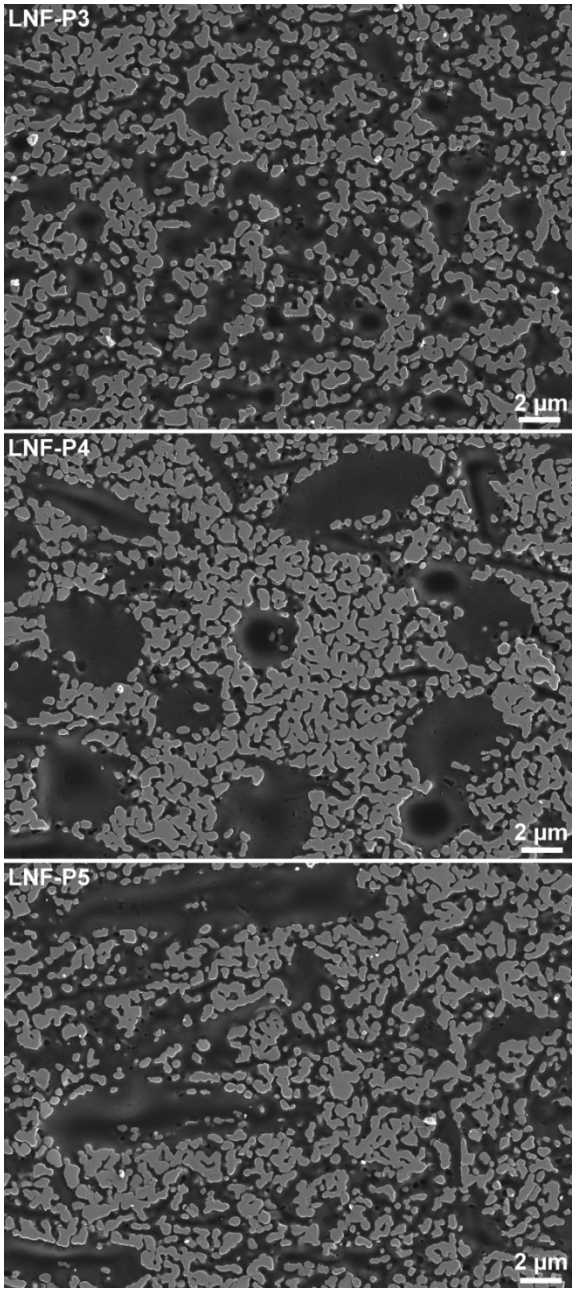

Figure 4 Polished cross sections of the LNF-P3, LNF-P4 and LNF-P5 electrode microstructures sintered at 1125 °C

Electrochemical activity of electrodes at RT in 1 M KOH

The electrochemical activity of the various electrodes listed in **Table 2** are tested at RT and pressure with the electrode facing the electrolyte bath (flooded mode) or with the electrode facing towards ambient air, away from the electrolyte bath (gas diffusion mode), implying that the electrolyte has to migrate through the porous 3YSZ membrane reach the electrode. No systematic approach as to what mode is tested first has been used.

The chronopotentiometry measurements are summarized in **Figure 5 a)** and **b)** The overpotential is generally lower for all samples when testing them as flooded electrodes compared to as gas diffusion electrodes. All electrodes exhibit similar overpotential, as flooded or as gas diffusion electrodes, up to around 2 mA cm^{-2}; above this value the performances begin to differ substantially – especially in the flooded mode. The LNF-P3 electrode was tested after sintering at both 1100 °C and 1125 °C and the performance was seen to improve with decreasing sintering temperature. The electrodes with an increasing amount of pore former, (LNF-P3, LNF-P3-2 and LNF-P3-3) sintered at 1100 °C are seen to perform better than the electrodes sintered at 1125 °C. In the gas diffusion mode the measurements were stopped at either 25 mA cm^{-2} or 50 mA cm^{-2} due to a sudden large increase in the overpotential. In the flooded mode this effect was not seen until 100 mA cm^{-2}.

The ECSAs, quantified from the double layer capacitance, for the respective samples are shown in **Figure 5 c)** and **d)**. In all cases it is seen to (eventually) decrease with increasing current density. In the flooded mode this decrease is far more pronounced than in the gas diffusion mode. It is also clear that the ECSA is well correlated with performance, i.e., the LNF-P3-1125 and LNF-P3_1100 samples tested in the flooded mode exhibit the highest and lowest overpotential respectively and the ECSA of the former is decreased to approximately unity around 5 mA cm^{-2} whereas the ECSA of the latter remains above 100 up to 25 mA cm^{-2}. The reproducibility of the results shown in **Figure 5** is not good. In each case at least two samples were tested in both modes. Performance varied significantly from sample to sample which is shown in **Figure S2** where the performance of two different LNF-P5_1125 samples has been included in**.** The sample exhibiting the best overall performance in both modes is included in **Figure 5.**

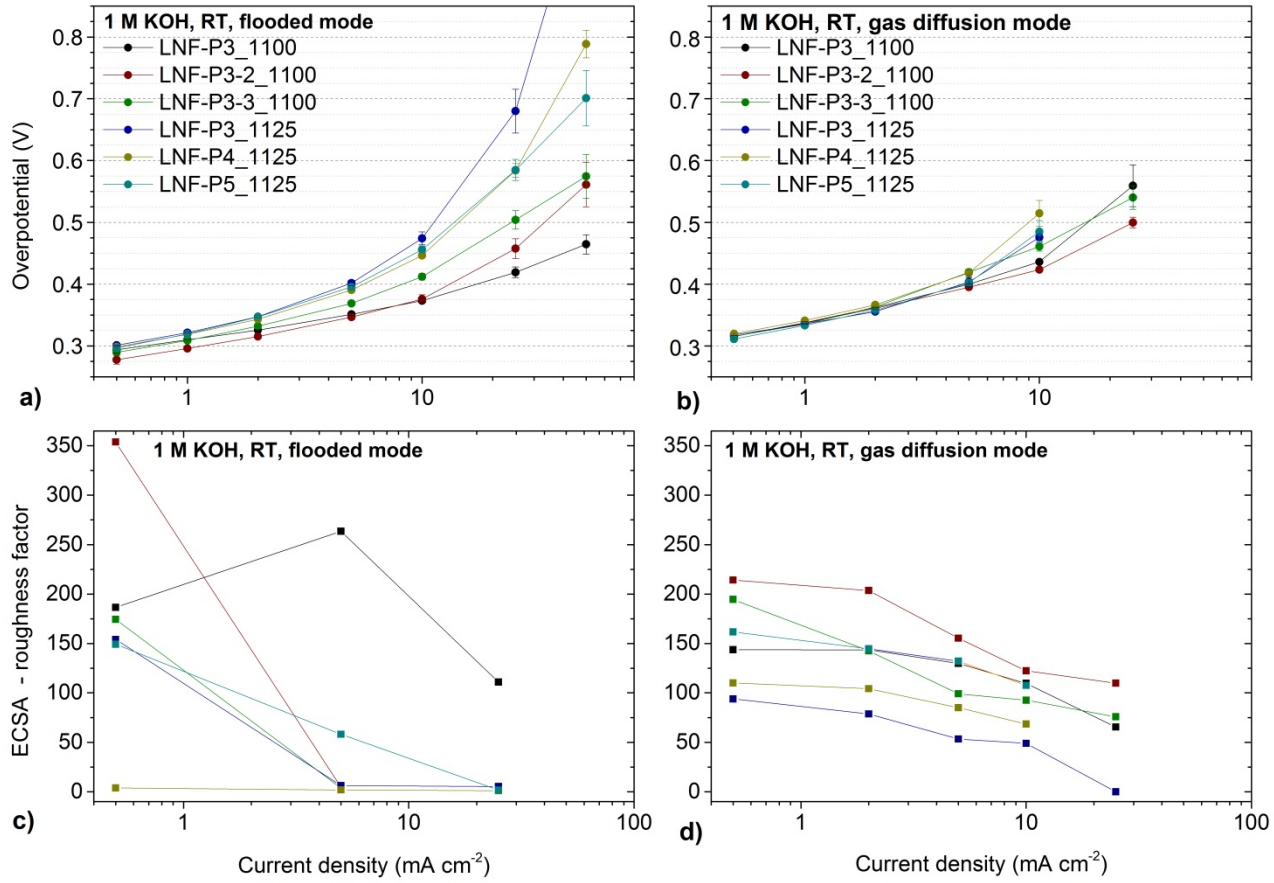

Figure 5 The overpotential vs current density of the LNF electrodes tested in the flooded mode (a) and in the gas diffusion mode (b) in 1 M KOH at RT. The same sample was used for each test. The ECSA for the flooded test and gas diffusion test is shown in(c) and (d) respectively.

Electrode performance of LNF-P3_1100/LNF-P3_1125 tested at 65 °C in 8 M KOH

LNF-P3 electrodes sintered at 1100 °C and 1125 °C have been tested in 8 M KOH at 25 °C and 65 °C. The chronopotentiometry measurements and associated galvanostatic EIS measurements of LNF-P3_1125 in flooded and gas diffusion mode at 65 °C in 8 M KOH are shown in **Figure 6 a)** to **d).** The performance is seen to be similar though slightly better at high current density in the flooded mode. Fluctuations of the data points increase, with increasing current density. This is also reflected in the EIS measurements (see **Figure 6 c)** and **d)**), which are very noisy in the flooded mode and above 25 mA cm^{-2} they can generally only be used to determine the serial resistance. In both the flooded and the gas diffusion mode two arcs can be identified. The low frequency arc is dominating and both arcs shrink with increasing current density or overpotential.

The performance of the LNF-P3_1100 and LNF-P3_1125 electrodes in the flooded and gas diffusion modes is shown in **Figure 7 a)** and **b)**, respectively. The IV-curves are relatively straight up to 10 $mA \cdot cm^{-2}$ after which the slope increases. In the gas diffusion mode at 65 °C the LNF-P3_1100/1125 electrodes exhibit similar performance up to 10 mA cm^{-2} after which the LNF-P3_1100 exhibits better performance. The LNF-P3_1100 sample broke during the sample mounting for 25 °C test and hence

no data is recorded. In the flooded mode the LNF-P3 electrodes exhibit similar performance at 65 °C whereas the LNF-P3_1100 electrode performs better than the LNF-P3_1125 electrode above 25 mA cm^{-2}. In the flooded mode the overpotential decreases with approximately 80 mV from 25 °C to 65 °C. In the gas diffusion electrode configuration a 100-160 mV decrease of the overpotential is observed from 25 °C to 65 °C. The performance of the LNF-P3_1100 electrode at 65 °C is seen to be slightly higher in the gas diffusion mode compared to in the flooded mode at current densities above 10 mA cm^{-2}. For the LNF-P3_1125 it is vice versa in the gas diffusion and flooded modes. The ECSA, shown in **Figure 7 c)** and **d)**, is higher initially compared to that in **Figure 5 c)** and **d)** and the drop is also smaller at comparable current densities.

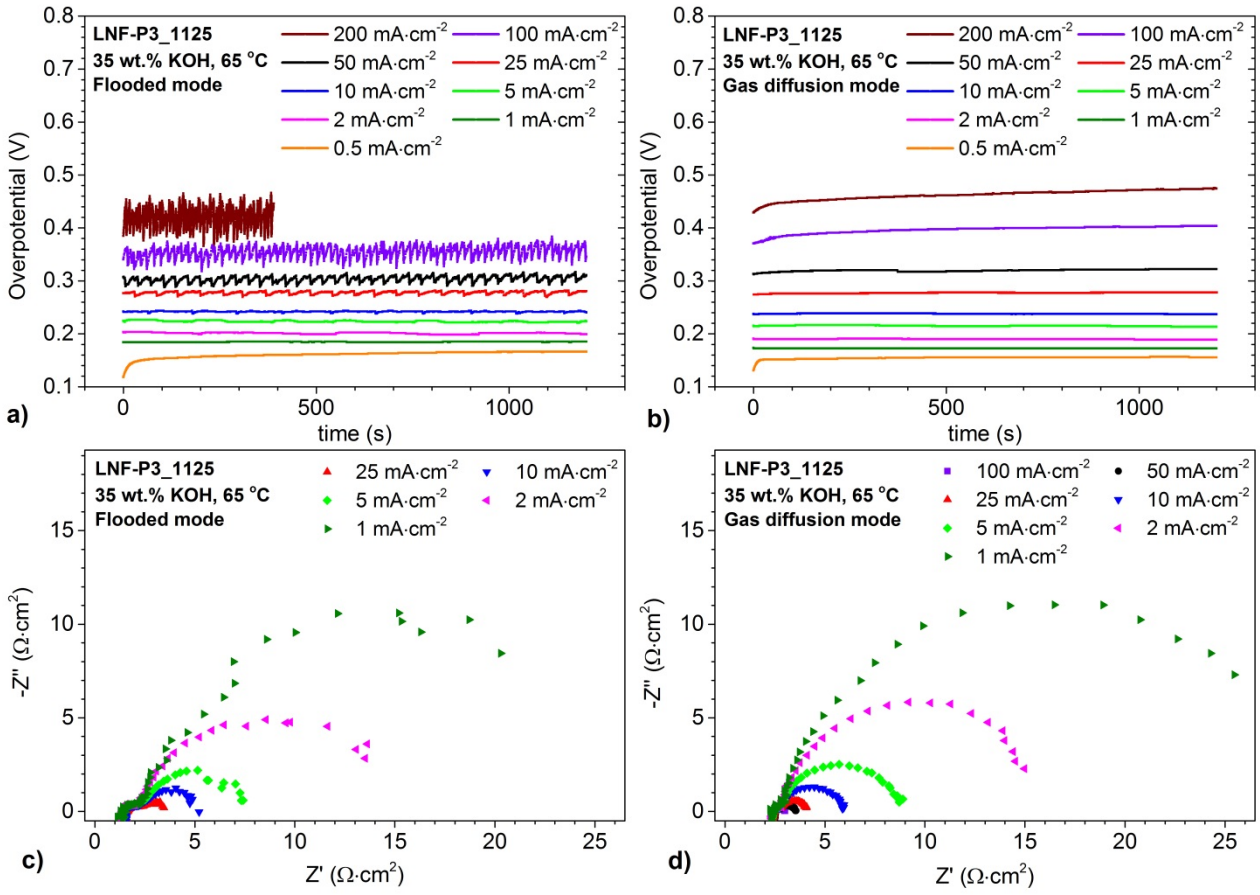

Figure 6 The chronopotentiometry measurements in the flooded mode, a), and the gas diffusion mode, b), of LNF-P3_1125 tested at 65 °C in 8 M KOH. The associated amperostatic EIS measurements are seen in c) and d). The 200 mA cm^{-2} test in a) was stopped prematurely due to a sudden increase in overpotential. In the flooded mode the EIS are generally very noisy so EIS results above 25 mA cm^{-2} are not shown. Randomly scattered data points have also been excluded. The EIS at 0.5 mA cm^{-2} is excluded to allow for better scaling of the axis.

It is observed that the increase in KOH concentration improves the electrode performance (**Figure 7)** compared to the 1M KOH measurements shown in **Figure 5.** It is also observed but not shown that the electrodes tested in 8 M KOH in the gas diffusion mode exhibit considerable less transient increase of the overpotential over time at high current densities compared to the 1 M KOH tests.

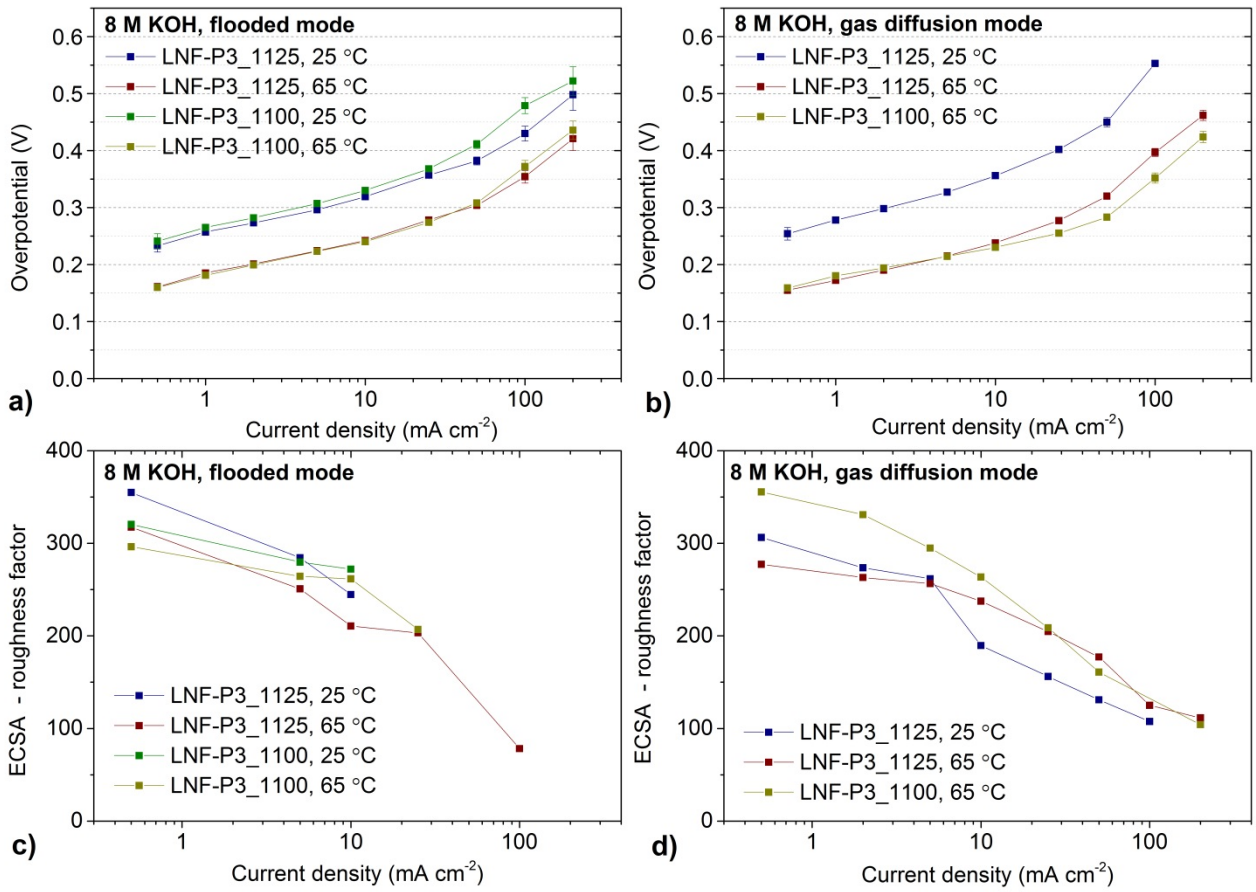

Figure 7 The overpotential vs current density of the LNF-P3_1125 and LNF-P3_1100 electrodes tested at 25 °C and 65 °C in the flooded and gas diffusion configuration in a 8 M KOH solution. The LNF-P3_1100 sample cracked prior to the test in the gas diffusion mode at 25 °C and no data is therefore included.

Characterization of LNF-P3_1100 / LNF-P3_1125 electrodes tested at 65 °C in 8 M KOH

A polished cross section and the top surface of the LNF-P3_1125 electrode before, **a)** and **b)**, and after ,**c)** and **d)**, testing for approx. 10 h at 65 °C is compared in **Figure 8**. The microstructure of the polished cross section appears unaffected by the testing but the top surface of the electrode in **Figure 8 d)** appear covered with something after testing. In addition, some small particles, less than 50 nm in size, lie scattered across the surface. These are too small to distinguish using EDX. Moreover, the particles were neither detected on the polished cross section nor were they found on the LNF-P3_1100 electrode surfaces. The EDX mapping shows that the relative fraction of La:Ni:Fe:O is constant before vs after testing and is representative of the LNF phase. The mapping also revealed ~2.5 at.% K after testing and none before testing. The LNF-P3_1100 electrode was structurally affected by the testing as small pieces of the electrode surface broke off during the flooded test at 65 °C and were found in the electrode chamber. As this was the first test, the subsequent tests were carried out with slightly altered electrode. The exposed and cracked surface did not reveal the underlying 3YSZ membrane and a polished cross section revealed no mechanical damage to the remaining electrode microstructure. The electrochemical stability of the LNF-P3_1125 electrode, assessed using XRD analysis, showed no secondary phase formation after polarization towards the OER for approx. 10 h at 65 °C. The comparison of XRD patterns for LNF-P3_1125 electrode before and after testing is shown in **Figure 9**

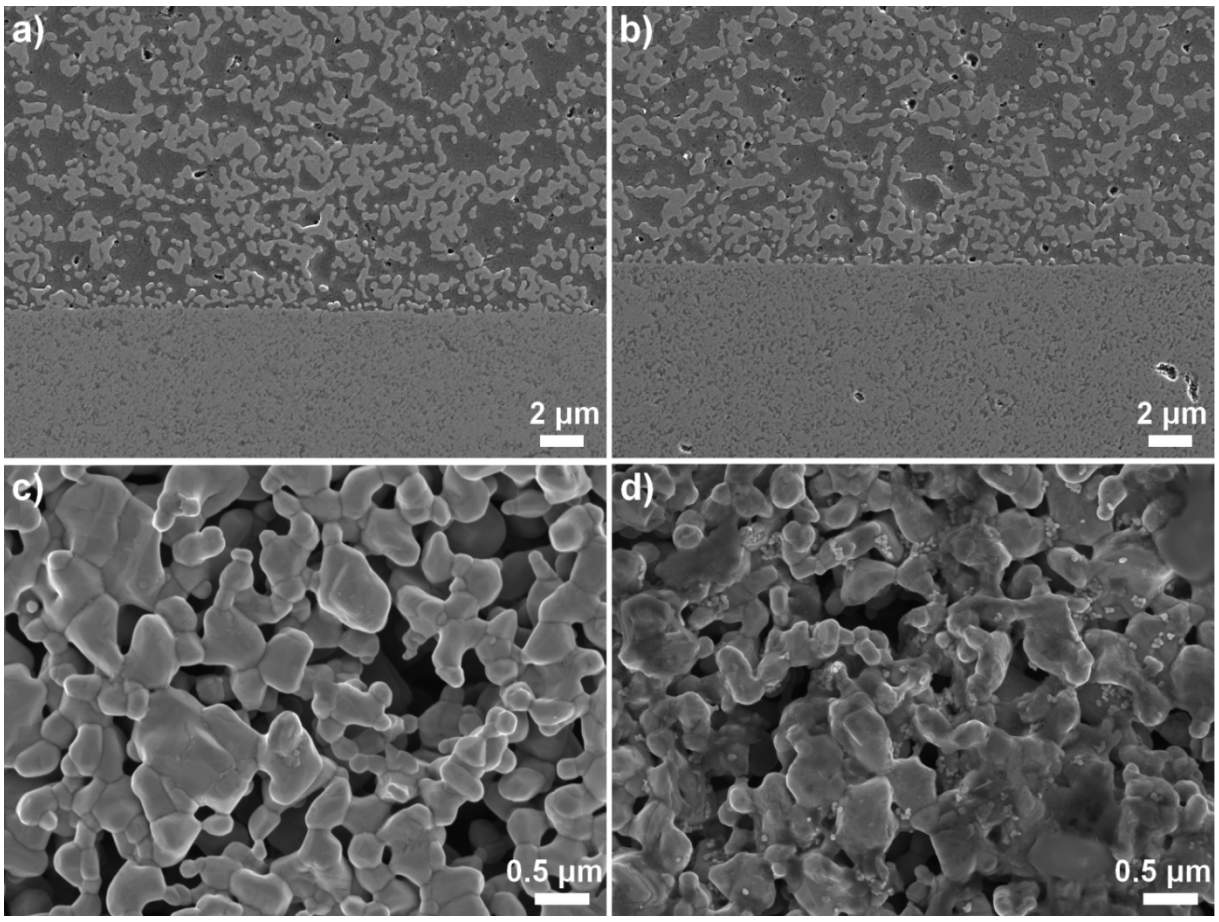

Figure 8 Polished cross sections of the LNF-P3_1125 electrode tested at 65 °C before a) and after testing (b). Similarly top surface of the electrode is shown before c) and after testing d).

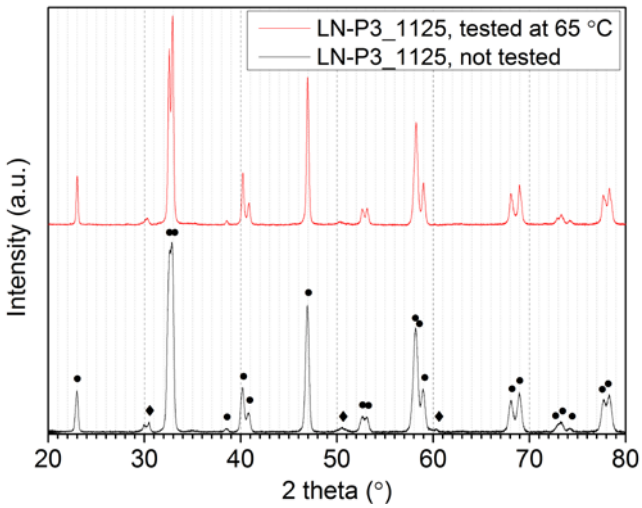

Figure 9 XRD analysis of the tested and non-tested LNF-P3_1125 electrode. The ● correspond to the LNF phase and the ♦ to 3YSZ phase.

Discussion

LNF electrode development

The LNF powder is well dispersed in the screen printing inks. The data in **Figure 1** suggests that most of the LNF particles are 0.1-0.5 μm in size with a few larger agglomerates. The addition of the pore formers is seen to increase the particle sizes in the ink. A bimodal particle size distribution is observed. The peak at 1-3 μm contains approx. 60 % of the total volume, suggesting some agglomerates of LNF are also formed since LNF accounts for 67 % of the solid volume. The bimodal particle size distribution is expected to lead to a bimodal pore size distribution in the sintered electrode with smaller pores and larger pores caused by the partial sintering and presence of pore formers respectively. The addition of the binder leads to no additional increases of the particle sizes, suggesting it only acts as a viscosity enhancing agent in the ink. The LNF-P4 and LNF-P5 inks contain pore formers with d50 > 6 μm but exhibited similar particle size distributions as the LNF-P3 ink, which suggest that the pore former sizes are decreased by planetary ball milling.

The rheological characterization of the inks was carried out to quality check the viscosity of the inks at low (1 s^{-1}) and high (100 s^{-1}) shear rate and to determine any thixotropic behaviour of the inks. A thixotropic behaviour is expected to be beneficial for the generation of a smooth printed surface. A similar thixotropic behaviour is observed for all inks though the more viscous inks have a higher thixotropy index (see [20]). In practice the thixotropic effect was limited as the pattern of the screen, which the inks were printed through, was visible in a microscope after drying. The sintered electrode thickness varies significantly as shown in **Table 2**, and it is observed that the less viscous inks, also the one with lowest solid loading of LNF and pore formers, print thicker than the more viscous inks. There is also variation in printed thickness across the same sample and again this variation is most pronounced on electrodes processed with the least viscous inks. Another factor leading to unevenness of the electrode layers is the 3SYZ membranes which thickness and flatness varies. This also helps explains the variations in printed thickness across the same samples.

The microstructure of the 3YSZ membranes

The 3YSZ membranes should ideally be as porous as possible while maintaining sufficient mechanical integrity. The membranes sintered at 1125 °C have a porosity of 28 % and are sufficiently strong. The membranes sintered at 1100 °C had significantly higher porosity, 40 %, and though this also compromises the mechanical integrity (they cracked more easily) it is preferable because it gives more space to the electrolyte which will have a higher effective conductivity in a more porous sample.

Microstructural characterization of LNF electrodes

The sintered electrodes, based on different inks, possess different microstructures which is evident from **Figure 4**. Round pores, found in the LNF-P3_1100/1125 and LNF-P4_1125 samples, reflect the use of different sizes of PMMA. The elongated pores, found in all three microstructures reflect the use of graphite as pore formers. It is noticed that the relatively few large pores are found in the LNF-P5_1125 microstructures suggesting that graphite is being broken up into smaller pieces during ink preparation. All three microstructures have same total amount of pore former and also exhibit similar porosities. A lowering of the sintering temperature is seen to increase the porosity of LNF-P3_1100

compared to LNF-P3_1125 due to less densification in between the LNF particles. Similarly the porosity is increased with an increasing amount of pore former fraction. In this case it is, interestingly enough, also mainly the smaller pore sizes increasing. The enhanced densification at the 3YSZ-LNF interface could be due to a reaction between elements from the two phases at their interface. It is known that $La_2Zr_2O_7$ formation occurs already at 1000 °C in the interface of 8 mol% YSZ and LNF[21] and EDX analysis also confirmed the presence of both La and Zr in the interphase. It is, however not known whether the $La_2Zr_2O_7$ phase will lead to enhanced densification. It is also possible that Fe from the LNF act as a sintering aid for the 3YSZ or Al for the LNF in the interphase. The electrochemical measurements do not suggest the densification to be a severe issue though.

The microstructural characterization of the electrodes using the semiautomatic threshold image analyser to segment the images has been compared to the line intercept method which provides mathematically accurate relations between the 1D segment lengths and 3D porosity[22]. The comparison was made for LNF-P3-1125 and gave a porosity of 60 % in each case but with a standard deviation of 7.5 % for the line intercept method compared to 2.4 % for threshold analyser method. The standard deviation of the line intercept method is significantly larger which is explained by the distribution of the pores in the microstructure. The larger micro-meter sized pores created by the combustion of the pore formers are not distributed homogenously and hence create a large deviation in porosity of the individual lines. The potential systematic error of the porosity is estimated to be +/- 3 % for the threshold analyser method. This is based on the difficulty of estimating, from the micrographs, the location of the exact interphase between the two phases. The random error or precision of the method is estimated to be +/- 0.3 % for the porous phase. It is hence fair to assume that the true porosity lies in the interval 57-63 %.

EIS measurements and ECSA determination

The EIS measurements generally contain two arcs in both the flooded and gas diffusion mode though some EIS patterns. The low frequency arc is assumed to be due to charge transfer resistance [23]. The high frequency arc could have several causes and cannot be determined from this data alone. The ECSA was determined from the amperostatic EIS measurements according to the procedure described in ref. [18]. It is clear from the fitting that the measurements performed in the gas diffusion mode exhibit good fits to the model whereas the measurements performed in the flooded mode are generally harder to fit, due to the more scattered data. This is attributed to bubble formation on the electrode surface, discussed further in the next sections.

Electrochemical testing of LNF electrodes tested

The initial screening of electrode performances, in **Figure 5** at RT in 1 M KOH, shows that at low current densities the electrodes exhibit similar overpotentials but at higher current density the differences in overpotential among the electrodes become substantial. At higher current densities it is further observed that the electrodes sintered at 1100 °C exhibit lower overpotentials than the electrodes sintered at 1125 °C. This is probably related to the higher porosity of these electrodes allowing for space for the electrolyte and gas phase. It was, however, also observed that the samples sintered at 1100 °C showed increasing fragility when increasing the amount of pore former so these microstructures are not considered sufficiently mechanically stable for long term use. The fact that pieces of the LNF-P3_1100 electrode surface fell off during testing at 65 °C further support this claim.

The electrodes tested in 8 M KOH exhibit better performance at 25 °C than the samples tested in 1 M KOH at ~25 °C which is probably due to the higher KOH concentration. One explanation could be that there are no or less limitations due to mass transport for the electrodes tested in 8 M KOH. Another explanation could be that the OER activity in alkaline media has, e.g., been shown to increase with pH, up to a pH of 14, on Ni-Fe(oxy)hydroxides and on Ru rutile dioxide surfaces[24,25]. The higher ECSA for the measurements performed in 8 M KOH support this hypothesis, though this increase could also be because the same double layer capacitance reference value is used in either case to determine the ECSA.

The performance is also enhanced at higher temperatures which is expected since both ionic transport and electrochemical activity increases exponentially with temperature. The equidistance of the 25 °C and 65 °C curves of the LNF-P3_1100 and LNF-P3_1125 electrodes with respect to current density (see **Figure 7**), further suggests that the factors limiting performance have the same current density dependence at the respective temperatures. The fact that the gradient of all the curves is seen to increase at around 25 $mA \cdot cm^{-2}$ is correlated well with the fact that this is also where bubble formation becomes apparent (fluctuating overpotential described below) which is increasing the effective current density, due to lower available surface area, and thereby also increasing the overpotential.

The serial resistance of the LNF-P3_1125 measurements in 8 M is 0.3 Ω cm^2 and 0.9 Ω cm^2 higher in the gas diffusion mode compared to in the flooded mode at 25 °C and 65 °C respectively, and it is independent of current density. The serial resistance of 0.3 Ω cm^2 at 25 °C is unexpectedly low. In fact, using eq. 5 below it is found to be around 1.45 Ω cm^2 and 0.75 Ω cm^2 at 25 °C and 65 °C respectively. It could be a matter of slight variations in contacting resistance between electrode and current collector giving rise to the deviations. At a current density of 0.1 $A \cdot cm^{-2}$, 0.9 Ω cm^2 serial resistance gives rise to a 90 mV overpotential which is considered acceptable.

Comparison of electrode performance with literature

The electrode performance obtained in this work is a bit lower than what is obtained for industrially relevant electrodes. As a benchmark of the performance, steel blasted Ni plated electrodes make a valid comparison. In [16,26] steel blasted Ni electrodes were tested at 70 °C in 50 wt% KOH and exhibited an overpotential of approx. 0.32 V at 0.1 $A \cdot cm^{-2}$. Activation with Raney Ni, (La,Sr)CoO_3 or Co_3O_4 decreased the overpotential by approximately 50 mV. In comparison, the average overpotential of the LNF-P3_1125 electrode tested in the flooded mode is 0.35 V at 65 °C and 0.43 V at 25 °C. A recent study, tested the intrinsic electrochemical activity of cathodically deposited nickel-iron oxyhydroxide thin films[27] which is one of the most active OER electrocatalysts known to date [10,24,28]. Results were reported on flat electrocatalyst layers (roughness factor ~1.3) and bubble formation was suppressed by using micro-electrodes. The overpotential in 30 wt.% KOH was 0.35 V at 60 °C and 0.40 V at 25 °C which is comparable to our results but obtained on electrodes with several hundred times smaller available surface area.

The microstructural characterization of tested LNF-P3 electrodes

The micrographs in **Figure 8 a) - d)** of the LNF-P3_1125 electrode microstructure tested at 65 °C showed that the microstructure remains relatively unaffected. The EDX also showed similar ratios of La:Ni:Fe:O before vs. after testing. Even though the samples were cleaned in Millipore water after

testing, K from the electrolyte is found on the surface of the electrode in **Figure 8 d)** and it may explain why the electrode surface appear slight smeared after testing. The presence of small nano particles on the LNF-P3_1125 electrode cannot be explained. Since these are neither observed on the top surface of the LNF-P3_1100 electrode nor on any of the polished cross sections, it has not been further investigated and the source of this contamination can therefore not be identified.

After the flooded test at 65 °C it became clear that the LNF-P3_1100 electrode's mechanical integrity is compromised. The pieces of electrode surface, which were broken off the electrode surface and found in the electrode compartment, suggest bubble growth inside the electrode initiated the crack formation. This means that the electrode is mechanically weak and the sintering temperature of the electrode is too low. This also infers, as already discussed, that bubble formation inside the porous electrode is substantial and hence a challenge that needs to be addressed.

Wetting of the porous electrode space

Wetting of the electrode surface is a crucial parameter for the performance. It is observed that the top surface of the electrode is well wetted when a droplet of KOH solution is placed there. According to the Young-Laplace equation a wetting fluid will tend to infiltrate a porous sample containing pores on the micro meter scale and below [29]:

$$\Delta P = \frac{2\gamma \cdot \cos(\theta)}{r_{pore}} \qquad \text{(eq. 1)}$$

where γ is liquid adhesion tension, taken as the surface tension, θ the contact angle and r_{pore} the pore radius. For a wetting liquid, with $\theta < 90$ °, the pressure drop is positive implying the liquid will penetrate into the pores and this pressure drop increases with decreasing pore size so smaller pores will be infiltrated faster than larger pores. It is hence clear that wetting of the electrode can be assumed adequate.

Factors influencing electrode performance

It should also be pointed out that the flooded and gas diffusion tests were not strictly performed in the same order. Above it was pointed out that the electrode microstructure and LNF phase remain stable, and it is therefore not considered critical.

The factors influencing the performance of the different electrode microstructures. The most likely causes seem to be that it is related to bubble formation on the surface of the porous electrode decreasing the ECSA, transport limitations of OH^- species or evolved O_2 or that it is caused by differences in the electrode thickness. These hypotheses are discussed below.

Given the current density is sufficiently high, gas bubbles will form on the electrode/electrolyte interface of all gas evolving electrodes [30]. The gas bubbles decrease the effective electrode surface area available for the OER and hence increase the effective current density. The ability of an electrode to nucleate a bubble, allow it to grow, release it and transport it away from the electrode surface is hence essential for electrode performance and electrolyser efficiency. The bubble formation process is complex and depends on several parameters including temperature, pressure, current density and wetting of the electrode [31–33]. In particular, the electrode area covered with gas bubbles increases

with increasing current density. In the case of porous electrodes it is important that any bubbles formed in the porous network can be effectively released. The fact that the fluctuation of the overpotential in the flooded mode become more pronounced upon increasing the current density is attributed to larger gas bubbles being formed on the surface; the gradual overpotential increase representing bubble growth and the abrupt decrease representing release from the electrode surface (cf. **Figure 6 a)**).

It is interesting that there seems to be very little bubble formation and release, on the electrode surface of the gas diffusion electrodes compared to the flooded electrodes as shown in **Figure 6 a)** and **b)**. A plausible explanation is that the electrode top surface is the most electrochemically active part of the flooded electrode and also the only place where bubbles are allowed to grow freely. In contrast the most active area of the gas diffusion electrode is close to the interface with the 3YSZ membrane where the electrolyte enters the electrode. Any bubble growth is here restricted by the pore sizes inside the electrode. Moreover, a substantial supersaturation of the electrolyte is required to form gas bubbles inside the porous network[34,35]. If bubbles are formed they are, however, less likely to be able to escape. The observed transient increase in overpotential in the gas diffusion mode can be related to the fact that bubbles are being formed inside the electrode and remain stuck there. The gradual decrease of ECSA with increasing current density supports this claim.

The fact that the gas diffusion electrodes perform worse than the flooded electrodes at RT in 1 M KOH does not seem to be directly related to the ECSA though. In fact, the decrease of the ECSA is more moderate in the gas diffusion mode compared to in the flooded mode. The reason for this is related to the fact that the electrochemical activity is highest in the area where the electrolyte enters the electrode. In the flooded mode this means on the electrode top surface. Bubbles formed here can grow freely and will restrict electrolyte access to the porous network. The bubbles formed on the top surface can, however, escape when they are released from the electrode surface and thereby gas evolution can be sustained.

The transient increase in overpotential in the gas diffusion mode at higher current densities could also be related to a concentration gradient of OH^- species building up in the vicinity of the electrode surface. In fact the LNF-P3_1125 electrode tested in 8 M KOH at 25 °C exhibit hardly any transient increase and has eight times higher KOH concentration. In addition, the electrodes (and thereby also the 3YSZ membrane) sintered at 1100 °C perform better than the electrode sintered at 1125 °C also support this statement because a lower sintering temperature leads to a lower densification and therefore more open space for the electrolyte.

The electrode thickness

The electrode thickness is an important parameter in the assessment of electrode performance because of the "competition" between the electrochemical reaction at the electrode surface and the OH- mobility into the electrode bulk of a given electrode. The reaction penetration depth is hereby calculated based on formula (36) in ref. [35] as an estimate of the electrode utilization thickness:

$$l_c = \sqrt{\frac{k_l^{eff}{}_b}{a\, z_e F k_{ox}}} \qquad \text{(eq. 2)}$$

Where l_c is the reaction penetration depth, k_l^{eff} is the effective electrolyte conductivity, b the tafel slope, a the specific surface area of the electrode, z_e the number of electrons participating in the OER, F Faradays constant and k_{ox} is the surface area specific reaction rate constant. To estimate the reaction penetration depth at low overpotentials in 1 M KOH at room temperate and in 8 M KOH at 65 °C a tafel slope of 0.1 and 0.06 V/dec and a reaction rate constant of $2 \cdot 10^{-10}$ and $3 \cdot 10^{-10}$ mol m^{-2} s^{-1} was used. The tafel slope was obtained from fits to the tafel equation using the current density range 0.5-5.0 mA cm^{-2}:

$$\eta = b \ln\left(\frac{i}{i_0}\right) \qquad \text{(eq. 3)}$$

Where b is the tafel slope, i the current density and i_0 the exchange current density. The reaction rate constant was obtained from the exchange current density determine from the tafel fit. In order to get the surface area specific reaction rate constant was divided by 100 as this is the order of magnitude of the ECSA.

$$k_{ox} = \frac{I_0}{4F} \qquad \text{(eq. 4)}$$

where η is the overpotential. The microstructural characterization carried out with the ThreshAlyser software was used to determine the specific surface area ($4.3 \cdot 10^6$ $m^2 \cdot m^{-3}$) of the electrode. The effective electrolyte conductivity (3 and 17.3 $S \cdot m^{-1}$) was determined using bulk electrolyte conductivities (σ_{bulk}) from ref. [36] and using the effective transport relation from ref. [37]:

$$\sigma_{eff} = \frac{\varepsilon}{\tau^2}\sigma_{bulk} \qquad \text{(eq. 5)}$$

Where σ_{eff} is the effective electrolyte conductivity, ε is the porosity taken from Table 2, τ is the tortuosity assumed to be 2. In the flooded mode at RT in 1 M KOH the reaction penetration depth is 35 mm and in 8 M KOH at 65 °C it is 47 mm. In order to check the validity of the results, tafel parameters obtained in previous work (cf. ref. [18]) on well-defined surface areas at RT in 1 M KOH are used for comparison. In this case the tafel slope is similar but the surface specifc reaction rate is approx. two orders of magnitude higher resulting in a reaction penetration depth of 3.3 mm. This value is assumed to be more valid because it was obtained on flat well-defined surfaces. In the gas diffusion mode the penetration depth is smaller, due to the lower effective conductivity of the electrolyte but still on the order of several millimeters. The main uncertainty in estimating the reaction penetration depth is related to the surface area specific reaction rate constant. The tafel fits suggest the uncertainty is approx. the same as the obtained value. It should also be stressed that it is a difficult parameter to estimate, and the determined value will be sensitive to where on the IV-curve the fit is made. The reaction penetration depth is hence only a rough estimate but it seems reasonable to state that the tested electrodes are too thin. Performance can hence be enhanced with thicker electrodes where a much larger surface area can be utilized and the reaction rate overpotential can be decreased.

Optimizing the microstructures in the flooded mode and in the gas diffusion mode

The optimum microstructure for flooded vs gas diffusion electrodes is not expected to be the same. The reason being that in flooded electrodes all the evolved O_2 has to escape as gas bubbles whereas in

the gas diffusion mode a porous network not flooded with electrolyte can be implemented. It seems clear though that the electrodes could benefit from being thicker.

In the flooded mode it is therefore inevitable that gas bubbles have to carry the O_2 away. In such an electrode, it is suggested that the pores should be large, on the order of 100 μm, to accommodate the evolved gas bubbles which are typically tens to hundreds of micrometre in size[31]. In this case other forces, such as drag forces arising from an imposed electrolyte flow, can be used to increase the rate of bubble detachment. Nano-sized pores, where bubbles are only formed when the electrolyte is highly supersaturated with electrolyte, can be used to increase the ECSA of the electrode while limiting bubble formation in these pores. Another relevant option, proposed and modelled in ref. [35] , could be to implement hydrophobic sites on the electrode surface that will act as preferential nucleation and growth sites for bubbles on the electrode surface which again will act as a sink for dissolved oxygen inside the porous network. This could allow for smaller pore sizes than approx. 100 μm and hence a larger ECSA.

In the gas diffusion mode the O_2 evolution flux will be highest close to the membrane separator, which explains why a porous network that can allow the evolved gas to escape is essential. It seems clear that bubbles should not be formed inside the pores as bubbles will have a hard time to escape. Further, it is, for example, found in [38] that electrolyzed water saturated with oxygen, contain 30 nm bubbles that grow to 250 nm over the course of several days, the point being that the bubbles remain stable in the solution. Nano-sized pores also seem is also an option in this case as the dissolved oxygen can diffuse directly to the gaseous phase in the larger gas diffusion pores.

Conclusion

The present work shows that porous LNF electrodes sintered at 1125 °C are electrochemically active and stable under conditions relevant for industrial AECs. The electrodes are screen printed onto porous 3YSZ membranes. Graphite and PMMA are used as pore formers. Different microstructures are obtained and microstructural parameters are quantified using 2D SEM images. The electrodes exhibit porosities of 58-72 %, d10 pore sizes in the range 0.19-0.28 μm and d90 pore sizes in the range 1.5-3.5 μm. Screening tests at RT in 1 M KOH reveal that the flooded electrodes tend to perform better than gas diffusion electrodes and electrodes sintered at 1100 °C tend to perform better than samples sintered at 1125 °C. It does not reveal any clear correlations between type of microstructure and performance though. ECSA measurements suggest that this is correlated to electrode performance, higher ECSA meaning higher performance. The electrochemical testing of the LNF-P3_1100/1125 electrodes, tested at industrially relevant conditions, 8 M KOH at 65 °C, shows that they perform similarly in the flooded electrode mode and in the gas diffusion electrode mode. In comparison to conventional Ni electrodes the porous LNF electrodes perform slightly worse. At current densities above 10 mA cm^{-2} it can be concluded that part of the overvoltage is due to the formation and subsequent adhesion of oxygen bubbles on the outer and the inner surface of the electrodes which leads to a decrease of the available electrode surface area with increasing current density. A part of the overpotential at higher current densities is in the gas diffusion mode possibly related to OH^- starvation near the electrode surface. Moreover, determination of the electrolyte penetration depth suggest, that performance can be enhanced by making thicker electrodes on the order of hundreds of micrometres.

Acknowledgements

The authors would like to thank Jeanette Krambech for tape casting the 3YSZ membranes. The authors would also like to thank Ebtisam Abdellahi, Kjeld B. Andersen, Jacob Bowen, Søren P. V. Foghmoes, Lene Knudsen, Jeanette Krambech, Henrik Paulsen, Søren Bredemose Simonsen and Mads G. Sørensen for their assistance with sample preparation, characterization and all their essential advice about the lab work carried out. The authors would lastly like to thank Vanesa Gil for her helpful inputs.

References

[1] Cédric Philibert. Producing ammonia and fertilizers: new opportunities from renewables, International Energy Agency; 2017. https://www.iea.org/media/news/2017/Fertilizer_manufacturing_Renewables_01102017.pdf [accessed 7th August 2018]

[2] A. Ursúa, L.M. Gandía, P. Sanchis. Water Electrolysis : Current Status and Future Trends. Proc. IEEE. 2012, 100: 410-426. doi:10.1109/JPROC.2011.2156750

[3] Bruckner T., I. A. Bashmakov, Y. Mulugetta, H. Chum, A. de la Vega Navarro, J. Edmonds, A. Faaij, B. Fungtammasan, A. Garg, E. Hertwich, D. Honnery, D. Infield, M. Kainuma, S. Khennas, S. Kim, H. B. Nimir, K. Riahi, N. Strachan, R. Wiser, and X. Zhang. 2014: Energy Systems. In: Edenhofer, O., R. Pichs-Madruga, Y. Sokona, E. Farahani, S. Kadner, K. Seyboth, A. Adler, I. Baum, S. Brunner, P. Eickemeier, B. Kriemann, J. Savolainen, S. Schlömer, C. von Stechow, T. Zwickel and J.C. Minx, editors. Climate Change 2014: Mitigation of Climate Change. Contribution of Working Group III to the Fifth Assessment Report of the Intergovernmental Panel on Climate Change Cambridge & New York: Cambridge University Press; 2014.

[4] J.D. Holladay, J. Hu, D.L. King, Y. Wang. An overview of hydrogen production technologies. Catal. Today. 2009; 139. doi:10.1017/CBO9781107415416.013

[5] J. Ivy. Summary of Electrolytic Hydrogen Production: Milestone Completion Report. Colorado, USA. 2004.

[6] F. Allebrod, C. Chatzichristodoulou, M.B. Mogensen. Alkaline electrolysis cell at high temperature and pressure of 250 °c and 42 bar. J. Power Sources. 2013; 139: 22–31. doi:10.1016/j.jpowsour.2012.11.105

[7] C. Chatzichristodoulou, F. Allebrod, M.B. Mogensen. High Temperature Alkaline Electrolysis Cells with Metal Foam Based Gas Diffusion Electrodes. J. Electrochem. Soc. 2016; 163: 3036–3040. doi:10.1149/2.0051611jes.

[8] J.O. Bockris, T. Otagawa. The Electrocatalysis of Oxygen Evolution on Perovskites. J. Electrochem. Soc. 1984; 131: 290–302. doi:10.1149/1.2115565.

[9] J. Suntivich, K.J. May, H. a. Gasteiger, J.B. Goodenough, Y. Shao-Horn. A Perovskite Oxide Optimized for Oxygen Evolution Catalysis from Molecular Orbital Principles. Science 2011; 334: 1383. doi:10.1126/science.1212858.

[10] L. Trotochaud, J.K. Ranney, K.N. Williams, S.W. Boettcher. Solution-Cast Metal Oxide Thin Film Electrocatalysts for Oxygen Evolution. J. Am. Chem. Soc. 2012; 134: 17253. doi:10.1021/ja307507a.

[11] A. Habrioux, I. Abidat, C. Canaff, C. Morais, C. Comminges, T. Napporn, K.B. Kokoh. Co-Based Mesoporous Spinels for Oxygen Evolution Reaction in Alkaline Medium. ECS Trans. 2017; 77: 15–24. doi: 10.1149/07709.0015ecst

[12] A.H.A. Monteverde Videla, P. Stelmachowski, G. Ercolino, S. Specchia. Benchmark comparison of Co3O4 spinel structured oxides with different morphologies for oxygen evolution reaction under alkaline conditions. J. Appl. Electrochem. 2017; 47: 295-304. doi:10.1007/s10800-016-1040-3.

[13] J.Y.C. Chen, J.T. Miller, J.B. Gerken, S.S. Stahl. Inverse spinel NiFeAlO4 as a highly active oxygen evolution electrocatalyst: Promotion of activity by a redox-inert metal ion. Energy Environ. Sci. 2014; 7: 1382–1386. doi:10.1039/c3ee43811b.

[14] C.C. Tseung, S. Jasem. Oxygen evolution on semiconducting oxides. Electrochim. Acta. 1977; 22: 31–34. doi:10.1016/0013-4686(77)85049-4.

[15] J. Balej. Electrocatalysts for oxygen evolution in advanced water electrolysis. Int. J. Hydrogen Energy. 1985; 10: 89–99. doi:10.1016/0360-3199(85)90041-2.

[16] H. Wendt, H. Darmstadt, V. Plzak. Materials Research and Development of Electrocatalysts for Alkaline Water Electrolysis. Mater. Chem. Phys. 1989; 22: 27-49. doi: 10.1016/0254-0584(89)90030-8.

[17] D.S. Bick, J.D. Griesche, T. Schneller, G. Staikov, R. Waser, I. Valov. $Pr_xBa_{1-x}CoO_3$ Oxide Electrodes for Oxygen Evolution Reaction in Alkaline Solutions by Chemical Solution Deposition. J. Electrochem. Soc. 2016; 163: F166–F170. doi:10.1149/2.0311603jes.

[18] J.Q. Adolphsen, B.R. Sudireddy, V. Gil, C. Chatzichristodoulou. Oxygen Evolution Activity and Chemical Stability of Ni and Fe Based Perovskites in Alkaline Media. J. Electrochem. Soc. 2018; 165: F827–F835. doi:10.1149/2.0911810jes.

[19] J. Bowen. ManSeg (software for image analysis), ver. 0.37. DTU Energy 2018.

[20] T.G. Mezger. The Rheology Handbook: For Users of Rotational and Oscillatory Rheometers. 4th edition. Hannover: Vincentz Network. 2011.

[21] M. Bevilacqua, T.T. Montini, C. Tavagnacco, E. Fonda, P. Fornasiero, M. Graziani. Preparation, Characterization, and Electrochemical Properties of Pure and Composite $LaNi_{0.6}Fe_{0.4}O_3$ -Based Cathodes for IT-SOFC. Chem. Mater. 2007; 19: 5926–5936. doi:10.1021/cm071622n.

[22] E.E. Underwood, Stereology, or the quantitative evaluation of microstructures. J. Microsc. 1969; 89: 161–180. doi:10.1111/j.1365-2818.1969.tb00663.x.

[23] A. Lasia. Electrochemical Impedance Spectroscopy and its Applications. New York: Springer; 2014. doi:10.1007/0-306-46916-2_2.

[24] M. Gong, Y. Li, H. Wang, Y. Liang, J.Z. Wu, J. Zhou, J. Wang, T. Regier, F. Wei, H. Dai, An advanced Ni-Fe layered double hydroxide electrocatalyst for water oxidation, J. Am. Chem. Soc. 2013; 135; 8452–8455. doi:10.1021/ja4027715.

[25] K.A. Stoerzinger, R.R. Rao, X.R. Wang, W.T. Hong, C.M. Rouleau, Y. Shao-Horn. The Role of Ru Redox in pH-Dependent Oxygen Evolution on Rutile Ruthenium Dioxide Surfaces. Chem. 2017; 2; 668–675. doi:10.1016/j.chempr.2017.04.001.

[26] H. Wendt, V. Plzak. Electrocatalytic and Thermal Activation of Anodix Oxygen- and Cathodic Hydrogen Evolution in Alkaline Water Electrolysis. Electrochim. Acta. 1983; 28: 27–34. doi:0013-4686(83)85083-X

[27] S. Watzele, Y. Liang, A.S. Bandarenka. Intrinsic Activity of some Oxygen and Hydrogen Evolution Reaction Electrocatalysts under Industrially Relevant Conditions. ACS Appl. Energy Mater. 2018; In progress. doi:10.1021/acsaem.8b00852.

[28] D.A. Corrigan. The Catalysis of the Oxygen Evolution Reaction by Iron Impurities in Thin Film Nickel Oxide Electrodes. J. Electrochem. Soc. 1987; 134: 377–384. doi:10.1149/1.2100463.

[29] M. Gong, Y. Li, H. Wang, Y. Liang, J.Z. Wu, J. Zhou, J. Wang, T. Regier, F. Wei, H. Dai. An advanced Ni-Fe layered double hydroxide electrocatalyst for water oxidation. J. Am. Chem. Soc. 2013; 135: 8452–8455. doi:10.1021/ja4027715

[30]H. Bruus. Theoretical Microfluidics. Oxford: Oxford University Press. 2007.

[31] H. Vogt, R.J. Balzer. The bubble coverage of gas-evolving electrodes in stagnant electrolytes, Electrochim. Acta. 2005; 50: 2073–2079. doi:10.1016/j.electacta.2004.09.025.

[32] L.J.J. Janssen, C.W.M.P. Sillen, E. Barendrecht, S.J.D. van Stralen. Bubble behaviour during oxygen and hydrogen evolution at transparent electrodes in KOH solution. Electrochim. Acta. 1984; 29; 633–642. doi:10.1016/0013-4686(84)87122-4.

[33] S.H. Ahn, I. Choi, H.-Y. Park, S.J. Hwang, S.J. Yoo, E. Cho, H.-J. Kim, D. Henkensmeier, S.W. Nam, S.-K. Kim, J.H. Jang. Effect of morphology of electrodeposited Ni catalysts on the behavior of bubbles generated during the oxygen evolution reaction in alkaline water electrolysis. Chem. Commun. 2013; 49: 9323. doi:10.1039/c3cc44891f.

[34] H. Vogt. The Quantities Affecting the Bubble Coverage of Gas-Evolving Electrodes. Electrochim. Acta. 2017; 235: 495–499. doi:10.1016/j.electacta.2017.03.116.

[35] Q. Chen, L. Luo, H.S. White. Electrochemical generation of a hydrogen bubble at a recessed platinum nanopore electrode. Langmuir. 2015; 31; 4573–4581. doi:10.1021/acs.langmuir.5b00234.

[36] T. Kadyk, D. Bruce, M. Eikerling. How to Enhance Gas Removal from Porous Electrodes?. Sci. Rep. 2016; 6: 1–14. doi:10.1038/srep38780.

[37] R.J. Gilliam, J.W. Graydon, D.W. Kirk, S.J. Thorpe. A review of specific conductivities of potassium hydroxide solutions for various concentrations and temperatures. Int. J. Hydrogen Energy. 2007; 32: 359–364. doi:10.1016/j.ijhydene.2006.10.062.

[38] G. Gaiselmann, M. Neumann, V. Schmidt, O. Pecho, T. Hocker, L. Holzer. Quantitative relationships between microstructure and effective transport properties based on virtual materials testing. AIChE J. 2014; 60; 1983–1999. doi:10.1002/aic.

[39] K. Kikuchi, A. Ioka, T. Oku, Y. Tanaka, Y. Saihara, Z. Ogumi, Concentration determination of oxygen nanobubbles in electrolyzed water. J. Colloid Interface Sci. 2009; 329: 306–309. doi:10.1016/j.jcis.2008.10.009.

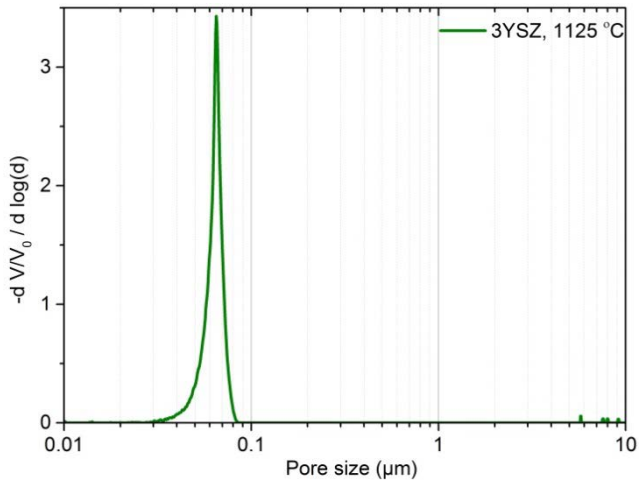

Figure S1 The pore size distribution of the 3YSZ membrane sintered at 1125 °C.

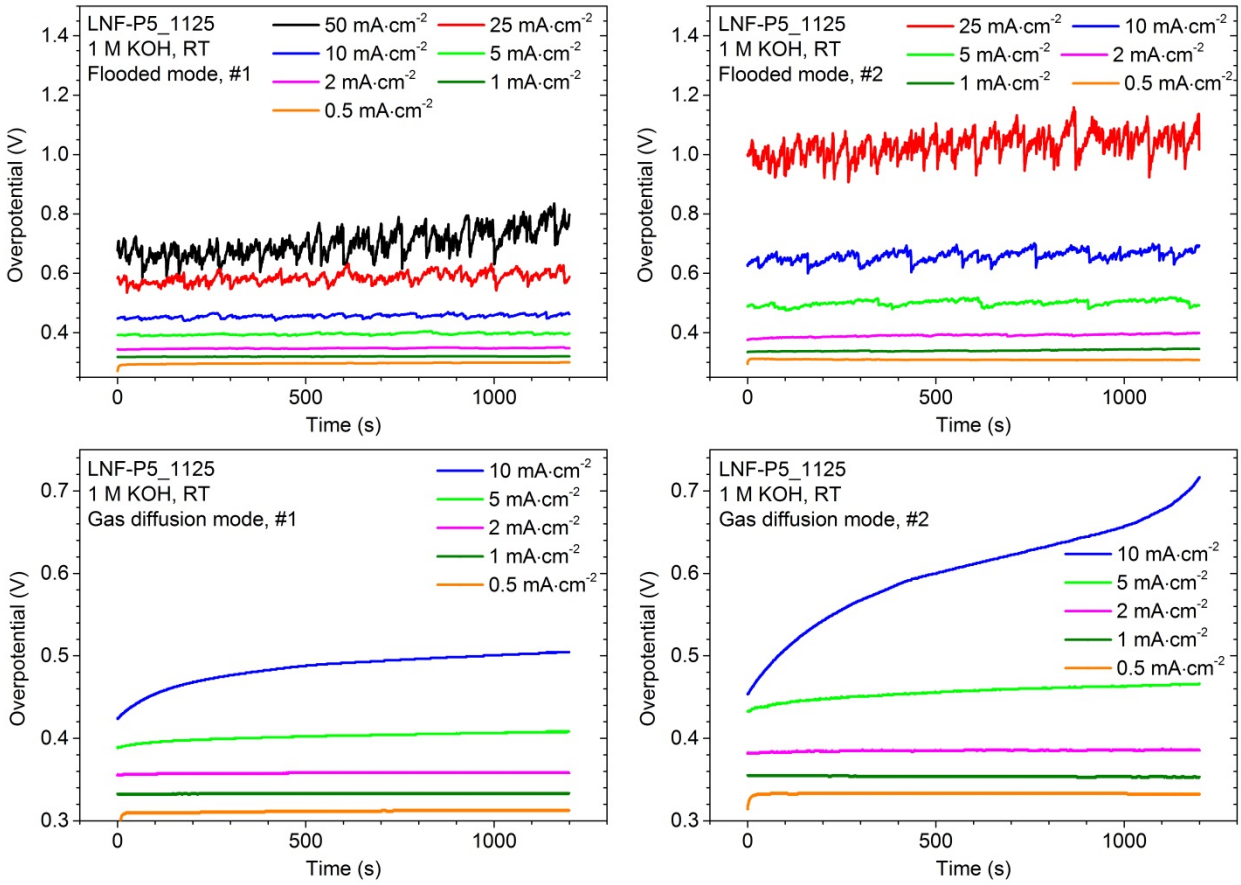

Figure S2 The chronopotentiometry tests of two different LNF-P5_1125 samples tested in both flooded and gas diffusion mode. Both samples were test in the flooded mode first.

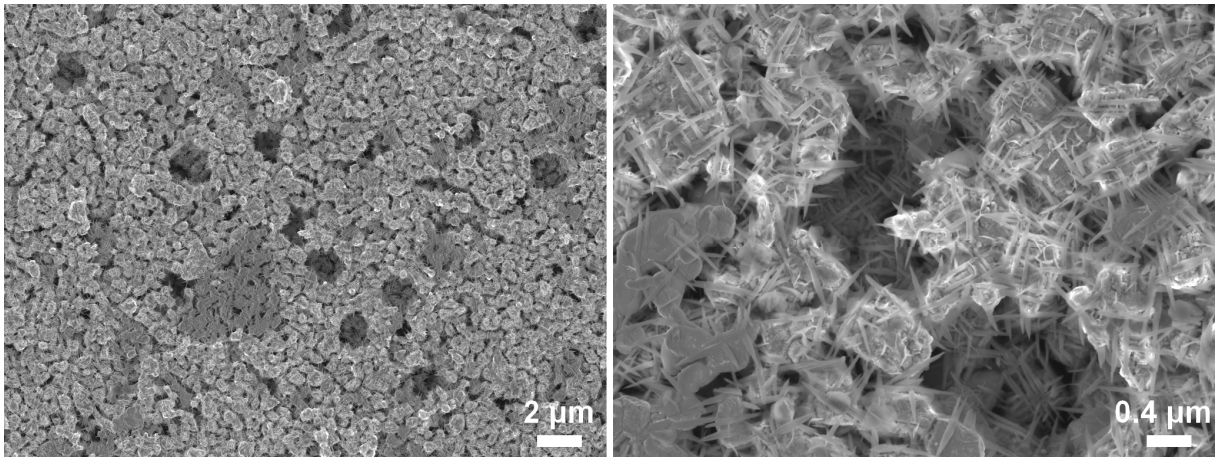

Figure 4.2: SEMs image at two magnifications of an LNF-P3_1100 electrode fragment recovered from the KOH solution after the test at 65 ℃ in 8 M KOH.

4.4.1 On stability of the tested LNF-3YSZ half cells

The porous LNF electrodes tested at 65 ℃ in 8 M KOH appear to be sufficiently stable though any detailed investigation of the surface chemistry was not performed so changes in the surface layer of the electrodes is not well investigated. It is appropriate to refer to section 4.5.2 where SEM micrographs showed that changes to the surface do occur. In fact SEM images of a fragment from the LNF-P3_1100 surface that broke off during testing, reveal some similar nano-sized needle-like objects which are shown in Figure 4.2. These have been investigated with scanning tunneling electrotron microscopy-energy dispersive x-ray spectroscopy(STEM-EDX). The needle-like structures were identified as crystalline La_2O_3 and the TEM images can be seen in Figure 4.3. It is peculiar that these needle-like objects are not found anywhere on the electrode surface but only on the fragment recovered from the KOH solution after finishing the test. The fragments were not rinsed in water after recovering them. The tested electrode was rinsed very gently, mainly to remove KOH, by immersing it in water.

It is not apparent why the La_2O_3 is formed on this electrode fragment and not on the actual electrode. The best explanation seem to be that the excess KOH has become increasingly concentrated upon water evaporation eventually leading to formation of La_2O_3 on the surface.

On the top surface of the LNF-P3_1125 electrode small particles, ≈50 nm in size, were identified. These were only found on this electrode surface, neither on the LNF-P3_1100 electrode surface nor on any of the polished cross sections. There was no time for a rigorous analysis but an EDX point analysis revealed that the particles contained 4.5 at.% Zr which is significantly higher than the rest of the electrode that contained approx 0.7 at.%. The latter obtained with a EDX surface mapping. It is clear that the penetration depth of the EDX signal is at least a micrometer so the composition of nano meter sized particles cannot be accurately determined. The EDX does suggest, however, that the particles are ZrO_2 which is plausible since the 3YSZ mainly contains ZrO_2. The fact that these particles

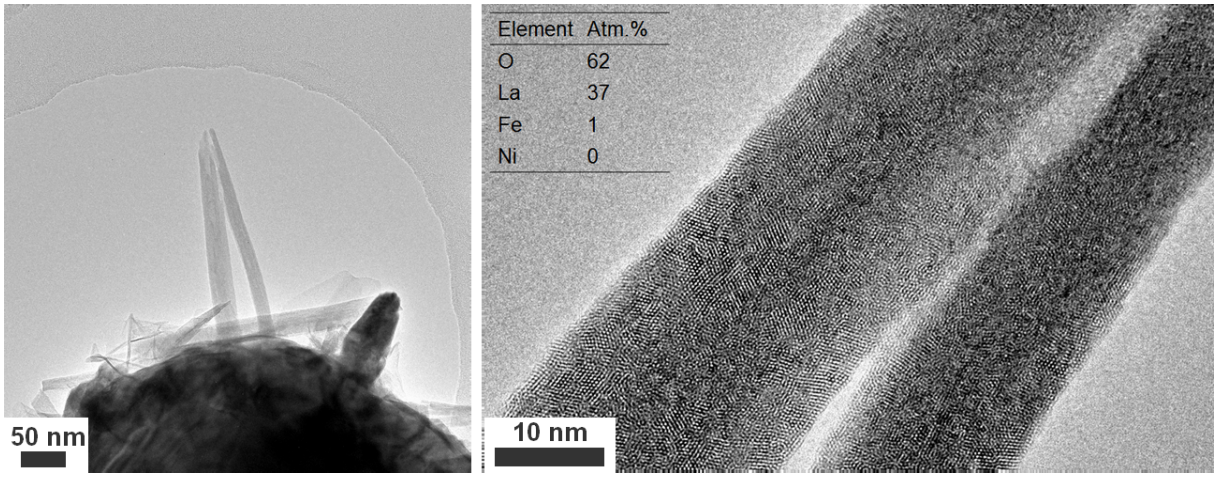

Figure 4.3: TEM images of the needle like structures observed on the fragment from the tested LNF-P3_1100 electrode. The composition is determined with STEM-EDX.

were not found anywhere else makes it difficult to conclude anything. In particular it should be more likely to find ZrO_2 particles on the LNF-P3_1100 electrode surface as this is sintered at a lower temperature so if the mechanical integrity of the membrane is compromised this should be more evident on the sample sintered at only 1100 ℃. For future experiments it is, of course, essential to find out if the chemical stability of the 3YSZ membrane is adequate.

4.4.2 Bubble formation on gas evolving electrodes

The evolution of gas bubbles during the OER has been studied, in-situ with a microscope, on several model systems . In general the bubble size is known to decrease with increasing current density [125]. At higher current densities, above 0.1 A cm^{-2}, it has been shown, on transparent Ni electrodes in 1 M KOH at 30 ℃, that an increase in applied current density leads to an increase in bubble detachment size. Perhaps this is due to the increase in bubble population density with increasing current density, which means adjacent bubbles coalesce faster thus speeding up bubble growth [126, 127]. The bubble detachment size generally decreases with increasing pressure and KOH concentration whereas bubble population density increases. [125, 126, 128]. This is shown in figure 4.4. A forced convective flow tend to decrease the bubble detachment size due to a decreased residence time. The bubble detachment size at current densities from 0.1-0.5 A cm^{-2} is typically around 0.01-0.1 mm.

The main underlying physics governing the bubble growth is the mass transfer of dissolved product to the bubble surface and bulk respectively, but it becomes pretty clear from the literature that understanding the bubble formation, growth and detachment phenomena is highly complex. Semi-empirical relations between applied current density and fractional bubble coverage exists [130], but they are not very useful in understanding the bubble phenomena as many other physical quantities are known to affect the fractional bubble coverage. Extensive research has been carried out by H. Vogt to try and

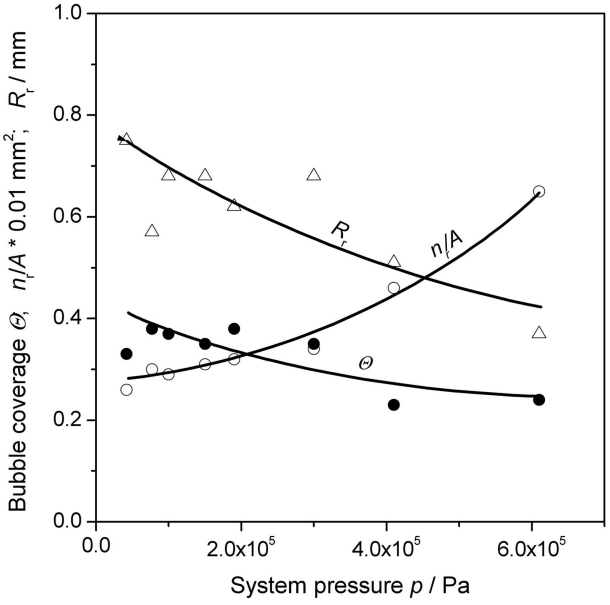

Figure 4.4: The fraction bubble coverage of an oxygen evolving Ni electrode vs system pressure. The fractional bubble coverage is seen to decrease with increasing system pressure . The bubble break-off radius (R_r) is also decreasing whereas bubble population density (n_r/A) is seen to increase. Graph from [125] with data from [129]

understand the bubble processes occurring at gas evolving electrodes and explain it with mathematical relations, see for example ref. [125, 130–132]. Based on experimental measurements some of this work has led to a relation between the fractional bubble coverage (Θ) of an electrode and the gas evolution flux ($\frac{\dot{V}_G}{A}$). This relation depends on various parameters, which even though these parameters are interrelated as well, elucidates some general relations between fractional bubble coverage and measurable physical quantities:

$$\Theta = \frac{\pi R_r^2}{2V_r} t_r \frac{\dot{V}_G}{A} = \frac{\pi R_r^2 t_r}{2V_r} \frac{f_G \Phi_B J}{(\nu_e/\nu_B)} \frac{RT}{F(p-p_s)} = \frac{\pi R_r^3}{2V_r} R_r \frac{t_r}{R_r^2} \frac{f_G \Phi_B J}{(\nu_e/\nu_B)} \frac{RT}{F(p-p_s)} \tag{4.1}$$

where R_r is the bubble break-off radius V_r is the bubble volume at break-off, t_r is the bubble residence time, f_G is the gas evolution efficiency or fraction of dissolved O_2 forming gas bubbles, Φ_B is the current efficiency, J is the applied current density, ν_e/ν_B is the ratio of stoichiometric numbers of electrons to product gas molecules and hence constant, R is the universal gas constant, T is the temperature, F is Faraday's constant, $(p-p_s)$ is the partial pressure of products in the gaseous phase (applied pressure - vapour pressure of solvent).

From eq.4.1 it is important to stress the relative importance of the different parameters. The bubble shape factor ($\frac{Re_r^3}{V_r}$) is known to be essentially constant for wetting electrodes (contact angle $< 90^o$), whereas it has a larger impact for non-wetting electrodes (contact angle $> 90^o$). The bubble break-off radius was already touched upon previously in this section. It is affected by several quantities, the most important being the electrode wetting. In particular, on non-wetting electrodes detaching bubbles are larger than on wetting electrodes which is mainly due to a higher impact from coalescence of neighbouring bubbles [133]. The current density (or more satisfactorily the overpotential) is

also affecting the bubble break-off radius, and at high current densities bubble coalescence before detachment becomes important. The growth ratio ($\frac{R_r^2}{t_r}$) is another important factor. In fact it is approximately constant for wetting electrodes and described by the Fourier number [125]. This implies that the bubble radius grows with the square root of time:$R_r^{1/2} \propto t$ so large bubbles grow faster than small bubbles. For non-wetting electrode the relation has been found to be: $R_r^{1/3} \propto t$ [133].

The gas evolution efficiency(f_G) is proportional to the fractional bubble coverage and is directly related to the competing mass transfer of products from the electrode surface to the liquid bulk and to the bubble surfaces respectively. Elaborating on this, bubble induced micro-convective mass transfer becomes an important factor at industrially relevant current densities and increases the gas evolution efficiency [134]. Forced macro-convection can also significantly impact the gas evolution efficiency as it drags bubbles off the surface. Rotating disc electrodes are examples of the forced convection. The current efficiency (Φ_B) is generally as high as feasibly possible during water electrolysis and not relevant. The nominal current density (J) is, as already explained above, highly influential on the fractional bubble coverage and used as a general descriptor. It is also important to mention that it influences other parameters, such as the local temperature at the electrode surface due to its correlation to the overpotential. Mass transfer is eventually also affected due to larger gradients between surface and bulk concentrations.

Among the last parameters the temperature and pressure are both important. An increase in temperature activates the electrode kinetics and mass transfer processes, and not only affects the fractional bubble coverage directly, but also leads to an increase of the solvent vapour pressure which promotes bubble formation and thereby the gas evolution. So for AECs operated at 80 ℃ compared to 25 ℃ the bubble coverage is more than tripled due to the direct influence of the increase in temperature. The temperature also influences the vapour pressure of the electrolyte and leads to $\approx 30\,\%$ decrease of the partial pressure of products in the gaseous phase. The partial pressure of products in the gas phase ($p - p_s$) can be increased by applying an external pressure (p) which effectively decreases the fractional bubble coverage. The solvent partial pressure (p_s) tend to increase with increasing concentration of electrolyte species and is, as already mentioned, correlated to temperature.

Now examining the case of HTP-AECs, the applied pressure is 20-40 bar to limit evaporation from the electrolyte and this will hence also suppress bubble coverage. The partial pressure of products in the gas phase($p - p_s$) will increase by a factor of 15-45 in a HTP-AECs (assuming operation at 200 ℃ with a pressure in the range 20-40 bar and a 45 wt.% KOH solution) compared to a conventional AEC (assuming operation at 80 ℃ at ≈ 1 bar operation with a 35 wt.% KOH) [135]. HTP-AECs will therefore suppress the increase in fractional bubble coverage that comes from increasing the current density in HTP-AEC with a factor of $\approx$ 3-10 compared to conventional AEC. The increase in temperature in HTP AECs will, besides the direct influence on fractional bubble coverage, affect the wetting of the electrode surface as the surface tension decreases with increasing temperature.

From the above paragraphs it can be extracted that to handle bubbles from gas evolving electrodes several parameters can be changed. The operational parameters temperature, pressure and current density are important and it is clear that increases in temperature and current density will increase the fractional bubble coverage. For large values of fractional bubble coverage, this will also influence the overpotential of the cell. Applying a pressure can help suppress the fractional bubble coverage and the bubble size at detachment. This will make it feasible to operate at higher temperatures and current densities. Another parameter that can be tuned is the residence time before detachment of the gas bubbles growing on the electrode surface. Forced convection is one obvious strategy which can aid this. The wetting of the electrolyte on the electrode surface is another highly important parameter. This can be effectively implemented by altering the microstructure. In ref. [136] it was shown that by making Ni electrode microstructures more hierarchical with higher root mean square roughness, the contact angle was decreased. This resulted in an increase in the current density at the same overpotential and led to a more stable performance over time.

This discussion has provided an overview of some of the main factors influencing the bubble formation and release process and provide some suggestions as to how these can be tuned. At the end of the day it is important to stress that it is the overall performance of the electrode, or cell, that needs to be optimized and not just the bubble issue in itself.

4.5 Overall Discussion

4.5.1 Selection of materials

The initial selection of electrode materials for the OER was based on a literature study presented in section 2.4.1. The group of materials reviewed was oxide ceramics focusing on pervoskites, metal (oxy)hydroxides/metal oxides and spinel structures. This study made it clear that the Ni,Fe (oxy)hydroxides probably are the most active electrocatalysts towards the OER which have been widely investigated. The transition metals most commonly employed in electrocatalysts are Ni, Co and Fe and these are also commonly thought of as the active site for OER. In particular for the metal (oxy)hydroxides Fe have shown to enhance the OER activiy of both Ni- and Co (oxy)hydroxides [137].

A challenge with the Ni,Fe (oxy)hydroxides is the limited electronic conductivity, though it is sufficient when used as an electrocatalyst where there is maximally a couple of hundred nm between electrocatalyst and current collector, it becomes a problem if the electrode and electrocatalyst are the same material. This is one reason why Ni,Fe(oxy)hydroxides did not seem so appealing because an electronically conductive backbone would be required to limit the overpotential stemming from electrocatalyst resistivity. Several perovskites, such as $LaNiO_3$ and several compositions in the $La_{1-x}Sr_xFe_{1-y}Co_yO_3$ series, which are relevant as OER electrode materials, show semiconducting to metallic electronic conductivity [78, 79]. This is considered an advantage as it allows these materials to be used as electrodes, and the electrocatalytic activity can always be improved by applying electro-

catalysts on the surface of the electrode.

Getting back to the synergy between Ni-Fe observed in Ni,Fe (oxy)hydroxides, it was hypothesized that a similar synergy might be present in other Ni-Fe based oxides. Moreover, it is clear that Fe stabilizes the LaNiO structure which is difficult to synthesize in a phase pure form and prone to thermal decomposition [45, 138, 139]. It was therefore proposed that improved thermal stability could also mean a higher chemical stability in alkaline medium. Based on the above observations, it was termed relevant to test a series of La,Ni,Fe-based perovskites towards the OER in alkaline media. A study related to solid oxide cell research had shown that $LaNi_{0.6}Fe_{0.4}O_3$ is the most electronically conductive material in the $LaNi_{1-x}Fe_xO_3$ series over a wide temperature range. It was also a priority that the materials be available from commercial suppliers of ceramics oxide powders, which is the case for $LaNi_{0.6}Fe_{0.4}O_3$.

The A-site decifient materials ($La_{0.97}NiO_3$ and $La_{0.97}Ni_{0.6}Fe_{0.4}O_3$) were interesting to investigate, mainly, because a small deficit of La have been shown to lead to secondary phase formation of NiO [140] which we hypothesized might lead to improved activity towards the OER due to a formation of Ni,Fe (oxy)hydroxide phases on the surface. The Ruddlesden Popper phase ($La_2Ni_{0.9}Fe_{0.1}$) was chosen because it is a perovskite related structure consisting of stacked perovskite and rock salt layers. This will alter the surface properties, including the bonding strength between the metal cations and the oxygen anion, compared to the pure perovskite, and therefore potentially lead to enhanced OER activity. In addition, it contains Ni and Fe, and it has decent electronic conductivity [107].

The OER stability in alkaline media is generally not well investigated for electrocatalysts, even at room temperature, and it was therefore a difficult parameter to make a decision upon [44]. It had been reported that several highly active perovskites are seen to undergo surface amorphization [65] during the OER which initially leads to a better performance. The long term effects were, however, not properly understood. A thermodynamic explanation for the universal correlation between OER activity and corrosion of oxide catalysts over time, due to lattice oxygen evolution, had been reported [55] but how to identify meta-stable oxide electrocatalysts is still not properly understood. Long term testing is the soundest method to asses long term stability of an electrocatalyst but is rarely done. Therefore it was clear that choosing electrocatalysts was done with little certainty as whether they would be stable or not.

4.5.2 Determinination of the OER activity of the materials

The OER activity of the La,Ni,Fe-oxides was evaluated with densely sintered and polished bars of pressed powders. In the case of LNF, L97NF and LNF-RP this was fine as they could be sintered dense at high temperatures without decomposition taking place. From the TG analysis of LN and L97N it was clear that they decomposed around 1000 ℃ and 1070 ℃ in air and O_2 respectively. The fact that the LN phase decomposed at relatively low temperatures also made it clear that sintering dense LN bars would not be possible. It was hence not possible to test the pure LN phase.

The main reason why densely sintered bars were chosen for electrocatalyst screening, was that only the OER activity of the ceramic oxide was going to be evaluated. A very common way to determine intrinsic activity of electrocatalysts is using a glassy carbon rotating disc electrode upon which an ink is deposited that contains the ceramic oxide particles. The ink often also contains acetylene black carbon (AB carbon) as a conductivity enhancing agent, a binder such as Nafion or PTFE and some solvent. In this way the electrocatalyst loading can be well controlled and other factors such as conductivity are not affecting the OER activity to a significant extent. It is, however, problematic, that for example the AB carbon has shown to enhance the electrocatalytic activity, observed in e.g. BSCF, and moreover it is not stable under OER conditions [70].

Initially, the intention was to determine the OER activity of the chosen materials at HTP conditions which made it important not to have too many other materials due to possible instability of these. Moreover, a rotating disc electrode could not be employed in this setup. Using pressed powders with only the ceramic material was therefore the best option but in order to get a well-defined surface area the bars had to be sintered dense, which required high temperature sintering. In the end we decided not to perform the OER activity measurements at HTP conditions. The main reason for this was that the chemical stability measurements in concentrated KOH at 220 ℃ showed that non of the ceramic oxide powders were stable under these conditions. In addition, the experimental setup posed a challenge so it was not straight forward; specifically a conventional reference elecrtrode could not be used at HTP conditions so a dynamic hydrogen electrode was developed which had to be calibrated at the HTP conditions.

The primary method employed to determine the OER activity of the oxides towards the OER was chronopotentiometry (CP). The CP allowed the OER to reach a steady state which is generally not possible with cyclic voltammetry (CV), another common electrochemical characterization method. In addition electrochemical impedance spectroscopy (EIS) could be performed after each CP step and the serial resistance could therefore be determined at each current density together with the ECSA.

4.5.3 The stability of the oxides in the light of the OER- and chemical stability measurements

Identifying stable materials for the HTP-AECs is probably the main challenge associated with this technology. From this work it is also clear that in particular stability of the materials should be a main concern. As mentioned in section 2.3.1 electrodes are greatly activated during HTP conditions so electrode materials that might not be suitable for conventional AEC could be relevant for HTP-AECs due to the improved kinetics.

The SEM observations following the OER activity measurements showed that the surface of all the tested materials changed upon testing. In particular crack formation was observed (cf. Figure 7 in section 4.1). This was most severe on the LN and LNF-RP

surface where it appeared that etched trenches had been formed. In the case of the LN it was visible around the NiO grains, and on the LNF-RP surface etching had also taken place around some small clusters, which though they appeared darker than the rest of the surface, were not identified as a separate phase. On the LNF surface only smaller cracks were observed. It seems likely that the etching effect observed could be at grain boundaries where the crystal orientation changes. The chemical stability measurements complimented the SEM observations to some degree. The LNF phase appeared most stable. The LN phase was, however, significantly more unstable than the LNF-RP phase with secondary phases forming already after the room temperature chemical stability assessment.

As already mentioned several times, in section 2.4.1 and section 4.5.1, it has been shown by Bininger et. al. that all metals oxides eventually must become thermodynamically unstable (or chemically unstable) under OER conditions at any pH due to the lattice oxygen evolution reaction (LOER) taking place at the metal oxide surface. This implies subsequent structural changes or cation dissolution from the surface which has been shown experimentally for perovskites [52, 53, 65]. Hence the kinetics between OER and LOER also seem to be closely coupled. The logical conclusion they make is that meta-stable phases have to be identified. This could imply that the OER and LOER are adequately decoupled, e.g. by very slow oxygen anion diffusion in the lattice. In this way hydrous amorphous layer can be formed on the surface which increases the ECSA. The inherent stability of this surface layer is going to be decisive for the long term stability of a ceramic oxide electrocatalyst. The above argumentation provides some guidelines as to what materials will be electrocatalytically active and possess long-term stability. It also seems suggests that very high apparent OER activity often comes at the cost of poor long term stability.

Based on the previous discussion and the discussion in section 4.2 it seems relevant to implement other more sensitive methods of determining the stability of the materials. ICP mass spectroscopy could be used to check for dissolution of the cations after OER. A highly sensitive method to determine any mass losses or gains during the experiments would also be relevant together with various surface sensitive spectroscopy methods. It makes sense to also keep assessing the chemical stability at elevated temperatures of potential candidate materials with XRD. It is clear that stability of the electrode eventually needs to be assessed during OER conditions at HTP, but it could make sense to postpone these measurements until a screening has been performed first. The main figure of merit from the HTP alkaline electrolysis measurements should be stability of the electrode performance over time, regardless of what microstructural changes that might be occurring.

4.5.4 Porous electrodes with tailored pore size distribution in aqueous and organic solvents

The desired microstructure of the porous LNF electrodes developed in the project was one which allowed for flooding of the smaller inter-particle pores and left the larger macro

pores electrolyte free, when testing the electrode in the gas diffusion mode. Essentially, this meant a percolating solid, liquid and gas phase. This to maximize the surface area on which the OER could take place while allowing the evolved O_2 gas to escape. It was hypothesized that small macro pores similar in size to the 3YSZ membrane pores could act as flooded pores, while the larger macropores on the order of several micro meters could serve as gas diffusion pores. The basic assumption was that the smaller pores would be infiltrated first due to the higher Young-Laplace pressure of the liquid in these pore (cf. the discussion in section 4.4). There would, however, be a barrier towards flooding the larger pores from the smaller pores because of the change in the Young-Laplace pressure between large and small pores, preventing infiltration of the large pores from the small pores. The validity of this assumption has not been tested but the performance of the gas diffusion electrodes seem to indicate that O_2 is allowed to escape during the OER.

The approach termed most suitable to form a microstructure as described above was using a partial sintering to form the inter-particle pores and pore formers to form the larger macro pores. Initially, during an external stay at Stockholm University, an aqueous processing method was investigated using the starch consolidation casting (SCC) approach to form a macro porous network. This was attractive as the SCC step is known to form a percolating porous phase, due to cross-linking of the starch particles and is known to prevent crack formation, otherwise often encountered in aqueous processing. In addition using water and starch is environmentally friendly. The strategy turned out not to work as expected, though, as crack formation was a major issue. The reason probably being that the deposited layers were relatively thin layers which made water evaporate too quickly from the surface not allowing the SCC step to be properly implemented. The electrode structures that were sintered did come out with pore sizes on two length scales, round pores on the order of 0.1-0-3 μm and inter-particle pores on the order of 2-10 μm.

In the next iteration, screen printing inks were therefore developed with PMMA and graphite as pore formers. PMMA particles can be synthesized in many sizes and are approx. spherical which provide a poor interconnection of the pores when the PMMA has been removed. Flaky graphite is much more irregular shaped often with elongated shapes. From the experience in the department with electrode production for solid oxide cells, it was known that a combination of PMMA and graphite gives the best electrode performance because the pores become well interconnected. This approach was therefore pursued. The resulting microstructures turned out to meet the initial success criteria with pores on two length scales, each type exhibiting a percolating network and compared to the rice starch the larger pores appeared more interconnected. The next step in the quantification of these microstructures would be to do a X-ray computed tomography scan. This could provide more information on how well interconnected the larger pores in fact are, providing information about the microstructures' tortuosity and constrictivity.

The stabilization of the LNF in the suspensions was seen to work well with PVP in both water and in the glycol ethers used for the screen printing inks. In fact suspensions prepared with EtOH, early in the project, also showed good dispersing properties with PVP. PVP is hence a versatile dispersant for LNF. Moreover, PVP still proved efficient when mixing the pore formers (rice starch, PMMA and graphite) into the suspensions, as

the LNF phase remained well dispersed.

4.5.5 Testing of porous LNF electrodes

The performance of the LNF electrodes tested in 1 M KOH at room temperature showed that the sintering temperature and testing mode influences performance whereas it is difficult to identify any strong correlations between the microstructure and the performance of the electrodes. The results also showed, however, that performance differed substantially between the different samples of the same type of tested microstructures. These deviations are not well understood. It was observed during some of the tests that the overpotential would suddenly increase rapidly, reaching a set upper limit of 3 V after which the test was terminated. The best explanation available is an effect known as the "anode effect" [132]. In dilute electrolytes, it is typically a result of a large increase in the charge transfer resistance due to a limitation in mass transfer which causes the interfacial concentration of OH^- species to drop to zero. It does not explain the somehow stochastic element involved though - that the effect is only observed on some samples.

The tests at 25 ℃ and 65 ℃ in 8 M KOH showed more stable performance, in particular the overpotential in the gas diffusion measurements exhibited less gradual increase in the overpotential. This is mainly attributed to the higher KOH concentration. It is therefore concluded that conditions as close to the operating conditions should be used to get the most relevant information about the microstructural performance.

4.5.6 Controlling bubble formation in alkaline electrolysis cells

The fabrication of oxygen electrodes for HTP-AECs with optimal microstructures require some considerations. It is clear that the HTP-AECs will be operated at high current densities, 1-3 A cm^{-2}, and it is a well-known fact that electrode surface bubble coverage increases with increasing nominal current density. As evidenced in figure 4.5 this implies that the effective current density will deviate increasingly from the nominal current density when the latter increases [131]. It is therefore reasonable to postulate that handling bubble formation and release effectively should be a main concern when designing electrodes for alkaline electrolysis cells, and in particular HTP-AECs which are designed to operate at high current densities.

The porous LNF electrodes appear to be well wetted by the electrolyte so the electrolyte will flood the pores and bubbles can be formed in the pores. It is essential that bubbles formed inside the porous structure can easily escape the microstructure as they otherwise will block the pores. For a porous electrode with some degree of tortuosity and constrictivity this is going to be troublesome if the bubble size is on the same order of magnitude as the pore sizes. Several strategies therefore seem possible. Firstly, it is possible to make hierarchical microstructures consisting of gas diffusion pores and flooded pores, as done in this project. In this case it is important to suppress bubble formation inside the pores. Applying a large pressure (20-40 bar) will certainly help decrease bubble formation and

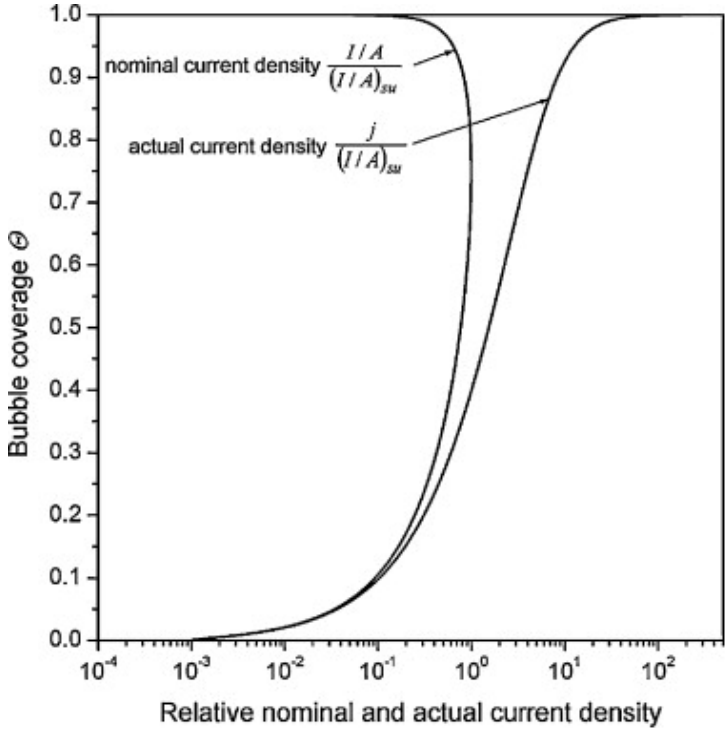

Figure 4.5: The fractional bubble coverage vs nominal and actual current density for typical gas evolution electrodes. From [130]

size inside the pores. Lowering the size of the electrolyte flooded pores to the meso-pore range will increase the supersaturation where dissolved O_2 in the electrolyte will start forming bubbles [141, 142]. Secondly, one can improve the mass transfer of electrolyte away from the electrode-electrolyte interface. It has been shown that hydrophobic zones on the electrode surface can serve as preferential bubble nucleation sites which can increase the gradient of dissolved O_2 in the electrolyte, thus driving the O_2 towards the preferential bubbles sites [133, 142].

4.5.7 My own experience working on a research project

Here I will sketch a few valuable lessons learned during my PhD work.

Lesson 1 What you measure or observe is correlated to the method you use to asses this, and the way you prepare your samples.

Lesson 2 Working in relatively fast iterations is convenient whenever possible, and especially when doing something you are not familiar with. It makes it possible to make corrections to and to optimize procedures while being agile so changes can be made quickly.

Lesson 3 Knowing and doing what is expedient is important to get progress in a project. There will always be plenty of literature you could read and small experiments that could be done. At the same time it also seems important once in awhile to follow a hunch if

something seems important or interesting but try to justify why in the progress to avoid creeping too far down into the rabbit hole.

Lesson 4 Do not try to do everything yourself - even as PhD student. You need to keep learning whether you are a student or a researcher but at the same time you will never master all techniques and disciplines. So what seems key is to have a broad idea of the possibilities and limitations of many experimental techniques; and more importantly to have an idea about where you can seek qualified advice.

Chapter 5

Conclusion and Outlook

5.1 Conclusions

The work presented in this thesis has been centered around the development of the oxygen electrode in HTP-AECs. The OER activity, on well defined surface areas, of La, Ni and Fe based perovskites, and a Ruddlesden-Popper phase, has been determined. All the materials exhibit overpotentials in the range 0.38-0.45 V at 10 mA cm^{-2} and the tafel slopes, determined between 0.5 mA cm^{-2} and 5 mA cm^{-2}, is 56-98 mV dec^{-1}. The LNF-RP and multiphase-LN were the best performing with an overpotential of 0.40 V and 0.38 V respectively at 10 mA cm^{-2}. The OER activity was seen to increase for the materials, which could be related to an increase of the ECSA over time and a change of the materials' surface chemistry. In fact, the polished surface was seen to change upon OER measurements and crack formation was clearly visible, in particular on the LN and LNF-RP surface. The XRD patterns from chemical stability measurements, carried out for 1 week in concentrated KOH at room temperature, 100 ℃ and 200 ℃, revealed that all materials decompose at 200 ℃ to simple oxides and hydroxides. The LN phase is the most chemically unstable material as NiO secondary phase formation is found already after the room temperature measurements. LNF and LNF-RP appear chemically stable up to 100 ℃, though a more sensitive analysis or longer test is needed to confirm this.

Porous LNF oxygen electrodes with hierarchical microstructures for HTP-AECs were processed using aqueous and solvent based suspensions. The aqueous LNF suspensions containing rice starch as pore former were processed using the starch consolidation casting approach and resulted in somehow hierarchical microstructures, though the consolidation casting step proved challenging. Specifically, issues with crack formation and delamination during drying of the deposited layers could not be avoided. The aqueous LNF suspensions were stabilized with different dispersants and characterized by means of particle size-, zeta potential-, sedimentation- and rheological measurements. LNF was found to be well stabilized, electrostatically in millipore water at the intrinsic pH, and using the polymer PVP. The solvent based approach proved more viable. Screen printing inks were processed using PVP as dispersant and binder with graphite and PMMA pore formers.

The LNF inks were screen printing onto porous 3YSZ membranes. The sintered LNF

electrode layers exhibit porosities in the range 58-72 % and d10 and d90 pore sizes in the ranges 0.19-0.28 µm and 1.5-3.5 µm respectively. Various sizes of PMMA and flaky graphite were used to successfully vary the pore sizes, shapes and resulting microstructures. The electrodes were tested as flooded electrodes, used in conventional alkaline electrolysis cells, and gas diffusion electrodes used in HTP-AECs. A screening of the different microstructures at room temperature in 1 M KOH showed that the performance, of the more porous samples with larger inter-particle pore sizes sintered at lower temperatures, improved but these also proved mechanically weak. No clear conclusion can be drawn on the relative performance of the microstructures with different types of pore formers. Performance in the flooded and gas diffusion mode was found to be similar at 65 ℃ in 8 M KOH with overpotentials of 0.42 V and 0.46 V respectively at 0.2 A cm^{-2}. The ECSA decreases with increasing current densities in both the testing modes which is correlated with observed bubble formation on the electrode surface in the flooded mode. At current densities above 10 mA cm^{-2} the bubble formation contributes significantly to the overpotential of the cells. In the gas diffusion mode bubble formation is also hypothesized to be an issue though it is harder to confirm this. Starvation of OH^- at the electrode surface, due to transport restrictions, is also believed to contribute to the overpotential in the gas diffusion mode.

5.2 Outlook

An important step in the development of HTP-AECs has been taken in the work reported in this thesis. It is clear from this and previous work that a particular challenge lies in the identification of oxygen electrode materials that are sufficiently stable during HTP-AECs conditions. The LNF electrode material identified in this work is not chemically stable at the HTP conditions, nonetheless it is relevant to test some of the LNF electrode materials during HTP conditions to get an idea of the stability over time under OER conditions, in particular how fast the performance evolves over time. This will also provide valuable information about how the microstructure(s) perform during operating condtions. In fact, it is clear that testing under conditions as close to the operating conditions as possible should always be a priority to get the most valid information possible. Tests performed under standard conditions, e.g. room temperature in dilute electrolyte solutions, cannot simply be extrapolated to that of typical operating conditions. The main reason being that the limiting factors are not necessarily the same. In particular, the transport of the evolved O_2 away from the electrode surface and the electrodes ability to efficiently handle bubbles seem to be essential processes for the optimized microstructures to handle.

For the future an emphasis should be put upon identifying and testing electrocatalyst materials that are sufficiently stable while also being active towards the OER. It seems pertinent not to look for the most active electrocatalysts as they often appear to be less stable. Instead adequate electrocatalytic activity and good stability should be the key requirements. The fact that the cells will be operating at 150-250 ℃ is expected to make them sufficiently active anyhow.

Development of optimized microstructures for HTP-AECs is another important task as this is still not properly understood. It is clear that the surface area should be maximized while allowing for optimal transport of OH^- species to the reactive sites and allowing the evolved O_2 to be transported away from the electrode. The thickness of the electrode layers is therefore also a parameter to be optimized together with the microstructures.

Until now, commercial metal foams with corrosion resistant coatings and electro-deposited electrocatalysts have been used. These have large pore sizes ($\approx 100\,\mu m$) and not very large specific surface area. The electrodes in this project have smaller pore sizes, larger surface areas and gas diffusion pores. They will be interesting to compare, in terms of performance, to the already tested metal foam based electrodes and guide the future efforts. In fact, initial tests have been perforned with the LNF-P3_1125 electrodes under HTP conditions and the performance is promising.

A suggested path is the development of electrocatalysts with nanometer-sized pores that can significantly enhance the specific surface area and suppress bubble formation inside the pores, thus increase the OER activity. The remaining microstructure will have to be optimized for transport of O_2 and OH^- species. It is expected, as envisioned in the motivation for this project, that a percolating electrolyte phase and a percolating gas filled phase is needed to optimize this part of the microstructure.

References

[1] IPCC. Contribution of working groups i, ii and iii to the fifth assessment report of the intergovernmental panel on climate change. In The Core writing team and Pachauri, Rajendra K. and Mayer, Leo, editor, *Climate Change 2014: Synthesis Report*. IPCC, Geneva, Switzerland, 2015.

[2] BP. BP Statistical Review of World Energy June 2017. Technical Report June, BP Statistical Review of World Energy, London, UK, 2017.

[3] Linda Doman. EIA projects 28% increase in world energy use by 2040. `https://www.eia.gov/todayinenergy/detail.php?id=32912#`, accessed August 22, 2018. September 14, 2017.

[4] Egbert Boeker and Rienk van Grondelle. *Environmental physics : sustainable energy and climate change*. Wiley, West Sussex, 2 edition, 2011.

[5] Lewis, Nathan S. and Nocera, Daniel G. Powering the planet: Chemical challenges in solar energy utilization. *Proceedings of the National Academy of Sciences*, 103(43):15729–15735, 2006.

[6] IEA. World Energy Outlook 2017 - Executive summary. report, International Energy Agency, Paris, France, 2017.

[7] IEA. Key world energy Statistics. Technical report, International Energy Agency, Paris, France, 2017.

[8] Mathiesen, B. V. and Lund, H. and Connolly, D. and Wenzel, H. and Østergaard, P. A. and Möller, B. and Nielsen, S. and Ridjan, I. and Karnøe, P. and Sperling, K. and Hvelplund, F. K. Smart Energy Systems for coherent 100% renewable energy and transport solutions. *Appl. Energy*, 145:139–154, 2015.

[9] Davis, Steven J and Lewis, Nathan S and Shaner, Matthew and Aggarwal, Sonia and Arent, Doug and Azevedo, Inês L and Benson, Sally M and Bradley, Thomas and Brouwer, Jack and Chiang, Yet-Ming and Clack, Christopher T M and Cohen, Armond and Doig, Stephen and Edmonds, Jae and Fennell, Paul and Field, Christopher B and Hannegan, Bryan and Hodge, Bri-Mathias and Hoffert, Martin I and Ingersoll, Eric and Jaramillo, Paulina and Lackner, Klaus S and Mach, Katharine J and Mastrandrea, Michael and Ogden, Joan and Peterson, F and Sanchez, Daniel L and Sperling, Daniel and Stagner, Joseph and Trancik, Jessika E and Yang, Chi-Jen and Caldeira, Ken. Net-zero emissions energy systems. *Science*, 360:1419, 2018.

[10] Joseph Impullitti. Zero Emission Cargo Transport II - San Pedro Bay Ports Hybrid & Fuel Cell Electric Vehicle Project. https://www.energy.gov/sites/prod/files/2016/06/f33/vs158_impullitti_2016_o_web.pdf, accessed August 30, 2018. June 9, 2016.

[11] Nikola staff. Nikola raises $100 million in august. https://nikolamotor.com/press_releases/nikola-raises-100-million-in-august-49, accessed August 22, 2018. August 7, 2018.

[12] Zeman, Frank S. and Keith, David W. Carbon neutral hydrocarbons. *Philos. Trans. R. Soc. A Math. Phys. Eng. Sci.*, 366(1882):3901–3918, 2008.

[13] Graves, Christopher and Ebbesen, Sune D. and Mogensen, Mogens and Lackner, Klaus S. Sustainable hydrocarbon fuels by recycling CO_2 and H_2O with renewable or nuclear energy. *Renew. Sustain. Energy Rev.*, 15(1):1–23, 2011.

[14] Bertuccioli, Luca and Chan, Alvin and Hart, David and Lehner, Franz and Madden, Ben and Eleanor Standen. Development of Water Electrolysis in the European Union. Technical Report February, Fuel cells and hydrogen Joint undertaking, 2014.

[15] Reuters staff. Toyota to ramp up hydrogen fuel cell vehicle sales around 2020. https://www.reuters.com/article/us-toyota-fuelcell/toyota-to-build-fuel-cell-stack-plant-ramp-up-fuel-cell-vehicle-sales-from-2020-idUSK August 22, 2018. May 24, 2018.

[16] EIA staff. Few transportation fuels surpass the energy densities of gasoline and diesel. https://www.eia.gov/todayinenergy/detail.php?id=9991 accessed August 22, 2018. February 14, 2013.

[17] Philibert, Cédric. Producing ammonia and fertilizers: new opportunities from renewables. Technical Report October, International Energy Agency, 2017.

[18] Hanley, Nick and Shogren, Jason F. and White, Ben B. *Introduction to environmental economics*. Oxford University Press, Oxford, 2001.

[19] Johanna Ivy. Summary of Electrolytic Hydrogen Production: Milestone Completion Report. Technical Report September, National Renewable Energy Laboratory, Colorado, USA, 2004.

[20] Smolinka, Tom and Ojong, Emile Tabu and Garche, Jürgen. Hydrogen Production from Renewable Energies-Electrolyzer Technologies. In Patrick∼T. Moseley and Jürgen Garche, editors, *Electrochemical Energy Storage for Renewable Sources and Grid Balancing*, chapter Chapter 8, pages 103–128. Elsevier, Amsterdam, 2015.

[21] Kai Zeng and Dongke Zhang. Recent progress in alkaline water electrolysis for hydrogen production and applications. *Prog. Energy Combust. Sci.*, 36(3):307–326, 2010.

[22] Alexander Buttler and Hartmut Spliethoff. Current Status of water electrolysis for energy storage, grid balancing and sector coupling via power-to-gas and power-to-liquids: a review. *Renew. Sustain. Energy Rev.*, 82:2440–2454, 2018.

[23] Ursúa, Alfredo and Gandía, Luis M. and Sanchis, Pablo. Water Electrolysis : Current Status and Future Trends. *Proc. IEEE*, 100(2):410–426, 2012.

[24] Mikkel Rykær Kraglund. *Alkaline membrane water electrolysis with non-noble catalysts*. PhD thesis, Department of Energy Conversion and Storage, Technical University of Denmark, 2017.

[25] Ebbesen, Sune Dalgaard and Jensen, Søren Højgaard and Hauch, Anne and Mogensen, Mogens Bjerg. High Temperature Electrolysis in Alkaline Cells, Solid Proton Conducting Cells, and Solid Oxide Cells. *Chem. Rev.*, 114(21):10697–10734, 2014.

[26] Holladay, J. D. and Hu, J. and King, D. L. and Wang, Y. An overview of hydrogen production technologies. *Catal. Today*, 139(4):244–260, 2009.

[27] R∼L Leroy. Industrial water electrolysis: present and future. *Int. J. Hydrogen Energy*, 8(6):401–417, 1983.

[28] Kraglund, Mikkel Rykær and Aili, David and Jankova, Katja and Christensen, Erik and Li, Qingfeng and Jensen, Jens Oluf. Zero-Gap Alkaline Water Electrolysis Using Ion-Solvating Polymer Electrolyte Membranes at Reduced KOH Concentrations. *J. Electrochem. Soc.*, 163(11):F3125–F3131, 2016.

[29] Liu, Zengcai and Sajjad, Syed Dawar and Gao, Yan and Yang, Hongzhou and Kaczur, Jerry J. and Masel, Richard I. The effect of membrane on an alkaline water electrolyzer. *Int. J. Hydrogen Energy*, 42(50):29661–29665, 2017.

[30] Miles, M. H. Effect of Temperature on Electrode Kinetic Parameters for Hydrogen and Oxygen Evolution Reactions on Nickel Electrodes in Alkaline Solutions. *J. Electrochem. Soc.*, 123(3):332, 1976.

[31] Juergen Fischer, Hans Hofmann, Gerhard Luft, and Hartmnt Wendt. Fundamental investigations and electrochemical engineering aspects concerning an advanced concept for alkaline water electrolysis. *AIChE J.*, 26(5):794–802, 1980.

[32] Davidson, C.R. and Kissel, G. and Srinivasan, S. Electrode Kinetics of the Oxygen Evolution Reaction at $NiCo_2O_4$ from 30% KOH. *J. Electroanal. Chem.*, 132:129–135, 1982.

[33] Ogata, Y and Hori, H and Yasuda, M and Hine, F. On the Cathode Behavior and the Cell Voltage in NaOH Solutions under Elevated Temperatures. *J. Electrochem. Soc.*, 431(January):76–83, 1988.

[34] Ganley, Jason C. High temperature and pressure alkaline electrolysis. *Int. J. Hydrogen Energy*, 34(9):3604–3611, 2009.

[35] Wendt, H and Hofmann, H. Cermet diaphragms and integrated electrode-diaphragm units for advanced alkaline water electrolysis. *Int. J. Hydrogen Energy*, 10(6):375–381, 1985.

[36] Divisek, J and Schmitz, H. A Bipolar Cell for Advanced Alkaline Water Electrolysis. *Int. J. Hydrogen Energy*, 7(9):703–710, 1982.

[37] Frank Allebrod. *High Temperature Alkaline Electrolysis*. PhD thesis, Department of Energy Conversion and Storage, Technical University of Denmark, 2013.

[38] Allebrod, Frank and Chatzichristodoulou, Christodoulos and Mogensen, Mogens B. Alkaline electrolysis cell at high temperature and pressure of 250 ℃ and 42 bar. *J. Power Sources*, 229:22–31, 2013.

[39] Allebrod, Frank and Chatzichristodoulou, Christodoulos and Mogensen, Mogens B. Cobalt and molybdenum activated electrodes in foam based alkaline electrolysis cells at 150-250 ℃ and 40 bar. *J. Power Sources*, 255:394–403, 2014.

[40] Allebrod, Frank and Chatzichristodoulou, Christodoulos and Mogensen, Mogens B. Foam Based Gas Diffusion Electrodes for Reversible Alkaline Electrolysis Cells. *ECS Trans.*, 64(3):1029–1038, 2014.

[41] Allebrod, Frank and Chatzichristodoulou, Christodoulos and Mogensen, Mogens B. Cobalt and molybdenum activated electrodes in foam based alkaline electrolysis cells at 150-250 ℃ and 40 bar. *J. Power Sources*, 255:394–403, 2014.

[42] Chatzichristodoulou, C. and Allebrod, F, and Mogensen, M. B. High Temperature Alkaline Electrolysis Cells with Metal Foam Based Gas Diffusion Electrodes. *J. Electrochem. Soc.*, 163(11):3036–3040, 2016.

[43] Matsumoto, Y. and Sato, E. Electrocatalytic properties of transition metal oxides for oxygen evolution reaction. *Mater. Chem. Phys.*, 14(5):397–426, 1986.

[44] Emiliana Fabbri, Anja Habereder, Kay Waltar, Rudiger Kötz, and Thomas Schmidt. Developments and perspectives of oxide-based catalysts for the oxygen evolution reaction. *Catal. Sci. Technol.*, 4:3800–3821, 2014.

[45] Bockris, John O'M. and Otagawa, Takaaki. The Electrocatalysis of Oxygen Evolution on Perovskites. *J. Electrochem. Soc.*, 131(2):290–302, 1984.

[46] Trasatti, S. Electrocatalysis in the anodic evolution of oxygen and chlorine. *Electrochim. Acta*, 29(11):1503–1512, 1984.

[47] Suntivich, J. and May, K. J. and Gasteiger, H. a. and Goodenough, J. B. and Shao-Horn, Y. A Perovskite Oxide Optimized for Oxygen Evolution Catalysis from Molecular Orbital Principles. *Science*, 334(6061):1383–1385, 2011.

[48] Holger Dau, Christian Limberg, Tobias Reier, Marcel Risch, Stefan Roggan, and Peter Strasser. The Mechanism of Water Oxidation: From Electrolysis via Homogeneous to Biological Catalysis. *ChemCatChem*, 2(7):724–761, 2010.

[49] Rossmeisl, J. and Qu, Z. W. and Zhu, H. and Kroes, G. J. and Nørskov, J. K. Electrolysis of water on oxide surfaces. *J. Electroanal. Chem.*, 607(1-2):83–89, 2007.

[50] Man, Isabela C. and Su, Hai-Yan and Calle-Vallejo, Federico and Hansen, Heine a. and Martínez, José I. and Inoglu, Nilay G. and Kitchin, John and Jaramillo, Thomas F. and Nørskov, Jens K. and Rossmeisl, Jan. Universality in Oxygen Evolution Electrocatalysis on Oxide Surfaces. *ChemCatChem*, 3(7):1159–1165, 2011.

[51] Paul Sabatier. Hydrogénations et déshydrogénations par catalyse. *Berichte der deutschen chemischen Gesellschaft*, 44(3):1984–2001, 1911.

[52] Bick, D S and Kindsmüller, A and Staikov, G and Gunkel, F and Müller, D and Schneller, T and Waser, R. and Valov, I. Stability and Degradation of Perovskite Electrocatalysts for Oxygen Evolution Reaction. *Electrochim. Acta*, 218:156–162, 2016.

[53] Bick, Daniel and Krebs, Tobias B. and Kleimaier, Dominik and Zurhelle, Alexander F. and Staikov, Georgi T. and Waser, Rainer and Valov, Ilia. Degradation Kinetics during Oxygen Electrocatalysis on Perovskite-based Surfaces in Alkaline Media. *Langmuir*, 34:1347, 2018.

[54] Watzele, Sebastian and Liang, Yunchang and Bandarenka, Aliaksandr S. Intrinsic Activity of some Oxygen and Hydrogen Evolution Reaction Electrocatalysts under Industrially Relevant Conditions. *ACS Appl. Energy Mater.*, page acsaem.8b00852, 2018.

[55] Binninger, Tobias and Mohamed, Rhiyaad and Waltar, Kay and Fabbri, Emiliana and Levecque, Pieter and Kötz, Rüdiger and Schmidt, Thomas J. Thermodynamic explanation of the universal correlation between oxygen evolution activity and corrosion of oxide catalysts. *Sci. Rep.*, 5:12167, 2015.

[56] L∼Trotochaud, J∼K Ranney, K∼N Williams, and S∼W Boettcher. Solution-Cast Metal Oxide Thin Film Electrocatalysts for Oxygen Evolution. *J. Am. Chem. Soc.*, 134(41):17253–17261, 2012.

[57] Hong, Wesley T. and Risch, Marcel and Stoerzinger, Kelsey A. and Grimaud, Alexis and Suntivich, Jin and Shao-Horn, Yang. Toward the rational design of non-precious transition metal oxides for oxygen electrocatalysis. *Energy Environ. Sci.*, 8:1404–1427, 2015.

[58] Vesborg, Peter C. K. and Jaramillo, Thomas F. Addressing the terawatt challenge: scalability in the supply of chemical elements for renewable energy. *RSC Adv.*, 2(21):7933, 2012.

[59] Wendt, H. and Hofmann, H. and Plzak, V. Materials research and development of electrocatalysts for alkaline water electrolysis. *Mater. Chem. Phys.*, 22(1-2):27–49, 1989.

[60] McCrory, Charles C. L. and Jung, Suho and Peters, Jonas C. and Jaramillo, Thomas F. Benchmarking Heterogeneous Electrocatalysts for the Oxygen Evolution Reaction. *J. Am. Chem. Soc.*, 135:16977–16987, 2013.

[61] Miles, M. H. and Huang, Y. H. and Srinivasan, S. The Oxygen Electrode Reaction in Alkaline Solutions on Oxide Electrodes Prepared by the Thermal Decomposition Method. *J. Electrochem. Soc.*, 125(12):1931–1934, 1978.

[62] Subbaraman, Ram and Tripkovic, Dusan and Chang, Kee-Chul and Strmcnik, Dusan and Paulikas, Arvydas P. and Hirunsit, Pussana and Chan, Maria and Greeley, Jeff and Stamenkovic, Vojislav and Markovic, Nenad M. Trends in activity for the water electrolyser reactions on 3d M(Ni,Co,Fe,Mn) hydr(oxy)oxide catalysts. *Nat. Mater.*, 11(6):550–557, 2012.

[63] Louie, Mary W. and Bell, Alexis T. An investigation of thin-film Ni-Fe oxide catalysts for the electrochemical evolution of oxygen. *J. Am. Chem. Soc.*, 135(33):12329–12337, 2013.

[64] Li, Guangfu and Anderson, Lawrence and Chen, Yanan and Pan, Mu and Abel Chuang, Po-Ya. New insights into evaluating catalyst activity and stability for oxygen evolution reactions in alkaline media. *Sustain. Energy Fuels*, pages 237–251, 2018.

[65] May, Kevin J. and Carlton, Christopher E. and Stoerzinger, Kelsey A. and Risch, Marcel and Suntivich, Jin and Lee, Yueh-Lin and Grimaud, Alexis and Shao-Horn, Yang. Influence of Oxygen Evolution during Water Oxidation on the Surface of Perovskite Oxide Catalysts. *J. Phys. Chem. Lett.*, 3(22):3264–3270, 2012.

[66] Lee, Youngmin and Suntivich, Jin and May, Kevin J and Perry, Erin E and Shao-Horn, Yang. Synthesis and Activities of Rutile IrO2 and RuO2 Nanoparticles for Oxygen Evolution in Acid and Alkaline Solutions. *J. Phys. Chem. Lett.*, 3:399–404, 2012.

[67] Grimaud, Alexis and May, Kevin J and Carlton, Christopher E and Lee, Yueh-Lin and Risch, Marcel and Hong, Wesley T and Zhou, Jigang and Shao-Horn, Yang. Double perovskites as a family of highly active catalysts for oxygen evolution in alkaline solution. *Nat. Commun.*, 4:2439, 2013.

[68] Chen, Jamie Y.C. and Miller, Jeffrey T. and Gerken, James B. and Stahl, Shannon S. Inverse spinel $NiFeAlO_4$ as a highly active oxygen evolution electrocatalyst: Promotion of activity by a redox-inert metal ion. *Energy Environ. Sci.*, 7(4):1382–1386, 2014.

[69] Su, Chao and Wang, Wei and Chen, Yubo and Yang, Guangming and Xu, Xiaomin and Tadé, Moses O. and Shao, Zongping. $SrCo_{0.9}Ti_{0.1}O_{3-\delta}$ as a new electrocatalyst for the oxygen evolution reaction in alkaline electrolyte with stable performance. *ACS Appl. Mater. Interfaces*, 7(32):17663–17670, 2015.

[70] Mohamed, R. and Cheng, X. and Fabbri, E. and Levecque, P. and Kotz, R. and Conrad, O. and Schmidt, T. J. Electrocatalysis of Perovskites: The Influence of Carbon on the Oxygen Evolution Activity. *J. Electrochem. Soc.*, 162(6):F579–F586, 2015.

[71] Esswein, Arthur J and Mcmurdo, Meredith J and Ross, Phillip N and Bell, Alexis T and Tilley, T Don. Size-Dependent Activity of Co_3O_4 Nanoparticle Anodes for Alkaline Water Electrolysis. *J. Phys. Chem. C*, 113:15068–15072, 2009.

[72] Suen, Nian-Tzu and Hung, Sung-Fu and Quan, Quan and Zhang, Nan and Xu, Yi-Jun and Chen, Hao Ming. Electrocatalysis for the oxygen evolution reaction: recent development and future perspectives. *Chem. Soc. Rev.*, 46(2):337–365, 2017.

[73] A.C.C. Tseung and Jasem, S. Oxygen evolution on semiconducting oxides. *Electrochim. Acta*, 22(1):31–34, 1977.

[74] Balej, J. Electrocatalysts for oxygen evolution in advanced water electrolysis. *Int. J. Hydrogen Energy*, 10(2):89–99, 1985.

[75] MonteverdeVidela, Alessandro H A and Stelmachowski, P and Ercolino, Giuliana and Specchia, Stefania. Benchmark comparison of Co3O4 spinel structured oxides with different morphologies for oxygen evolution reaction under alkaline conditions. *J. Appl. Electrochem.*, 47(3):295–304, 2017.

[76] Crystal structure of spinel. `https://commons.wikimedia.org/wiki/File:Spinel.GIF`, accessed on August 27, 2018. Created by "Materialscientist" for Wikipedia Commons, April 18, 2009.

[77] Crystal structure of perovskite. `https://commons.wikimedia.org/wiki/File:Perovskite.jpg`, accessed on August 27, 2018). Created by "Cadmium" for Wikipedia Commons, April 10, 2006.

[78] Pena, M a and Fierro, J L G. Chemical structures and performances of perovskite oxides. *Chem. Rev.*, 101:1981–2017, 2001.

[79] Matsumoto, Y. and Yamada, S and Nishida, T and Sato, E. Oxygen Evolution on $La_{1-x}Sr_xFe_{1-y}Co_yO_3$ Series Oxides. *J. Electrochem. Soc.*, 127(11):2360–2364, 1980.

[80] Mohamed, R. and Fabbri, E. and Levecque, P. and Kötz, R. and Schmidt, T. J. and Conrad, O. Understanding the Influence of Carbon on the Oxygen Reduction and Evolution Activities of BSCF/Carbon Composite Electrodes in Alkaline Electrolyte R. Mohamed. *ECS Trans.*, 58(36):9–18, 2014.

[81] Qiu, Yang and Xin, Le and Li, Wenzhen. Electrocatalytic oxygen evolution over supported small amorphous ni-fe nanoparticles in alkaline electrolyte. *Langmuir*, 30(26):7893–7901, 2014.

[82] Diaz-Morales, Oscar and Ledezma-Yanez, Isis and Koper, Marc T. M. and Calle-Vallejo, Federico. Guidelines for the Rational Design of Ni-Based Double Hydroxide Electrocatalysts for the Oxygen Evolution Reaction. *ACS Catal.*, 5(9):5380–5387, 2015.

[83] Fabio Dionigi and Peter Strasser. NiFe-Based (Oxy)hydroxide Catalysts for Oxygen Evolution Reaction in Non-Acidic Electrolytes. *Adv. Energy Mater.*, 6(23), 2016.

[84] Burke, Michaela S and Zou, Shihui and Enman, Lisa J and Kellon, Jaclyn E and Gabor, Christian A and Pledger, Erica and Boettcher, Shannon W. Revised Oxygen Evolution Reaction Activity Trends for First-Row Transition-Metal (Oxy)hydroxides in Alkaline Media. *J. Phys. Chem. Lett.*, 6:3737–3742, 2015.

[85] Ming Gong and Hongjie Dai. A mini review on NiFe-based materials as highly active oxygen evolution reaction electrocatalysts. *Nano Res.*, 8(1):23–39, 2015.

[86] Corrigan, Dennis A. The Catalysis of the Oxygen Evolution Reaction by Iron Impurities in Thin Film Nickel Oxide Electrodes. *J. Electrochem. Soc.*, 134(2):377–384, 1987.

[87] Trotochaud, Lena and Young, Samantha L. and Ranney, James K. and Boettcher, Shannon W. Nickel-Iron oxyhydroxide oxygen-evolution electrocatalysts: The role of intentional and incidental iron incorporation. *J. Am. Chem. Soc.*, 136(18):6744–6753, 2014.

[88] Zhang, Cuijuan and Fagan, Randal D. and Smith, Rodney D. L. and Moore, Stephanie A. and Berlinguette, Curtis P. and Trudel, Simon. Mapping the performance of amorphous ternary metal oxide water oxidation catalysts containing aluminium. *J. Mater. Chem. A*, 3(2):756–761, 2015.

[89] Lu, Zhiyi and Qian, Li and Tian, Yang and Li, Yaping and Sun, Xiaoming and Duan, Xue. Ternary NiFeMn layered double hydroxides as highly-efficient oxygen evolution catalysts. *Chem. Commun.*, 52(5):908–911, 2016.

[90] Chi, Bo and Li, Jianbao and Han, Yongsheng and Chen, Yongjun. Effect of temperature on the preparation and electrocatalytic properties of a spinel NiCo2O4/Ni electrode. *Int. J. Hydrogen Energy*, 29(6):605–610, 2004.

[91] Habrioux, A. and Abidat, I. and Canaff, C. and Morais, C. and Comminges, C. and Napporn, T. and Kokoh, K. B. Co-Based Mesoporous Spinels for Oxygen Evolution Reaction in Alkaline Medium. *ECS Trans.*, 77(9):15–24, 2017.

[92] Singh, R. N. and Mishra, D. and Anindita and Sinha, a. S K and Singh, a. Novel electrocatalysts for generating oxygen from alkaline water electrolysis. *Electrochem. commun.*, 9(6):1369–1373, 2007.

[93] Jeon, Hyo Sang and Jee, Michael Shincheon and Kim, Haeri and Ahn, Su Jin and Hwang, Yun Jeong and Min, Byoung Koun. Simple Chemical Solution Deposition of Co 3 O 4 Thin Film Electrocatalyst for Oxygen Evolution Reaction. *ACS Appl. Mater. Interfaces*, page acsami.5b06189, 2015.

[94] Suntivich, J. and May, K. J. and Gasteiger, H. a. and Goodenough, J. B. and Shao-Horn, Y. Suppoting material for A Perovskite Oxide Optimized for Oxygen Evolution Catalysis from Molecular Orbital Principles. *Science (80-.).*, 334(6061):1383–1385, 2011.

[95] Jie Yu, Jaka Sunarso, Yinlong Zhu, Xiaomin Xu, Ran Ran, Wei Zhou, and Zongping Shao. Activity and Stability of Ruddlesden-Popper-Type $La_{n+1}Ni_nO_{3n+1}$(n =1, 2, 3,

and ∞) Electrocatalysts for Oxygen Reduction and Evolution Reactions in Alkaline Media. *Chem. - A Eur. J.*, 22:2719–2727, 2016.

[96] Karina Elumeeva, Justus Masa, Frank Tietz, Fengkai Yang, Wei Xia, Martin Muhler, and Wolfgang Schuhmann. A Simple Approach towards High-Performance Perovskite-Based Bifunctional Oxygen Electrocatalysts. *ChemElectroChem*, 3(1):138–143, 2016.

[97] Zhuang Wang, Mian Li, Chenghao Liang, Liquan Fan, Jianan Han, and Yueping Xiong. Effect of morphology on the oxygen evolution reaction for $La_{0.8}Sr_{0.2}Co_{0.2}Fe_{0.8}O_{3-\delta}$ electrochemical catalyst in alkaline media. *RSC Adv.*, 6(73):69251–69256, 2016.

[98] Fang Song and Xile Hu. Exfoliation of layered double hydroxides for enhanced oxygen evolution catalysis. *Nat Commun*, 5, jul 2014.

[99] Rahaman, Mohammed N. *Ceramic Processing*. Taylor & Francis, 2007.

[100] Richerson, David W. *Modern Ceramic Engineering*. Taylor & Francis, 3. edition, 2006.

[101] Reed, J. S. *Principles of Ceramics Processing*. Wiley, 1995.

[102] Burmeister, Christine Friederike and Kwade, Arno. Process engineering with planetary ball mills. *Chem. Soc. Rev.*, 42(18):7660–7667, 2013.

[103] Peter Baláž. High-energy milling. In *Mechanochemistry in Nanoscience and Minerals Engineering*, chapter∼2., pages 103–132. Springer-Verlag Berlin Heidelberg, 2008.

[104] Lewis, J. A. Colloidal Processing of Ceramics. *J. Am. Ceram. Soc.*, 83(10):2341–2359, 2000.

[105] Electrostatic stabilisation. `https://commons.wikimedia.org/wiki/File:Diagram_of_zeta_potential_and_slipping_planeV2.svg`, accessed August 29, 2018. made by Larrisgood and Mjones1984 for Wikipedia Commons, February 1, 2012.

[106] Christopher Hammond. *The Basics of Crystallography and Diffraction*. Oxford University Press, New Jersey, 2 edition, 2001.

[107] Tsipis, E.V. and Naumovich, E.N. and Patrakeev, M.V. and Waerenborgh, J.C. and Pivak, Y.V. and Gaczyński, P. and Kharton, V.V. Oxygen non-stoichiometry and defect thermodynamics in $La_2Ni_{0.9}Fe_{0.1}O_{4+\delta}$. *J. Phys. Chem. Solids*, 68(7):1443–1455, 2007.

[108] Brunauer, Stephen and Emmett, P. H. and Teller, Edward. Adsorption of Gases in Multimolecular Layers. *J. Am. Chem. Soc.*, 60(2):309–319, 1938.

[109] Thommes, Matthias and Kaneko, Katsumi and Neimark, Alexander V. and Olivier, James P. and Rodriguez-Reinoso, Francisco and Rouquerol, Jean and Sing, Kenneth S.W. Physisorption of gases, with special reference to the evaluation of surface area

and pore size distribution (IUPAC Technical Report). *Pure Appl. Chem.*, 87(9-10):1051–1069, 2015.

[110] Tamari, S. and López-Hernández, R. I. Optimum design of the comparative gas pycnometer for determining the volume of solid particles. *Meas. Sci. Technol.*, 15:549–558, 2004.

[111] Chartoff, Richard P. and Menczel, Joseph D. and Dillman, Steven H. Dynamic Mechanical Analysis (DMA). In Menczel, Joseph D. and Prime, R. Bruce, editor, *Thermal Analysis of Polymers: Fundamentals and Applications*, pages 387–495. John Wiley & Sons, New Jersey, 2009.

[112] Prime, R. Bruce and Bair, Harvey E and Vyazovkin, Sergey and Gallagher, Patrick K. and Alan, Riga. Thermogravimetric Analysis (TGA). In Joseph∼D. Menczel and R.∼Bruce Prime, editors, *Thermal Analysis of Polymers: Fundamentals and Applications*, pages 241–317. John Wiley & Sons, New Jersey, 2009.

[113] Merkus, Henk G. *Particle Size Measurements - Fundamentals, Practice, Quality.* Springer Science+Business Media B.V., 2009.

[114] Kimiko Makino and Hiroyuki Ohshima. Electrophoretic mobility of a colloidal particle with constant surface charge density. *Langmuir*, 26(23):18016–18019, 2010.

[115] T.G. Mezger. *The Rheology Handbook: For Users of Rotational and Oscillatory Rheometers.* European coatings tech files. Vincentz Network, Hannover, Germany, 4th edition, 2011.

[116] Anton Paar. Instruction Manual {MCR} series, apr 2014.

[117] Azema,N. Sedimentation behaviour study by three optical methods - granulometric and electrophoresis measurements, dispersion optical analyser. *Powder Technol.*, 165(3):133–139, 2006.

[118] Reference Electrode HydroFlex – Hydrogen Electrode – Reference Electrode – Indicator Electrode. `https://www.referenceelectrode.info/`, accessed August 15, 2018, 2018.

[119] Andrzej Lasia. *Electrochemical Impedance Spectroscopy and its Applications.* Springer Science+Business Media, New York, 2014.

[120] FlexCell-Test cell for Electrochemistry, Voltammetry, Corrosion, 2018.

[121] Zhou, Weilie and Apkarian, Robert P. and Wang, Zhong Lin and Joy, David. Fundamentals of scanning electron microscopy. In Weilie Zhou and Zhong∼Lin Wang, editors, *Scanning Electron Microsc. Nanotechnol. Tech. Appl.*, chapter∼1, pages 1–40. Springer, New York, 2007.

[122] Jørgensen, Peter S. Threshalyzer ver. 1.01. Image analysis software, 2018.

[123] Bowen, Jacob R. Manseg ver. 0.37. Image analysis software, 2018.

[124] Herbert Giesche. Mercury porosimetry: A general (practical) overview. *Part. Part. Syst. Charact.*, 23(1):9–19, 2006.

[125] Vogt, H. The Quantities Affecting the Bubble Coverage of Gas-Evolving Electrodes. *Electrochim. Acta*, 235:495–499, 2017.

[126] Janssen, L. J. J. and Sillen, C. W. M. P. and Barendrecht, E. and van Stralen, S. J. D. Bubble behaviour during oxygen and hydrogen evolution at transparent electrodes in KOH solution. *Electrochim. Acta*, 29(5):633–642, 1984.

[127] Sides, Paul J. A Close View of Gas Evolution from the Back Side of a Transparent Electrode. *J. Electrochem. Soc.*, 132(3):583, 1985.

[128] Wedershoven, H. M.S. and de Jonge, R. M. and Sillen, C. W.M.P. and van Stralen, S. J.D. Behaviour of oxygen bubbles during alkaline water electrolysis. *Int. J. Heat Mass Transf.*, 25(8):1239–1243, 1982.

[129] Janssen, L. J. J. and van Stralen, S. J. D. Bubble Behaviour on and Mass Transfer To an Oxygen- Evolving Transparent Nickel Electrode in Alkaline Solution. *Electrochim. Acta*, 26(8):1011–1022, 1981.

[130] Vogt, H. The actual current density of gas-evolving electrodes - Notes on the bubble coverage. *Electrochim. Acta*, 78:183–187, 2012.

[131] Vogt, H. and Balzer, R. J. The bubble coverage of gas-evolving electrodes in stagnant electrolytes. *Electrochim. Acta*, 50(10):2073–2079, 2005.

[132] Vogt, H. On the various types of uncontrolled potential increase in electrochemical reactors - The anode effect. *Electrochim. Acta*, 87:611–618, 2013.

[133] Brussieux, C. and Viers, Ph and Roustan, H. and Rakib, M. Controlled electrochemical gas bubble release from electrodes entirely and partially covered with hydrophobic materials. *Electrochim. Acta*, 56(20):7194–7201, 2011.

[134] Vogt, H. On the gas-evolution efficiency of electrodes. II - Numerical analysis. *Electrochim. Acta*, 56(5):2404–2410, 2011.

[135] Balej, J. Water vapour partial pressures and water activities in potassium and sodium hydroxide solutions over wide concentration and temperature ranges. *Int. J. Hydrogen Energy*, 10(4):233–243, 1985.

[136] Ahn, Sang Hyun and Choi, Insoo and Park, Hee-Young and Hwang, Seung Jun and Yoo, Sung Jong and Cho, Eunae and Kim, Hyoung-Juhn and Henkensmeier, Dirk and Nam, Suk Woo and Kim, Soo-Kil and Jang, Jong Hyun. Effect of morphology of electrodeposited Ni catalysts on the behavior of bubbles generated during the oxygen evolution reaction in alkaline water electrolysis. *Chem. Commun.*, 49(81):9323, 2013.

[137] Burke, Michaela S. and Enman, Lisa J. and Batchellor, Adam S. and Zou, Shihui and Boettcher, Shannon W. Oxygen Evolution Reaction Electrocatalysis on Transition Metal Oxides and (Oxy)hydroxides: Activity Trends and Design Principles. *Chem. Mater.*, 27:7549–7558, 2015.

[138] Höfer, Heidi E. and Kock, Wulf F. Crystal Chemistry and Thermal Behavior in the La(Cr, Ni)O3 Perovskite System. *J. Electrochem. Soc.*, 140(10):2889–2894, 1993.

[139] Zinkevich, M. and Aldinger, F. Thermodynamic analysis of the ternary La-Ni-O system. *J. Alloys Compd.*, 375(1-2):147–161, 2004.

[140] Konysheva, Elena and Suard, Emmanuelle and Irvine, John T. S. Effect of oxygen non stoichiometry and oxidation state of transition elements on high-temperature phase transition in a-site deficient $La_{0.95}Ni_{0.6}Fe_{0.4}O_{3-\delta}$ perovskite". *Chem. Mater.*, 21(21):5307–5318, 2009.

[141] Chen, Qianjin and Luo, Long and White, Henry S. Electrochemical generation of a hydrogen bubble at a recessed platinum nanopore electrode. *Langmuir*, 31(15):4573–4581, 2015. PMID: 25811080.

[142] Kadyk, Thomas and Bruce, David and Eikerling, Michael. How to Enhance Gas Removal from Porous Electrodes? *Sci. Rep.*, 6:1–14, 2016.